

Reduction of Bridge Deck Cracking through Alternative Material Usage



Prepared by:
Anil Patnaik

Prepared for:
The Ohio Department of Transportation,
Office of Statewide Planning & Research

State Job Number 135260

December 2017

Final Report



Technical Report Documentation Page

1. Report No.	2. Government Accession No.	3. Recipient's Catalog No.	
FHWA/OH-2017/44			
4. Title and Subtitle		5. Report Date	
Reduction of Bridge Deck Cracking through Alternative Material Usage		December 2017	
		6. Performing Organization Code	
7. Author(s)		8. Performing Organization Report No.	
Anil Patnaik			
9. Performing Organization Name and Address		10. Work Unit No. (TRIS)	
The University of Akron 302 Buchtel Common Akron, OH 44325		11. Contract or Grant No.	
		SJN 135260	
12. Sponsoring Agency Name and Address		13. Type of Report and Period Covered	
Ohio Department of Transportation 1980 West Broad Street Columbus, Ohio 43223		Final Report	
		14. Sponsoring Agency Code	
15. Supplementary Notes			
16. Abstract			
<p>ODOT routinely deploys a large number of continuous span structural slab bridges. Despite being designed to strictly satisfy all the relevant AASHTO and ODOT BDM requirements, many such bridge decks show transverse cracks, with widths greater than those predicted using AASHTO 2012 and ACI 318-14 guidelines, after being in service for less than one year. The addition of polypropylene fiber to deck concrete has the potential to reduce such cracking. The overall goal of this project was to identify materials and methods to reduce the extent and severity of deck cracking for structural slab bridges and determine the effectiveness of fiber for this purpose. From the crack surveys of 30 bridges in various ODOT districts, sampled from the 63 bridges suggested from the bridge inventory, it was found that crack widths of transverse cracks were in excess of the recommended limit of 0.007" on 26 of the surveyed bridges. Meeting the maximum crack width limit of 0.007" for bridge decks reinforced with epoxy-coated bars is unrealistic and unachievable with current ODOT practices, and this limit may need to be reconsidered. The addition of fiber to deck concrete without any changes to the reinforcement details of continuous span structural slab bridges was determined to reduce the extent and the severity of cracking by a factor of about 3 to 4, making it plausible to reduce crack widths in future bridge decks. The beneficial effects of fiber primarily stem from the improved performance of the concrete with fiber under freeze-thaw and sustained loading as well as from the enhanced response of concrete to static and fatigue loading. The ease of placement, effective consolidation and acceptable finish achieved with concrete incorporating polypropylene fiber at a rate of 10 lb/yd³ in a pilot bridge in Medina County (Ohio) makes the proposed solution implementable by ODOT without any deviations from the current practices except for the addition of fiber to deck concrete.</p>			
17. Keywords		18. Distribution Statement	
Continuous span structural slab bridges, bridge deck cracking, crack widths, epoxy coated bars, load testing, fiber reinforced concrete deck slabs.		No restrictions. This document is available to the public through the National Technical Information Service, Springfield, Virginia 22161	
19. Security Classification (of this report)	20. Security Classification (of this page)	21. No. of Pages	22. Price
Unclassified	Unclassified		

Reduction of Bridge Deck Cracking through Alternative Material Usage

Prepared by:

Anil Patnaik, Ph.D.

Professor of Structural Engineering
The University of Akron
Department of Civil Engineering
302 Buchtel Common
Akron, Ohio 44325
Phone: (330) 972-5226
Fax: (330) 972-6020
Email: Patnaik@uakron.edu

December 2017

Prepared in cooperation with the Ohio Department of Transportation
and the U.S. Department of Transportation, Federal Highway Administration

The contents of this report reflect the views of the author(s) who is (are) responsible for the facts and the accuracy of the data presented herein. The contents do not necessarily reflect the official views or policies of the Ohio Department of Transportation or the Federal Highway Administration. This report does not constitute a standard, specification, or regulation.

ACKNOWLEDGMENTS

Ohio Department of Transportation (ODOT) provided funding for this project, and we are grateful for this support. The extensive input and feedback provided by Mr. Perry Ricciardi, Dr. Waseem Khalifa, and Mr. Teddy Antonios, the ODOT Subject Matter Experts for this project, is gratefully acknowledged. Their contributions in completing the project and finalizing this report have been very valuable. Several graduate students of the University of Akron, Srikanth Marchetty, Mohamed Habouh, Mohamed Essili, Abdullah Alzlfawi, Umang Pawar, and Sourav Khatua, performed all the testing described in this project and provided extensive assistance as and when needed for the completion of this project. Dave McVaney, Dale Ertley, Bill Wenzel and Brett Bell of the University of Akron also provided assistance in completing the experimental work. Sheila Pearson helped in proofreading and editing the draft final report.

TABLE OF CONTENTS

ACKNOWLEDGMENTS.....	iv
TABLE OF CONTENTS.....	v
LIST OF FIGURES	vii
LIST OF TABLES	vii
EXECUTIVE SUMMARY	1
Problem Statement.....	1
Goals and Objectives of the Study.....	1
Research Findings.....	2
Summary.....	2
PROJECT BACKGROUND.....	3
Introduction.....	3
Need for the Research	4
RESEARCH CONTEXT.....	5
Goals and Objectives of the Study.....	5
Specific Tasks Accomplished in the Project	5
Summary of Literature Search.....	6
Cracking Due to Shrinkage and Freeze-Thaw	6
Structural Cracking	6
Corrosion of Slab Reinforcement	6
RESEARCH APPROACH	7
Crack Surveys of Bridges.....	7
Effects of Chloride Penetration into Concrete.....	7
Shrinkage and Freeze-Thaw Tests with the Addition of Fiber.....	9
Structural Tests for Determining the Effectiveness of Fiber and Reinforcement Alternatives.....	10
Pilot Project and Performance Monitoring.....	12
Summary.....	14
RESEARCH FINDINGS AND CONCLUSIONS	15
Research Findings.....	15
Conclusions.....	16
RECOMMENDATIONS FOR IMPLEMENTATION OF RESEARCH FINDINGS.....	17
Recommendation for Implementation.....	17
Steps Needed for Implementation	17
Expected Benefits from Implementation	17
Potential Risks and Obstacles to Implementation.....	17

Strategies to Overcome Potential Risks and Obstacles.....	17
Potential Users and Other Organizations that may be Affected.....	17
Suggested Time Frame for Implementation	17
Estimated Cost of Implementation	18
Recommendations on How to Evaluate the Ongoing Performance of the Implemented Result.....	18
BIBLIOGRAPHY	19
List of Citations.....	19
Appendix.....	20

LIST OF FIGURES

Fig. 1	Comparison of Typical Crack Widths	4
Fig. 2	Typical Structural Cracks over Pier Caps.....	4
Fig. 3	Nearly Full-Depth Flexural Cracks	4
Fig. 4	Typical Permanent Crack Under Dead Load.....	4
Fig. 5	ODOT District Map Showing Location of Inspected Bridges	7
Fig. 6	Severely Cracked Bridge Deck.....	8
Fig. 7	Typical Setup for Corrosion Tests.....	8
Fig. 8	Test Setup for Long Prisms.....	10
Fig. 9	Typical Cracks on Prism Specimens with Fibers.....	10
Fig. 10	Details of Flexural Test Slabs.....	11
Fig. 11	Test Setup for Slab Tests.....	11
Fig. 12	Typical Stress versus Crack Width of 14" x 8" Slabs with and without Fiber.....	12
Fig. 13	Increase in Crack Widths with Load Cycles.....	12
Fig. 14	Increase in Deflection with Load Cycles.....	12
Fig. 15	Test Slab Placement at Osborne Test Site.....	13
Fig. 16	General View of the Placement of Concrete.....	14
Fig. 17	Finishing of Concrete.....	14

LIST OF TABLES

Table 1	Allowable Crack Widths from ACI 224R-01.....	3
Table 2	Summary of the Effects of Various Factors on Crack Widths	16

EXECUTIVE SUMMARY

Problem Statement

The Ohio Department of Transportation (ODOT) routinely designs, builds, and maintains a large number of continuous span structural (CSS) slab bridges. In a recent ODOT project (Patnaik and Baah, 2015), it was documented that despite being designed to strictly satisfy all the relevant AASHTO requirements, many such bridge decks constructed in the last several years show transverse cracks with widths greater than those predicted using AASHTO 2012 and ACI 318-14 guidelines. Several permanent transverse structural cracks as wide as 0.1 to 0.125 inch developed on such slab bridges parallel to the intermediate pier supports. Crack measurements were made when the bridges were not occupied by traffic (i.e., under dead load alone). The measured crack widths were over 10 times the ACI 224R-01 limit of 0.007" for slabs exposed to deicing salts. The extent of cracking and crack widths were found to increase with time based on multiple surveys of the same bridges over a 2- to 4-year period.

The flexural crack control requirements of ACI 318-14 and AASHTO Eq. 5.7.3.4-1 (2012) were developed primarily for uncoated black bars, and not for members reinforced with epoxy-coated bars (ECB). However, due to the lack of any other better method, these equations continue to be used for members with ECB. The specified spacing limits for flexural reinforcement to control crack widths were found to be inadequate, and suitable modifications to this practice may be needed. Prior to the issuing of ODOT standard drawing CS-01-08, ODOT standard drawings that incorporated AASHTO standard specifications were CS-1-03 and CS-1-93. The bridges inspected in our previous projects were designed to comply with the details given in these earlier versions of ODOT standard drawings. Additional evaluation of the cracking behavior of bridge decks designed to comply with CS-01-08 is therefore warranted.

In laboratory tests reported previously by Patnaik and Baah (2015), it was found that slabs reinforced with ECB exhibited about twice the crack widths compared to those in identical slabs reinforced with black bars. From a limited test program in that project, it was found that the addition of polypropylene fiber to concrete has the potential to provide significant reduction in crack widths and the extent of cracking in slabs, even for those reinforced with ECB. It was recommended in that project to further explore this potential solution.

It is fully recognized that ODOT stopped using black steel in 1980s in bridge decks and replaced it with ECB due to the anticipated corrosion protection. However, some DOTs (e.g., VDOT) recently found that the use of ECB did not provide the expected corrosion protection, and moreover, increased the maintenance costs due to frequent crack sealing and, therefore, the life cycle costs of bridge decks (Sharp and Moruza, 2009).

Fatigue loading is expected to increase the width of any cracks that develop on a bridge deck. Wider cracks can result in accumulation of dirt and moisture in the crack crevices and prevent cracks from closing after the passing of wheel loads. Freeze-thaw conditions and fatigue are expected to compound these problems and cause progressive increases in crack widths over time.

There is a need to study the effects of the factors affecting the cracking behavior of bridge decks. A verification of the potential of fiber addition to reduce cracking is needed. Based on the above background, this project was developed primarily to study the role of the addition of fiber to control bridge deck cracking.

Goals and Objectives of the Study

The overall goal of this project was to reduce the extent and severity of cracking in continuous span structural slab bridge decks by using polypropylene fiber. This project was also designed to provide insight into the potential use of different corrosion-resistant bars as an alternative to epoxy-coated reinforcing bars. The specific objectives were to:

- (i) Quantify the beneficial use and study the potential implementation of the addition of polypropylene fiber to concrete in order to reduce cracking in bridge decks.
- (ii) Study the suitability of other alternatives to ECB for bridge deck applications, particularly in terms of cracking behavior of continuous span structural slab bridge decks.
- (iii) Study the suitability of AASHTO specifications on maximum spacing limits for reinforcing bars and the ACI 224R-01 suggested limit for maximum crack width under deicing chemical exposure condition when epoxy-coated bars are used in bridge decks.

Research Findings

Transverse cracking was observed and documented for CSS slab bridges in various ODOT districts. The selected bridges were designed to comply with the CS-01-08 standard. Average crack widths in most cases ranged from 0.03 to 0.05", but cracks with 0.1" widths were found on some of the bridges. The revised details provided in CS-01-08 in comparison to CS-1-93 and CS-1-03 may have reduced the problem, but they did not reduce it sufficiently to meet ACI 224R-01 limit of 0.007" for bridge decks exposed to deicing salts. Meeting this maximum crack width limit for bridge decks reinforced with ECB is unrealistic and unachievable with current ODOT practices, and the rationale to meet the 0.007" limit may need to be reconsidered.

Structural slab tests with different bar types without and with fiber revealed that slabs with ECB have larger crack widths than those with all other bar types. Of all the alternatives studied in this project, continuous zinc galvanized bars (CGR) and corrosion-resistant alloy steel bars (MMFX) performed the best in terms of cracking behavior and corrosion resistance, particularly when fiber is used. Fiber reduced the crack widths in test specimens under static loading by 35% to 48% compared to crack widths of identical specimens with no fiber. Fatigue tests on slabs with ECB but without fiber revealed that crack widths and deflections increased by about 23% due to 2×10^6 load cycles at a maximum steel stress of 50% of its yield (30 ksi). Under identical fatigue loads, the crack widths of slabs reinforced with ECB and containing 10 lb/yd³ of fiber also increased, but such an increase in crack widths was 13% instead of 23% for slabs without fiber, proving that the increase in crack widths under fatigue loading is reduced when fiber is used in slabs reinforced with ECB.

Freeze-thaw tests under identical thermal cycles and sustained loading comparable to the self-weight of bridge deck slabs alone (i.e., resulting in a steel stress of about 18 ksi or 30% of its yield) showed that the crack widths increase with freeze-thaw cycles for slabs with ECB as well as for slabs with black bars. After 60 cycles, the increase for slabs with black bars was 75% of the initial crack width, while the increase was 150% for slabs with ECB, meaning that slabs with ECB will exhibit cracks with 2.5 times the initial crack widths after 60 freeze-thaw cycles and sustained loading. For slabs without fiber, the increase for slabs with ECB (0.015") is greater than for slabs with black bars (0.007") by a factor of 2. However, it is possible to reduce this increase in crack width by a factor of about 2.0 (i.e., reduced from 0.015" to 0.008") by adding 10 lb/yd³ of fiber for slabs reinforced with ECB subjected to freeze-thaw cycles while sustained loading is maintained.

Slabs with ECB having induced defects adequate to develop accelerated corrosion that is comparable to the corrosion and peeling of epoxy coating found in a recently demolished bridge showed a capacity loss of 32% compared to slabs with other bar types under the same amount of accelerated corrosion. Fiber addition to concrete for slabs with ECB reduced this capacity loss of slabs from 32% to 25% for the same amount of corrosion corresponding to the test duration in this study. Longer duration tests will show increased benefits.

An implementation project completed on a bridge in Medina County (Ohio) with a polypropylene fiber dosage of 10 lb/yd³ demonstrated that placement, consolidation and finishing of the proposed fiber-reinforced concrete were very similar to that of normal concrete. No visible cracks were found to have developed on the deck surface or over the piers for more than 5 months following construction.

Summary

The addition of fiber to bridge deck concrete without any changes to the reinforcement details of continuous span structural slab bridges was determined to reduce the extent and the severity of cracking by a cumulative factor of about 3 to 4. The beneficial effects of fiber primarily stem from the improved performance of the concrete containing fiber in terms of enhanced concrete response to static and fatigue loading and under freeze-thaw and sustained loading conditions. Constructability of bridge decks with a polypropylene fiber dosage of 10 lb/yd³ was verified to be feasible. The ease of placement, effective consolidation and acceptable finish is compatible or superior to that of decks constructed using ODOT standard mixes. Satisfactory constructability achieved in the pilot bridge makes this solution implementable by ODOT without any deviation from the current practices other than the addition of fiber to the deck concrete.

Recommendation

It is recommended from the findings of this project that the addition of polypropylene fiber to deck concrete at a dosage of 10 lb/yd³ be implemented in ODOT's continuous span structural slab bridge decks to reduce the extent and severity of cracking.

PROJECT BACKGROUND

Introduction

ODOT routinely designs, builds, and maintains a large number of continuous span structural slab bridges. This type of bridge is also a popular choice of other transportation agencies in the US for short and medium span bridges. Despite being designed to strictly satisfy all relevant AASHTO requirements, many such bridge decks constructed in the last several years show transverse cracks with widths greater than those obtained from theoretical predictions. Permanent transverse structural cracks develop on such slab bridges parallel to the intermediate pier supports.

In a recently completed ODOT research project (Patnaik et al. 2012), continuous span structural slab bridges were found to have a higher tendency to develop wider cracks than stringer supported bridges. Several large structural cracks that were parallel to the intermediate supports were as wide as 0.1 to 0.125 inch and remained permanently open, even when there was no traffic loading. Such crack widths are over 10 times the limit recommended in ACI 224R-01 (Table 1) for bridge decks exposed to deicing salts (Figs. 1 to 4). The extent of cracking increased with time. Nearly full depth permanent cracks were also observed near the intermediate piers of bridges (Fig. 3). These cracks were much wider than what would be predicted by commonly used crack width equations. The use of current ACI 318-14 or AASHTO (2012) Eq. 5.7.3.4-1 to limit the spacing of flexural reinforcement in order to control crack widths was found to be inadequate, and suitable modifications to this practice may be needed. These bridges were designed to comply with details given in versions of ODOT standard drawings prior to the release of CS-01-08, and a need to capture the cracking behavior of bridge decks designed to comply with CS-01-08 was identified.

Table 1 Allowable Crack Widths from ACI 224R-01

Exposure Condition	Maximum Allowable Crack Width, inch
Dry Air	0.016
Humidity, Moist Air, Soil	0.012
Deicing Chemicals	0.007
Sea Water	0.006
Water Retaining Structures	0.004

In a more recent project on bridge deck cracking (Patnaik and Baah, 2015), ECBs were found to be contributing to the problem of wider cracks but it was still inconclusive to as why wide cracks occurred even though the theoretical equations would predict much smaller crack widths. Laboratory load testing proved that the crack widths of slabs with ECB were about twice the width of cracks in slabs reinforced with black bars. ECB-reinforced test slabs also failed at smaller loads and had larger deflections under service loads. Due to the inferior bond strength of ECB with concrete, fatigue loading is expected to increase the crack widths. Wider cracks can also result in accumulation of dirt and moisture in the crack crevices. Freeze-thaw conditions and fatigue loading can compound these problems and cause progressive increases in crack widths over time.

The addition of polypropylene fiber to concrete was proved to provide significant improvement to the cracking behavior of slab elements in a laboratory environment. Fibers in hardened concrete help reduce macro cracks and allow micro cracks to develop. Not only are the crack widths in concrete decreased by the addition of fiber, but also the ultimate cracking strain is increased. The ability of fiber to modify the cracking mode results in quantifiable benefits, which include reduced permeability; increased surface abrasion resistance; and increased impact, corrosion and fatigue resistance. The addition of fiber increases the pull-out (bond) strength and reduces crack widths significantly, as demonstrated in the research project by Patnaik and Baah (2015).

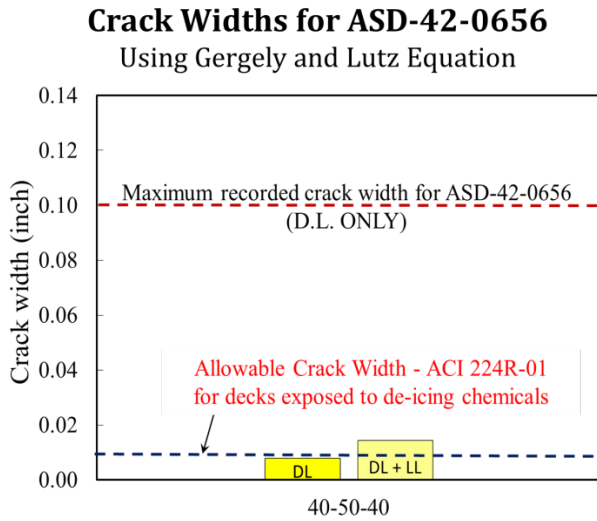


Fig. 1 Comparison of Typical Crack Widths

Fig. 2 Typical Structural Cracks over Pier Caps

The accuracy of crack width equations and the crack control specifications of limiting the maximum spacing of flexural reinforcement as given in ACI 318-14 and AASHTO (2012) was found to be questionable. AASHTO (2012) Eq. 5.7.3.4-1 is generally more conservative than the ACI 318-14 requirements and results in impractical spacing values (very small or even negative) depending on the exposure factor for a large concrete cover. Therefore, an investigation into the accuracy of AASHTO Eq. 5.7.3.4-1 for bar spacing, the relevant crack width equations for bridge deck applications, and the rationale for applying a crack width limit of 0.007 inch to bridge decks reinforced with ECB under an exposure condition relevant to deicing chemicals is needed.



Fig. 3 Nearly Full-Depth Flexural Cracks

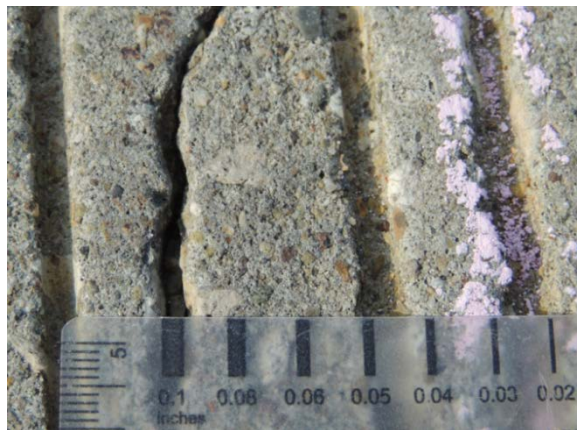


Fig. 4 Typical Permanent Crack Under Dead Load

Need for the Research

The use of ECB in bridge decks has many deficiencies that contribute to the worsening of the problem of severe cracking that was documented in previous research projects. Remedial measures are needed to overcome the identified deficiencies. One plausible remedial measure to counter the severe cracking problem related to ECB is the use of polypropylene fiber in concrete at a high dosage. The demonstrated success at a laboratory scale of fiber addition as a solution to the problem is expected to significantly reduce the problem of deck cracking in continuous span structural slab bridges. This project directly provides a verification of this premise through systematic and coordinated bridge inspections, theoretical studies, laboratory tests, and a field demonstration.

RESEARCH CONTEXT

Goals and Objectives of the Study

The overall goal of this project is to reduce the extent and severity of cracking in continuous span structural slab bridge decks. The technology readiness level and the potential advantages of fiber addition for reducing the extent of cracking and improving the overall performance have been demonstrated in the project. The potential benefits are being validated on a recently constructed bridge deck. Another goal for this project is to develop required insight into the possible use of different corrosion-resistant bars as an alternative to epoxy-coated reinforcing bars. The specific objectives were to:

- (i) Quantify the beneficial use and implement the addition of polypropylene fiber to concrete in order to reduce cracking in actual bridge decks.
- (ii) Study the suitability of other alternatives to ECB for bridge deck applications, particularly in terms of cracking behavior of continuous span structural slab bridge decks.
- (iii) Study the suitability of AASHTO specifications on maximum spacing limits for reinforcing bars and the ACI 224R-01 limit for maximum crack width under deicing chemical exposure condition when epoxy-coated bars are used in bridge decks.

The central theme of the project is to minimize the cracking of structural slab bridges in the negative moment regions over the pier caps. Therefore, fiber-reinforced concrete material was developed and validated to minimize the cracking in continuous span structural slab bridge decks. Other alternatives to the currently used epoxy-coated bars were also evaluated.

Specific Tasks Accomplished in the Project

The proposed project was structured into three parts. In Part I of the project, the focus was on facilitating the implementation of the use of fiber along with shrinkage reducing admixtures (SRA) and crack-reducing admixture (CRA) in concrete mixes that are typically used for constructing bridge decks in Ohio. The fatigue performance and freeze-thaw performance of slabs with fiber were studied. In Part II, studies focused on the theoretical aspects of the adequacy of the crack control requirements given in AASHTO equation 5.7.3.4-1. The rationale for the maximum crack width limit of 0.007 inch as given in ACI 224R-01 was also investigated, and possible relaxation of this requirement was considered. In Part III of the project, different types of alternative reinforcing bars were evaluated to determine if there are suitable alternatives to the ECB that is currently used in bridge decks. The three parts of the project were organized into the following tasks:

- Task 1: Literature Review
- Task 2: State-of-Practice and Past Trials on the Use of Potential Alternatives
- Task 3: Inventory of Structural Slab Bridges and Selection of Bridges for Inspection
- Task 4: Evaluation of AASHTO and ACI-318 Requirements for Flexural Crack Control and the Maximum Limit for Flexural Cracks Given in ACI 224R-01
- Task 5: Study the Effects of Chloride Penetration on Epoxy-Coated Bars
- Task 6: Shrinkage Panel Tests with the Addition of Fiber and SRA/CRA
- Task 7: Structural Tests for Reinforcement Alternatives
- Task 8: Analysis of Test Results and Development of Implementation Plan for a Pilot Project
- Task 9: Pilot Project and Performance Monitoring
- Task 10: Reports

Summary of Literature Search

The complete details of the literature review are provided in Appendix A.

Cracking Due to Shrinkage and Freeze-Thaw

Shrinkage is the most common cause of early age cracking in bridge decks. The two main types of shrinkage are plastic (before hardening) and drying shrinkage (after hardening). The rate and severity of shrinkage are affected by several factors, which can be attributed to material properties, construction practices and design factors. When the tensile stresses exceed the concrete's modulus of rupture, cracking will occur.

Shrinkage reducing admixtures (SRA) reduce shrinkage by lowering the surface tension of pore water in both plastic and hardened concrete. There are two methods of application of SRA to concrete: one is impregnation or topical application of SRA and the other is the integration of the SRA into the mix. SRA and crack reducing admixtures (CRA) greatly reduce shrinkage with some side effects. Fiber is also commonly used to mitigate shrinkage cracking in concrete. The addition of fiber significantly reduces the number and width of cracks while improving freeze-thaw resistance and fatigue performance. The effect of fiber when used in combination with SRA or CRA is even more advantageous in reducing concrete cracking.

Structural Cracking

Many researchers and state transportation agencies have suggested the use of different concrete mixes, construction practices, placement procedures, and curing methods to reduce cracking in bridge decks. Despite these efforts, the issue of cracking still remains widespread.

The crack width limit equations initially recommended in ACI 224R-92, as well as current design specifications for flexural crack control in AASHTO (2012) and ACI 318-14 were established with the maximum bar spacing specified to limit crack widths without regard to the reinforcement type. Merely applying these equations to slabs reinforced with ECB is inadequate for limiting crack widths to the corresponding recommended values. ECBs can cause wider cracks in bridge decks as compared to conventional black bars. Some agencies in states like Virginia (e.g., VDOT) found that the use of ECB did not provide the expected corrosion protection, and moreover, increased the maintenance costs due to crack sealing and, therefore, life cycle costs of bridge decks (Sharp and Moruza, 2009). Repeated traffic loading causes these cracks to grow with time at a faster rate due to insufficient bond between the embedded bars and the surrounding concrete. Under sustained loading, cracks were observed to double in width over time, while the crack spacing remained relatively unchanged (Nilson, 2010). Cyclic loading due to traffic volume causes the bars to slip from the surrounding concrete at the location of the cracks, leading to expansion of the cracks (Soltani, 2010). Use of fiber-reinforced concrete reduces crack widths significantly under static flexural loading (Patnaik and Baah, 2015).

Corrosion of Slab Reinforcement

Defects introduced to the epoxy coating of ECB during handling of bars at the job site cause serious corrosion and peeling of the epoxy coating from the base steel. Damage to epoxy coating also occurs during concrete placement (Sharp and Moruza, 2009). Corrosion of reinforcing bars affects the pull-out strength of the bars and will reduce the moment strength of reinforced concrete slabs. Addition of fiber to the concrete counteracts this deleterious effect and reduces the corrosion damage under sustained loading while providing significant resistance to crack formation and growth.

RESEARCH APPROACH

In this section, the tasks completed in the project are briefly described. The complete details of the activities conducted in each task are included in the relevant appendices.

Crack Surveys of Bridges

The bridges inspected in two earlier projects by the PI were designed based on ODOT standard drawings prior to the introduction of CS-01-08 (ODOT, 2008). A list of three-span CSS bridges that were designed based on ODOT standard drawing CS-01-08 (ODOT, 2008) was compiled from the state bridge inventory. A total of 63 three-span CSS bridges located in various districts were suggested by ODOT SMEs to be suitable for crack surveys in this project. The spans of these bridges range from 16'-20'-16' to 46'-57.5'-46' with deck thicknesses ranging from 12 inches to 27 inches, respectively. These bridges were constructed or rebuilt between 2008 and 2016. From the list of 63 proposed bridges, 30 bridges in various districts (see Fig. 5) were selected by the research team based on the span lengths and the physical location of the bridge. The selected bridges were inspected in order to record the crack patterns, measure the crack widths and lengths, and record crack locations relative to the centerline of the pier caps (Fig. 6). The details for each bridge are documented in Appendix B. Average crack widths on most bridges ranged from 0.03 to 0.05 inch, but crack widths of 0.1 inch were also recorded on some of the bridges. Therefore, it is reasonable to conclude that the details provided in CS-01-08 may have reduced the problem, but they did not sufficiently reduce it to the extent of meeting the ACI 224R-01 recommended limit of 0.007".

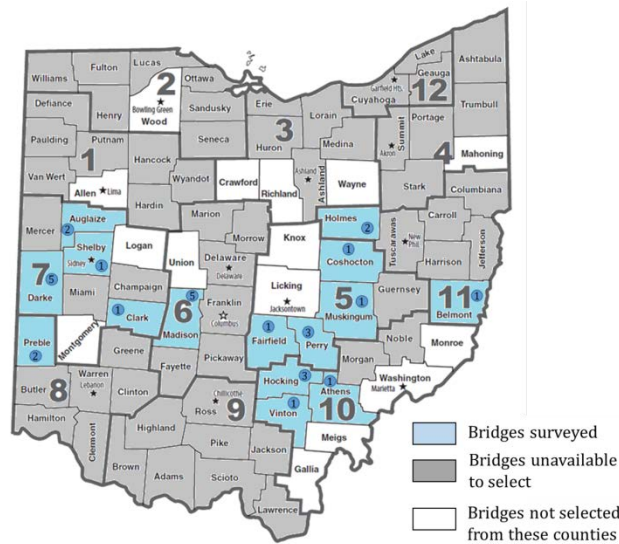


Fig. 5 ODOT District Map Showing Location of Inspected Bridges
Note: Number of bridges inspected is shown in circles

Effects of Chloride Penetration into Concrete

Continuous span structural slab bridges are constantly subjected to the dead loads of the bridge that keep cracks open in the tension region near the pier supports. These crack openings provide a pathway for chlorides to reach the embedded reinforcement. Service live loads on the bridges allow these cracks to open further, leading to an increase in the amount of chlorides passing through the deck to the reinforcement. To replicate this condition in laboratory tests, the corrosion process on the bridge decks was simulated by using an accelerated corrosion process while the test specimens are subjected to sustained loading to simulate the permanently acting dead loads as seen in Fig. 7.



Fig. 6 Severely Cracked Bridge Deck

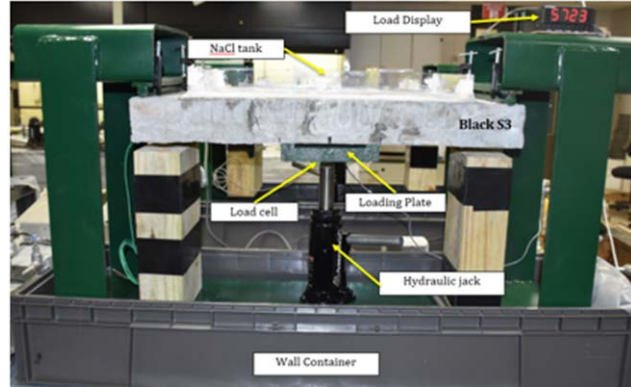


Fig. 7 Typical Setup for Corrosion Tests

A total of 80 slab specimens were cast with conventional black steel as well as with several types of corrosion-resistant reinforcing bars (epoxy-coated bars, hot-dipped galvanized bars, stainless steel bars, and MMFX). All these bar types are known to be resistant to corrosion. MMFX bars are ChromX 9100 bars conforming to ASTM A1035-CS Grade 100 with a tested yield strength of 131 ksi and tensile strength of 164 ksi. These bars have 9.42% chromium and 0.58% magnesium, resulting in good corrosion resistance. The slab specimens were cast using typical job mix formulas (JMFs) from ODOT projects for slabs with and without 10 lb/yd³ of polypropylene fiber. The test setup for the corrosion testing was designed to replicate the actual conditions on the bridge decks. Each slab was supported in a specially fabricated test frame, and a constant sustained load was applied to the slab using a mechanical jack. A salt solution tank, which was assembled and glued to the tension face of the slab, contained a salt solution (5% NaCl as recommended in ASTM B895) to act as an electrolyte and simulate a deicing salt on a bridge deck. A stainless steel plate was placed in the salt solution tank to act as a cathode, and a wire from the stainless steel plate was connected to the negative terminal of a direct current (DC) power supply to complete the corrosion cell in order to accelerate the corrosion process. Fig. 7 shows the test setup for the accelerated corrosion of a typical test slab.

On visual comparison of slabs made with and without fibers, the surface condition of the slabs made with fibers showed less deterioration than that of the slabs made without fibers for all bar types. Both transverse and longitudinal crack widths were reduced drastically due to the addition of fibers, without much damage to the bars embedded within the concrete for all bar types. It was evident that the addition of fibers substantially improved the performance of slabs under a highly accelerated corrosion process.

Slabs with epoxy-coated bars with 5% damage induced on the coating showed the greatest extent of corrosion compared to the other bar types, in terms of maximum flexural capacity loss due to corrosion. A condition of 5% damage was used to achieve the desired level of deterioration under accelerated corrosion tests in a reasonable amount of time (about 3 weeks) while simulating the peeling of epoxy coating due to corrosion similar to the samples obtained from a recently demolished bridge in ODOT District 3. MMFX bars showed the best corrosion resistance and the lowest bond loss. In hot-dip galvanized bars, the zinc coating protected the bar from corrosion for a few days. However, once the sacrificial layer was compromised, the base metal showed a similar effect as the black bars. The capacity loss for the slab with hot-dip galvanized bars is much closer to that of slabs with black bars. Slabs with stainless steel bars also showed better performance after corrosion with a smaller loss of flexural capacity due to corrosion compared to epoxy-coated bars. Similar results and trends were obtained from pull-out tests. These tests demonstrated an increase in resistance to corrosion from the addition of 10 lb/yd³ of polypropylene fiber to concrete.

Shrinkage and Freeze-Thaw Tests with the Addition of Fiber

Shrinkage cracking on bridge decks starts shortly after concrete placement and continues for years. The problem is exacerbated due to crack expansion from freeze-thaw and fatigue load cycles. Restrained concrete ring tests, free shrinkage prism tests, plastic shrinkage panel tests and freeze-thaw including those with sustained loading were conducted in this project. Six mixes were used in the testing program: a control mix, two mixes that were similar to the control mix but contained admixtures — either MasterLife SRA or Masterlife CRA — and three additional mixes that were similar to these control, SRA, and CRA mixtures, but with the addition of fibers. These mixes were based on typical ODOT mixes for bridge decks with minor modifications to suit the laboratory testing conditions. The test specimens used concrete cast with Type I Portland cement, slag, and limestone coarse aggregate and cured for 24 hours prior to the initiation of drying. Freeze-thaw specimens were placed in a curing tank filled with lime water (diluted calcium hydroxide solution) for a period of 10 days. The complete details of the test procedures and results are presented in Appendix E.

From shrinkage panel tests, the addition of fiber to concrete was found to reduce plastic shrinkage cracking by a factor of 8.5. The use of SRA and CRA reduces the amount of free shrinkage (based on AASHTO T160 test or ASTM C 157 test) at 28 days by 38% and 52%, respectively; the use of CRA seems to greatly reduce the amount of shrinkage during the first two to three days, with minimal or no shrinkage occurring during this period. The use of fibers, while effective in reducing the amount of shrinkage in the first seven to ten days, was found to cause an increase in free shrinkage at later ages. The use of polypropylene fibers in concrete mixtures containing slag can cause this type of increased shrinkage compared to non-fiber mixtures. Therefore, it is useful to minimize the amount of slag to offset this effect in mixes that also include polypropylene fiber.

Restrained shrinkage tests performed using AASHTO PP34-99 or ASTM C1581 ring tests showed that the concrete mixture with SRA developed a smaller crack width in 28 days than that of the control mix. The mixes with CRA did not develop any cracks even after 28 days in the environmental chamber. In the fiber-reinforced concrete mixtures, none of the rings showed cracking by the end of the testing period of 28 days. The use of SRA and CRA was found to reduce the strains due to shrinkage by 40–50% and 60–70%, respectively. The use of CRA seems to greatly reduce the strains due to shrinkage during the first two to three days, with minimal or no shrinkage occurring during this period. The use of fibers was found to cause marginal increase in strains due to shrinkage, which was similar to the observation from the free shrinkage tests.

Results from the freeze-thaw tests conducted similar to the procedure given in AASHTO T161 and ASTM C666 (modified to suit the available freeze-thaw chamber) show that the use of SRA and CRA had no significant impact on the damage due to freezing or thawing. The addition of CRA seems to increase the scaling in both fiber and non-fiber mixtures compared to the addition of SRA, with less of an effect for the fiber-reinforced mixtures. The addition of polypropylene fibers was found to reduce the weight loss for all mixes, implying improved resistance to scaling due to freezing and thawing in the fiber-reinforced concrete mixtures compared to those mixes without fibers.

From the freeze-thaw tests performed while maintaining a sustained load that is comparable to the service loads on typical bridge decks, the initial crack widths as well as the rate of crack widening in slabs with ECB and no fiber were higher by a factor of 2.5 compared to those for slabs with black bars under identical test conditions. Addition of 10 lb/yd³ of fiber reduced the crack widths by a factor of 2 for slabs with ECB in such freeze-thaw tests with sustained loading.

Structural Tests for Determining the Effectiveness of Fiber and Reinforcement Alternatives

An extensive and elaborate experimental program was designed to develop insight into the factors that cause structural cracking in bridge decks and to reduce cracking by using alternative materials such as various corrosion-resistant bars as well as by incorporating polypropylene fibers in the concrete. The tests included direct tension tests on prism specimens (Figs. 8 and 9), flexural testing of full-scale and reduced-scale slab specimens, fatigue tests on slabs to study crack widening, pull-out tests to understand the bond behavior between the reinforcing bar and surrounding concrete, and tests on the connection between a typical slab and pier caps. The reinforcing bars evaluated in the experimental program were black steel bars (control), epoxy-coated bars (ECB), Grade 2304 stainless steel bars, MMFX corrosion-resistant alloy steel bars, hot-dipped galvanized bars, and zinc galvanized bars (CGR). As very little research has been performed on the use of corrosion-resistant bars as a means for reducing cracks on bridge decks, various experiments were designed to gain insight specifically into the effects of each reinforcement type on bridge deck cracking.

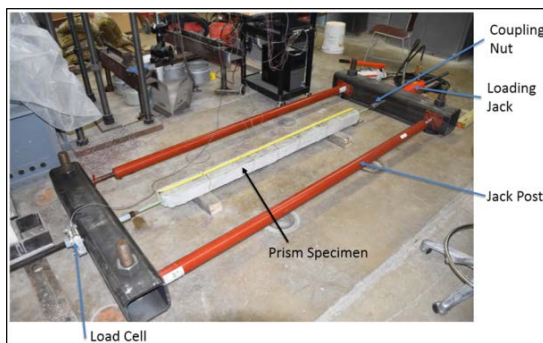


Fig. 8 Test Setup for Long Prisms

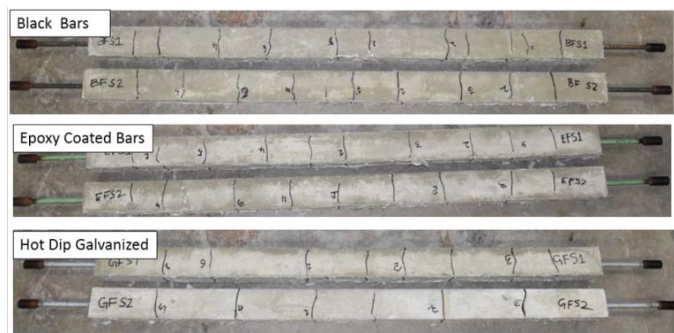


Fig. 9 Typical Cracks on Prism Specimens with Fibers

The prism specimens showed that the crack widths on specimens with epoxy-coated bars were wider but fewer in number compared to the specimens with other types of bars, whereas specimens with MMFX and CGR bars showed smaller crack widths and more closely spaced cracks. A similar trend was observed in specimens with fibers; crack widths were reduced by about 25% for specimens with fibers as compared to the corresponding specimens without fibers.

Two slabs that were 16 ft. in length, 13 inches wide (to accommodate two #9 bars at a spacing of 6.5”), and 19 inches deep were cast as full-scale specimens to replicate the negative moment region of a typical bridge deck between the inflection points. These specimens were detailed to have the same reinforcement as needed for a typical three-span bridge with spans of 30 ft. – 37.5 ft. – 30 ft. One specimen was cast with uncoated black bars and the other was cast with epoxy-coated bars. Four additional specimens (two with uncoated reinforcement and two with epoxy-coated reinforcement) were also cast with the same reinforcement and section details but using only half the span length (i.e., 8 ft. as seen in Fig. 10). All specimens were cast using the same mix design (Class QC2 concrete mix) to understand the cracking behavior for the full-span and half-span slab specimens and the scaling effects. Load was applied using a manually operated hydraulic jack, and the strains and applied loads were recorded continuously. The deflections at the mid-span and the quarter-span were recorded. Crack data such as crack widths, crack patterns, and crack spacing were also collected during the testing.

The crack widths measured on both types of slabs with a 15 ft.-span and a 7.5-ft. span were mostly similar at the same steel stress level for the same bar type as long as the steel reinforcement ratio and the effective concrete cover were the same.

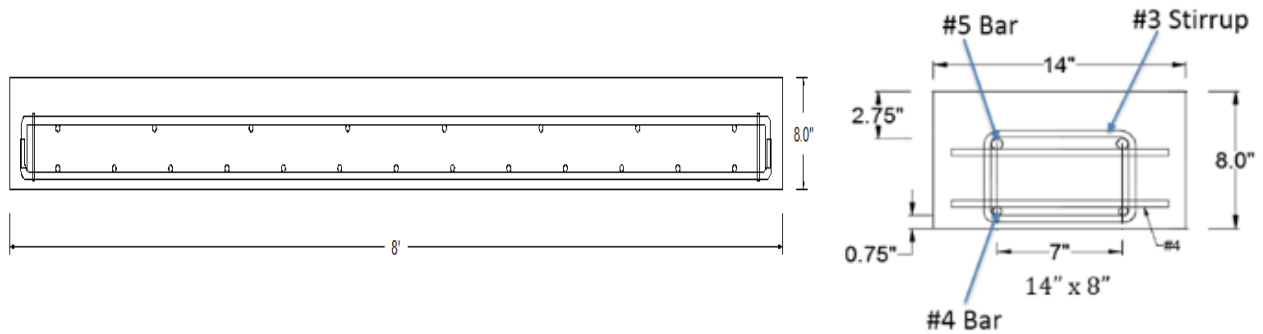


Fig. 10 Details of Flexural Test Slabs (Not to Scale)

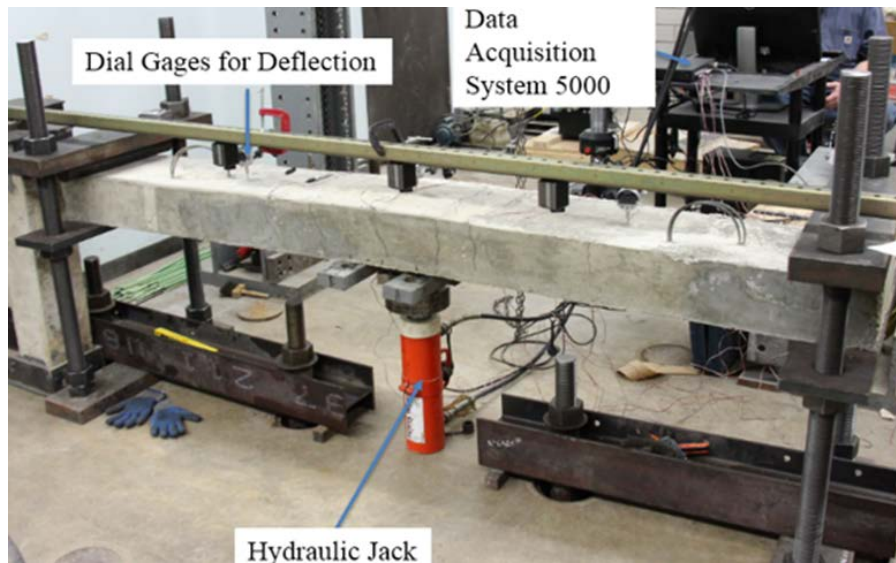


Fig. 11 Test Setup for Slab Tests

After establishing the lack of scaling effect on smaller slabs (8' long \times 14" wide \times 8" high), a total of 24 slabs with six reinforcement types, both with and without fibers, were tested. Two specimens of each bar type were tested to obtain average values. Deflections, crack spacing, crack widths, and stresses in the bars for different levels of applied load were the parameters considered in the tests. A test setup as shown in Fig. 11 was adopted for the testing of these slabs. Data acquisition was used to capture the strains and applied load during the test, whereas deflections, crack spacing and crack widths were measured manually. The crack widths were averaged from the results of two specimens of each bar type. Fig. 12 shows the stress versus crack widths of slab specimens with and without fibers. In the case of slabs without fibers, the slabs with epoxy-coated bars showed wider cracks compared to those with other bar types, whereas slabs with MMFX and CGR showed smaller crack widths. In cases of slabs with fibers, a similar trend was observed, with much smaller crack widths (about 35% to 48% reduction) for most bar types due to the use of polypropylene fibers.

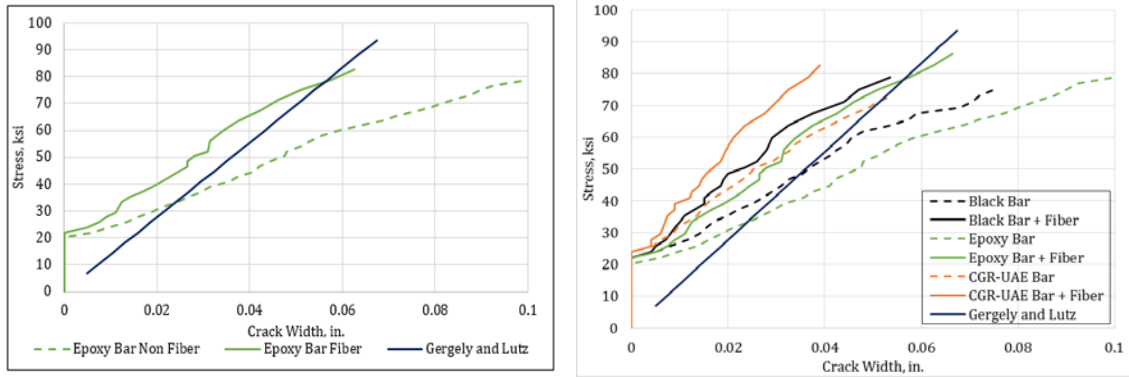


Fig. 12 Typical Stress versus Crack Width of 14"×8" Slabs with and without Fiber

Four slabs with epoxy-coated bars with and without fibers were also tested under fatigue loading at a frequency of 2 Hz (cycles per second) for two million cycles. The load was cycled through a minimum that corresponds to the permanent dead load on a typical bridge and a maximum that corresponds to the bridge service loads. Plots showing an average increase in crack widths and also an average increase in deflections with time are presented in Figs. 13 and 14 for two specimens of each bar type and slabs with and without fibers, respectively. In the case of slabs without fibers, the cracks grew at an increasing rate, whereas in the case of slabs with fibers, the cracks grew at a slower rate. A similar trend was observed in the case of deflections at the mid-span. These figures demonstrate that the crack widths and deflections increase with fatigue loading over time, and also that the rate of such increase of crack widths can be reduced by a factor of about 1.5 with the addition of fiber.

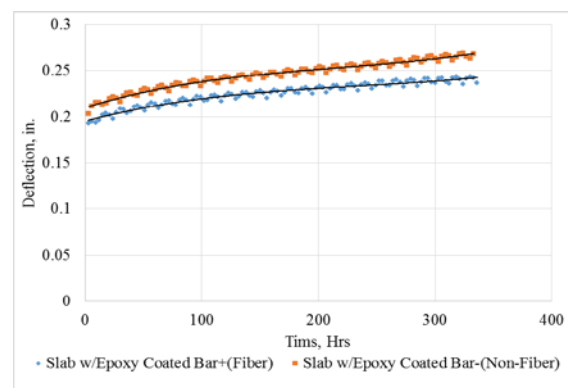
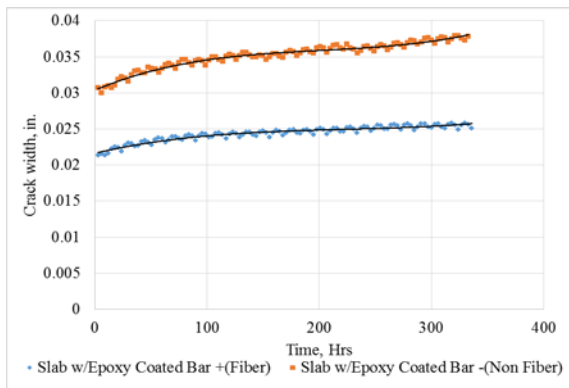


Fig. 13 Increase in Crack Widths with Load Cycles **Fig. 14** Increase in Deflection with Load Cycles

The effects of a change in the slab and pier-cap connection from a rigid connection to a pinned connection were studied to investigate the difference in the negative moment values over the pier region. In addition, scaled-down tests were performed to determine the differences in crack patterns and crack widths on the tension side of the slab when using these two types of connections. The structural tests did not show much difference in the crack widths of the two types of connections, perhaps because the symmetric loading applied in the tests is more similar to a dead load condition.

Pilot Project and Performance Monitoring

Based on the findings from this project, it was recommended to use polypropylene fibers in the concrete mix for bridge decks with a high dosage of 10 lb/yd³ to arrest cracks and consequently

increase the service life of bridge decks in Ohio. This dosage was selected in the laboratory tests and for the implementation project to study the feasibility of such dosage and at the same time maximize the benefit from the addition of fiber in terms of crack control.

A bridge located in Hinckley (Medina County, Ohio), was selected as the site for a demonstration project. The selected bridge was a three-span continuous slab bridge with spans of 24 ft.–30 ft.–24 ft. and a slab thickness of 16 inches. Since this demonstration project was the first of its kind to use a high dosage of fibers, a trial concrete placement as seen in Fig. 15 was done to develop a mix design that is easily workable to meet the requirements for slump and air content including an acceptable surface finish.



Fig. 15 Test Slab Placement at Osborne Test Site

The implementation project completed in Hinckley that used a polypropylene fiber dosage of 10 lb/yd³ demonstrated that placement, consolidation and finishing of the proposed fiber-reinforced concrete were very similar to that of normal concrete (Figs. 16 and 17). The bridge was opened to traffic after a month from the day the deck was cast. The bridge was visually inspected several times after being opened to traffic to determine if any cracks developed over the negative moment region. It was found that no visible cracks had developed on this pilot bridge over a period of more than five months after deck placement. Similar bridges with no fiber incorporated in the deck

concrete would normally have shown distinct and clearly visible wide cracks parallel to the intermediate pier caps within two to three months.



Fig. 16 General View of the Placement of Concrete



Fig. 17 Finishing of Concrete

Summary

As outlined in this section, all research efforts in this project were focused to ensure that the various aspects of the addition of fiber to concrete are studied in sufficient detail to determine the effectiveness of fiber in controlling cracks on continuous span structural slab bridges. From the tests described in this section, it is possible to explain the excessive crack widths measured on ODOT bridges relative to those predicted from ACI 318-14 and AASHTO (2012) equations. Addition of fiber was demonstrated from the laboratory tests to be beneficial in reducing crack widths by a factor of 3 to 4. The pilot project also proved that the potential solution recommended from the findings of this project is readily implementable.

RESEARCH FINDINGS AND CONCLUSIONS

Research Findings

Transverse cracking was observed and documented for CSS slab bridges in various ODOT districts. Such cracks with widths greater than those from theoretical predictions were recorded on 26 out of 30 surveyed slab bridges despite these bridges being designed to strictly satisfy all the relevant AASHTO requirements. Furthermore, the selected bridges were designed to comply with CS-01-08 standard. Average crack widths in most cases ranged from 0.03 to 0.05", but cracks with 0.1" widths were found on some bridges. The revised details provided in ODOT standard drawing CS-01-08 in comparison to CS-1-93 and CS-1-03 may have reduced the problem, but they did not reduce it sufficiently to meet the ACI 224R-01 limit of 0.007" for bridge decks exposed to deicing salts. Meeting this maximum crack width limit for bridge decks reinforced with ECB is unrealistic and unachievable with current ODOT practices, and the 0.007" limit may need to be reconsidered.

Structural slab tests with different bar types without and with fiber revealed that slabs with ECB have larger crack widths than those with all other bar types. Of all the alternatives studied in this project, continuous zinc galvanized bars (CGR) and corrosion-resistant alloy steel bars (MMFX) performed the best in terms of cracking behavior and corrosion resistance, particularly when fiber is used. Fiber reduced the crack widths in test specimens under static loading by 35% to 48% compared to crack widths of identical specimens with no fiber. Fatigue tests on slabs with ECB but without fiber revealed that crack widths and deflections increased by about 23% due to 2×10^6 load cycles at a maximum steel stress of 50% of its yield (30 ksi). Under identical fatigue loads, the crack widths of slabs reinforced with ECB and containing 10 lb/yd³ of fiber increased, but the increase in crack widths and deflections was only about 13%, proving that the increase in crack widths under fatigue loading is reduced when fiber is used in slabs with ECB.

Freeze-thaw tests under identical thermal cycles and sustained loading comparable to the self-weight of bridge deck slabs alone (i.e., resulting in a steel stress of about 18 ksi or 30% of its yield) showed that the crack widths increase with freeze-thaw cycles for slabs with ECB as well as for slabs with black bars. After 60 cycles, such increase for slabs with black bars was 75% of initial crack width while it was 150% for slabs with ECB, meaning that the crack widths of slabs with ECB will develop cracks that are 2.5 times its initial crack widths after 60 freeze-thaw cycles and sustained loading. This increase is higher for slabs with ECB (0.015") than for slabs with black bars (0.007") by a factor of 2 when no fiber is added. However, it is possible to reduce this increase in crack width by a factor of about 2.0 (i.e., reduced from 0.015" to 0.008") by adding 10 lb/yd³ of fiber for slabs with ECB subjected to freeze-thaw cycles while sustained loading is maintained. A similar reduction is possible for slabs reinforced with black bars.

Slabs with ECB having defects adequate to develop accelerated corrosion that is comparable to the corrosion and peeling of epoxy-coating found in a recently demolished bridge showed a capacity loss of 32% compared to slabs with other bar types under the same amount of accelerated corrosion. Fiber addition to concrete for slabs with ECB reduced the capacity loss of slabs from 32% to 25% for slabs with the same amount of corrosion.

The implementation project completed in Medina County (Ohio) with a polypropylene fiber dosage of 10 lb/yd³ demonstrated that placement, consolidation and finishing of the proposed fiber-reinforced concrete were very similar to that of normal concrete. No visible cracks were found to have developed on the deck surface or over the piers for a period of over 5 months following construction.

Conclusions

The addition of fiber to bridge deck concrete without any changes to the reinforcement details of continuous span structural slab bridges was determined to reduce the extent and the severity of cracking by a cumulative factor of about 3 to 4, as shown in Table 2.

Table 2 Summary of the Effects of Various Factors on Crack Widths

Factor	Effect
Use of crack width prediction methods from ACI 318-14 and AASHTO (2012)	These equations are based on crack widths for black bars; use of the same equations for ECB may be inaccurate by a factor of 1.2 to 1.5.
Use of ACI 224R-01 limit of 0.007" or AASHTO 2012 implied limit on crack width	For decks with ECB, this maximum crack width may be an unrealistic and unachievable limit.
Use of CS-01-08	Decreased maximum crack width relative to bridges designed using CS-1-03 or CS-1-93; while decrease was noticeable, it is unclear how to quantify this decrease because there is no one-to-one comparison.
Use of Epoxy-Coated bars	<ul style="list-style-type: none"> Increases crack width by a factor of 2 relative to black bars under static load. Fatigue loading of 2×10^6 cycles with maximum steel stress of $0.5f_y$ increases crack widths and deflections of slabs with ECB by 23% relative to crack width under static loading for identical slabs with ECB.
Fatigue loading (2×10^6 cycles) with maximum steel stress of $0.5f_y$	Increases crack width for slabs with ECB by a factor of 2.5 relative to the initial crack width under static loading.
Freeze-thaw along with sustained load	Freeze-thaw cycles (tested up to 60 cycles) simultaneously applied with sustained load causing steel stress of $0.3f_y$ increase crack widths of slabs with black bars by 75% of initial crack widths and by 150% for slabs with ECB.
Addition of Fibers to Slab Concrete	
Static Loading	Decreases crack width of slabs with ECB by 35% to 48% relative to ECB slabs without fiber.
Plastic Shrinkage	Decreases plastic shrinkage by a factor of about 8.
Freeze-thaw cycles applied simultaneously with sustained load	Freeze-thaw cycles (tested up to 60 cycles) applied simultaneously with sustained load causing steel stress of $0.3f_y$ reduces the increase in crack widths of slabs with ECB by a factor of 2 (i.e., it reduced crack width in our tests from 0.015" to 0.008").
Corrosion	Addition of fiber to slab concrete that is later subjected to corrosion reduces the moment capacity loss by about 6% as compared to a slab without fiber subjected to the same amount of corrosion.

The beneficial effects of fiber addition primarily stem from the improved performance of concrete slabs due to enhanced concrete response to static and fatigue loading, and under freeze-thaw and sustained loading. Constructability of bridge decks with a polypropylene fiber dosage of 10 lb/yd³ was verified to be feasible. The ease of placement, effective consolidation and acceptable finish are compatible or superior to that for decks constructed using ODOT standard mixes. Satisfactory constructability achieved in the pilot bridge makes this solution implementable by ODOT without any deviation from current practices other than the addition of fiber to the deck concrete.

RECOMMENDATIONS FOR IMPLEMENTATION OF RESEARCH FINDINGS

Recommendation for Implementation

It is recommended from the findings of this project that the addition of polypropylene fiber to deck concrete at a dosage of 10 lb/yd³ be implemented in ODOT's continuous span structural slab bridge decks to minimize the extent and severity of cracking. The potential for this implementation has been demonstrated in this project and was found to be beneficial in many ways. The durability of bridge decks and the expected service life is projected to increase substantially due the addition of fiber to deck concrete. It is also recommended that ODOT consider implementing fiber in other structural elements that are subjected to corrosive environments such as piers, pier caps, abutments, bridge columns, approach slabs, and bridge parapets to minimize or at least delay corrosion-related cracking and spalling. A smaller fiber dosage than 10 lb/yd³ is perhaps possible, but the effectiveness in controlling cracks by using a smaller fiber dosage needs to be verified.

Steps Needed for Implementation

For superstructure concrete, the provisions of Item 499 and Item 455 in ODOT's "Construction and Materials Specifications" for the construction of bridge decks and approach slabs need to be modified to include an approved job mix formula and a quality control/quality assurance process that incorporates fiber addition.

Expected Benefits from Implementation

The expected benefits from implementation are primarily a significant reduction in the extent and severity of bridge deck cracking. Other intangible benefits include a potential increase in wear resistance, durability and subsequent extension of the service life of bridge decks.

Potential Risks and Obstacles to Implementation

A marginal cost increase due to initial costs of incorporating fiber into bridge deck concrete could be a potential obstacle. Not all ready-mix concrete suppliers and contractors in Ohio are conversant with the production and placement of fiber-reinforced concrete with a high fiber dosage.

Strategies to Overcome Potential Risks and Obstacles

A life-cycle cost analysis by ODOT engineers will demonstrate the benefits of the implementation and prove that any marginal increase in the initial costs will be rapidly offset by the projected increase in service life of bridge decks and the subsequent delay of their replacement. With increased use of fiber-reinforced concrete, ODOT vendors will be able to supply and place concrete at a competitive market rate that is closer to the rate for concrete without fiber. This will lead to reduced initial cost of implementation.

Potential Users and Other Organizations that may be Affected

Several other bridge owners, such as the Department of Defense, transportation agencies in other states and counties in Ohio and elsewhere can benefit from the findings of this project.

Suggested Time Frame for Implementation

Implementation is possible immediately.

Estimated Cost of Implementation

Based on the figures provided by the contractor for the pilot bridge deck in Medina County (Ohio), the estimated increase in the cost of concrete with 10 lb/yd³ polypropylene fiber for the bridge was about \$100 to \$130 per cubic yard. The cost of concrete without fiber is estimated to be \$700 per cubic yard. For the pilot bridge with total quantity of deck concrete of about 110 yd³, the additional cost is between \$11,000 and \$14,300. If the reduced cracking due to the addition of fiber can reduce maintenance cost by preventing at least one cycle of crack sealing, that additional cost will be offset within a short period of time. Of the \$130 per cubic yard, the material cost is estimated to be \$82, and the workmanship cost was \$10 more per cubic yard than for a standard mix. The contractor also included \$38 per cubic yard to cover their risk. With more widespread use of fiber and competition, these costs to ODOT are likely to go down in the future because the current cost of just the polypropylene fiber in open market is likely to be about \$2 to \$3 per pound.

Recommendations on How to Evaluate the Ongoing Performance of the Implemented Result

It is recommended that the pilot bridge deck in Medina County (Ohio), where the research results were implemented, be monitored for crack development and growth with time over a period of next three to five years so as to verify if the problem of severe cracking is adequately addressed through the use of fiber in the deck concrete. Evaluation after one year will show the difference between bridge decks with no fiber and the pilot bridge deck with fiber because crack are normally fully formed on decks without fiber within one year and grow in width and number in later years.

BIBLIOGRAPHY

A bibliography including a full listing of references is given in Appendix A (Literature Review). The following are the references cited in this report only.

List of Citations

- AASHTO, "LRFD Bridge Design Specifications", US Customary Units, Washington, DC, ISBN: 978-1-56051-523-4, 2012.
- ACI 224R-01, "Control of Cracking in Concrete Structures", American Concrete Institute, Farmington Hills, MI, 17 pages.
- ACI 318-14, "Building Code Requirements for Structural Concrete (ACI 318-14)", American Concrete Institute, Farmington Hills, MI, 519 pages.
- FHWA Publication No. FHWA-HRT-09-020 "Corrosion Resistant Alloys for Reinforced Concrete", April 2009, 150 pages.
- Maggenti, R., Knapp, C., and Fereira, S., "Controlling Shrinkage Cracking", Concrete International, July 2013, pp. 36-41.
- Patnaik, A., and Baah, P., "Cracking Behavior of Structural Slab Bridge Decks", Final Report, ODOT/FHWA SJN 134708, January 2015, 214 pages.
- Patnaik, A.K., Ganapuram, S., and Adams, M., "Quantification of Cracks in Concrete Bridge Decks in Ohio District 3", Final Report, FHWA/OH-2012/3, Ohio Department of Transportation, Feb. 2012, 108 pages.
- Patnaik, A.K., Ramakrishnan, V., Wehbe, N., and Sigl, A., "Evaluation of Crack-Free Bridge Decks", Draft Final Report SD2005-11-F, South Dakota Department of Transportation, July 2015, 122 pages.
- Russell, H.G., Kleinhans, D.D., and Mertz, D.R., "Control of Cracking", Aspire - The Concrete Bridge Magazine, Prestressed/Precast Concrete Institute, Summer 2015, pp. 38-40.
- Salomon, A.L. and Moen, C.D., "Structural Design Guidelines for Concrete Bridge Decks Reinforced With Corrosion-Resistant Reinforcing Bars", Virginia Department of Transportation, Charlottesville, VA, Oct. 2015, 46 pages.
- http://www.virginiadot.org/vtrc/main/online_reports/pdf/15-r10.pdf
- Sharp, S. R. and Moruza, A., "Field Comparison of the Installation and Cost of Placement of Epoxy-Coated and MMFX 2 Steel Deck Reinforcement: Establishing a Baseline for Future Deck Monitoring", Final Report VTRC 09-R9, Virginia Transportation Research Council, Charlottesville, VA, May 2009, 82 pages.
- http://www.virginiadot.org/vtrc/main/online_reports/pdf/09-r9.pdf
- Transportation Research Circular E-C107, "Control of Cracking in Concrete - State of the Art", TRB Report, October 2006.

APPENDIX

The following reports have been added as appendices:

- APPENDIX A: Literature Review
- APPENDIX B: Crack Surveys of Bridges
- APPENDIX C: Evaluation of Crack Width Equations
- APPENDIX D: Corrosion Resistance of Slabs
- APPENDIX E: Shrinkage and Freeze-Thaw Effects
- APPENDIX F: Structural Cracking
- APPENDIX G: Effects of Slab-Pier Cap Connection
- APPENDIX H: Implementation

Reduction of Bridge Deck Cracking through Alternative Material Usage

APPENDIX A LITERATURE REVIEW

Prepared by:
Anil Patnaik, Ph.D.
and
Srikanth Marchetty

Prepared for:
The Ohio Department of Transportation,
Office of Statewide Planning & Research

State Job Number 135260
November 2017
Draft Final Report



TABLE OF CONTENTS

TABLE OF CONTENTS.....	1
LIST OF FIGURES	3
LIST OF TABLES.....	6
APPENDIX A.....	7
LITERATURE REVIEW	7
A.1 INTRODUCTION	7
A.2 TYPES OF CONCRETE CRACKING ON BRIDGE DECKS.....	8
A.3 FACTORS CAUSING CRACKING ON BRIDGE DECKS	9
A.3.1 <i>Material and mix design factors</i>	10
A.3.2 <i>Construction and environmental factors</i>	12
A.3.3 <i>Structural design factors</i>	12
A.4 PREVIOUS STUDIES OF NON-STRUCTURAL CRACKING OF BRIDGE DECKS.....	13
A.4.1 <i>Use of Admixtures to Control Shrinkage Cracking</i>	13
A.4.1.1 <i>Function and Theory</i>	14
A.4.1.2 <i>Application Techniques</i>	14
A.4.1.3 <i>Material Properties</i>	14
A.4.1.4 <i>Research on SRA and CRA</i>	15
A.4.2 <i>Use of Fibers to Control Shrinkage Cracking</i>	18
A.4.3 <i>Testing Methods on Non-Structural Cracking</i>	19
A.4.3.1 <i>Unrestrained (Free) Shrinkage Test</i>	20
A.4.3.2 <i>Restrained Shrinkage Tests (Ring Tests)</i>	21
A.4.3.3 <i>Plastic Shrinkage (Panel) Test</i>	21
A.4.3.4 <i>Freeze-Thaw Durability of Concrete</i>	23
A.5 LITERATURE REVIEW ON STRUCTURAL CRACKING	25
A.5.1 <i>Factors Causing Widening of Cracks on Bridge Decks</i>	25
A.5.2 <i>Control of Crack Widths</i>	26
A.5.3 <i>Test Methods Adopted for Structural Crack Studies</i>	29
A.5.3.1 <i>Direct Tension Testing of RC Structures</i>	29
A.5.3.2 <i>Flexure Testing of RC Members</i>	35

A.5.3.3 Pullout strength of reinforcing bar embedded in concrete	39
A.5.3.4 Bond Mechanism of steel in Concrete	39
A.5.3.5 Bond Strength Equations	40
A.5.3.6 Previous Studies on Pullout Tests	41
A.5.3.7 Effect of Fatigue on Bridge Decks.....	46
A.5.3.8 Studies on Connection between Slab and Pier of RC Bridge	50
A.6 LITERATURE REVIEW ON CORROSION	58
<i>A.6.1 Accelerated Corrosion Process.....</i>	<i>58</i>
<i>A.6.2 Accelerated Corrosion under Sustained Loading</i>	<i>60</i>
A.7 USE OF ALTERNATE REINFORCEMENT IN BRIDGE DECKS	64
A.8 SUMMARY OF LITERATURE REVIEW	69
BIBLIOGRAPHY	71

LIST OF FIGURES

Figure A.1 Transverse Cracking on Bridge Deck with a Measured Crack Width of 0.1 Inch	7
Figure A.2 Classification of Cracks Based on TRC E-C107 (Transportation Research Committee, 2006)	8
Figure A.3 Types of Concrete Bridge Deck Cracking Based on Orientation (Russell, 2004)	9
Figure A.4 Factors Causing Cracking on Bridge Decks (Patnaik and Baah, 2015)	10
Figure A.5 Effect of SRA on Concrete Drying Shrinkage (ASTM C157).	15
Figure A.6 Effect of CRA Compared to Conventional SRA (Nmai et al. 2014)	18
Figure A.7 Effect of Polypropylene Fibers on Crack Width (Grzybowski and Shah, 1990)	18
Figure A.8 Typical Plot of Crack Patterns of Test Slabs Without Fibers (<i>left</i>) and With 0.3 kg/m ³ (0.5 lbs/yd ³) Monofilament Fibers (<i>right</i>) (Ramakrishnan, Zellers and Patnaik et al., 2007)	19
Figure A.9 Free Shrinkage Test Specimen (ASTM C 157)	20
Figure A.10 Free Shrinkage Test Setup	20
Figure A.11 Ring Test Setup According to Different Standards (AASHTO T334)	21
Figure A.12 Panel Test Setup (Kraai, 1985)	22
Figure A.13 Shrinkage Panel Forms (Ramakrishnan, Zellers and Patnaik et al., 2007)	22
Figure A.14 Freeze-Thaw Test Chamber	23
Figure A.15 Comparison of Plain and Fiber Reinforced Concretes Under Freeze-Thaw (Balaguru and Ramakrishnan, 1986)	24
Figure A.16 Typical Cracking Mechanism in Direct Tension Test Specimens (Source: Baah and Patnaik, et. al. 2015)	29
Figure A.17 Specimen for Uniaxial Tension Testing (Mimura, 2011)	30
Figure A.18 Test Setup For Uniaxial Tension Test (Mimura, 2011)	30
Figure A.19 Strain Distribution in Cross Section of Member (Mimura, 2011)	30
Figure A.20 Definition of Slip and Bond Stress (Mimura, 2011)	31
Figure A.21 (a) Bond Stress and Resulting Steel and Concrete Strain Distribution before Cracking. (b) No Additional Cracks Developed after the First Series of Cracks at the Tension Load T_I (Soltani et al., 2013)	33
Figure A.22 Bond Stress, Steel and Concrete Strain Distribution between Adjacent Cracks in a Reinforced Concrete Member (Soltani et al., 2013)	34

Figure A.23 Average Crack Widths Corresponding to Bar Stress for Reinforcement Ratios of 0.015 and 0.02 (Soltani et al., 2013)	34
Figure A.24 Cracked Flexure Member	35
Figure A.25 Controlling Crack Spacing	36
Figure A.26 Cross-Sectional Details for Slabs	37
Figure A.27 Slab Specimen Test Setup (Sim and Frosch, 2014)	37
Figure A.28 Measuring Crack Widths on the Slab during the Testing (Sim and Frosch, 2014)	38
Figure A.29 Cracks Developed in the Constant Moment Region of the Slab	38
Figure A.30 Maximum Crack Width Versus Stress in the Bar for Slabs with 12-inch Bar Spacing (Sim and Frosch, 2014)	38
Figure A.31 (a) Geometry of Deformed Bar; (b) Force Distribution in RC Member during Pullout Test (Bajaj, 2012)	39
Figure A.32 Pullout Specimen Details (Source: Mansoor and Zhang, 2013)	41
Figure A.33. Electro-Chemical Corrosion Process (Source: Mansoor and Zhang, 2013)	42
Figure A.34 Typical Load vs Displacement Curve for a Pullout Specimen with Various Levels of Corrosion (Mansoor and Zhang, 2013)	42
Figure A.35 Steel Crimped Fibers (<i>left</i>) and Recron 3S Fibers (<i>right</i>) (Deepthi and Sabeena, 2016)	43
Figure A.36 Casting of Pullout Specimens (Deepthi and Sabeena, 2016)	43
Figure A.37 Test Setup (<i>left</i>) and the Failed Pullout Specimens (<i>right</i>) (Source: Deepthi and Sabeena, 2016)	44
Figure A.38 Meshed Specimen Model (<i>left</i>); Specimen Showing Pulling of Rod (<i>right</i>) (Source: Deepthi and Sabeena, 2016)	44
Figure A.39 Bond Slip Behavior of Pullout Specimens: (a) Experimental Results; (b) Analytical Results (Deepthi and Sabeena, 2016)	45
Figure A.40 Curve Showing Stress Range Applied Over Time	46
Figure A.41 Fatigue Life Prediction Area (Zhang et al., 1999)	47
Figure A.42 Distribution of Normal Stress in the Critical Cracked Section (Pedersen (1996))	49
Figure A.43 Classification of Connection in Structural Slab Bridges	51
Figure A.44 Integral Connection Types (Based on Bridge Plan Drawings)	51
Figure A.44 Integral Connection Types (Based on Bridge Plan Drawings) (continued)	52

Figure A.45 Non-Integral Connection Types (Designer’s Preference)	52
Figure A.46 Non-Integral Connection Types (Designer’s Preference), continued	53
Figure A.47 Standard Integral Connection Type from Iowa DOT (Iowa DOT, 2006)	53
Figure A.48 (a) Non-Integral Connection Type from Iowa DOT; (b) Section Showing Joint Material (Iowa DOT, 2006)	54
Figure A.49 Comparison of Bending Moment Due to Dead Load for Fixed and Pined Connection of a Single Span Bridge (Bhagwat, 2014)	55
Figure A.50 Comparison of Bending Moment Due to Dead Load for Fix and Pin Connection for a Two-Span Bridge (Bhagwat, 2014)	55
Figure A.51 Comparison of Bending Moment Due to Dead Load for Fixed and Pined Connection for Three Spans Bridge (Bhagwat, 2014)	56
Figure A.52 3D Finite-Element Model in SAP2000 (Hou and Chen, 2017)	57
Figure A.53 Idealized Intermediate Bent Connections (Hou and Chen, 2017)	57
Figure A.54 Moment Demand /Capacity for Different Geometries (Hou and Chen, 2017)	57
Figure A.55 Setup for Corrosion under Sustained Load (Yoon et al., 2000)	61
Figure A.56 Test Setup of Accelerated Corrosion (El Maaddawy et al., 2003)	61
Figure A.57 Test Setup for Accelerated Corrosion under Sustained Load	62
Figure A.58 Testing of RC Slab for Corrosion under Sustained Load	63
Figure A.59 Comparison of Cracks and Load-Deflection Plots for Uncorroded and Corroded Slab Specimens (Gao et al, 2016)	63
Figure A.60 Transverse Crack Width Growth Rate Observed for a Typical Corrosion Specimen (Gao et al, 2016)	64
Figure A.61 Direct and Indirect Cost of ECR and CRR Deck Reinforcement by Components	65
Figure A.62 Bridge with ASTM A1035 (left) and ASTM A955 Steel (right)	65
Figure A.63 Test Concrete Block (Clemena and Virmani (2003), as Presented in AMEC Earth & Environmental, 2006)	68
Figure A.64 Life Cycle Estimated from Life 365 Model (Clemena and Virmani (2003), as Presented in AMEC Earth & Environmental, (2006))	69

LIST OF TABLES

Table A.1 Maximum Allowable Crack Widths given by ACI 224R-01 for Various Exposure Conditions	7
Table A.2: Design Factors Affecting Stringer-Supported Bridge Deck Cracks	13
Table A.3 Crack Width Prediction Formulas from Various Codes	26
Table A.4 Empirical Equations for Crack Width Prediction Proposed by Various Researchers .	27
Table A.5 Crack Spacing Equations Proposed by Various Researchers	28
Table A.6 Bond Strength Equations Developed by Various Researchers	40
Table A.7 Detail of Bridge Models.....	54
Table A.8 Bridge Configurations.....	56
Table A.9 Various Corrosion Resistant Bars and the Corrosion Threshold	68

APPENDIX A LITERATURE REVIEW

A.1 Introduction

Cracking on bridge decks is a problem concern for transportation agencies throughout the United States, as millions of dollars are spent each year on maintenance and construction of bridges. Once a bridge deck is cast and set for curing, shrinkage cracks begin to develop because of various environmental and material factors. Once the formwork is removed and the bridge is opened to traffic, structural cracks begin to form due to the self-weight of the slab and traffic loading. These cracks widths are limited based on the conditions to which the bridge will be exposed to during its service life. Table A.1 presents the maximum allowable crack widths based on exposure condition recommended by the American Concrete Institute ACI 224R-01(ACI, 2008).

Table A.1 Maximum Allowable Crack Widths given by ACI 224R-01 for Various Exposure Conditions

Exposure Condition	Maximum Allowable Crack Width
Dry Air	0.016 in.
Humidity, Moist Air, Soil	0.012 in.
Deicing Chemicals	0.007 in.
Sea Water	0.006 in.
Water Retaining Structures	0.004 in.

Limiting crack widths on deck slabs plays a vital role in durability and service life of bridge decks. Cracks connecting the voids in concrete provide pathways for the ingress of chlorides from deicing salts, thereby increasing the saturation in bridge posing a risk of freeze and thaw damage (Fanous et al., 2000). Cracks result in corrosion of reinforcing bars, loss of residual strength, and finally a loss of structural integrity. Most of the transverse cracking on bridge decks occurs in the negative moment region, i.e. the area above the intermediate piers. Some of the bridges have crack widths as large as 0.1 inches, which is more than ten times the allowable crack width. Figure A.1 shows a typical crack measured on the bridge deck during the bridge survey.

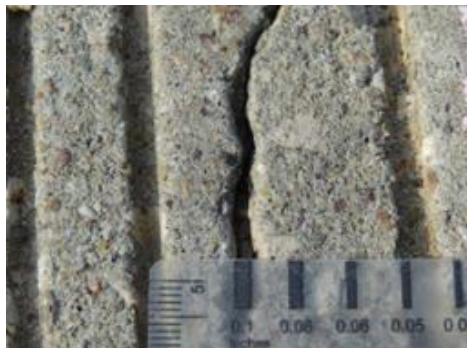


Figure A.1 Transverse Cracking on Bridge Deck with a Measured Crack Width of 0.1 Inch

A.2 Types of Concrete Cracking on Bridge Decks

Cracks in concrete are formed once the concrete extreme fiber stresses exceed the tensile strength of concrete. Cracks are classified as “before” and “after” hardening of concrete. Cracks that are formed before cracking are mostly due to plastic shrinkage of concrete, and frost damage. Cracks that are formed after hardening are mainly due to design loads, volumetric changes in time, corrosion of reinforcing bars and effects of freeze and thaw action. Figure A.2 shows the classification of cracks before and after the hardening of the concrete.

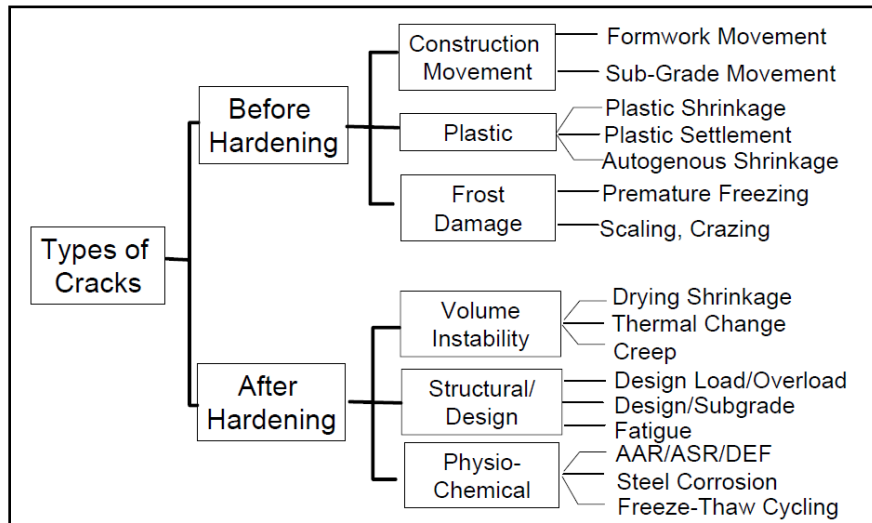


Figure A.2 Classification of Cracks Based on TRC E-C107
(Transportation Research Committee, 2006)

Classification of cracks based on orientation on the bridge deck are further classified as transverse cracks, longitudinal cracks, diagonal cracks and map cracks:

- Transverse cracks, the most critical type of crack observed on bridge decks, are usually formed in the negative moment region over the piers. These cracks run perpendicular to the girders and sometimes are parallel to the skew of the bridge.
- Longitudinal cracks are cracks that form parallel to the longitudinal axis of the bridge, running right above the reinforcing steel. These cracks are formed due to the differential movements or rotation of the beams about their longitudinal axis.
- Diagonal cracking is usually seen in bridges with skew, and they occur more frequently in the corner areas because of the restraint provided by abutments and piers.
- Map or pattern cracks are often the product of improper curing, when the surface moisture on the concrete evaporates too quickly and the volumetric change of the concrete is restrained (Schmitt and Darwin, 1995). Figure A.3 shows several types of cracks observed on bridge decks based on orientation.

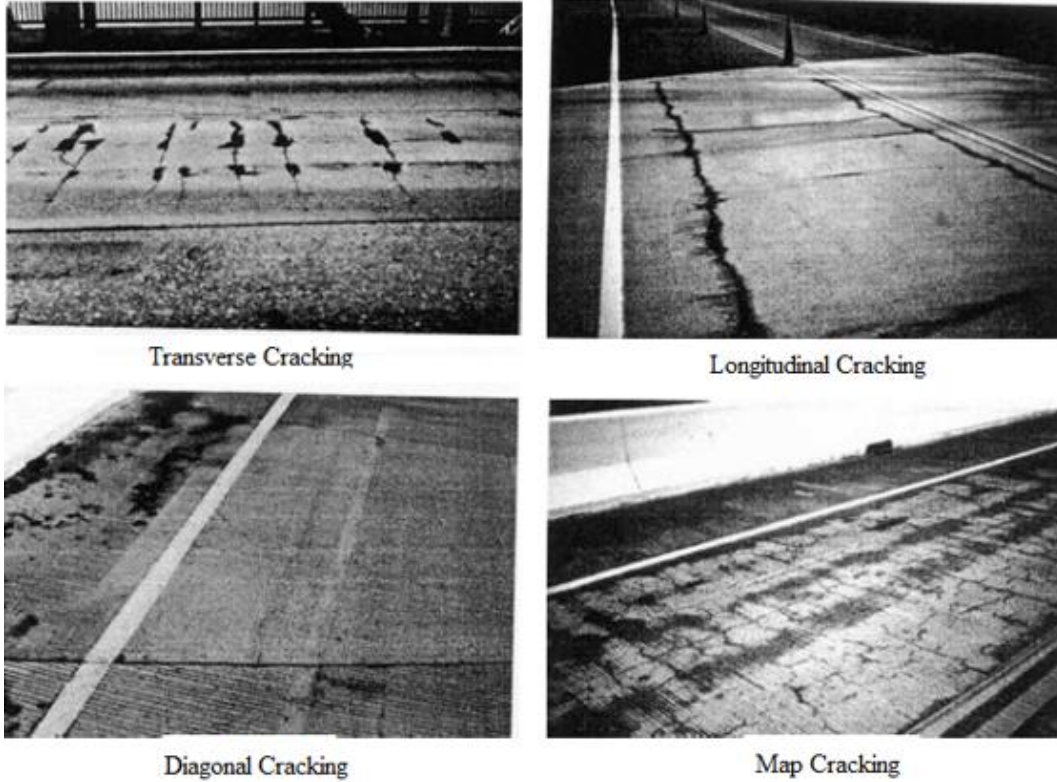


Figure A.3 Types of Concrete Bridge Deck Cracking Based on Orientation (Russell, 2004)

A.3 Factors Causing Cracking on Bridge Decks

Early age cracking on bridge decks not only affects the appearance of a bridge but also reduces its durability and service life. Such cracks allow chlorides and other deicing salts to penetrate the cracks and result in corrosion of the embedded reinforcement. Early age cracking depends on a number of factors, as shown in Figure A.4, including materials and mix design, construction and environmental conditions, structural and foundation issues, traffic related factors and other factors (Patnaik and Baah, 2015). These factors are discussed in detail in the following subsections.

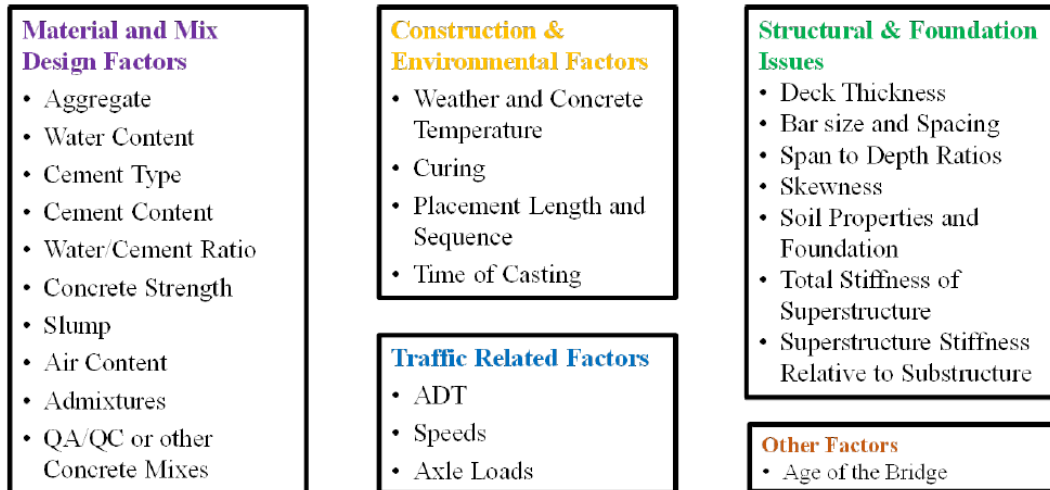


Figure A.4 Factors Causing Cracking on Bridge Decks (Patnaik and Baah, 2015)

A.3.1 Material and mix design factors

Several material and mix design factors are related to shrinkage cracking in concrete bridges. These factors include the following:

- **Cement type:** The cement type plays a key role in reducing shrinkage cracking. Several researchers recommend the use of cement type II and to avoid finely ground cement and Type III cement in warm weather conditions. Concrete with a lower cement content and Type II cement has a lower risk of cracking than Type I cement, because Type II cement has a lower heat of hydration (TRS1105, Minnesota Department of Transportation, 2011; Shing and Abu-Hejleh, 1999; Krauss and Rogalla, 1996).
- **Water-to-cement ratio:** The water-to-cement ratio also affects the concrete strength. With a given amount of cement, a higher water-to-cement ratio produces more cement paste generating a weaker yet more workable concrete. The lowest possible water-to-cement ratio to meet the workability requirements will minimize the cracking tendency by reducing shrinkage (McDonald et al., 1995).
- **Concrete mixes:** Concrete mixtures made using higher cement contents are very conducive to cracking by producing higher heat of hydration, greater shrinkage, higher modulus of elasticity, and lower creep. Frequent use of high strength concretes in the construction industry tends to encourage increased cement contents increasing the cost of the mixture and increasing cracking. TRC E-C107 (TRC, 2006) highly recommends proper planning during materials selection and mixture proportioning, a crack-resistant concrete having lower cement content, which still meets durability and performance specifications, can be produced.
- **Concrete strength:** It may seem that high early strength of concrete may reduce cracking but since the strength gain of concrete is usually accompanied by a gain in modulus of elasticity, it can't be easily said that higher strength reduces cracking. There is no general agreement among studies that considered this factor. Schmitt and Darwin (1995; 1999)

noticed increased cracking with increased compressive strength. Shing and Abu Hejleh (1999) also recommended against fast strength gain in deck concrete. Krauss and Rogalla (1996) recommended the use of concrete with low early strength. On the other hand, Ramey et al. (1997) recommended increasing compressive strength.

- Slump: Schmitt and Darwin (1995) noted that cracking increases with increasing slump. This could be a result of the effect of increased slump on settlement cracking or the effects of a higher water and/or cement content corresponding to the increase in slump. Issa (1999) attributed cracking of concrete to use of high slump concrete.
- Admixtures: Admixtures may have both positive and negative effects on deck cracking (TRC E-C107, 2006). Chemical admixtures, except for air-entraining admixtures, should conform to the requirements of AASHTO specification M194, which lists the following types of admixtures: Type A (water-reducing), Type B (retarding), Type C (accelerating), Type D (water-reducing and retarding), Type E (water-reducing and accelerating), Type F (water-reducing, high-range) and Type G (water-reducing, high-range, and retarding). Water-reducing admixtures are particularly beneficial in increasing workability while maintaining a constant w/cm or maintaining workability while lowering the w/cm. This facilitates the development of a workable concrete mix for which a maximum w/cm is specified. In projects with closely spaced or congested reinforcement, the use of high-range water-reducing admixtures help concrete flow around these obstructions without segregation (NCHRP Synthesis-333; TRB, 2004). Retarding admixtures reduce the rise in temperature of the concrete and may be used to reduce the potential for thermal shrinkage cracking. Retarders are particularly useful when the ambient temperature is expected to reach or exceed 24°C (75°F). Water reducers are used because they result in reduction in the amount of mix water and resulting drying shrinkage. Shrinkage reducing admixtures may also be used for some applications to reduce shrinkage by as much as 50% (Weiss and Berke, 2002).
- Air content: Air content is usually used to increase freeze thaw durability of concrete. But it may be advantageous to use high values of air content in moderate and warm climates. Cheng and Johnson (1985) observed that increase in air content reduces cracking. Schmitt and Darwin (1999) even noticed significant decreases in cracking with air content more than 6% and recommend at least 6% air content. French et al. (1999) recommend air content of 5.5–6%. On the other hand, Stewart and Gunderson (1969) found no relationship between air content and cracking, which in recent times has been disproved.
- Aggregate type and size: Aggregate type and size can influence the strength, elastic modulus, shrinkage and creep. Both aggregate quantity and quality should be carefully examined when designing a crack resistant deck mixture. Increasing aggregate content will allow a reduction in the paste content while reducing the mixture component that is most susceptible to shrinkage and thermal stresses (TRC E-C107; TRC, 2006). Suggestions from prior studies include using largest possible size of aggregate, maximizing aggregate volume and using low shrinkage aggregate to reduce cracking (Babaei and Purvis, 1994; Krauss and Rogalla, 1996; French et al., 1999; Portland Cement Association, 1970).

A.3.2 Construction and environmental factors

Construction practices and environmental conditions during and after the concrete pour can influence the creation of shrinkage cracks on the surfaces of bridge decks. The weather during placement of the concrete bridge deck can affect the tendency for cracking. In general, it is recommended to cast the deck when the temperature is between 40°F to 90°F (4°C to 32°C) and to avoid on days when the temperature difference between the high and low temperature is greater than 50°F (or the difference is greater than 28°C), because additional thermal stresses will be produced in the deck (French et al., 1999). In addition, thermal stresses can be generated when concrete is cast on girders in cold weather due to the differences in temperature of the girders and the heat of hydration of the concrete deck. In hot weather and on windy days, rapid surface evaporation can lead to the formation of plastic shrinkage cracks or drying shrinkage cracks. By monitoring the evaporation rate, precautions can be taken to reduce concrete moisture losses by using sunscreens, windbreaks, fog mist, and chemical curing films (McDonald et al., 1995; Schmitt and Darwin, 1995). Scheduling the casting of the deck in the early evening or at night can also help to reduce the tendency for cracking.

Steps can also be taken during the curing process to eliminate plastic shrinkage cracking and to reduce drying shrinkage cracking. In the early stages of concrete curing, the hydration process is relatively slow and requires the cement to be saturated with water. If water is allowed to evaporate from the deck surface, the concrete will not acquire any additional strength. Thus, it is important to begin wet curing of the concrete immediately after finishing the deck. Curing can be accomplished by ponding water on the deck or by covering the deck with wet burlap, which is then covered with plastic sheeting. It is necessary to keep the deck wet until the curing process is complete. The longer the deck is cured, the higher the concrete strength will be, the lower the shrinkage will be, and the lower the likelihood that transverse cracks will form. McDonald et al. (1995) recommended to continue moist curing the bridge deck for at least seven days.

A.3.3 Structural design factors

The severity of cracking depends, to a certain extent, on the structural aspects of the bridge deck. Table A.2 presents design factors that affect deck cracking in stringer-supported bridges.

Table A.2: Design Factors Affecting Stringer-Supported Bridge Deck Cracks

Design Factors	Influence on Cracking	Level of Influence	Recommendations
Continuous/Simple Span	Continuous span bridges are more susceptible to cracking than simple-span bridges.	Moderate	
Girder Type	Cracking is more severe with steel girders than with concrete girders	Moderate	
Girder End Conditions	Restrained ends induce more cracks.	Moderate to High	Reduce longitudinal restraints.
Deck Thickness	Thinner decks are more susceptible to cracking. However, there is no conclusive evidence to support this.	Moderate	Deck thickness should not be less than 8.5 in (215 mm).
Concrete Cover	A thicker concrete cover may reduce settlement cracks.	Minor	Use concrete cover not less than 2 in.
Girder Size and Spacing	Decks with larger girders at closer spacing are more susceptible to cracking than those with smaller girders at farther spacing.	Moderate	
Transverse Reinforcing Bars	Most transverse cracks are right above the top transverse bars. A Minnesota study (reference?) indicates that decks with No. 6 bars have more severe cracks than those with No. 5 bars. They recommend using No. 5 bars at 5.5" spacing or No. 6 bars at 6.5 to 7.0" spacing.	Moderate	Avoid alignment of top and bottom transverse bars within the same vertical plane. Place top longitudinal steel above transverse steel. Use smaller bars at closer spacing.
Creep of Prestressed Concrete Girders	Creep of prestressed concrete girders may induce stresses in decks.	Not clear	Avoid tension in prestressed concrete girders.

Source: Shing and Abu-Hejleh (1999).

A.4 Previous Studies of Non-Structural Cracking of Bridge Decks

Non-structural cracking is mainly caused during the initial days of the bridge construction. These cracks are widespread over the area of the deck exposed to environmental conditions. Cracking due to concrete mixture can be controlled using various admixtures and by including fibers in the mix design. The following sections discuss control measures for non-structural cracking.

A.4.1 Use of Admixtures to Control Shrinkage Cracking

The use of SRAs (shrinkage reducing admixture) to control shrinkage cracks in concrete is a relatively a new concept (Nmai et al., 1998). SRAs were first introduced in Japan in 1982. In 1985, U.S. Patent Number 4,547,223 was granted to Goto et al. (1985) for developing the main component of SRA, which is polyoxyalkylene alkyl ether, a lower alcohol alkyleneoxide adduct. Berke et al. (1997) patented the product in the U.S. Shrinkage-reducing admixtures provide an effective method for reducing strains caused by shrinkage and the resulting stresses while maintaining the original concrete mixture proportions and mixing requirements.

A.4.1.1 Function and Theory

Whittmann (1976) explained the reasons behind plastic shrinkage cracking of the concrete surface. According to his research, the evaporation of bleed water on the surface of concrete creates air-liquid menisci in the liquid between the solid particles on the surface. These menisci cause tensile stress to develop in the pore fluid, leading to shrinkage. The viscous nature of the material at these early ages causes the majority of the shrinkage to occur in the vertical direction. As the system shrinks, the pore fluid is brought to the surface and evaporates (Whittmann, 1976). SRA works by reducing the surface tension of the pore water and thus lowering the plastic shrinkage (Lura et al., 2006). This decrease of surface tension in the pore fluid in the SRA mixtures results in less evaporation, reduced settlement, reduced capillary pressure, and lower crack-inducing stresses at the topmost layer of the mortar. Therefore, SRA reduces the potential for the development of plastic shrinkage cracks.

The mechanisms responsible for drying shrinkage are not yet fully understood; however, its occurrence is mainly attributed to capillary stresses (L'Hermite, 1988). When pore water evaporates from capillary pores in hardened concrete during drying, tension in the liquid is transferred to the capillary walls, resulting in drying shrinkage (Foliard and Berke, 1997). For a given pore size distribution, the internal stress generated upon evaporation is proportional to the surface tension of the pore water solution. SRAs reduce drying shrinkage by lowering the surface tension of pore water in hardened concrete. Thus, upon evaporation from capillary pores during drying, there is less tendency for shrinkage and the stresses that result from it.

A.4.1.2 Application Techniques

There are two ways to apply SRA. The first method is to simply brush it or spray it on the surface of the concrete, which is referred to as the *impregnation method* or *topical application*. The second method is the *integration method*, where SRA is incorporated into the mix during the mixing of the concrete, separately from any other admixtures. It has been found that the integration method provides much better results in reducing drying shrinkage (Ah-Sha et al., 2001). Nmai et al. (1998) also noticed that drying shrinkage was reduced by about 50 to 60 percent when a 1.5 to 2.0 gal/yd³ dosage of SRA was integrated into the mix.

A.4.1.3 Material Properties

A number of shrinkage-reducing admixtures (SRA) are commercially available in the US. In this project, MasterLIFE SRA 035 (developed by BASF, Ludwigshafen, Germany) was used. The manufacturer recommended that the SRA be added in a typical dosage ranging from 0.5 to 1.5 gal/yd³. However, dosages outside of this range may be required, depending on the level of shrinkage reduction needed. BASF also strongly recommends that drying shrinkage testing be performed to determine the optimum dosage for each application and each set of materials. Since the SRA itself contains no water, the manufacturer specifies that the mix water content should be reduced to account for the quantity of SRA used. If the delayed addition method is used, the manufacturer recommends mixing the concrete at high speed for 3 to 5 minutes after the addition of SRA admixture to ensure uniformity of the mixture. The SRA does not substantially affect slump; however, it may increase bleed time and bleed ratio (10% higher). It may also delay the initial time of set by 1 to 2 hours, depending on the dosage and temperature. BASF suggests that

compressive strength loss is also minimal when SRA is used. BASF warns that concrete applications exposed to freezing and thawing environments must be pre-approved and require field trials prior to incorporating the SRA. Figure A.5 shows the effect of the SRA on drying shrinkage in concrete.

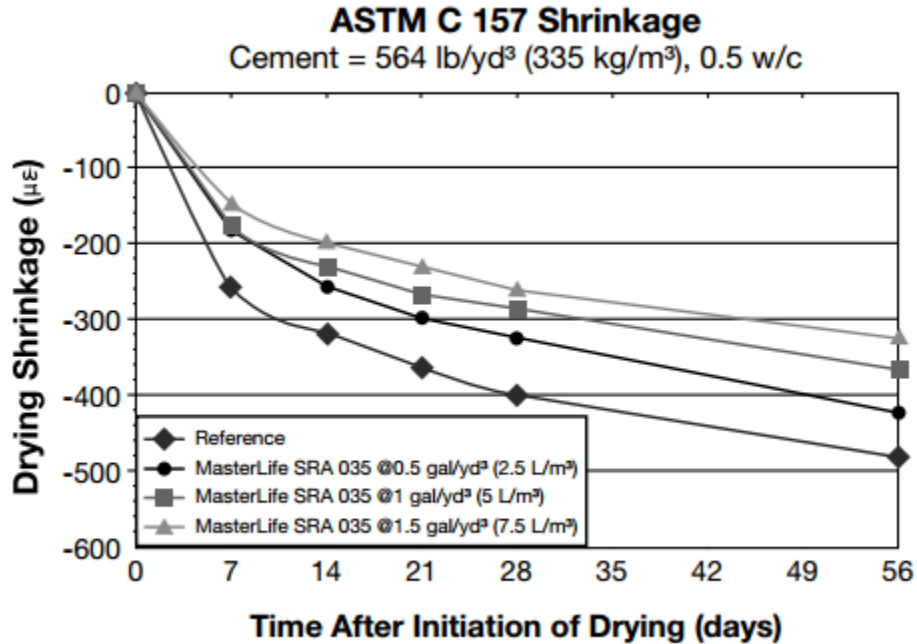


Figure A.5 Effect of SRA on Concrete Drying Shrinkage (ASTM C157).

A.4.1.4 Research on SRA and CRA

A wide variety of tests have been implemented to evaluate the shrinkage and cracking behavior of concrete. Due to its simplicity, the ring test is most widely used to determine cracking tendency (Tritsch et al., 2005). Plate tests are also used to evaluate plastic shrinkage in fresh concrete immediately exposed to drying. The geometry of the plates limits the mixes to a small coarse aggregate or none at all. The small cross sections in the linear tests also restrict the size of the coarse aggregate (Kraai, 1985). Some linear tests require complicated instrumentation that monitors shrinkage and applies a tensile force to restrain the specimen (Paillère et al., 1989). In contrast to other tests, ring tests allow actual concrete mixes to be evaluated under restraint that is similar to the restraint caused by girder systems on bridge decks. Instrumenting the rings with strain gages allows the strain development to be monitored and provides an accurate indication of time-to-cracking. With the ring test, several mixes can be evaluated under the same conditions to determine which mix exhibits the best shrinkage and cracking behavior.

State transportation agencies in a number of states have sponsored research on the use of SRA to control shrinkage and cracking in concrete. These research efforts include the following:

- Oregon: In 2013, a research project carried out by Ideker et al. (2013) for the Oregon Department of Transportation investigated the shrinkage threshold limits and testing protocols for ODOT high performance concrete mixes. Several testing methods were implemented including ASTM C157 test for free shrinkage and ASTM C 1581 and

AASHTO PP34-98 for restrained shrinkage. Results showed that when incorporating SRA alone or a synergistic mixture of SRA and FLWA, the cracking resistance of ODOT HPC was significantly improved. The HPC with a combination of SRA and LWFA showed the most significant benefits in improving the cracking resistance.

- California: A study was performed by Maggenti et al. (2013) for the California Department of Transportation (CalTrans) on the combined effects of addition of SRA and Fibers to the concrete mix for the purpose of shrinkage control. It was found that the addition of SRAs to meet the Caltrans shrinkage performance requirements (0.030% at 28 days and 0.045% at 180 days) led to “a dramatic reduction in cracking”. Upon inspection, several decks constructed using SRAs between 2002 and 2008 were reported to be free of visible cracking. According to CalTrans reports, the use of SRAs could eliminate the need to specify low-strength concrete, long curing times, a low w/cm, or large aggregates.
- Kansas and Missouri: A joint study by the state DOTs of Kansas and Missouri in 2005 (Tritsch et al., 2005) found that adding a shrinkage-reducing admixture to concrete significantly reduces free shrinkage and restrained shrinkage rate, but also makes achieving consistent concrete properties (i.e., air content) difficult, thus requiring more air entraining admixtures.
- Nevada: Results from a research program conducted by Ah-Sha et al. (2001) for the Nevada Department of Transportation recommend the implementation of the SRA in environments where moderate and severe freezing and thawing is not a concern. It also recommended that the maximum addition rate to not exceed 2.5% by weight of cementitious material. In addition, the SRA concrete should be designed at a minimum targeted compressive strength of 31 MPa (4500 psi) at 28 days, with a maximum W/C ratio not exceeding 0.45. NDOT warns that the implementation of SRA in environments of moderate to severe freezing and thawing must be done cautiously. Moreover, NDOT strongly encourages using a minimum of 7% plastic air content. It also recommends addition of Fly ash to SRA concrete in order to achieve desirable performance in resisting chloride ion penetration.
- Hawaii: HDOT’s use of SRA began in early 2001 in the construction of the Keaiwa Stream Bridge on Hawaii Island. SRA of 96 oz per cubic yard in a concrete bridge deck was implemented to reduce shrinkage in lieu of the 30-day delayed poured closure strip. To determine its effectiveness and the effects of reinforcing, a research project was undertaken by HDOT to monitor the shrinkage strains in the Keaiwa Stream bridge deck and in eight 36 × 36 × 8 inch concrete specimens. These specimens were categorized into two groups, with and without the SRA and varying amounts of steel reinforcements of 0.3 to 1.2 percent. Vibrating strain gages were used to monitor shrinkage, strain and creep for one year. Results showed a 60% reduction in shrinkage in the unreinforced test specimens with SRA. Creep was also reduced by 30 percent. The reinforced sections also showed reductions in shrinkage and creep (Carnate, 2014).

Many other researchers have studied the effects of SRA on concrete. Berke et al. (1997) found that shrinkage reduction is directly related to the SRA addition rate as a percentage of the mixing water. Moreover, data on large-scale field experiments show that substantial reduction in cracking is obtained for concretes treated with SRA (Berke et al., 1997). Palacios and Puertas (2007) found that SRA reduced the shrinkage by up to 85% and 50% when the alkali-activated

slag mortar specimens were cured at a relative humidity of 99% and 50%, respectively. Shah et al. (1997) found that a major advantage of SRA was the delay of cracking in ring specimens from restrained shrinkage, and the age of the first visible crack depended on the amount of SRA. Cracks in concrete mixes with an SRA content of 1 percent formed at around 10 to 15 days. Concrete mixes with an SRA of 2 percent showed significantly improved cracking performance as compared with plain concrete, showing first cracks at about 48 days (Shah et al., 1997).

Bentz and co-workers (Bentz et al., 2008; Bentz et al., 2001) found that the addition of SRA to concrete can reduce the surface tension by a factor of two, significantly decreasing the strains from autogenous shrinkage. It was also found that the addition of SRA results in less evaporation, reduced settlement, reduced capillary tension, and lower crack-inducing stresses at the topmost layer of the mortar, greatly mitigating the effects of plastic shrinkage (Bentz, 2008; Mora-Ruacho et al., 2009). However, a serious drawback of SRA is that it increases the freezable water content of cement pastes cured under saturated conditions at early ages, which may have negative implications for the early-age frost resistance of these materials (Bentz, 2007; 2008).

Rajabipour et al. (2008) explored other possible negative side effects of SRA. They found that the addition of SRA reduces the polarity of mixing water, which lowers the tendency of alkalis to dissolve and ionize in the mixing water. The reduced alkalinity of the pore fluid was found to greatly slow the rate of cement hydration and can contribute to retardation in hydration and strength development of concrete that contains SRA. They recommend delaying the addition of SRA (e.g., addition of SRA to concrete at the job site instead of addition during the initial mixing at the concrete plant) to help alleviate the retardation of hydration (Rajabipour et al., 2008).

A recent study by Nmai et al. (2014) showed that SRAs have a minimal, if any, effect on crack width when cracking occurs. They proposed using a new admixture to reduce not only drying shrinkage but also the initial crack width, should cracking occur. This innovative crack-reducing admixture (CRA), also developed by BASF, is based on a specialty alcohol alkoxyolate and is being marketed under the trade name MasterLife CRA 007 admixture. The effects of the CRA on the properties of concrete, particularly setting time and strength, are similar to the effects of SRAs. Therefore, depending on dosage, as well as on the temperature of the concrete and the ambient temperature, setting time may be slightly delayed. In addition, a slight reduction in strength may occur depending on the dosage of the CRA. Compared with conventional SRAs, CRA has been shown to provide internal stress relief in ASTM C1581/C1581M ring tests, resulting in a change in the mode of failure from a sudden release of all compressive strain in the inner ring to a gradual release of compressive strain. The net benefit of the internal stress relief provided by the CRA is a greater delay in the time-to-cracking in the ring test and a lower initial crack width: about 0.004 in. (0.1 mm) compared to 0.04 in. (1 mm) in specimens made with untreated concrete and SRA-treated concrete. Figure A.6 demonstrates the effect of CRA on shrinkage behavior.

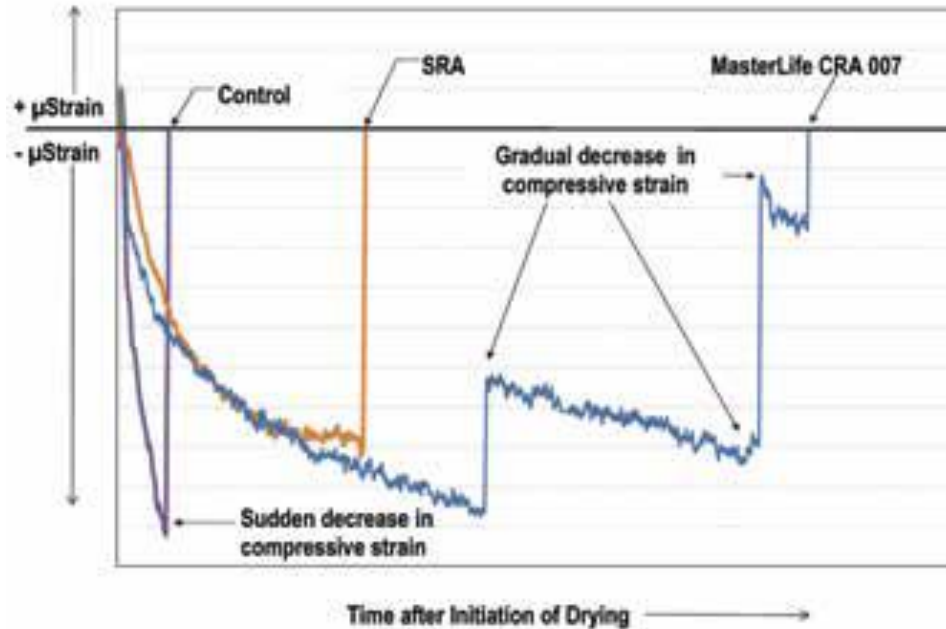


Figure A.6 Effect of CRA Compared to Conventional SRA (Nmai et al. 2014)

A.4.2 Use of Fibers to Control Shrinkage Cracking

Grzybowski and Shah (1990) conducted shrinkage tests using ring specimens to study the effects of fibers on concrete shrinkage properties. Two types of fibers (steel and polypropylene), amounts of fibers (0.1 to 1.5 percent by volume), age of concrete (2 hr or 4 days), and period of drying (up to six weeks) under a given environment (40 percent relative humidity and 20°C (68°F)) were studied. It was found that while fiber addition did not significantly decrease the overall amount of shrinkage, it can substantially reduce crack widths resulting from restrained drying shrinkage as shown in Figure A.7.

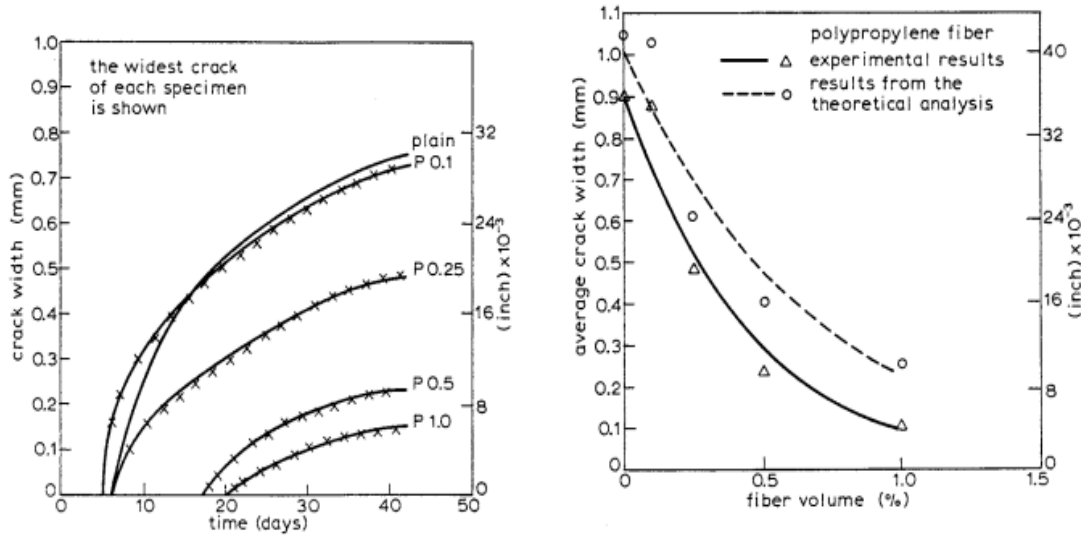


Figure A.7 Effect of Polypropylene Fibers on Crack Width (Grzybowski and Shah, 1990)

Ramakrishnan, Zellers and Patnaik et al. (2007) evaluated the effect of newly developed high tenacity monofilament polypropylene fiber on the plastic shrinkage of concrete. The crack reduction potential of the fiber was studied using cement-rich concrete and the performance of the fiber was compared with that of three other presently available fibers. Performance of these fibers was evaluated by comparing the area of plastic shrinkage cracks developed in control slabs (with no fibers) with the crack area of fiber reinforced concrete slabs. Results showed that the new fiber with fiber length of about 18 mm [$\frac{3}{4}$ inch], and a fiber dosage of 0.593 kg/m^3 (1.0 lb/yd^3) was most effective in reducing the plastic shrinkage cracks in concrete, as shown in Figure A.8.



Figure A.8 Typical Plot of Crack Patterns of Test Slabs Without Fibers (*left*) and With 0.3 kg/m^3 (0.5 lbs/yd^3) Monofilament Fibers (*right*) (Ramakrishnan, Zellers and Patnaik et al., 2007)

Research by Qian and Stroeven (2000) shows that short fiber types greatly increase the number of fibers used in the concrete and are typically used to decrease cracking and increase durability, whereas long fibers are used more often to increase mechanical properties of the concrete. Addition of hybrid fibers created synergy in the concrete and lead to similar significant improvements in monofiber-reinforced concrete having the higher total fiber content. A study by Aly et al. (2008) suggests that the addition of polypropylene (PP) macro fibers may have an adverse effect on free shrinkage, increasing it in comparison to free shrinkage of non-fiber concrete mixtures. One explanation is that concrete mixtures that incorporated PP fiber are more permeable and hence are more vulnerable to drying, as evidenced by more moisture lost during the period of drying than companion mixtures without fibers. That effect was noticed to be further amplified in mixtures containing slag.

A.4.3 Testing Methods on Non-Structural Cracking

Non-Structural cracking is mainly caused due to the concrete properties and environmental factors. The concrete mix design needs to be tested for both plastic and drying shrinkage in order to estimate the cracking potential of the mix design.

A.4.3.1 Unrestrained (Free) Shrinkage Test

Tests to measure the unrestrained shrinkage of concrete are widely used and often performed simultaneously with restrained shrinkage tests. Several test methods have been developed, including those that use rectangular and ring-shaped specimens. The most common procedure is described in ASTM C 157, “Standard Test Method for Length Change of Hardened Hydraulic-Cement Mortar and Concrete.” It is a common method to determine the shrinkage by measuring the change in length of hardened concrete prisms that are 75mm × 75mm × 285mm (3 × 3 × 11.25 in) in size. In this test method, rectangular concrete prisms are cast with gage studs at either end. A length comparator is used to measure shrinkage relative to an initial reading. Figures A.9 and A.10 demonstrates the test setup.

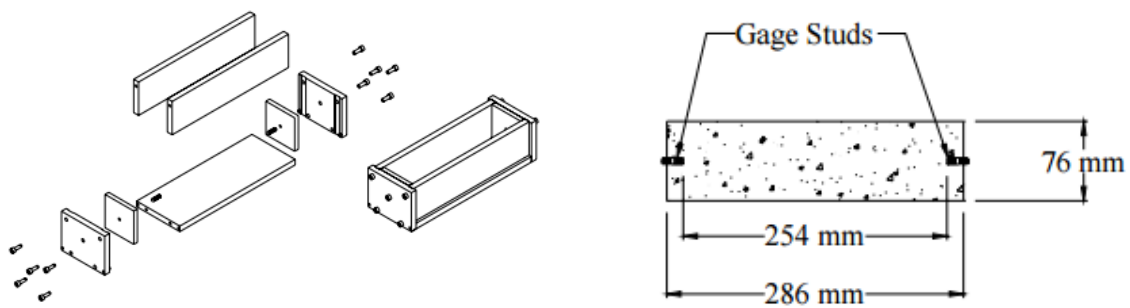


Figure A.9 Free Shrinkage Test Specimen (ASTM C 157)



Figure A.10 Free Shrinkage Test Setup

A.4.3.2 Restrained Shrinkage Tests (Ring Tests)

Over the last few decades, the shrinkage ring test has been frequently used as a testing technique to identify potential cracking risks of certain concrete and mortar mixtures. In the restrained ring test, a concrete ring is cast around an inner steel ring. The steel ring restrains the shrinking concrete, producing an internal pressure on the concrete ring, which causes tensile hoop stresses to develop in the concrete. When the tensile stresses minus the relaxation due to creep exceed the tensile strength of the concrete, cracking will occur. The steel ring can be instrumented to monitor the strain development and determine time to cracking. There are two standard testing procedures based on similar principles: ASTM C1581- 2009 and AASHTO T334-08. The major difference is the concrete thickness. The thickness of the concrete ring specimen for ASTM C1581 is 1.5 in., and the thickness for the AASHTO T334 ring is 3 in., as shown in Figure A.11. Factors such as aggregate source and gradation, aggregate-paste bond, cement type, cement content, water content, mineral admixtures, fibers, and chemical admixtures can be evaluated. The test does not predict concrete cracking in actual service, but rather compares the relative cracking potential of different mixes.

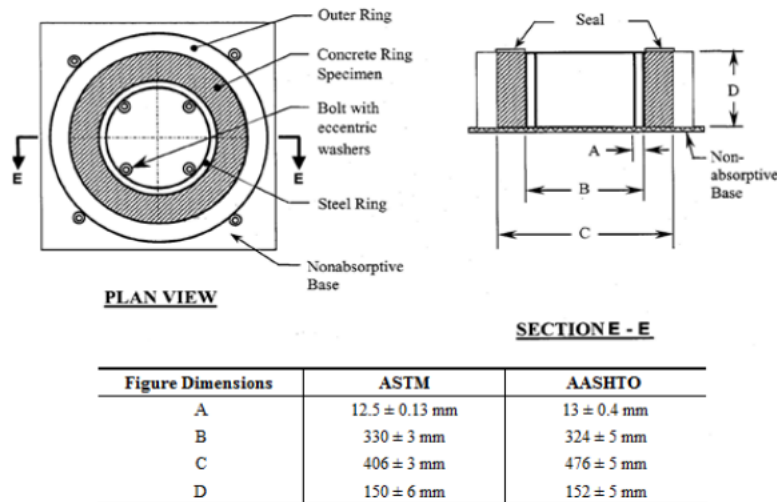


Figure A.11 Ring Test Setup According to Different Standards (AASHTO T334)

A.4.3.3 Plastic Shrinkage (Panel) Test

Kraai (1985) proposed a test to determine the cracking potential due to drying shrinkage of concrete. The test makes use of flat concrete specimens exposed to severe drying conditions, thereby increasing the cracking tendency of the concrete.

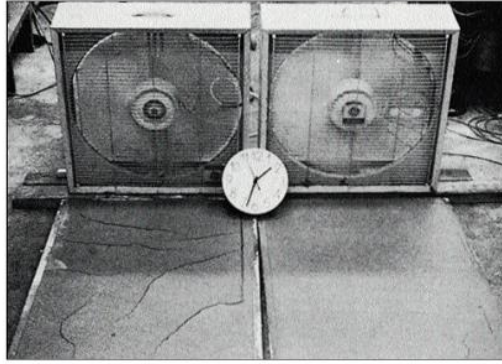


Figure A.12 Panel Test Setup (Kraai, 1985)

The cracking potential in the concrete mix is determined by comparing the cracking of two test panels exposed simultaneously to a set of conditions designed to cause cracking (Figures A.12 and A.13). One panel is a control panel; the other is a similar panel except that a single parameter is altered to study its effect. The second panel could also be made identical in materials but then be subjected to different temperatures or drying conditions. For the control panel, those factors that affect drying shrinkage cracking are chosen that are thought to maximize the amount. In one recent version of the test, the following conditions were applied to the control panel for this purpose: the concrete test panel specimen is only $\frac{3}{4}$ inch in thickness, but the exposed top surface is 2 ft. \times 3 ft. to accelerate the rate of evaporation and shrinkage. Because the thickness of the specimen is only $\frac{3}{4}$ in., no coarse aggregate was used in the panels (Kraai, 1985). The mixes contained 418 kg/m^3 (705 lb/yd^3) of cement and a high water-cement ratio of 0.70. After 24 hours of drying, the concrete panels were inspected and crack lengths and widths were measured. Kraai found that cracking began around one hour after drying was initiated and that most of the cracking occurred within 4 hours (1985).



Figure A.13 Shrinkage Panel Forms (Ramakrishnan, Zellers and Patnaik et al., 2007)

A.4.3.4 Freeze-Thaw Durability of Concrete

One of the most damaging actions affecting concrete is changes in minimum and maximum temperatures (freeze-thaw cycles). There are two main types of deterioration of concrete structures subjected to cyclic freezing and thawing: one is surface scaling (characterized by weight loss) and the other is internal crack growth (characterized by the loss of dynamic modulus of elasticity) (Shang et al., 2013). ASTM test standard C-666 (AASHTO T-161) recommends in detail the test procedures for concrete in freeze-thaw conditions. The test focuses on measuring these two main symptoms of damage experienced by concrete during freezing and thawing. Scaling damage is measured using scales to determine the amount of weight loss, while internal damage is determined using ASTM procedure C215 for fundamental transverse resonant frequency of concrete. Figure A.14 demonstrates the test setup.



Figure A.14 Freeze-Thaw Test Chamber

The test method covers the determination of the resistance of concrete specimens to rapidly repeated cycles of freezing and thawing in the laboratory by two different procedures: rapid freezing and thawing in water (procedure A) and rapid freezing in air and thawing in water (procedure B). Both procedures are intended for use in determining the effects of variations in the properties of concrete on the resistance of the concrete due to the freezing-and-thawing cycles.

The test consists of a suitable chamber in which the specimens may be subjected to the specified freezing-and-thawing cycle, together with the necessary refrigerating and heating equipment and controls to produce continuously, and automatically, reproducible cycles within the

specified temperature requirements. The specimens are arranged such that each specimen is surrounded by between 1 and 3 mm of water at all times. ASTM C666 specifies that the specimens should be subjected to 300 freeze-thaw cycles, with their scaling and freeze-thaw properties measured every 30 cycles.

Balaguru and Ramakrishnan (1986) compared the performance of fiber reinforced concrete (RC) specimens with plain concrete specimens and found that their behavior under freeze-thaw loading is essentially similar. For the same air content, freeze-thaw durability was the same for both plain and fiber reinforced concrete. The research also found an increase in the water absorption after the concretes were subjected to freezing and thawing. That increase is smaller in the case of fiber concretes, indicating that fiber concretes were less permeable both before and after freeze-thaw damage. Figure A.15 compares the performance of fiber-reinforced concrete under freeze-thaw with plain concrete.

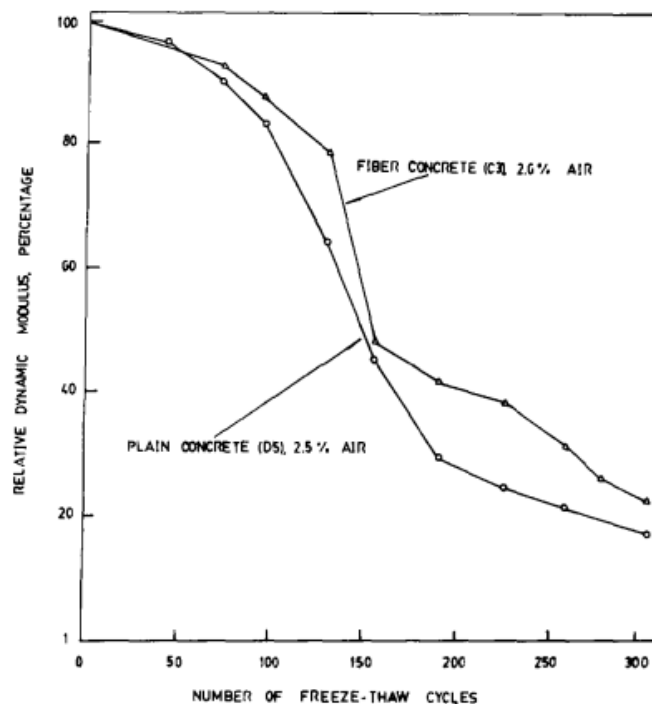


Figure A.15 Comparison of Plain and Fiber Reinforced Concretes Under Freeze-Thaw (Balaguru and Ramakrishnan, 1986)

Berkowski and Kosior-Kazberuk (2015) further studied the effect of diverse types of steel and polypropylene fibers on the surface scaling resistance of concrete subjected to cyclic freezing and thawing in the presence of deicing salt. The test parameters included fiber type and dosage as well as the type of concrete surface subjected to freezing and thawing. Both the cut and cast surfaces of specimens were tested. The dispersed steel reinforcement was found to improve the scaling resistance significantly. However, the effectiveness of fibers was related to their shape and dimensions, with steel fibers showing greater efficiency than polypropylene fibers.

A.5 Literature Review on Structural Cracking

Structural cracking is one of the major problems for on bridge decks. These cracks are much wider compared to those of non-structural cracking, and they act as pathways to allow de-icing salts to penetrate the bridge deck, causing further damage to the structure. Numerous factors causing these cracks including reinforcement detailing, bond of concrete and steel, concrete quality, diameter of rebar, concrete cover, loading conditions, and design errors. These cracks form over the negative moment regions and widen over time due to several factors as discussed in the following section. Controlling structural cracking is a vital task, as it involves many factors. An approach to minimize structural cracking is being investigated in this project.

A.5.1 Factors Causing Widening of Cracks on Bridge Decks

Cracks that are formed due to various reasons can widen over time. Studying the widening of crack widths on bridge decks is an important factor to be considered for the durability and service life of bridges. The factors that cause the widening of cracks over time include a sustained load (i.e., the dead load of the bridge deck), dynamic effects due to traffic, repeated action of freeze and thaw cycles and corrosion of reinforcing bars.

- Sustained loading: Structural slab bridges have thick deck slabs that are typically connected to pier caps. These bridges have large dead loads due to self-weight that are constantly acting. Over time, the crack widths on these bridges can widen due to creep effect. It has been reported that tests performed by having a constant sustained load showed a doubling of crack widths (ACI-224R-01). Under the action of sustained loading, the crack spacing remains unchanged over time (Nilson, 2010).
- Dynamic loading: Traffic on bridges is an important factor when considering cracking on bridge decks. Dynamic load due to traffic volume causes cracks to open and close at a regular frequency, resulting in permanent widening over time. Cyclic loading causes the reinforcement bars to slip from the surrounding concrete at the location of the crack, leading to expansion of cracks (Soltani, 2010). These cracks not only widen over time but also penetrate more deeply into the deck slab.
- Bond of reinforcing bar with concrete: Failure of bond between the reinforcement and the surrounding concrete is a major parameter resulting in extreme cracking on bridge decks. Once the bond fails, stresses are no longer transferred from the steel to the concrete. It is important to study the bond behavior of corrosion-resistant bars, as most of these bars are convention black steel bars with some kind of epoxy or metal coating.
- Freeze-thaw action: For bridges in states where temperature fluctuations are predominant, the durability of bridge decks becomes a major concern. Ohio is one such state, and cracks on structural slab bridges widen under the action of freezing and thawing. During the freeze cycle, the water in the cracks form into ice, expanding the crack widths; during the thaw cycle, the ice converts back to water or evaporates. These repeated cycles over time cause a permanent increase in crack widths. Air content in the concrete mix can also affect the durability of concrete under the freeze and thaw action.

A.5.2 Control of Crack Widths

Limiting the crack widths on bridge decks will improve the durability and increase their service life. Adopting better construction materials, construction practices, and proper curing procedures would reduce initial cracking. Usage of corrosion-resistant bars can reduce cracks that are formed during the corrosion of reinforcement inside the concrete due to the ingress of deicing salts. Usage of fiber reinforced concrete would also reduce structural cracks and crack widths, thereby reducing the further damage due to cracks.

Design considerations that use smaller diameter bars with closer spacing have an impact on cracking. Several researchers have developed equations for crack width predictions as well as suggested limiting the spacing of reinforcing bars; these are summarized in Table A.3. Several code provisions have been recommended to control cracking, including ACI-318-11, AASHTO, CEB/FIP, Australia AS 3600, and Eurocode EC2. These approaches were discussed in detail in the report by Patnaik and Baah (2015).

Several researchers have developed equations for predicting crack widths in reinforced concrete by using different approaches. Some approaches used experimental data and a few used analytical approaches to propose equations. A review of equations in predicting flexural crack widths and spacing is summarized in Tables A.3, A.4 and A.5. These equations were based on parameters such as concrete strength, reinforcement ratio, concrete cover, stress in the bar, and other factors.

Table A.3 Crack Width Prediction Formulas from Various Codes

No.	Code	Formula
1	CEB-FIP(1978) & NZS 3101 (1982)	$w_{\max} = 1.7 \left[2 \left(c + \frac{s}{10} \right) + a_1 a_2 \frac{db}{\rho_r} \right] \frac{f_s}{E_s} \left[1 - b_1 b_2 \left(\frac{f_{sr}}{f_s} \right)^2 \right]$
2	AASHTO (1996) & UBC (1997)	$w_{\max} = \left[10,86 \sqrt[3]{A t_b f_s} \frac{h_2}{h_1} \right] 10^{-6}$
3	SNI 03-2847-2002 ACI 318-99 (1999)	$w_{\max} = 11.10^{-6} \beta f_s \sqrt[3]{d_c A} \leq 0,30$
4	AS 3600 (2000)	$w_{\max} = \frac{d_b f_s}{2 \tau_m (1 + n \rho_s)} \frac{1}{2 E_s} \frac{f_s}{E_s}$
5	EC-2 (2000)	$w_{\max} = 1,7 \left(50 + k_1 k_2 \frac{db}{4 \rho_c} \right) \frac{f_s}{E_s} \left[1 - \beta_1 \beta_2 \left(\frac{f_{sr}}{f_s} \right)^2 \right]$

Source: Rasidi et al. (2013).

Table A.4 Empirical Equations for Crack Width Prediction Proposed by Various Researchers

No.	Investigator	Proposed Formula
1	Chi & Kirstein (1958)	$w_{\max} = \frac{5\tau\phi}{E_s} \left(f_s - \frac{438}{\tau\phi} \right)$
2	Broms (1965b)	$w_{\max} = 2 c \varepsilon_{s,ave}$
3	Broms & Lutz (1965)	$w_{\max} = 4 c_f \varepsilon_{s,ave}$
4	Venkateswarlu & Gesund (1972)	$w_{\max} = \frac{2.4 \times 10^{-5} \phi (1462 - f_s) f_s}{1 + n\rho_m (662 - f_s)}$
5	Oh & Kang (1987)	$w_{\max} = \{159 (\phi_1)^{4.5} + 2.83(\phi_2)^{1/2}\} + (\varepsilon_s - 0.0002)\phi_2$
6	Beeby (1979)	$w_{\max} = \frac{3 a_{cr} \varepsilon_m}{\left(1 + 2 \frac{(a_{cr} - c)}{(h - x)}\right)}$
7	Watstein, Parsons & Clark (1956)	$w_{\max} = 1.29 \times 10^{-6} \left(\frac{h-d}{d}\right) \frac{\phi}{\rho} [2.56 f_s - 1\rho + 8]$
8	Kaar & Mattock (1963)	$w_{\max} = 1.57 \times 10^{-5} f_s \sqrt{A_e}$
9	Gergely & Lutz (1968)	$w_{\max} = \left[10.86 \sqrt{A_t} t_b f_s \frac{h_2}{h_1}\right] 10^{-6}$
10	Lan & Ding (1992)	$w_{\max} = 1.41 (2.7 c + 0.11 \phi / \rho_{te}) v \varepsilon_s \psi$
11	Chowdhury & Loo (2001)	$w_{\max} = 0.9 \varepsilon_s (c - s_b) + 0.1 \left(\frac{\phi}{\rho}\right)$
12	Ferry & Borges (1966)	$w_{\max} = \frac{1.70}{E_s} \left(1.5c + \frac{0.04 db}{\rho_w}\right) \left(f_s - \frac{0.75}{\rho_w}\right)$
13	Vis & Sagel (1987)	$w_{\max} = 0.2 \frac{ft' db}{\mu \rho_e} f_s 10^{-5}$
14	Hughes & Cifuentes (1988)	$w_{\max} = 0.25 \frac{ft db (1 + n\rho_c)}{\mu \rho_c (1 + 2n\rho_c) E_s} f_s$
15	Rao & Dilger (1993)	$w_{\max} = 2.55 \cdot 10^{-6} f_s dc \left(\frac{At}{As}\right)^{0.5}$
16	Balazs (1993)	$w_{\max} = 0.4 \left[\frac{d_b f_s^2}{\sqrt{f'_c} E_s}\right]^{1/1.4}$
17	Beeby & Narayanan (2000)	$w_{\max} = 1.7 \left(50 + k_1 k_2 \frac{db}{4 \rho_c}\right) \frac{f_s}{E_s} \left[1 - \beta_1 \beta_2 f_s r f_s^2\right]$
18	Padmarajaiah & Ramaswamy (2001)	$w_{\max} = \frac{(D - x) 4 A_{ef} k_t \sigma_t f_s}{(d - x) k_b f_{bu} \sum \pi d E_s}$

Source: Rasidi et al. (2013).

Table A.5 Crack Spacing Equations Proposed by Various Researchers

Formula for average crack spacing (s_{rm})	Generalised form of formula	Proposed by
$s_{rm} = \kappa c$	$s_{rm} = A_1 c$	Broms and Lutz ¹⁶
$s_{rm} = 2 \left(c + \frac{\phi_s}{2} \right)$	$s_{rm} = A_1 c + A_2 \phi_s$	Broms ¹⁷
$s_{rm} = 50 + \kappa s$	$s_{rm} = A_1 + A_2 s$	Janovic and Kupfer ⁸
$s_{rm} = 50 + 0.637(s) \frac{d}{25}$	$s_{rm} = A_1 + A_2 s$	Janovic and Kupfer ¹⁸
$s_{rm} = \frac{4}{3} [50 + 1.5 \kappa \times s]$	$s_{rm} = A_1 + A_2 s$	Jaccoud ¹⁹
$s_{rm} = k [4c + 0.7(s - \phi_s)]$	$s_{rm} = A_1 c + A_2 s + A_3 \phi_s$	JSCE ²⁰
$s_{rm} = \frac{2}{3} \times \frac{\phi_s}{3 \cdot 6 \rho_{ef}}$	$s_{rm} = A_1 \frac{\phi_s}{\rho_{ef}}$	CEB-FIP Model Code 1990 ⁴
$s_{rm} = 0.157 \frac{\phi_s f_{cm}}{4 \rho_{rbm}}$	$s_{rm} = A_1 \frac{\phi_s}{\rho_{ef}}$	Saliger ²¹
$s_{rm} = 50 + 0.25 k_1 k_2 \frac{\phi_s}{\rho_{ef}}$	$s_{rm} = A_1 + A_2 \frac{\phi_s}{\rho_{ef}}$	Eurocode 2 ³
$s_{rm} = \frac{1}{1.7} \left(30 + \frac{\phi_s}{4 \rho_{ef}} \right)$	$s_{rm} = A_1 + A_2 \frac{\phi_s}{\rho_{ef}}$	Fehling and König ²²
$s_{rm} = 1.5c + 0.12 \frac{\phi_s}{\rho_{ef}}$	$s_{rm} = A_1 c + A_2 \frac{\phi_s}{\rho_{ef}}$	Farra and Jaccoud ²³
$s_{rm} = \kappa_1 c + \kappa_2 \frac{\phi_s}{\rho_{ef}}$	$s_{rm} = A_1 c + A_2 \frac{\phi_s}{\rho_{ef}}$	Ferry-Borges ²⁴
$s_{rm} = k_1 c + 0.25 k_2 k_3 \frac{\phi_s}{\rho_{ef}}$	$s_{rm} = A_1 c + A_2 \frac{\phi_s}{\rho_{ef}}$	Braam ²⁵
$s_{rm} = 3.5c + k_w \frac{\phi_s}{\rho_{ef}}$	$s_{rm} = A_1 c + A_2 \frac{\phi_s}{\rho_{ef}}$	Ålander ²⁶
$s_{rm} = \frac{3\phi_s}{k} \left(1 + \frac{1}{10\rho_{ef}} \right)$	$s_{rm} = A_1 \phi_s + A_2 \frac{\phi_s}{\rho_{ef}}$	Brice ²⁷
$s_{rm} = 2 \left(c + \frac{s}{10} \right) + \kappa_1 \kappa_2 \frac{\phi_s}{\rho_{ef}}$	$s_{rm} = A_1 c + A_2 s + A_3 \frac{\phi_s}{\rho_{ef}}$	CEB-FIP Model Code 1978 ²⁸
$s_{rm} = 2 \left(c + \frac{s}{10} \right) + 0.1 \frac{\phi_s}{\rho_{ef}}$	$s_{rm} = A_1 c + A_2 s + A_3 \frac{\phi_s}{\rho_{ef}}$	AU ²⁹
$s_{rm} = 2 \left(c + \frac{s}{10} \right) + k \frac{\phi_s}{10\rho_{ef}}$	$s_{rm} = A_1 c + A_2 s + A_3 \frac{\phi_s}{\rho_{ef}}$	Menn ³⁰
$s_{rm} = 1.65 + 0.56 \sqrt{c \frac{A_{c,ef}}{\sum \phi_s}}$	$s_{rm} = A_1 + f(c; \phi_s)$	Holmberg ³¹
$s_{rm} = 5(\phi_s - 7.2) + 0.08 \frac{\phi_s}{\rho_{ef}} + K_1(c; s)$	$s_{rm} = A_1 + A_2 \phi_s + A_3 \frac{\phi_s}{\rho_{ef}} + f(c; s)$	Leonhardt ³²
$s_{rm} = 3.1 \times k \left(\frac{(0.22 f_{ctm}/\rho)^{0.88}}{f_{ctm}^{0.66}} \phi_s \right)^{0.89}$	$s_{rm} = f(\rho; f_{ctm}; \phi_s)$	Noakowski ¹⁰
$s_{rm} = \frac{1}{2} \frac{\sigma_s}{\alpha \alpha_{c1}} \phi_s$	$s_{rm} = f(\sigma_s; f_{ctm}; \phi_s)$	Jankó ³³
$s_{rm} = 2 \left[d + A c h^{-1} \sqrt{\frac{\sigma_s}{\sigma_s - (f_{ctm}/\rho_{ef})}} \right]$	$s_{rm} = f(\sigma_s; f_{ctm}; \rho_{ef})$	Bernardi <i>et al.</i> ³⁴
$\frac{s_{rm}}{\phi} = 25.7 \left(\frac{h-d}{h-x_2} \right)^{4.5} + 1.66 \left(\frac{1}{n} \frac{A_{c,ef}}{A_s} \right)^{1/3} + \frac{0.236 \cdot 10^{-6}}{\epsilon_s^2}$	-	Oh and Kang ³⁵

Source: Borosnyoi and Balazs (2005).

A.5.3 Test Methods Adopted for Structural Crack Studies

Several researches have conducted studies to investigate cracking behavior of reinforced concrete structures and developed the empirical equations as discussed above. These experiments include direct tension testing, flexural testing, pullout strength of bars embedded in concrete, fatigue performance of reinforced concrete members, and investigating the effects of the connection between slabs and piers in bridge decks.

A.5.3.1 Direct Tension Testing of RC Structures

Two types of cracks in RC are usually formed: visible cracks that propagate to the surface (*primary cracks*) and invisible cracks that typically form near the bonded surface of the steel and concrete (*secondary cracks*) (Broms, 1965). Primary cracks are wider near the surface and narrower at the steel level (Goto, 1971). Since the tensile properties of concrete vary over the length of a RC member, the bond integrity of the bar tends to cause variations in crack spacing, as shown in Figure A.16.

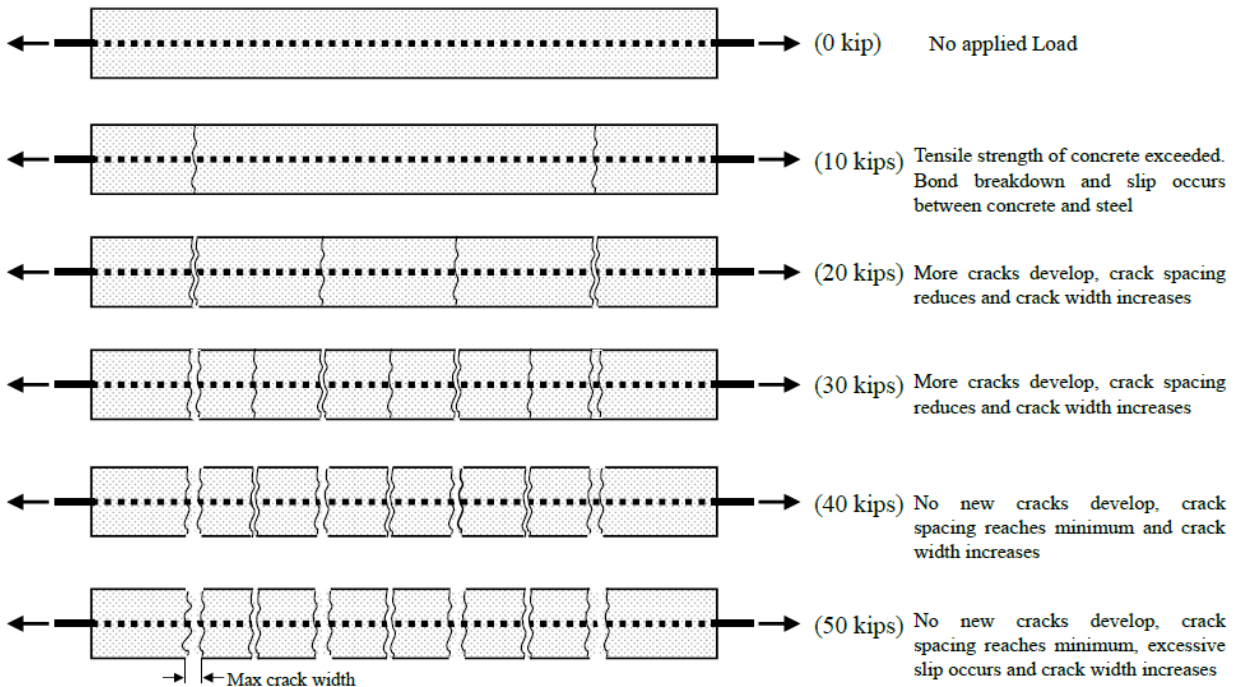


Figure A.16 Typical Cracking Mechanism in Direct Tension Test Specimens (Source: Baah and Patnaik, et, al. 2015)

Mimura et al. (2011) conducted a study on uniaxial tension test of early age slender reinforced concrete members. Specimens with dimensions $100 \times 100 \times 1560$ mm embedded with a reinforcing bar in the center of a section with #4 bar as shown in Figure A.17. Strain gages were attached over the bar through-out the length of the member to monitor the strain distribution in the section over the length of the member.

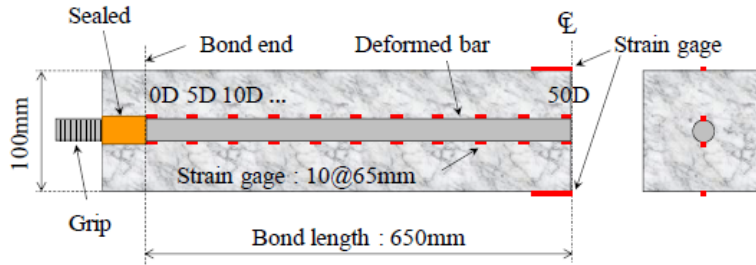


Figure A.17 Specimen for Uniaxial Tension Testing (Mimura, 2011)

The ends of the rebar were attached to the loading jig. The loading was applied manually and measured using a load cell of 100 kN. The tensile force was applied at a rate of 0.1 kN/s approximately. A maximum load of 35.1 kN, was applied, where the behavior of yielded bar was not included. Figure A.18 shows the test setup of uniaxial tension test.

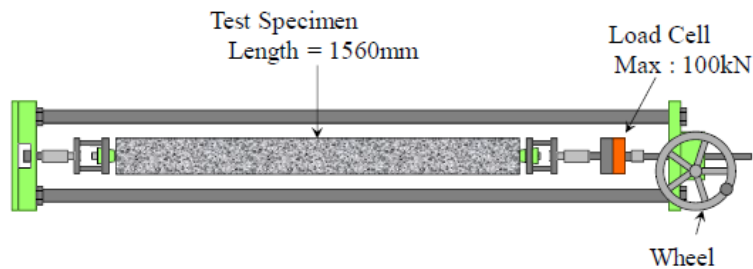


Figure A.18 Test Setup For Uniaxial Tension Test (Mimura, 2011)

It was observed that the strain distribution in the member was more uniform in the mid region whereas at the ends, it was more near the steel and less on the surface. Figure A.19 shows the strain distribution in the cross section of the member.

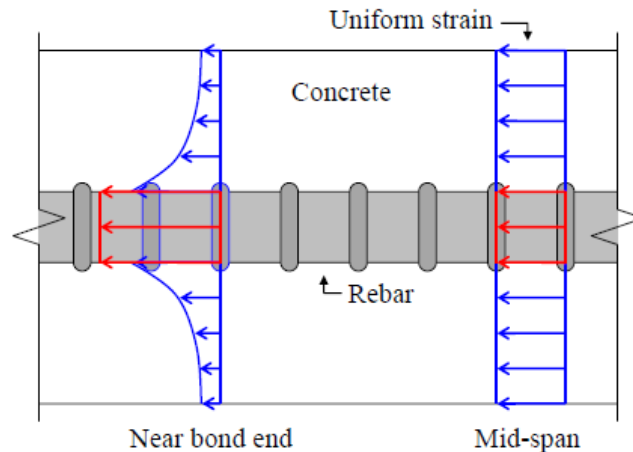


Figure A.19 Strain Distribution in Cross Section of Member (Mimura, 2011)

In addition, bond stress–slip relation was developed based on the age of concrete of 1 day, 1.5 days as shown in Figure A.20. The relationship for mature concrete can be predicted by the following relation:

$$\frac{\tau}{f_c^{1/3}} = \frac{a \cdot Z/D}{\frac{Z}{D} + b} \dots\dots\dots (1)$$

where a and b are coefficients of the regression curve. The coefficient a is 0.39 (1 day), 0.7 (1.5 days), and 0.9 (after 2 days); the coefficient b is a constant 0.12.

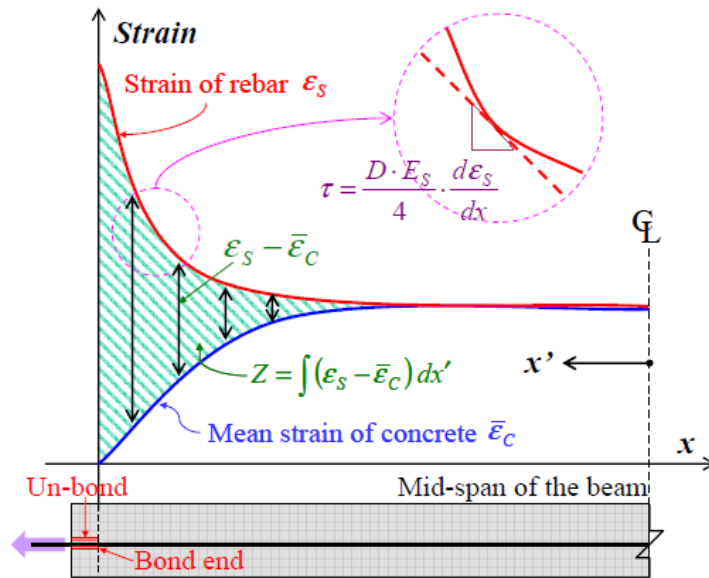


Figure A.20 Definition of Slip and Bond Stress (Mimura, 2011)

It was observed that the tensile stress–strain response of early age concrete was linear. The empirical equation for mature concrete could be applied to the relationship between uniaxial tensile strength and splitting tensile strength. Bond behavior after 2 days is uniform so the empirical equation could be applied.

Soltani et al. (2013) investigated the crack opening behavior of concrete reinforced with high strength steel. Concrete members reinforced with high strength steel reinforcement ($f_y > 100$ ksi) were found to have different behavior due to the expectedly higher service loads as compared to concrete members with conventional steel bars ($f_y = 60$ ksi).

Currently, ACI-318-14 permits the use of steel with a yield strength not exceeding 80 ksi, whereas AASHTO LRFD Bridge Design Specifications (AASHTO, 2010) limits the use of reinforcing steel with yield strength no less than 60 ksi and not more than 75 ksi. This limit on yield strength also serves to control crack widths at service loads. Cracks in the first stage are usually formed when the stress in the steel is below 14 ksi. Cracks in the second stage result from the difference in the bonding forces that exists between the steel and concrete. The third stage is referred to as the *equilibrium stage*, where the steel stresses are greater than 30 ksi and where cracks will widen on further loading.

Control of crack widths and spacing is most important for the overall performance of a member. The numerous factors that influence the cracking include reinforcement stress, bond characteristics of steel, distribution of area subjected to tension, diameter of the bar, concrete cover and the concrete strength.

Frosch (2001) developed a physical model to predict crack width, w_c :

$$w_c = 2 \frac{f_s}{E_s} \beta \sqrt{(d_c^2 + (s/2)^2)} \dots \dots \dots (2)$$

Where f_s is the stress in the steel, E_s is the modulus of elasticity of steel, $\beta = 1+0.08d_c$, where d_c is the distance from the tension face to the centroid of the nearest reinforcing bar and s is the spacing between the bars. Tension stiffening in axial members is not quite the same as that in flexural members due to curvature (Ng et al., 2010). The decrease of relative displacement along the transmission length L_t is characterized by the difference between the steel (ϵ_s) and concrete (ϵ_c) strains.

$$\frac{ds}{dx} = \epsilon_s - \epsilon_c \dots \dots \dots (3)$$

If the stress and strain relationship was assumed linear and the concrete has not developed any cracks, the total tension force can be written as

$$T = A_s f_{s0} = A_s E_s \epsilon_s(x) + A_c E_c \epsilon_c(x) \dots \dots \dots (4)$$

$$\text{Where } 0 \leq x \leq L/2 \dots \dots \dots (5)$$

where L is the adequate development length of full bond stress. At a distance L_1 , the reinforcement and concrete have the same strain $\epsilon_s = \epsilon_c = \epsilon_2$. In the no slip region, the applied tension force is distributed in proportion to the stiffness of the effective concrete and reinforcement and the bond stress is equal to zero.

$$T = A_s f_{s0} = (A_s E_s + A_c E_c) \epsilon_2(x) \dots \dots \dots (6)$$

$$\text{Where } L_1 \leq x \leq L/2 \dots \dots \dots (7)$$

To obtain the value of L_1 and ϵ_2 , an additional relationship is required. Considering equilibrium on either side of a crack

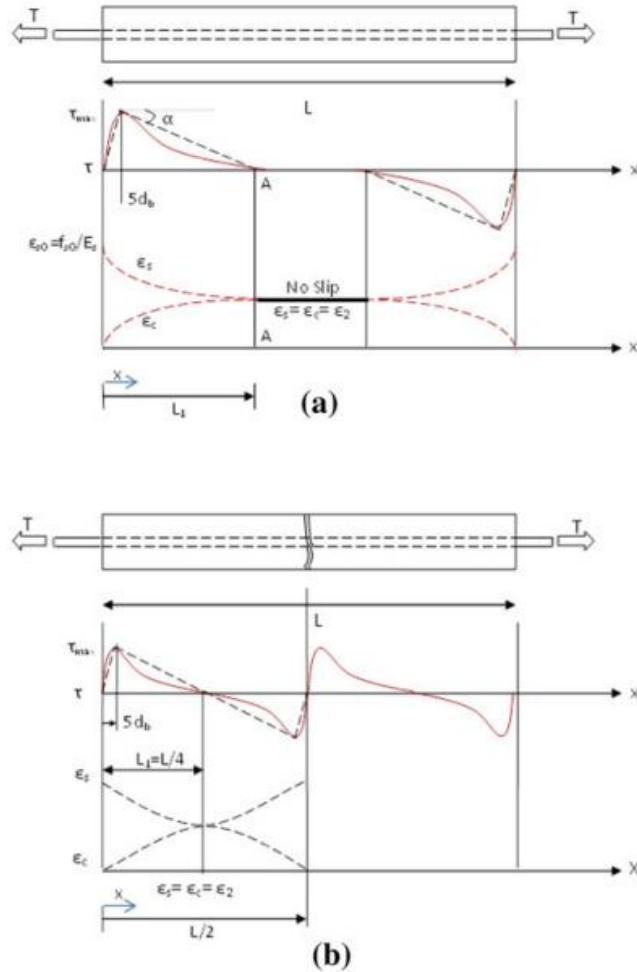


Figure A.21 (a) Bond Stress and Resulting Steel and Concrete Strain Distribution before Cracking. (b) No Additional Cracks Developed after the First Series of Cracks at the Tension Load T_1 (Soltani et al., 2013)

$$T(x) = T - \int_0^x \tau(x) p dx \dots\dots\dots (8)$$

Where $\tau(x)$ is the bond stress distribution along the length of the bar and p is the bar circumference assumed constant along the length of the bar. Therefore, at length L_1 :

$$T(L_1) = \epsilon_2 E_s A_s = f_{s0} A_s - \int_0^{L_1} \tau(x) p dx \dots\dots\dots (9)$$

The total force that is transmitted from the reinforcement to the concrete is calculated for crack development in a member.

$$T_c = f_c A_c = E_c \epsilon_2 A_c = \int_0^{L_1} \tau(x) p dx \dots\dots\dots (10)$$

If L_l is sufficiently long to transfer a cumulative tensile stress resulting in a concrete stress, f_c , greater than ultimate tension capacity of concrete f_{cr}

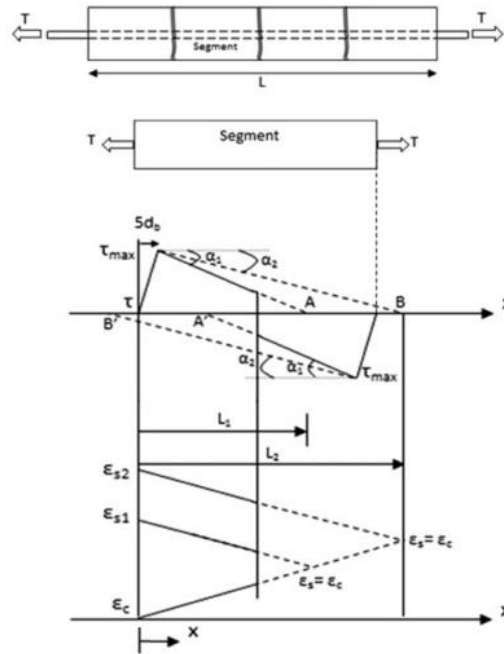


Figure A.22 Bond Stress, Steel and Concrete Strain Distribution between Adjacent Cracks in a Reinforced Concrete Member (Soltani et al., 2013)

Average crack width derived from the analysis was w_{avg} , using the slip-strain relationship.

$$w_{avg} = 2 \int_0^{s/2} (\epsilon_s - \epsilon_c) dx \dots\dots\dots (11)$$

Various reinforcement ratios, ranging from 0.02 to 0.0035 with #4, #6, #8 and #10 bars were considered. The total length of the prism was 200 inches. The specimens were loaded uniaxial to investigate the crack spacing and the crack widths corresponding to bar stress.

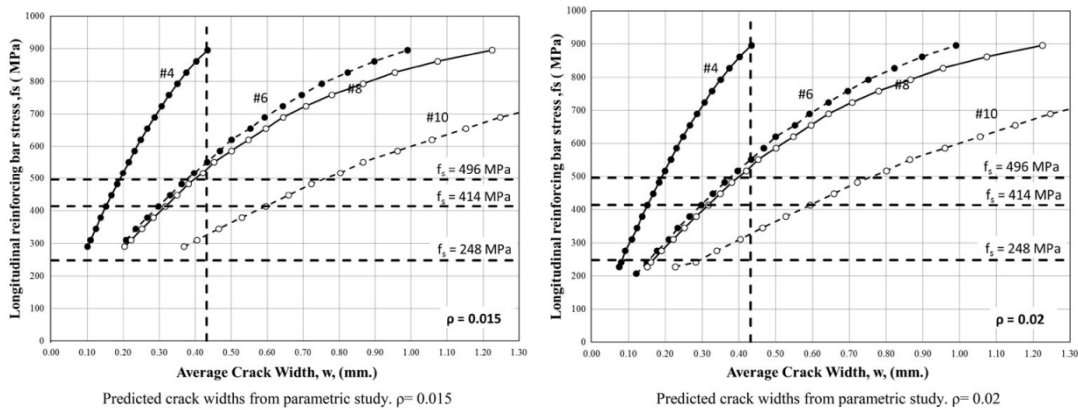


Figure A.23 Average Crack Widths Corresponding to Bar Stress for Reinforcement Ratios of 0.015 and 0.02 (Soltani et al., 2013)

A.5.3.2 Flexure Testing of RC Members

Reinforced concrete beams or slabs tend to crack once the extreme tensile stresses of concrete reach the f_t' (tensile strength of concrete). However, the crack spacing and crack widths depend on numerous factors. The indirect way of controlling cracking is to limit the spacing of the bars (ACI 318, 1999), which replaced the traditional z-factor method. Crack widths depend on stresses in the bar, the concrete cover, bond between the reinforcement and the surrounding concrete, bar diameter and spacing, etc. as shown in Figure A.24.

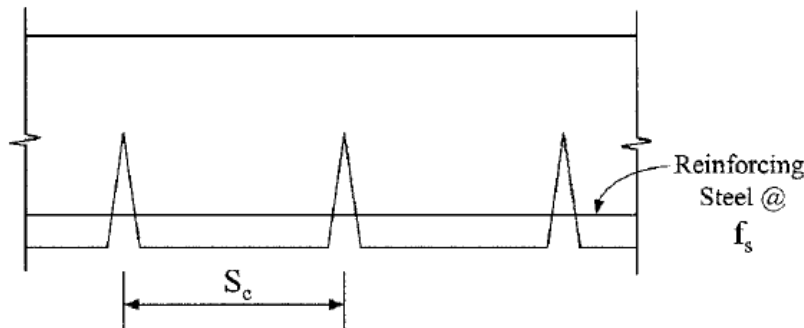


Figure A.24 Cracked Flexure Member

Gergely and Lutz (1968) performed a statistical evaluation of experimental cracking data to develop an equation to predict crack widths. Several crack measurements according to different sections were used to develop the equation. The adequacy of the Gergely and Lutz model to members with large concrete covers was a concern. A new crack control procedure that was based on the work of Frosh (1999) was developed and which was based on the crack control concept introduced by Broms (1965). The crack width at the tension face of the concrete member was given by:

$$w = 2 \frac{f_r}{E_r} \beta k_b \sqrt{(d_c^2 + (s/2)^2)} \dots \dots \dots (12)$$

where f_r , is the reinforcing bar stress, E_r is the modulus of elasticity of material, β is the ratio of the distance from neutral axis to the tension face of the member to the distance of the neutral axis to the centroid of the tensile steel; d_c is the effective concrete cover; s is the bar spacing; and k_b is the bond coefficient. Other investigations have developed similar crack width equations (Karr and Mattock, 1963), similar to that of Gergely and Lutz equation (Gergely and Lutz, 1968):

$$w_b = 0.155 \beta f_s^4 \sqrt{A} \dots \dots \dots (13)$$

Where A is the area of the concrete surrounding the reinforcing steel, and f_s is the stress in the bar. Also β , is given by the following equation

$$\beta = \frac{h-c}{d-c} \dots \dots \dots (14)$$

Where h is the total depth of the section, d is the effective depth and c is the depth of neutral axis. Crack spacing decreases with an increase in applied load, and it stabilizes once the stresses reach a critical stress. A further increase in stress will cause the cracks to widen. The critical stress range for covers up to 3 inches was found to be between 20 to 30 ksi, thus developing a stable crack pattern under service loads. The controlling crack spacing of a section is shown in Figure A.25. From analytical and experimental investigations by Broms (1965), it was found that crack spacing depends on the maximum concrete cover. It was also found that maximum theoretical crack spacing is twice the minimum. The crack spacing as per Broms was calculated as follows:

$$S_c = \Psi_s d^* \dots\dots\dots (15)$$

Where S_c is the crack spacing, d^* is the controlling cover distance and Ψ_s is crack spacing factor (1 = minimum, 1.5 = average, 2 = maximum).

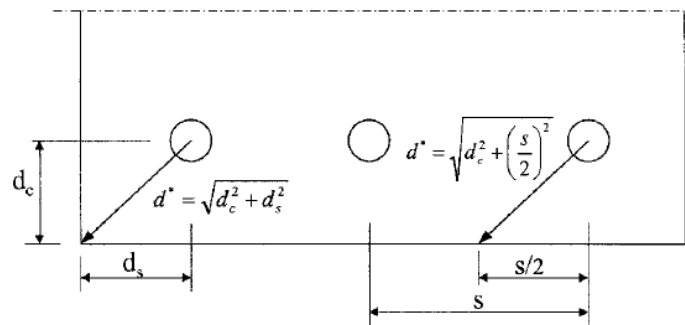


Figure A.25 Controlling Crack Spacing

Based on the previous research studies and by comparing various crack width predictive models, an equation very similar to the Frosch cracking model was also adopted by AASHTO. The following modifications were made to ACI 318 equation in developing the AASHTO equation for crack control:

- Crack widths were limited to approximately 0.017 inches instead of 0.016 inches.
- An exposure factor of γ_e was incorporated to maintain a distinction between different environmental conditions.
- A reinforcement factor of γ_r was incorporated to recognize the fact that research suggests smooth welded – wire fabric had reduced bond properties, most notably for wider wire spacing’s as compared to those in other types of reinforcement.
- The β -factor is an integral part of the equation rather an assumed average value.
- The d_c term is retained in the formal development of the cracking model instead of using a cover with an assumed average rebar size of #8.

Sim and Frosch (2014) performed experimentation to study the cracking performance of slabs with varying bar spacings. Three sections were designed with #5 reinforcing bars with slab width 36 inches and 8 inches deep. The cross-sectional details are shown in Figure A.26.

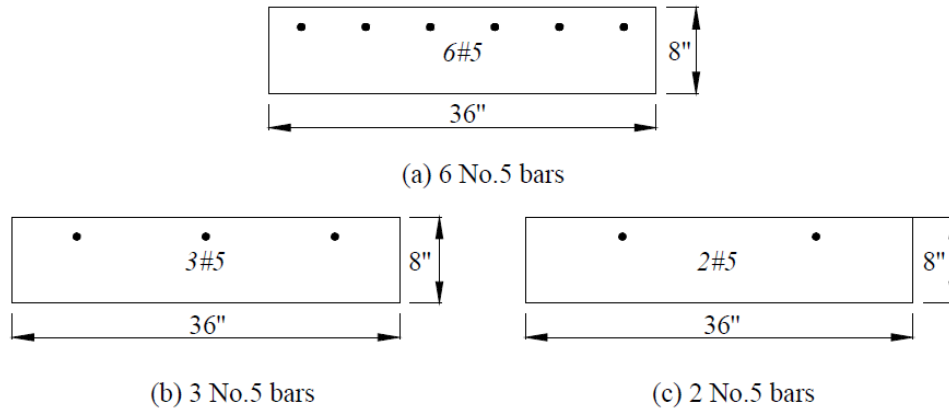


Figure A.26 Cross-Sectional Details for Slabs

The total length of the slab was 16 ft., with a constant moment region of 8 ft. was provided to develop sufficient number of cracks. Loading was applied 2 ft. from the supports to develop tension cracking at the top surface of the constant moment region as shown in Figure A.27.

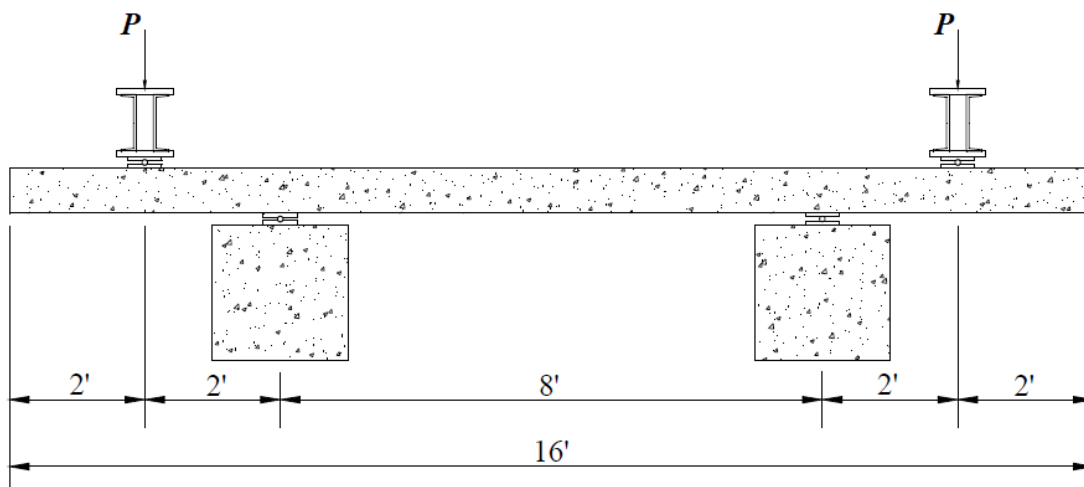


Figure A.27 Slab Specimen Test Setup (Sim and Frosch, 2014)

Crack performance of the various reinforcement type which include, black, epoxy, zinc clad 1, Zbar, MMFX II, stainless steel Duplex 2205, Stainless steel XM-28 were investigated. Concrete mix used had a targeted strength of 4000 psi, and the slabs were cast with reinforcement layouts of 6 inch, 12 inches and 18 inches bar spacing.

A roller support was obtained by placing a 1-inch diameter and 36-inch long steel rod between a flat steel plate that was 0.5 in. \times 12 in. \times 36 in., while pin support was obtained by placing a 1-inch-diameter and 36-in.-long steel rod between 0.75 in. \times 12 in. \times 36 in. steel plates that were grooved 0.25 inches. Loading was applied at two-kip intervals, and the deflections were recorded using the linear variable differential transformers and the data acquisition system. Cracks were monitored and mapped manually during the testing as shown in Figure A.28.

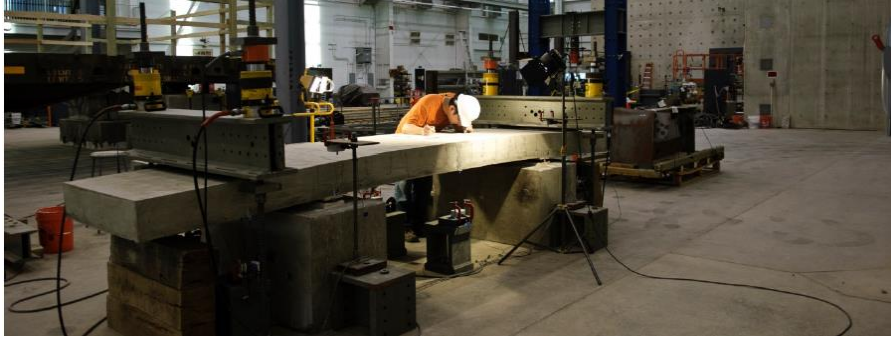


Figure A.28 Measuring Crack Widths on the Slab during the Testing (Sim and Frosch, 2014)

It was observed that primary cracks developed in the constant moment region and subsequently increased with load. After certain load limit, the development of primary cracks was stopped and the crack widths increase thereafter. The critical stress range has been previously reported to be approximately 20–30 ksi with cover thicknesses ranging from 1.25 to 3.0 in. and about 50 ksi at a thickness of 6 in., according to Broms (1965a). A typical crack pattern mapped during the testing is shown in Figure A.29.



Figure A.29 Cracks Developed in the Constant Moment Region of the Slab

The relation of crack width with bar spacing was studied and plots were developed for a typical crack width versus bar stress plotted for slab with bars spaced at 12 inches, as shown in Figure A.30.

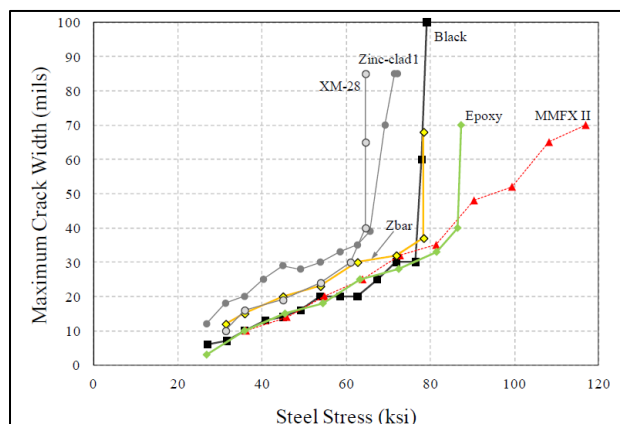


Figure A.30 Maximum Crack Width Versus Stress in the Bar for Slabs with 12-inch Bar Spacing (Sim and Frosch, 2014)

A.5.3.3 Pullout strength of reinforcing bar embedded in concrete

The bond between steel and concrete is an important parameter that helps in transferring the stresses. A weaker bond indicates loss in stresses, causing the bar to pull out from the concrete. Bond resistance differs based on the type and size of bar, along with concrete mix design properties (Bajaj et al., 2012).

Resistance to bond between steel and concrete is mainly due to the following factors:

- Chemical Adhesion
- Friction
- Mechanical interlock
- Gripping effect
- Anchoring effects
- The diameter, shape and spacing of the bars

A.5.3.4 Bond Mechanism of steel in Concrete

The reinforcing bar in a concrete member tends to slip under the application of external load due to weaker bonding, and this slippage is prevented by mechanical interlock and chemical adhesion between the rebar and concrete. The chemical adhesion between concrete and steel will break beyond certain load. The movement of the bar is then resisted by bearing of the ribs against concrete key, which is the concrete between the ribs of the reinforcing bar (Bajaj et al., 2012), as shown in Figure A.31.

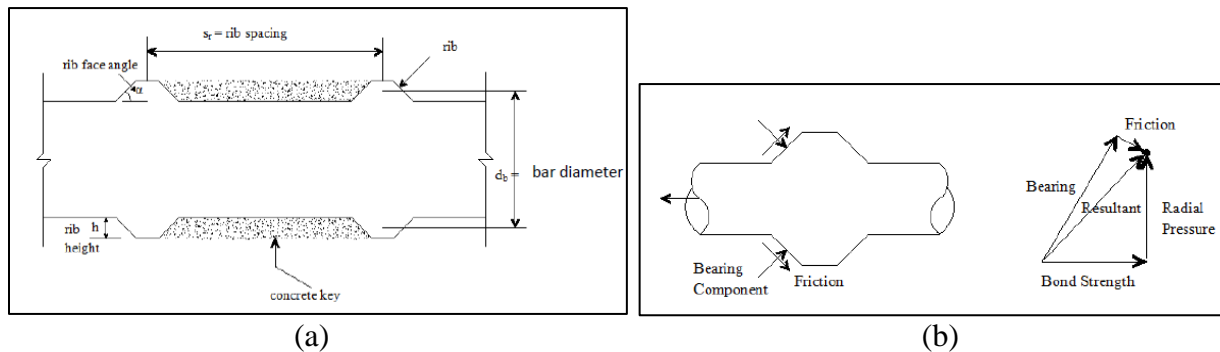


Figure A.31 (a) Geometry of Deformed Bar; (b) Force Distribution in RC Member during Pullout Test (Bajaj, 2012)

As a result of bearing forces applied by the ribs of the bar, the concrete cover splits. Sliding of the bar is also prevented by frictional forces developed at the interface of steel and concrete. The forces acting on the bar during the pullout test are shown in Figure A.31(b).

Epoxy-coated bars are commonly used in concrete applications where corrosion of reinforcing bars is a concern. Various studies performed by Treece and Jirsa (1989) and Cleary and Ramirez (1991) showed a bond strength due to epoxy coating of about 65% to 90% of bond strength as compared to that of conventional black steel.

Based on literature on epoxy-coated bars, the following conclusions can be drawn (Treece and Jirsa, 1989; Cleary and Ramirez, 1991):

- Epoxy coating reduces the bond strength, and the amount of the reduction depends on the type of failure
- Use of epoxy-coated bars resulted in wider crack widths
- In the ACI building code, for anchorage of epoxy-coated reinforcement, a cover-to-diameter ratio of 3 was considered as the transition point from pullout failure to splitting failure

A.5.3.5 Bond Strength Equations

Bond strength between the reinforcing bar and concrete depends on the diameter of the bar, concrete cover and concrete material properties. Bond strength is usually uniformly distributed for short embedment lengths (ACI, 1966, ACI Structural Journal, 1995). According to the many researchers the following equations were devised for short embedment lengths as presented in Table A.6.

Table A.6 Bond Strength Equations Developed by Various Researchers

Serial #	Researcher	Equation for Bond Strength
1	Orangun, 1977	$\mu_{cal} = \sqrt{f'_c} \left(1.2 + 3 \frac{c}{d_b} + 50 \frac{d_b}{l_d} \right)$
2	Esfahani and Rangan, 1988	$\mu = \mu_c \left(\frac{1 + \frac{1}{M}}{1.85 + .024\sqrt{M}} \right) \left(0.88 + 0.12 \frac{C_{med}}{c} \right)$ <p>Where,</p> $\mu_c = 2.7 \left(\frac{\frac{c}{d_b} + 0.5}{\frac{c}{d_b} + 3.6} \right) \sqrt{f'_c} \quad \text{and} \quad M = \cosh(0.0022L \sqrt{3 \frac{f'_c}{d_b}})$
3	Zuo and Darwin, 2000	$T = (f'_c)^{\frac{1}{4}} [59.8l_d(c_{min} + 0.5d_b) + 2350A_b] 0.1 \frac{C_{max}}{C_{min}} + 0.9)$
4.	Standards Association of Australia, 2009 (AS 3600)	$\mu_{cal} = 0.265 \sqrt{f'_c} \left(\frac{c}{d_b} + 0.5 \right)$

In all the above equations, μ is the bond strength; T is the force at failure; d_b is the bar diameter; C is the cover; l_d is the embedment length; A_b is the area of reinforcement; and f'_c is the compressive strength of concrete.

A.5.3.6 Previous Studies on Pullout Tests

A study conducted by Mansoor and Zhang (2013) on the effect on reinforcement bond strength behavior under different corrosion conditions. Accelerated corrosion was chosen to reflect the field conditions by corroding the specimens for 4, 6 and 8 days. The test specimen was designed to obtain a significant result by providing anchored length to avoid yield failure. The specimens were designed with a 10-mm-diameter bar with an embedment length that was 4 times the bar diameter to avoid yielding of the steel bar under pullout load (Kanakubo et al., 2008). A few of the specimens had stirrups with a diameter of 8 mm. To avoid corrosion, the stirrups were isolated from the main bar. The dimensions of the specimens were 150 mm × 150 mm × 150 mm, as shown in Figure A.32.

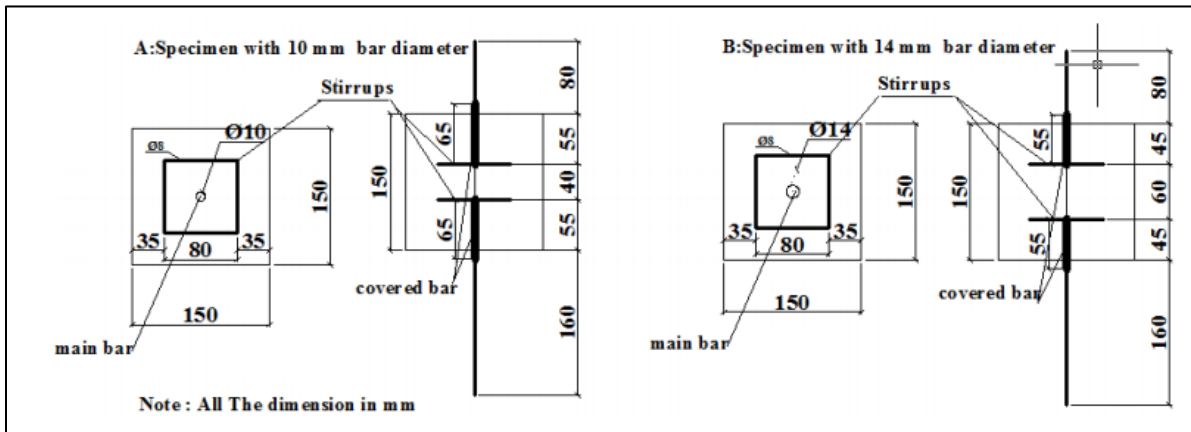


Figure A.32 Pullout Specimen Details (Source: Mansoor and Zhang, 2013)

The following parameters were studied during the testing of the specimens:

- Comparison between corroded and control specimens,
- Load–displacement behavior at failure for different corrosion levels, and
- Effect of corrosion level on the bond strength.

The bond strength was calculated corresponding to load and embedded length as following (China Standard, 2002c):

$$T = \frac{P}{L \times a} \dots\dots\dots (16)$$

where T is the bond strength, P is the maximum load (N), a represents the steel bar circumference (mm), and L represents embedded bar length (mm). The concrete specimens were partially immersed in 5% sodium chloride solution in such a way that the base was just in contact. The direction of the current was adjusted so that the reinforcing steel became the anode and the stainless-steel plate acted as the cathode, as shown in Figure A.33.

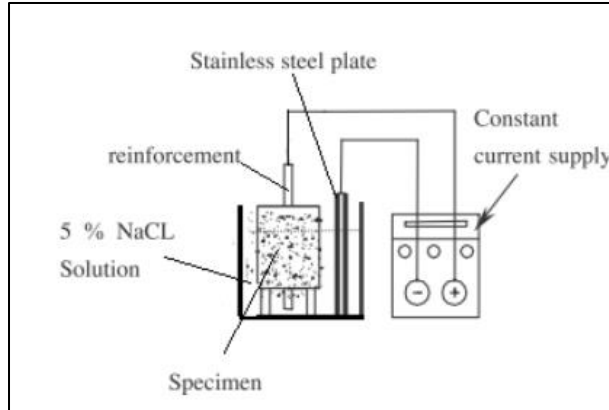


Figure A.33. Electro-Chemical Corrosion Process (Source: Mansoor and Zhang, 2013)

The common types of failure that occurred during the experiment were:

- **Bar pullout failure:** After the peak load is reached, slippage of the bar occurs without any splitting of the concrete.
- **Splitting failure:** When the bar holds a maximum load, the crack opens parallel to the applied force on the front face of the block as the bar pulls. Splitting failure can be sudden or gradual.
- **Bar yielding failure:** This type of failure occurs when the applied load is higher than the yield load of the bar. Bar yielding is not considered as the failure of the specimen.

It was found that the higher the corrosion rate, the greater was the reduction in bond strength. A typical load versus displacement of a specimen with a 14-mm bar and a concrete strength of 30 Mpa is shown in Figure A.34.

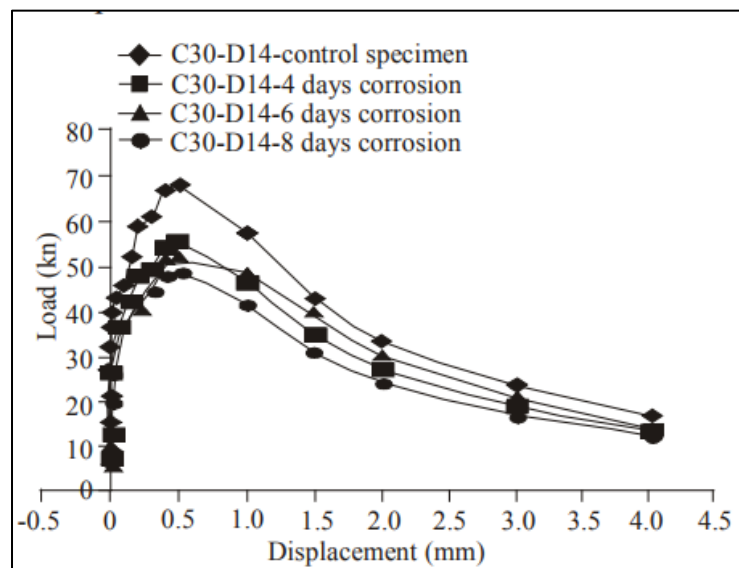


Figure A.34 Typical Load vs Displacement Curve for a Pullout Specimen with Various Levels of Corrosion (Mansoor and Zhang, 2013)

A study performed by Deepthi and Sabeena (2016) to compare the experimental and analytical data on the bond performance of reinforced bars embedded in fiber reinforced concrete. A total of 24 pullout specimens with different fiber volume fractions were cast with 16-mm and 20-mm bar diameters. Crimped steel fibers and Recron 3S fibers (shown in Figure A.35) were used in the concrete mix.



Figure A.35 Steel Crimped Fibers (*left*) and Recron 3S Fibers (*right*) (Deepthi and Sabeena, 2016)

Specimens with 150 mm × 150 mm × 150 mm were cast with 16 mm and 20 mm bars at the center of the section, with a 10-mm bar projecting out of the bottom of the cube to measure the slip of the bar during testing. The casting of specimens is shown in Figure A.36.



Figure A.36 Casting of Pullout Specimens (Deepthi and Sabeena, 2016)

The specimens were tested for pullout strength after 28 days of curing. A 600-kN capacity universal testing machine was used to pull the bar as shown in Figure A.37 (*left*). A linear variable differential transducer was used to measure the end of the bar for measuring the slip. The load was applied monotonically at a rate not greater than 22.5 kN/min. Assuming a uniform bond stress distribution over the embedment length, the average bond stress between the reinforcing bar and the surrounding concrete was calculated as follows:

$$\tau_b = P / (\pi d_b l_b) \dots\dots\dots (17)$$

Where, τ_b is the bond stress in Mpa, P is the applied load (N), d_b is the diameter of the bar (mm) and l_b is the embedment length of the bar. The failed pullout specimens were shown in Figure A.37 (right).



Figure A.37 Test Setup (left) and the Failed Pullout Specimens (right)
(Source: Deepthi and Sabeena, 2016)

The analytical work was performed in ANSYS to develop a three-dimensional model for the pullout specimens as shown in Figure A.38. The specimen was modeled using SOLID 186 elements, whereas the helical reinforcement was modelled with BEAM 188 element type. The contact between concrete and steel bar was modelled using CONTA 174 and TARGE 170 element types. An initial displacement of 3 mm was applied on the reinforcing bar and the concrete prism was restrained in one direction, while the displacement of the reinforcement was allowed only in the z direction.

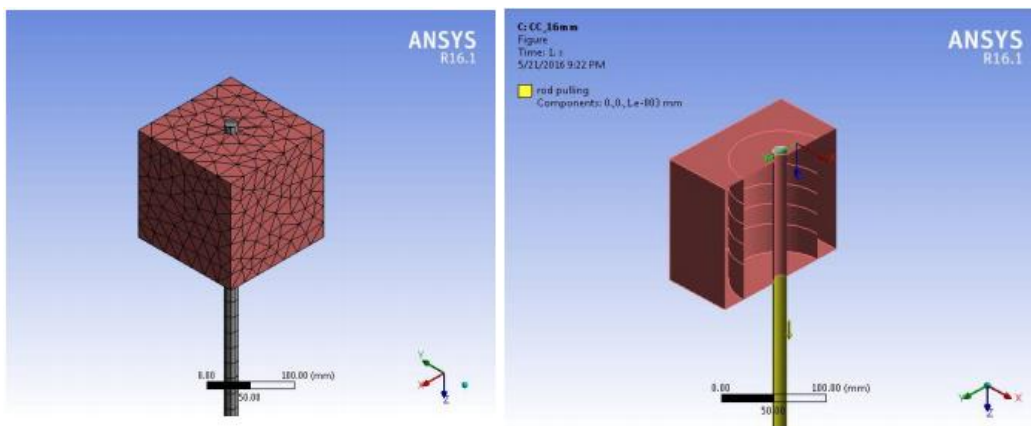
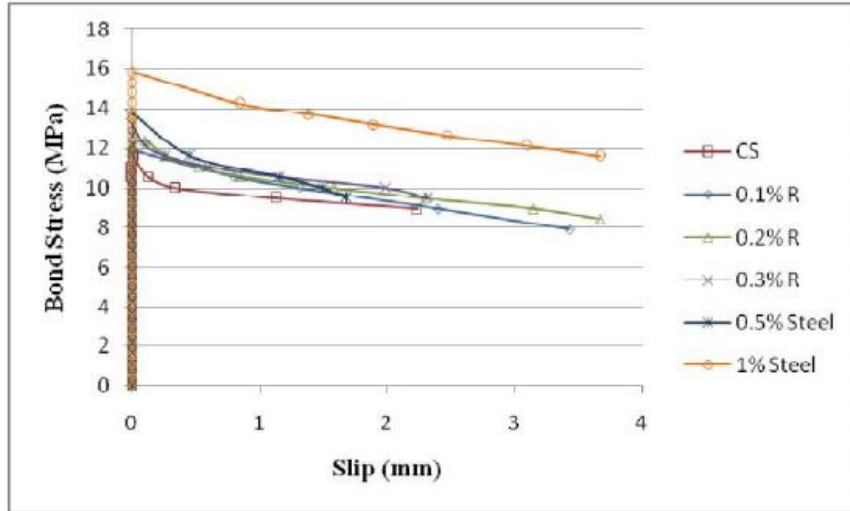
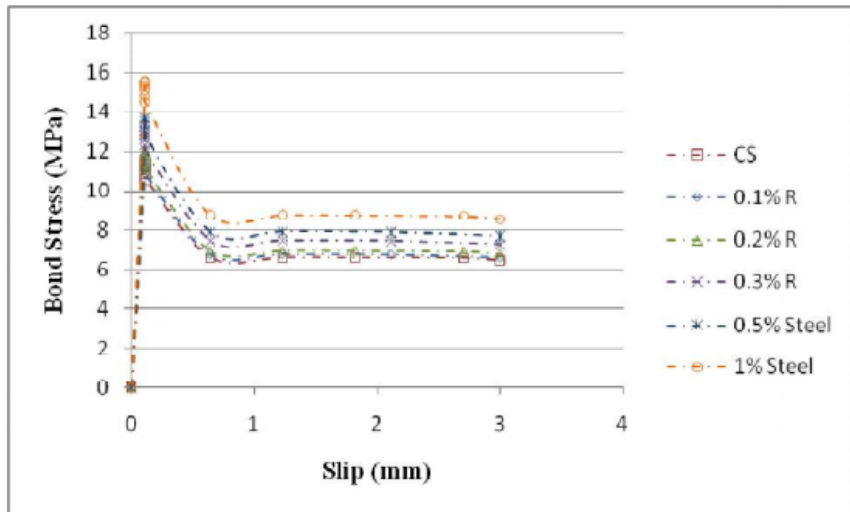


Figure A.38 Meshed Specimen Model (left); Specimen Showing Pulling of Rod (right)
(Source: Deepthi and Sabeena, 2016)

The results from the experiment and ANSYS model were compared. All the curves showed similar trend. Figure A.39 shows the experimental and analytical results for a pullout specimen with 16 mm bar. In the plots it was observed that, the post cracking behavior for specimens with 0.5% steel fiber were almost similar to that of the specimens with 0.1, 0.2, 0.3% Recron fibers.



(a)



(b)

Figure A.39 Bond Slip Behavior of Pullout Specimens: (a) Experimental Results; (b) Analytical Results (Deepthi and Sabeena, 2016)

It was concluded that polyester and steel fibers improved the bond stress for both 16-mm and 20-mm bars compared to the control specimens. But the increase in bond strength was higher in case of steel fibers. Also, the trend of bond slip behavior remained the same for both bar diameters.

A.5.3.7 Effect of Fatigue on Bridge Decks

Fatigue is usually a factor considered in the design of steel structures. However, in terms of concrete bridges, where repeated cyclic load is caused due to traffic, understanding the behavior of reinforced concrete under cyclic loading is an important consideration. A bridge deck usually experiences more than 20 million cycles over its service life, leading to progressive damage to concrete and steel reinforcement. In addition, on structural slab bridges, many transverse cracks that are formed, and these cracks widen over time. Fatigue is considered as one of the factors for widening of cracks on bridge decks. There are two types of fatigue that are usually experienced by structures, low-cycle fatigue and high-cycle fatigue. Low cycle fatigue means the load is applied to cause high stresses and for a relatively small number of cycles, while the high cycle fatigue corresponds to a load causing low stress for large number of cycles. Bridges usually experience somewhere in between low and high cycle fatigue.

- ***Fatigue behavior of Reinforced Concrete***

Since reinforced concrete is a composite material, failure due to fatigue can occur in several different ways: concrete and steel local failure; bond failure between concrete and steel; and compressive or tensile failure, depending on the crack propagation rate (Elfgrén and Gylltoft, 1977). The failure mainly depends on the stress levels, the stress range, and the number of loading cycles as shown in Figure A.40 (Olsson and Pettersson, 2010).

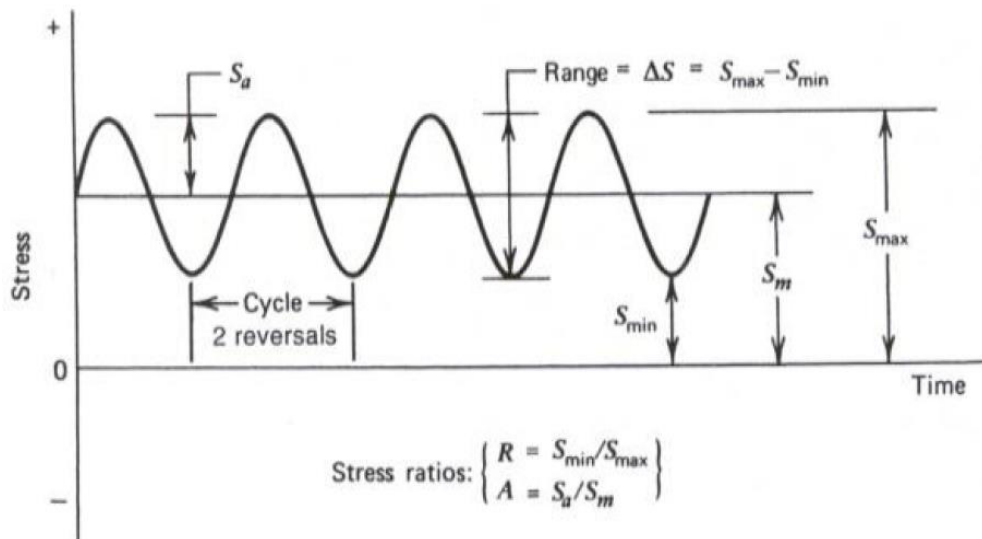


Figure A.40 Curve Showing Stress Range Applied Over Time

Bending Behavior

A progressive deterioration of bond between reinforcement and concrete is caused due to cyclic loading. Due to larger crack widths with smaller contribution of tension concrete between cracks, the deflection of the beams increases. Failure of beam in bending is usually caused by the failure of concrete or steel reinforcing bars due to fracture of material. Tensile failure due to bending occurs in the reinforcement, especially for an under reinforced cracked cross-section. For over-reinforced section the situation is much more complex. The compressive failure might take

place in the concrete, but it can also be influenced by effects between the compressive reinforcement and the concrete.

Shear Behavior

Slabs, usually are not provided with stirrups or shear reinforcement. They develop shear cracks, which cross the bending cracks and thereby leading to sudden failure. For beams with shear reinforcement, the failure would be ductile and the deformation increases slightly, with spalling of the surrounding concrete. The fatigue shear resistance is higher with shear reinforcement than without.

- **Fatigue behavior of fiber reinforced concrete**

Use of fibers in concrete is known to improve several properties, which includes cracking resistance, impact and wear resistance, and ductility. Fibers are now being used in structures to reduce cracking. Research on the behavior of fiber reinforced concrete (FRC) under cyclic loading are still ongoing. Empirical approaches were developed to predict the fatigue life of FRC structures figure A.41, but these must be backed up by experimental investigations, which should include many case studies over time.

In case of FRC structures, the material phase is classified as a matrix (i.e. cement paste and aggregates), fibers, interface of fiber and the matrix. Under the application of fatigue loading, microscopic changes occur in these phases, such as opening and growth of bond cracks at the interface between the coarse aggregates and hydrated cement paste (Neville and Brooks, 1987). Microscopic changes cause detrimental changes in the macroscopic material properties between the fibers and the aggregate bridging forces. Over repeated cycles, the bridging forces reduce fiber breakage due to surface abrasion (Matsumoto, 1998).

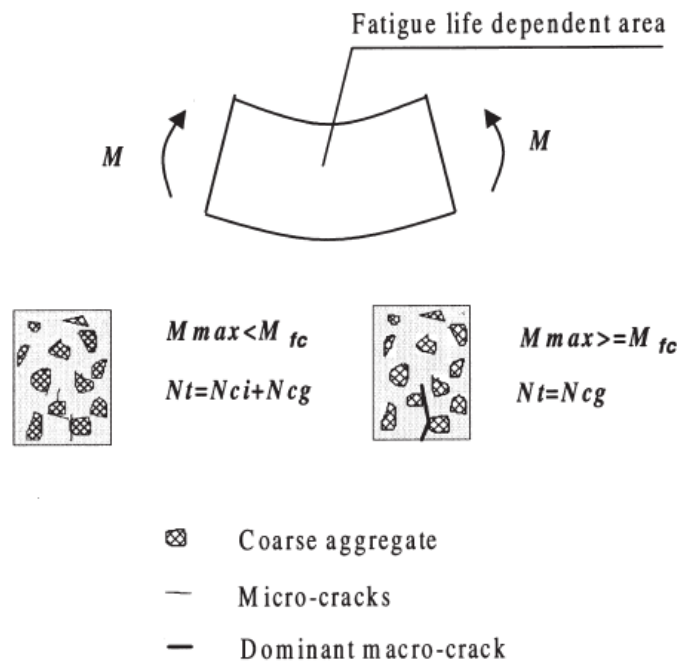


Figure A.41 Fatigue Life Prediction Area (Zhang et al., 1999)

Fatigue crack growth in FRC beams can be classified into two stages: the crack initiation stage and the crack propagation stage. Consider a rectangular beam, loaded in bending fatigue load with constant amplitude between maximum and minimum moments, M_{\max} and M_{\min} . When $M_{\max} < M_{fc}$, where M_{fc} is the first crack moment, the fatigue life of the beam is given by

$$N_t = N_{ci} + N_{cg} \dots\dots\dots (18)$$

When $M_{\max} \geq M_{cf}$, the fatigue life is given by

$$N_t = N_{cg} \dots\dots\dots (19)$$

where N_t is the total fatigue life, N_{ci} and N_{cg} are the fatigue life components for crack initiation and crack growth, respectively, as shown in Figure 2.40. In the case of fatigue load, where $M_{\max} \geq M_{cf}$, a few assumptions are made for the modeling:

- Once a fatigue crack is created, the fatigue crack growth is governed by bridging within the fracture zone.
- The stress at the crack tip remains constant and is equal to the material's tensile strength.
- Properties of material outside the fracture zone remain unchanged during fatigue loading.

It was also assumed that concrete and FRC materials show a linear response up to peak load. After the peak load, the bridging law is considered at the crack under fatigue loading. A semi-analytical model was developed for an under-reinforced FRC beam under bending load.

• ***Prediction of Crack growth in concrete and FRC under Bending loading***

A model was developed by Pedersen (1996) that considers a linear tension stiffening relationship. Maalej and Li and co-workers (Maalej, et. al., 1995, Li et al., 1992) developed a similar model for plain as well as FRC beams in bending based on equilibrium of force in the cracked section. Recent studies show that at crack widths less than 0.1 mm, bridging law strongly influences the structural behavior of beams in bending. An equilibrium of force approach was adopted to develop an analytical model.

Consider a rectangular simply supported beam of width B , depth h , and span L , subjected to a bending moment M . A maximum tensile strength will occur at the crack tip, and a moment corresponding to the first crack M_{fc} is caused by a load P_{fc} . The failure can be divided into two stages: a) linear elastic stage and b) a fictitious crack developing stage. In the first stage, according to classical theory as shown in Figure A.42.

$$M_{fc} = Bh^2/6 \sigma_t \dots\dots\dots (20)$$

where σ_t is the tensile strength of material.

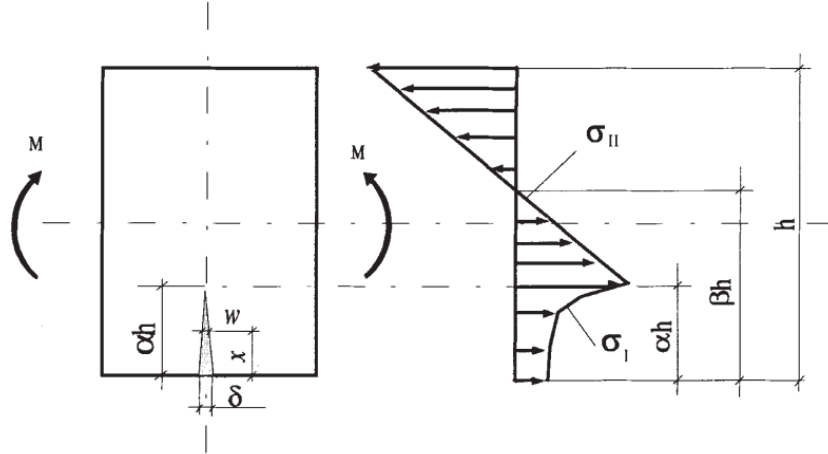


Figure A.42 Distribution of Normal Stress in the Critical Cracked Section (Pedersen (1996))

In the second stage, crack length αh , $\alpha \in [0,1]$, CMOD, δ and external moment can be related. The crack length is assumed to be linear opening profile as shown in Figure A.42 then,

$$w = \delta \left(1 - \frac{x}{\alpha h}\right) \dots\dots\dots (21)$$

Where w is the crack width at location x , from equilibrium we have

$$\int_0^{\alpha h} \sigma_I(x) dx + \int_{\alpha h}^h \sigma_{II}(x) dx = 0 \dots\dots\dots (22)$$

$$\int_0^{\alpha h} \alpha_I(x)(h-x)B dx + \int_{\alpha h}^h \sigma_{II}(x)(h-x)B dx = M \dots\dots\dots (23)$$

where $M=PL/4$ is for a three-point bending case and where $\sigma_I(x)$ and $\sigma_{II}(x)$ are the normal stress functions in the cracked and un-cracked portions of the beam.

$$\sigma_I(x) = \sigma(w) = \sigma \left(\delta \left(1 - \frac{x}{\alpha h}\right) \right) \dots\dots\dots (24)$$

$$\sigma_{II}(x) = \sigma_t \left(1 - \frac{x-\alpha h}{\beta h - \alpha h}\right) \dots\dots\dots (25)$$

where βh is the depth of tensile zone $\beta \in [0,1]$. According to the principal of superposition, the CMOD under bending can be written as

$$\delta = \delta_1 + \delta_{\sigma_I}(x) \dots\dots\dots (26)$$

where δ_M and $\delta_{\sigma_I(x)}$ are the CMOD components caused by external moments M and the bridging stress $\sigma_I(x)$. Where $\delta_{\sigma_I(x)}$ can be found by the expression

$$\delta_{\sigma_I(x)} = \delta_{M'} + \delta_{\sigma'} \dots\dots\dots (27)$$

Here M' and σ' are given by

$$M^1 = \int_0^{\alpha h} B\sigma_I(x) \left(\frac{h}{2} - x\right) dx \dots\dots\dots (28)$$

$$\sigma' = \frac{1}{h} \int_0^{\alpha h} \sigma_I(x) dx \dots\dots\dots (29)$$

According to Tada et al. (1985), the total CMOD can be expressed as

$$\delta = \frac{2\alpha}{BnE} [MV_1(\alpha) - MV_2(\alpha)] - \frac{4\sigma'\alpha h}{E} V_3(\alpha) \dots\dots\dots (30)$$

When under three-point loading,

$$V_1(\alpha) = 0.33 - 1.42\alpha + 3.87\alpha^2 - 2.04\alpha^3 + \frac{0.66}{(1-\alpha)^2} \dots\dots (31)$$

$$V_2 = 0.8 - 1.7\alpha + 2 \cdot 4\alpha^2 + \frac{0.66}{(1-\alpha)^2} \dots\dots\dots (32)$$

$$V_3 = \frac{1.46 + 3.42 \left(1 - \cos \frac{\pi\alpha}{2}\right)}{\left(\cos \frac{\pi\alpha}{2}\right)^2} \dots\dots\dots (33)$$

A.5.3.8 Studies on Connection between Slab and Pier of RC Bridge

The behavior of the connection between the superstructure and substructure is significant especially in bridges that have intermediate piers. In the United States, many bridges have experienced cracking in the negative moment region where the pier cap and slab are connected. It is necessary to study the connection behavior and its influence on the cracks over the connection region.

- **Classification of Connection Based on ODOT Bridge Drawing**

Based on the details mentioned in the bridge drawings, the type of connection between slab and pier can be classified as shown in Figure A.43:

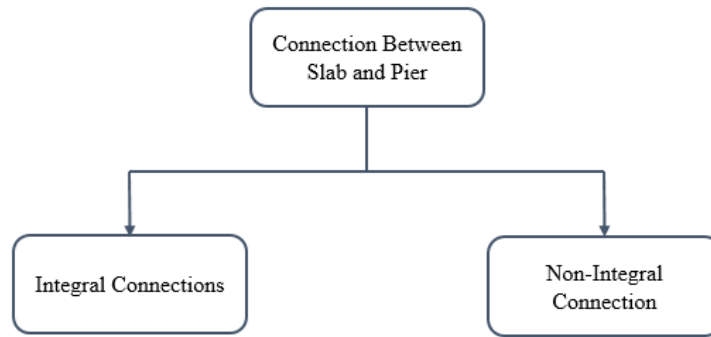
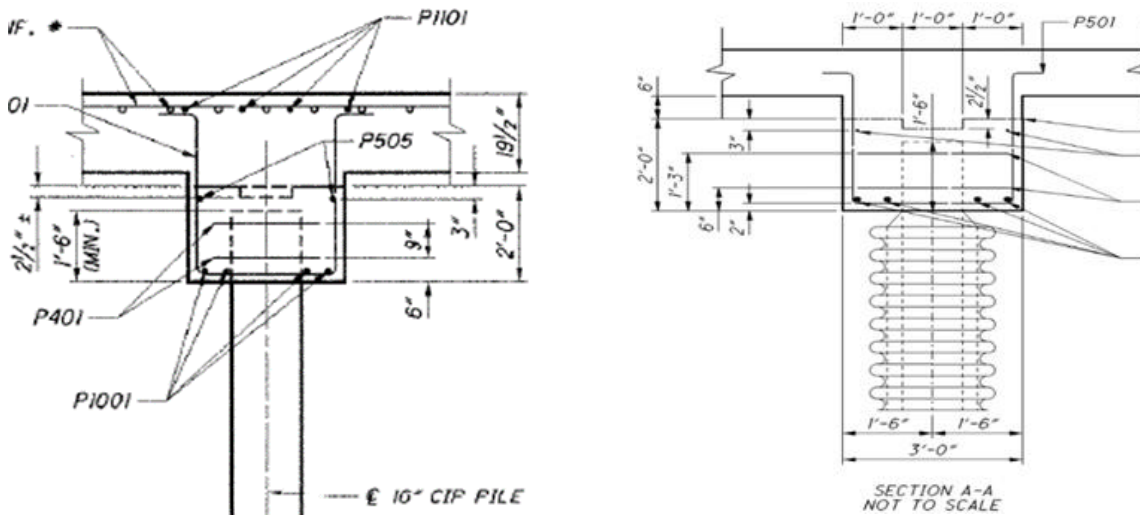


Figure A.43 Classification of Connection in Structural Slab Bridges

Integral Connections

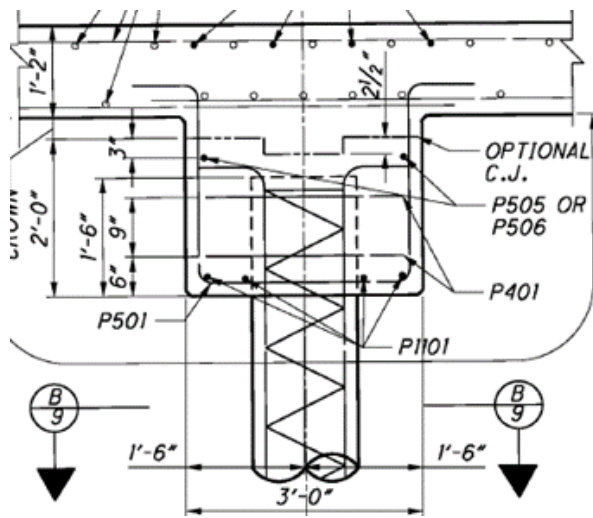
Based on bridge drawings, 95% of the bridges in ODOT inventory were classified as having an integral connection. These connections were designated as C2, in which a U-shaped bars connect the pier cap with the slab deck. The bent U-shaped bar were located at the top (C2T), middle (C2M) or bottom (C2B) of the slab thickness. Another type of integral connection has a U-shaped bar and a straight bar projecting from the pier that goes into the slab and is designated as (C2MI). The following connection types are shown in Figure A.44. These U-bars ensure the connection between the slab and pier cap to behave as a rigid connection between the slab and the pier cap.



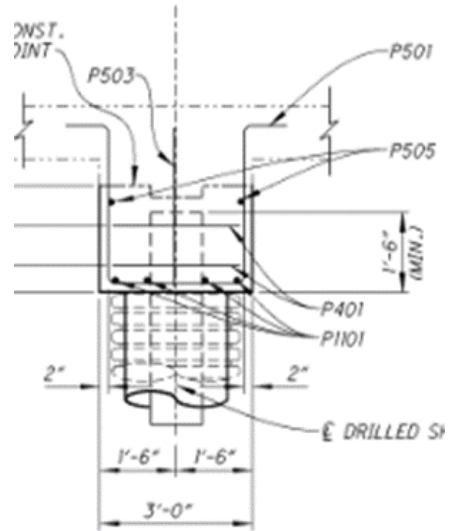
(a) C2T

(b) C2M

Figure A.44 Integral Connection Types (Based on Bridge Plan Drawings)



(c) C2B

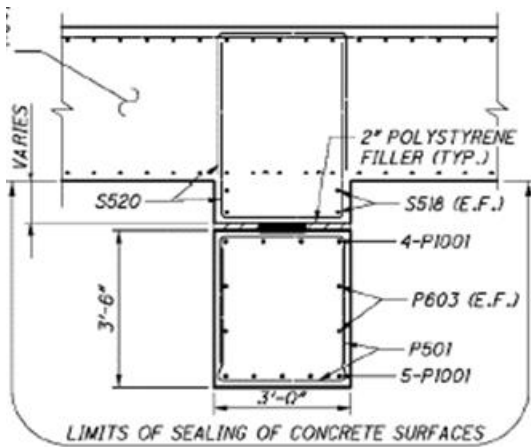


(d) C2MI

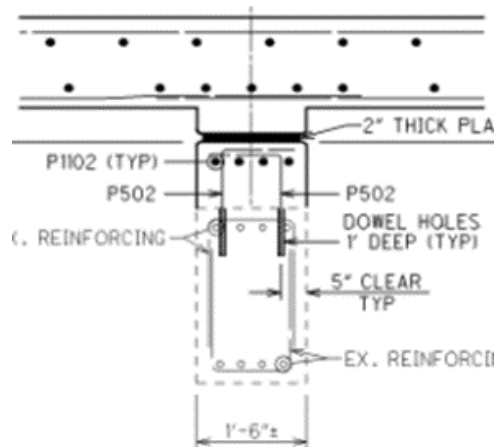
Figure A.44 Integral Connection Types (Based on Bridge Plan Drawings) (continued)

Non-Integral Connections

In this connection type, the slab deck is sometimes rested on the pier cap with a bearing pad at its interface. These can be full or half bearing based on the design requirements. The bearing pad that is commonly used is 2-inch-thick elastomeric bearing pad. A few other bridges are simply connected using a single dowel bar, which most likely acts as a pin connection as shown in Figure A.45.



(a) C1A



(b) C1B

Figure A.45 Non-Integral Connection Types (Designer's Preference)

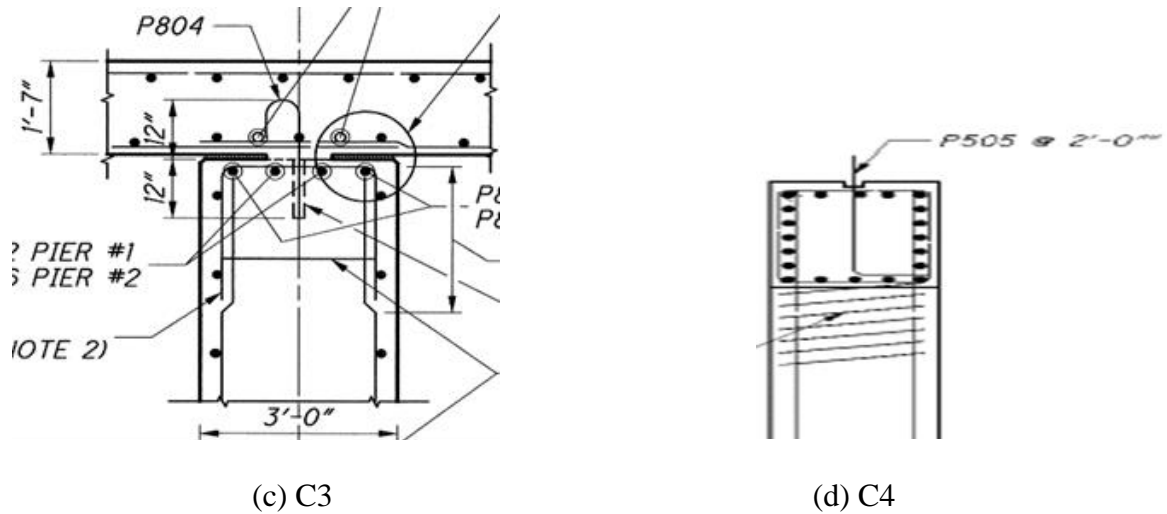


Figure A.46 Non-Integral Connection Types (Designer's Preference), continued

- **Comparison with Bridges in Iowa**

The connection type between slab deck and pier cap was compared with that in Iowa Department of Transportation (Iowa DOT, 2006) to observe major differences.

Integral Connection

The most common connection type used in Iowa bridges was an integral connection for bridges with spans ranging from 140 ft. to 300 ft. In Iowa, additional bent bars are used to connect both the slab and pier at the bottom of deck slab. The standard connection details for the integral connection type are shown in Figure A.47.

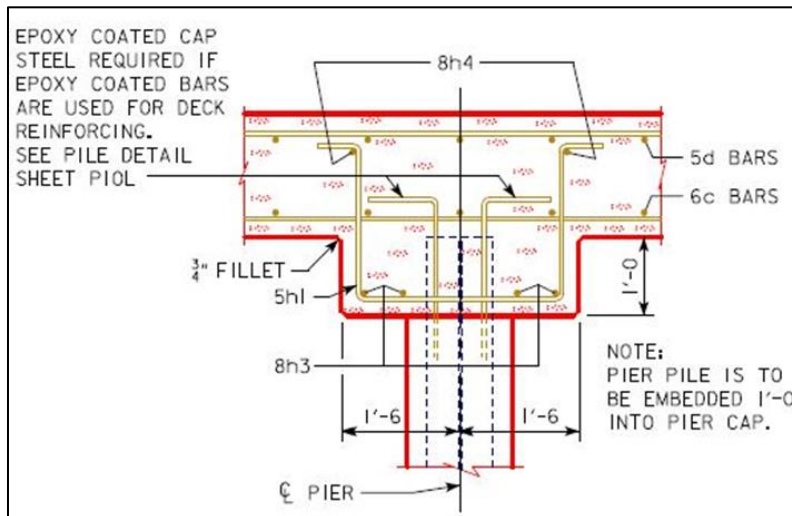


Figure A.47 Standard Integral Connection Type from Iowa DOT (Iowa DOT, 2006)

Non-Integral Connection

Non-integral connections are also called non-monolithic pier cap connections. In this connection, the slab is directly connected to the pier cap using a joint material. The sectional details and the thickness of the joint material is shown in Figure A.48.

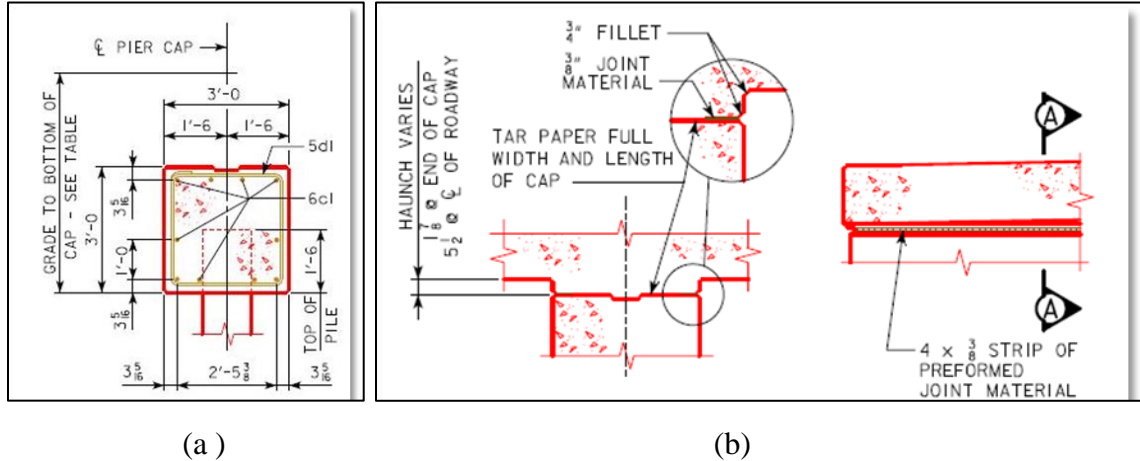


Figure A.48 (a) Non-Integral Connection Type from Iowa DOT; (b) Section Showing Joint Material (Iowa DOT, 2006)

• **Other Studies Based on SAP2000 Analysis**

Most of the studies on abutment connection used SAP2000. Bhagwat (2014) performed a study, “Effect on Superstructure of Integral Abutment Bridge under Fixed and Pinned Pile Head Connections.” The number of spans, span length, and connection of pile head considered in the model are shown in Table A.7. The slab thickness considered was 0.25 m, with a girder size of 0.35 m × 1.5 m, and a girder spacing of 2.4 m. The diameter of the pier was 1.2 m, and the abutment length was 3 m.

Table A.7 Detail of Bridge Models

Bridge Model	Bridge Length (m)	Number of span	Length of Each Span (m)	Connection of Pile Head
1	60	1	60	Fixed
2	60	1	60	Pinned
3	60	2	30	Fixed
4	60	2	30	Pinned
5	60	3	20	Fixed
6	60	3	20	Pinned

Source: Bhagwat (2014).

By changing the connection type from pinned to fixed, it was found that the maximum positive bending moment in the deck slab for a single span increased by 17.69%, as shown Figure A.49.

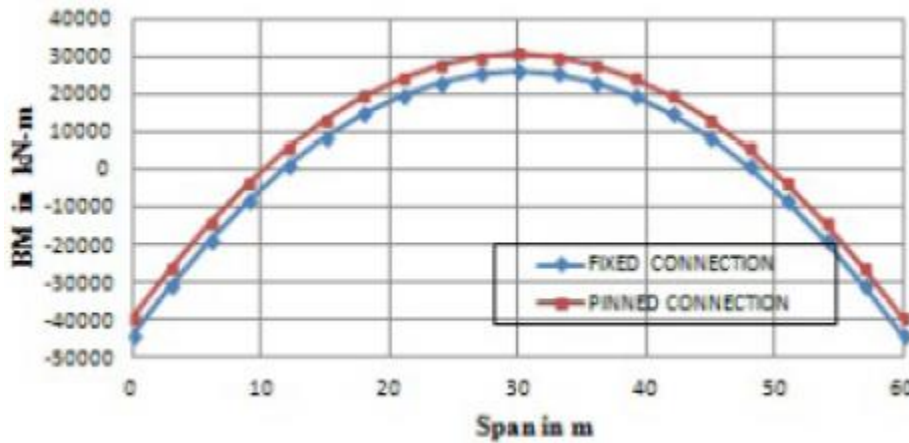


Figure A.49 Comparison of Bending Moment Due to Dead Load for Fixed and Pinned Connection of a Single Span Bridge (Bhagwat, 2014)

In two-span bridges, when changing the connection type from fixed to pinned, it was found that the maximum positive and negative bending moment were 10.93% and 11.4% respectively. The shift in the bending moment is due to the release in moment at the top of the pile head, where the maximum pile moment occurs when making a pinned connection, as shown in Figure A.50.

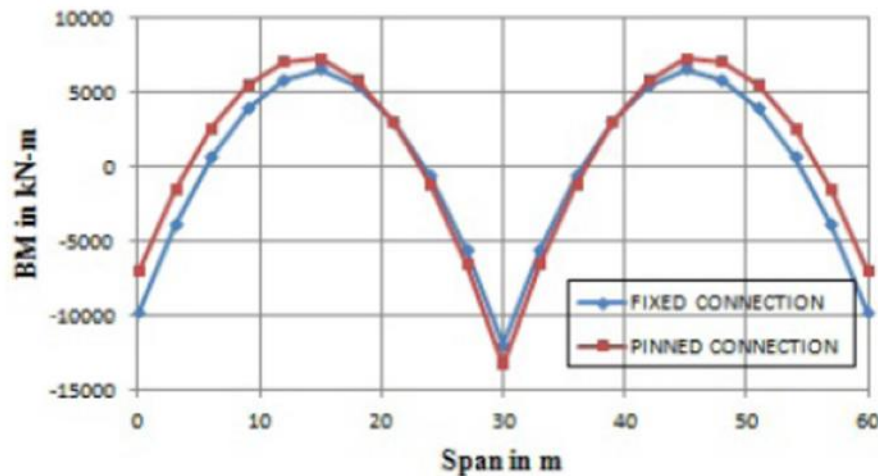


Figure A.50 Comparison of Bending Moment Due to Dead Load for Fix and Pin Connection for a Two-Span Bridge (Bhagwat, 2014)

However, no difference was found in a three-span bridge, in both maximum positive and negative bending moment for the deck slab even when releasing the moment at the top pile abutment, as shown in Figure A.51.

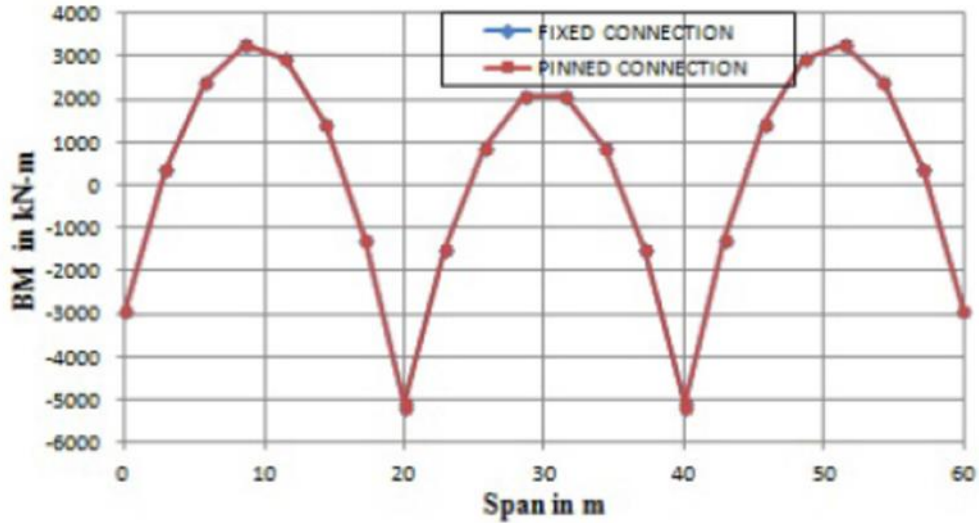


Figure A.51 Comparison of Bending Moment Due to Dead Load for Fixed and Pined Connection for Three Spans Bridge (Bhagwat, 2014)

Research conducted by Hou and Chen (2017) focused on the influence of earthquakes on bridge connections in regions with low to moderate seismic activity. Four bridges with three span lengths (listed in Table A.8) were modeled in 3D in SAP2000. The geometry of the bridge modeled is shown in Figure A.52. The concrete deck has a thickness of 8 inches, with a 68-in.-deep pre-stressed concrete I-girder that was supported by a pier cap with a depth of 5 ft.

Table A.8 Bridge Configurations

Bridge Name	Skew (degrees)	Curvature Radius (m (ft))	Super elevation (degrees)
R0S0	0	0 (0)	0
R0S30	30	0 (0)	0
R3000S0	0	914 (3000)	6
R3000S30	30	914 (3000)	6

Source: Hou and Chen (2017).

The substructures were 12 ft. × 3 ft. for both integral abutment and interior piers, as shown in Figure A.53. It was found that longitudinal and transverse moment demand/capacity (D/C) ratio at the base of the intermediate piers are less than 1. It was found that the curvature will cause an increase in the longitudinal moment D/C ratio, while skew will cause an increase in the transverse moment D/C ratio. In the case of a roller-connection model, seismic forces cannot be transmitted from the superstructure to the piers; therefore, a significant reduction in the base moment of the pier was observed after translational release.

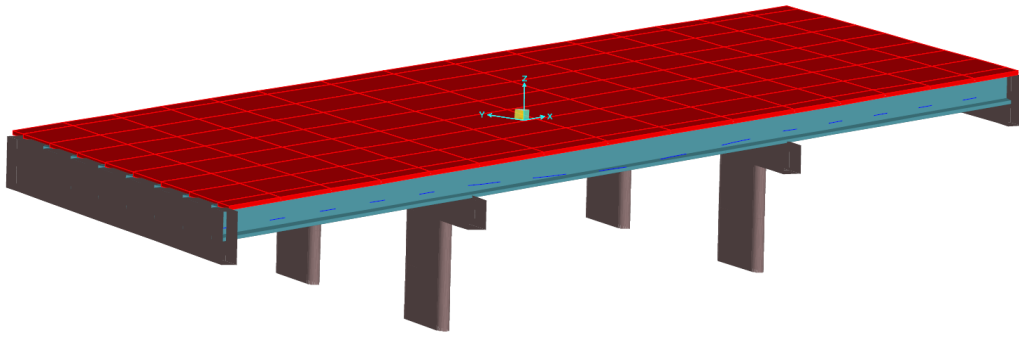


Figure A.52 3D Finite-Element Model in SAP2000 (Hou and Chen, 2017)

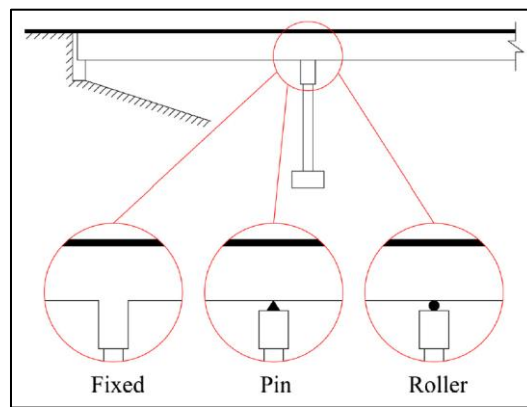


Figure A.53 Idealized Intermediate Bent Connections (Hou and Chen, 2017)

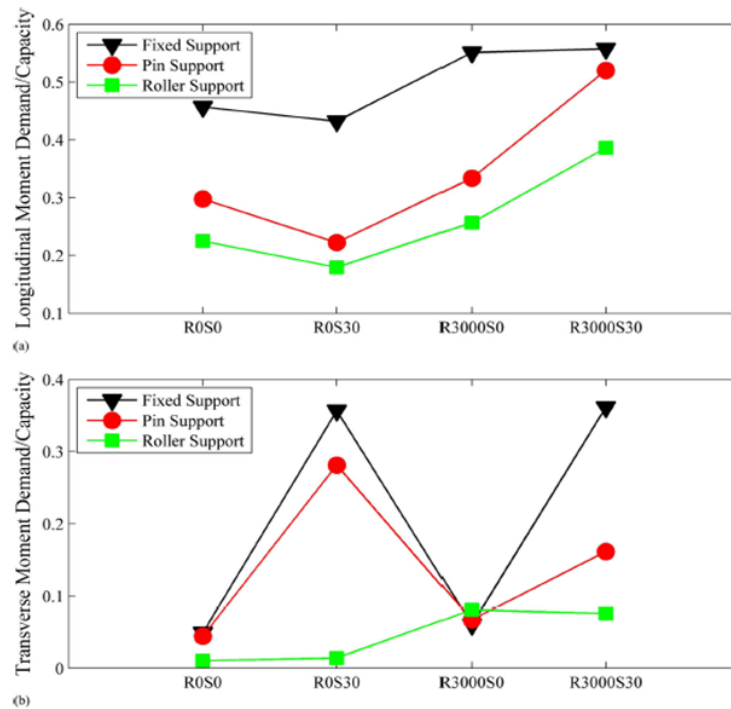


Figure A.54 Moment Demand /Capacity for Different Geometries (Hou and Chen, 2017)

A.6 Literature Review on Corrosion

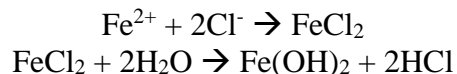
Corrosion of reinforced concrete bridge decks is a major concern in the infrastructure industry all over the United States. There is a grave concern in the states where deicing chemicals are used during winter. The presence of abundant calcium hydroxide and lesser amounts of alkali elements like sodium and potassium gives the concrete a very high alkalinity, with a pH of 12 to 13. This forms a protective layer around the steel bar at the early age of concrete. When salt mixed with water seeps through the porous concrete and cracks on the bridge decks reach the reinforcing steel, pH of the concrete changes from basic to acidic and breaks the protective film over the reinforcement, resulting in corrosion. Corrosion of reinforcement increases the volume of reinforcing bar, causing stresses on the surrounding concrete. The bond between the steel and the concrete is lost, and spalling of the concrete covers occurs, decreasing the flexural capacity of the deck. At locations where corrosion is severe, the structural integrity is lost, leading to collapse of the bridge.

Corrosion is mainly due to carbonation and chloride attack. Carbonation is a process resulting from the interaction of atmospheric carbon dioxide with the alkaline hydroxide in concrete, while chloride attack results from the destruction of the passive layer that is formed on the rebar due to chloride ions. Chloride ions are induced due to the deicing salts used on the bridges during winter. The process of replicating a natural corrosion process in laboratory has been a focus of prior research. For example, François and Arliguie (1998), Castel et al. (2003), Vidal et al. (2007), and Zhang et al., (2010) allowed their laboratory specimens to corrode naturally; they had to wait for four years for corrosion initiation and an additional two years for crack formation. Therefore, an electrochemical process is usually adopted to accelerate the corrosion process in reinforced concrete.

Corrosion of reinforcing steel using a macrocell setup is the most common method adopted in the laboratory to shorten the testing time by accelerating the corrosion process. The correlation from the accelerated tests to that of field conditions is still unknown at this point of time, and research is still ongoing. Standard ASTM test methods have been used to investigate the effect of chemical admixtures on corrosion of metal in concrete such as ASTM G109 (2007) and ASTM A955 (2009).

A.6.1 Accelerated Corrosion Process

The process of accelerating the corrosion by forming an electrochemical cell to corrode the reinforcing steel is used in laboratory. The top reinforcing steel acts as an anode and the stainless-steel plate in the in the tank containing salt solution acts as a cathode. Current is passed using an external power supply which forms a circuit connecting the stainless-steel plate (cathode) and the reinforcing steel (anode), causing flow of chloride ions. During this process, the chloride ions that are broken down from HCL as H^+ and Cl^- ions will not be consumed. This leads to a continuous break down of the passive film of the reinforcing bar.

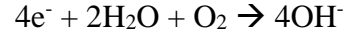


The concrete acts as a salt bridge permitting the anions creating an electrochemical circuit.

Anodic Reaction (Oxidation)



Cathodic Reaction (Reduction)



Current research aims to develop an understanding about the ultimate capacity loss of a section by losing metal due to corrosion (Mangat et al., 1999; Torres-Acosta et al., 2007; Azad et al., 2007). Based on the literature review on the experimental programs, three methods are typically used to simulate a corrosive environment:

- 1) Mix chloride ions into concrete or spray chloride solution into the chamber (Liu and Weyers, 1998; Alonso et al., 1998; Badawi and Sooudki, 2005);
- 2) Immerse the specimen in tanks with an NaCl solution (Fang et al., 2004; Ballim et al., 2001; Ballim and Reid, 2003); and
- 3) Expose the selected faces of concrete elements to chlorides (Yoon et al., 2000; Malumbela et al., 2009) or selectively spray them with a salt solution. For example, some researchers opted to mix concrete with chlorides ranging from 1% (Mangat and Elgarf, 1999) to 5% (El Maaddawy and Soudki, 2003) by weight of cement. Others immersed their cured samples in tanks with an NaCl solution with concentrations from 3% to 5% by weight of the solution. Chloride concentrations were often selected to simulate the chloride concentration of seawater, which has a salt concentration of about 3.5%.

Following discussions by Poursaee and Hansson (2009), Yuan and Ji (2009), Yuan et al. (2007), it is recommended that in accelerated corrosion tests the following requirements are needed to more closely understand the corrosion:

- Steel should be allowed to passivate before adding chlorides to concrete. This is equivalent to saying that the chlorides should be added externally and not be mixed with the concrete.
- Only selected faces of concrete elements should be contaminated with chlorides. Specimens should not be submerged in salt solutions.

Slab sections are typically not provided with stirrups, whereas shear reinforcement is provided for beams. Since there is no shear reinforcement for slabs, the failure modes of corroded RC slabs need to be understood through the use of corrosion-resistant reinforcing bars.

In the recent past, it was common to use epoxy-coated reinforcing bars inside the concrete to protect the bars from damage due to corrosion (Erdogu et al., 2001; Darwin and Scantlebury, 2002). It was also observed that defects on the epoxy-coated steel caused severe damage to the coating due to corrosion (Nguyen and Martin, 2004). Many researchers have studied the use of fibers in the concrete mix to improve the performance of the structure (Alhozaimy et al., 1996; Li et al., 2004).

Other researchers focused on the corrosion of slabs in the absence of sustained loading (Cairns et al., 2008; Rio et al., 2005; Ballim and Reid, 2003). It was observed that Faraday's laws under-predicted the gravimetric mass loss for low corrosion levels (<5%) and over-predicted for high corrosion levels (>10%). To simulate actual conditions, it was necessary to study the performance of RC slabs subjected to corrosion under the action of sustained loading.

A.6.2 Accelerated Corrosion under Sustained Loading

Under the action of sustained loading, the tension steel bars and the surrounding concrete are in tension and if the tension steel area is reduced due to corrosion, larger strains with an increased curvature and reduced stiffness will occur. At early levels of corrosion, the bond usually increases up to a certain level and then decreases as the surrounding concrete loses bond as it develops cracks due to the volumetric pressure of the rebar. Under the action of sustained loading, cracks will develop on the tension face of the concrete, and the cracks will provide a clear channel for the salt to penetrate the slab.

Yoon et al. (2000) performed an experimentation on RC slabs under the action of sustained loading. The dimensions of the specimens were $100 \times 150 \times 1170$ mm. The beams were tested under a sustained load using a loading frame with a lever arm. A plastic tank for accommodating the NaCl solution was made on the tension face of the RC slab to allow the ingress of the salt solution. The specimen was tested under four-point bending with a span of 1050 mm and with a constant moment region of 230 mm in the middle portion, as shown in Figure A.55. The sustained load level was equivalent to 0%, 20%, 45%, 60%, and 75% of the ultimate capacity of the virgin slab. A four-day wetting with 5% NaCl solution followed by a three-day drying period was adopted during testing. It was noted that the beams with higher sustained load had shorter corrosion initiation and no corrosion after 30 days for beams tested under 75%, 45% and 0% of the ultimate capacity. Since the drying and wetting cycles with NaCl solution used in the program do not overly accelerate the corrosion process and yet the service life in-service structures is in the order of tens of years.

Current passing through the corroding steel bars was monitored during the corrosion propagation stage and was converted to the rate of corrosion using Faraday's Law. The results showed that beams subjected to elevated levels of sustained loads and high previous loads had higher corrosion rates. These rates were found to generally increase with the duration of electrolysis. Mass loss of steel was also found to be higher for beams tested under a sustained load compared to beams that were previously loaded and then corroded in the absence of a sustained load. This mass loss was attributed to larger crack widths in specimens that were corroded under a sustained load.

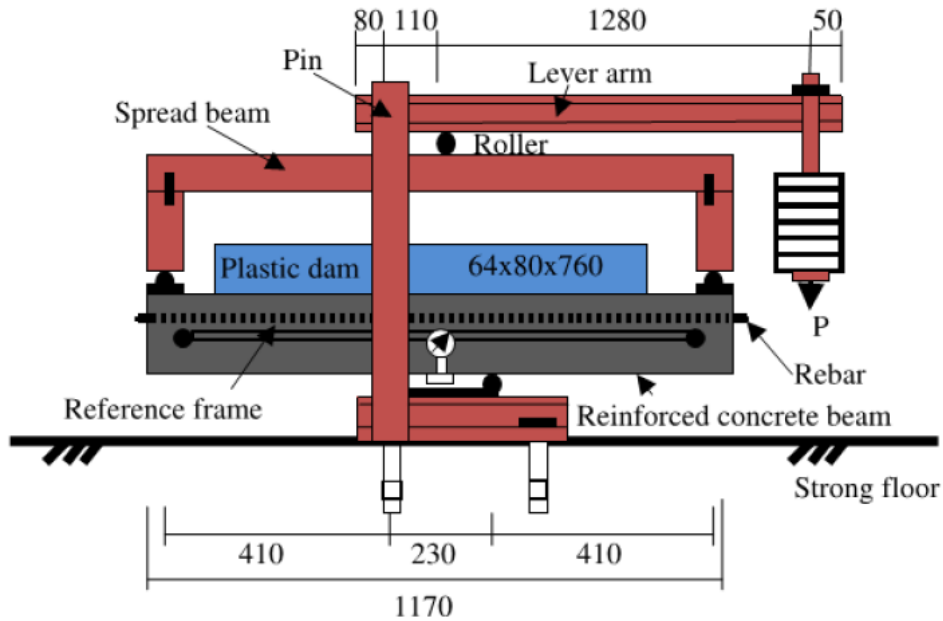


Figure A.55 Setup for Corrosion under Sustained Load (Yoon et al., 2000)

El Maaddawy et al. (2003) performed an experiment on eight quasi-full-scale RC beams with dimensions of $152 \times 254 \times 3200$ mm exposed to different levels of corrosion. Half of the beams were tested under the action of sustained loading, and the other half were tested in their absence. The testing frame is shown in Figure A.56. The test frame accommodated two beams, a bottom beam with tension face up and a top beam with tension face down. The sustained load was applied using lever arm action, and the load was transferred to the beams. The load was applied as four-point bending with a span of 3000 mm with a constant moment region of 1000 mm, as shown in Figure 2.55.

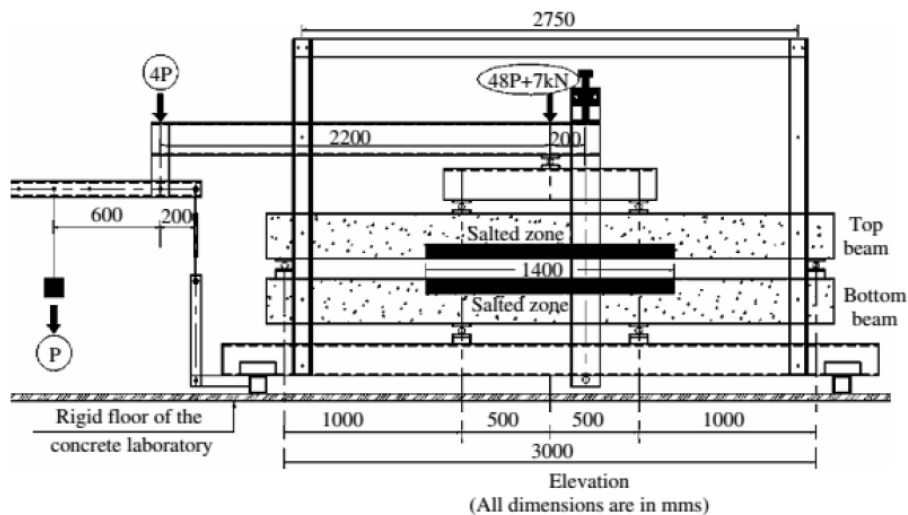


Figure A.56 Test Setup of Accelerated Corrosion (El Maaddawy et al., 2003)

Impressed current was applied under controlled humidity with a continuous spray of mist on the beams. The middle 1400 mm of the beam was cast with salt inside the concrete to achieve the desired corrosion level. It was found that for beams corroded under load, corrosion cracks appeared after 53 h; for beams corroded in the absence of a sustained load, cracks were observed after 95 h. It is worth noting that the difference between 95 h and 53 h may seem small, but the beams in the program were corroded at a corrosion density that is up to one thousand times more than the corrosion density of an in-service structure. This work, however, had few drawbacks that include the following:

- The arrangement of beams had limited access to the tensile face of the beam during the corrosion process. It was also observed that it was difficult to use this test frame to repair structures while under sustained load.
- It was not clear about the propagation of cracks in the other sections of the beam, as the cracks did not necessarily occur at the middle region.
- Though mass loss was measured at different lengths along the bar, it was averaged so that the crack map drawn at the ends of the corrosion process cannot be related to mass loss at every other point on the beam.

Patnaik and co-workers (Xia et al., 2011, 2013; Bajaj et al., 2014; Patnaik et al., 2013; Larsen et al., 2013) and Gao et al. (2016a, 2016b), also worked on understanding the corrosion of slabs reinforced with conventional and epoxy-coated steel with various testing conditions. Slab sections that were 12 inches wide, 3 inches depth and 28 inches long were chosen for the study. Different test conditions included specimens without pre-existing cracks and sustained load, specimens with pre-existing cracks but no sustained load, and specimens with pre-existing cracks and sustained load. Multiple corrosion levels (1% to 20%) were applied to different specimens. A 5 % NaCl solution along with the impressed current was applied during the corrosion process. A two-day wetting and one-day drying cycle was followed for 21 days. The schematic of typical test setup is shown in Figure A.57.

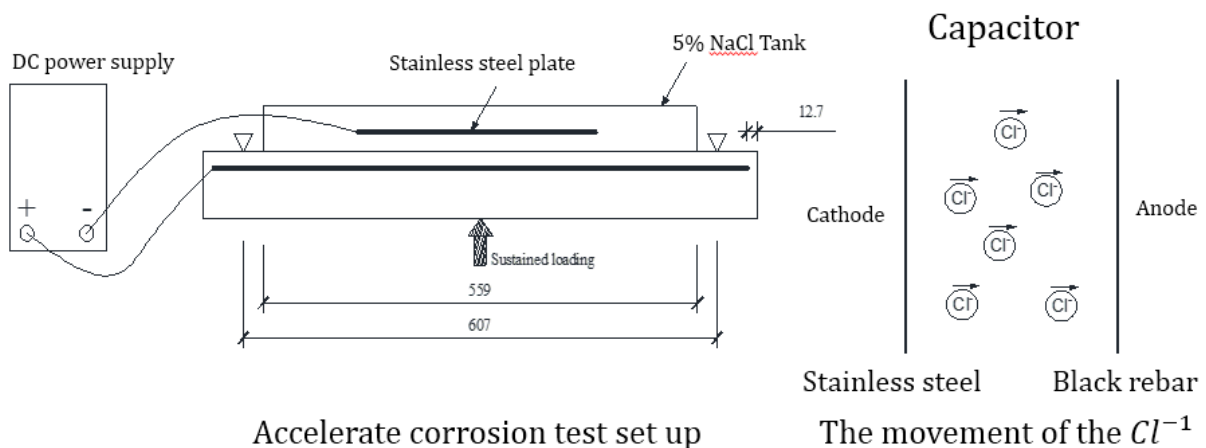


Figure A.57 Test Setup for Accelerated Corrosion under Sustained Load

Tests were performed to study the effect of sustained load and pre-existing cracks on the corrosion behavior of the RC slabs as well as to study the relationship between corrosion crack

width and metal loss. This study was extended to understand the influence of fibers on corrosion damage. Figure A.58 shows the testing frame along with the specimen under the action of sustained load.

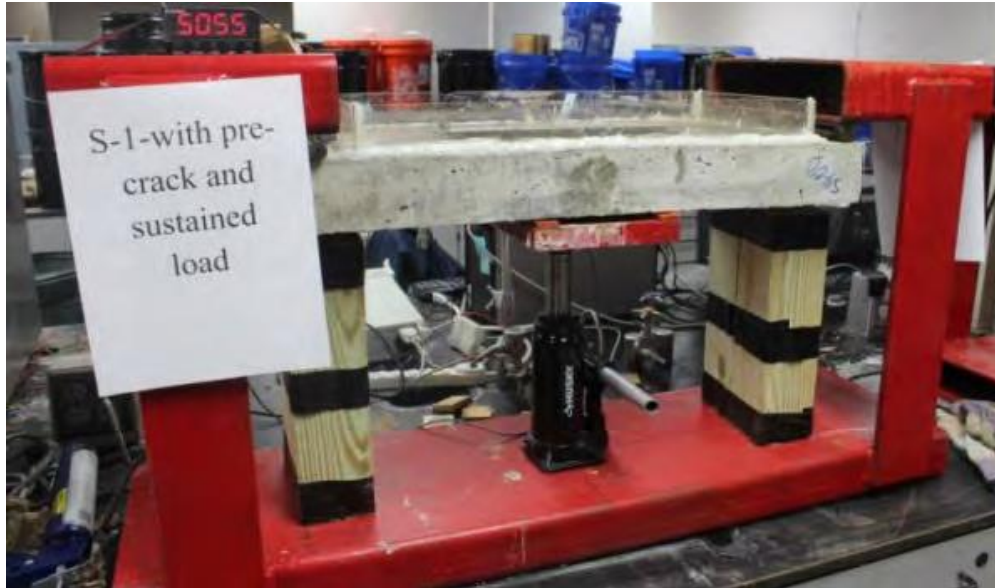
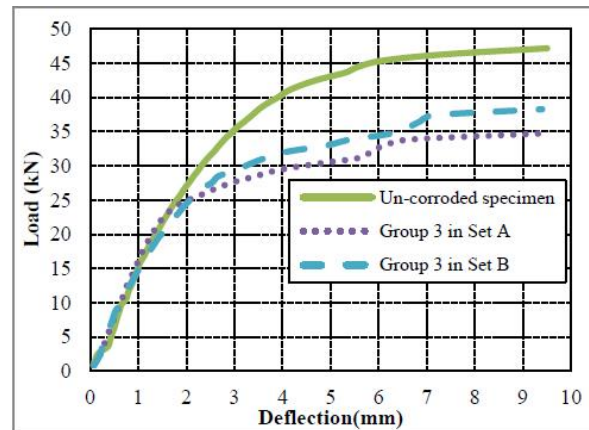
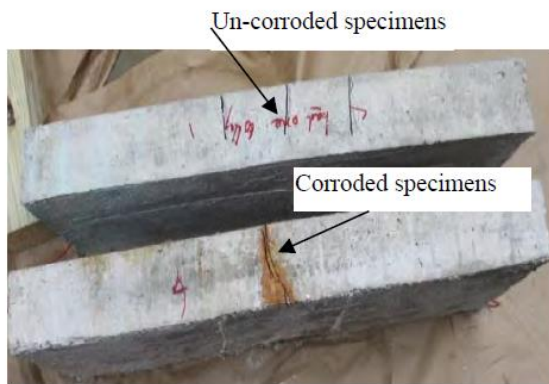


Figure A.58 Testing of RC Slab for Corrosion under Sustained Load

It was observed that corroded specimens suffered larger deflections with a smaller load than those of un-corroded specimens. The failure modes of the slabs were different; the un-corroded slabs exhibited several flexure cracks, while the corroded slabs had one wide crack in the transverse direction. Figure A.59 shows a comparison of the side crack of un-corroded and corroded slab along with the load deflection plots.

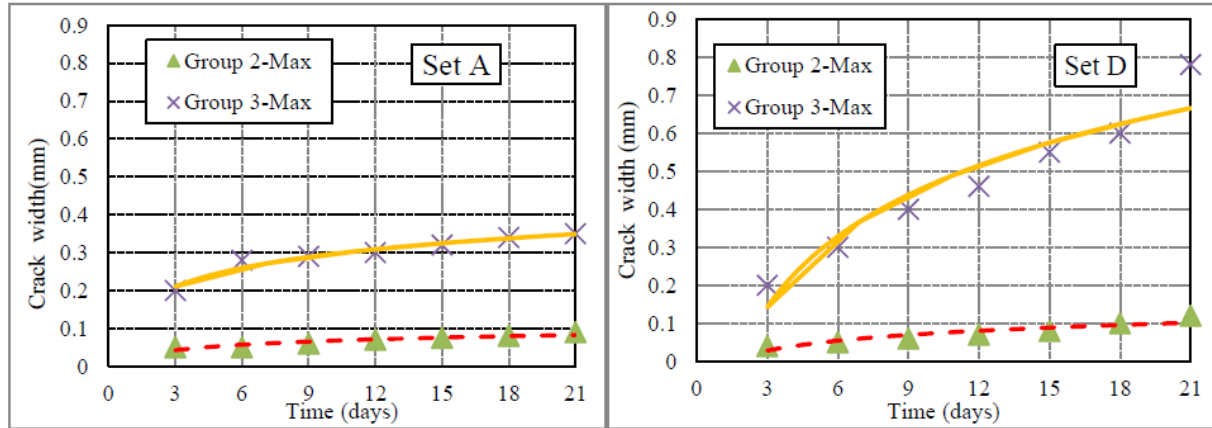


(a) The side surface cracks comparison between un-corroded and corroded specimens

(b) Load-deflection graph for un-corroded and corroded specimens

Figure A.59 Comparison of Cracks and Load-Deflection Plots for Uncorroded and Corroded Slab Specimens (Gao et al, 2016)

Metals loss due to corrosion over the length of the slab was also measured after the corrosion process, and charts were developed. The crack growth rates were also measured during the corrosion process, and Figure A.60 shows plots for typical slabs from Set A and Set D.



(a) Maximum transverse crack width growth for Set A

(b) Maximum transverse crack width growth for Set D

Figure A.60 Transverse Crack Width Growth Rate Observed for a Typical Corrosion Specimen (Gao et al, 2016)

A.7 Use of Alternate Reinforcement in Bridge Decks

Several studies were conducted and are being conducted to reduce bridge deck corrosion by using alternate reinforcement types. Virginia department of transportation is actively testing the use of corrosion-resistant reinforcing bars in bridge decks over ECB. One of the study by Mouruza and Sharp et al. (2010), was on the use of corrosion resistant reinforcement as a sustainable technology for bridge deck construction. The purpose of the study was to compare the cost of ECB and CRR (Corrosion Resistant Reinforcement) used in concrete bridge decks.

A total of 572,121 lbs. of ECR was used in the southbound deck and 674447 lbs. of CRR was used to construct the northbound deck. During the initial survey, it was found that both the bridge decks showed transverse cracking with an average of 9 cracks per span. The direct and indirect cost were estimated and compared for both ECR and CRR bars and presented in Figure A.61. In the year 2010 to 2012, VDOT has used about 8.8 million lbs. CRR, 20% of which was Stainless-Steel. Figure A.62 shows a bridge with ASTM A955 steel and ASTM A1035.

Bar	Deck Reinforcement, (lb)		Cost at unit bid prices, \$ (\$/lb)	Direct Costs, \$ (\$/lb)				Indirect Costs, \$ (\$/lb)			Total Unit Costs, (\$/lb)	
	Deck	Bolster		Labor ^{a,b}	Material ^b	Deck Seal	Total Direct Costs	Road User Costs ^b	VDOT Inspector Overtime ^b	Police Presence ^b	Excl. RUCs	Incl. RUCs
ECR	572,121	(4,702) ^c	293,040 (.51)	54,101 (.094)	238,939 (.414)	170,455 (.296)	463,495 (.804)	0.82-1.14 million (1.43-2.00)	2,800 (.0049)	300-1,000 (.0005-.0017)	.809-.811	2.24-2.81
CRR	631,089	43,358 ^d	526,069 (.78)	59,062 ^e (.088)	467,007 (.692)		526,069 (.780)				.780	

^a Ironworkers only

^b Estimated

^c Placed in northbound Span A

^d Excludes quantity of ECR placed in northbound Span A

^e Includes placement of ECR in northbound Span A

Figure A.61 Direct and Indirect Cost of ECR and CRR Deck Reinforcement by Components



Figure A.62 Bridge with ASTM A1035 (left) and ASTM A955 Steel (right)

VDOT has discontinued the use of epoxy coated and galvanized bars to use corrosion resistant metallic reinforcing bars to achieve a service life of more than 75 years. During this, It was observed that,

- Final in-place direct cost per unit of ECR, including deck sealing, was about 3 % higher than CRR.
- CRR became cost-competitive by reducing the maintenance cost towards corrosion of deck reinforcement.
- Care must be taken, while accepting bars at the job site.

The long term performance of three Ontario bridges constructed with galvanized reinforcement (Author: F. Pianca, H.Schell)

A report by Pianca and Schell (2005) documented a study of three Ontario bridges built in 1975 and 1976 using galvanized reinforcement. The investigations performed on these three bridges include measurement of corrosion potential, degree of delamination of concrete, chloride content, corrosion currents, and quality of concrete. Over a span of 30 years, the performance of

these bridges was evaluated; it was reported that galvanized reinforcement showed signs of corrosion, resulting in delamination of concrete when the chloride content exceeded the threshold to initiate corrosion.

Galvanized reinforcement is usually a black rebar coated with zinc coating up to a thickness of 75 to 125 microns, which is applied by a hot dipping galvanizing process. The coating acts as a barrier by isolating corrosion-inducing chemicals. Zinc corrosion products are usually more voluminous than iron corrosion products, thus developing less pressure on surrounding concrete. These bars perform better when the alkali content of the concrete is low. FHWA has stated that due to the increase in the alkali contents in cement (as a result of environmental regulations), the service life of galvanizing bars is decreasing.

Compared to epoxy-coated bars, galvanized bars can tolerate handling damage, avoiding defects to the bars. ACI committee 345 has stated that “At best, galvanized steel reinforcement is no better than non-galvanized reinforcement; further it is not as good as far as corrosion is concerned.” This project mainly focused on the long-term performance of the bridges by investigating various techniques such as measurement of electrical potentials on the top mat of the reinforcing steel, measurement of chloride ion content at the depth of reinforcement, measuring corrosion currents by using linear polarization technique, surveying for exposed deck areas to detect delamination, and measurement of clear concrete cover.

Based on the potential testing, it was found that a means of interpreting half-cell data was not currently available in the literature for galvanized reinforcements in concrete. As per ASTM C-876, if the passive layer is failing, the potential measure is more negative, indicating that corrosion activity is occurring.

The chloride ions present at the depth of the passive layer helps in breaking down the passive layer of oxide and allows for corrosion. The ratio of Cl/OH as well as oxygen availability influence the rate and threshold of corrosion. A conservative threshold value for corrosion initiation based on acid soluble chloride is about 0.025% by weight of concrete. Based on linear polarization techniques, the current and potential relationship close to the corrosion potential is determined. If a high current is applied, the corrosion rate is high and vice versa. This method can also be used for other types of reinforcements.

In the study, cores were drilled from the bridge and used to find the compressive strength and air void. Concrete is properly air-entrained if the air content of the hardened concrete exceeds 3%, the spacing factor is less than 0.23 mm, and the specific surface exceeds $25 \text{ mm}^2/\text{mm}^3$. Depth of the concrete cover has a direct relationship with the time of corrosion. A low concrete cover results in increased rates of corrosion. Pachometers or covermeters are used to estimate the depth of cover by using magnetic properties. The magnitude of distortion is proportional to the bar size and distance.

The three bridges that were studied in this project were Victoria steel bridge built in 1975, Bridge street bridge by replacing the deck in 1976 and Bathurst street bridge over Nordheimer Ravine, built in 1975. All these three bridges were built to Canadian standards. From the field study, the following conclusions were drawn:

- Corrosion of galvanizing reinforcing bars was initiated soon after the chloride corrosion threshold was reached at the top level of reinforcement.
- Corrosion caused serious delamination and cracking.
- Galvanizing bars, are not recommended as the primary means of corrosion protection for structures in Ontario.

- Waterproofing membrane, was effective in delaying the time of initiation of corrosion.
- Adequate concrete cover and excellent quality concrete would help in minimizing the corrosion rate.

Reinforcement alternative for concrete bridge decks (University of Kentucky, 2003) by Chris Hill, Choo Ching Chiaw, and Issam E. Harik

A project from the Kentucky Transportation Center (Hill et al., 2003) mainly dealt with the application of various reinforcement types in concrete bridge decks as a potential replacement. The reinforcements studied were epoxy-coated bars, stainless steel-clad bars, MMFX bars, and carbon fiber-reinforced polymer. The material properties of each material were evaluated and a full-scale, two-span reinforced concrete deck were tested to evaluate the performance. The stress-strain relation for each of the reinforcing bars was studied, and it was found that ECS (Epoxy Coated Steel) and SSC (Stainless Steel Clad) have a well-defined yield point, whereas MMFX reinforcement has initially linear stress-strain followed by an extensive non-linear response. CFRP reinforcement remains linear-elastic to failure.

Full-scale concrete slab panels with each type of reinforcement were tested to simulate actual loading conditions. When compared with AASHTO specifications, each panel exceeded the AASHTO guidelines for ultimate load. The final failure mode of all the specimens was in diagonal shear, and the specimens were ductile, providing ample warning before final failure. It was observed that considerable load distribution and cracking prior to failure indicated that each reinforcement type experienced sufficient straining to ensure ductile failure. The stress strain relationship for each reinforcement type was determined. Once the lab testing was noted to be satisfactory, the reinforcement types were deployed in the field in actual bridges. In a two-span bridge in Scott County, the longitudinal reinforcement used was ECS, whereas the transverse reinforcement in Span 1 was MMFX (top and bottom) and was SSC (top and bottom) in Span 2.

For the laboratory test, the specimen of size 7 ½” × 33” × 13’6” was considered. A six-foot span was simulated. The cover for the top mat of SSC, MMFX and CFRP panels was selected to be 1½” assuming ½” cover concrete is sacrificial concrete. Strain gages were used in each mat reinforcement at interested locations. LVDT was placed at the centerline of the support to study the movement at the support as well as at the mid-span to note the deflections due to flexure. Moment capacities of the slabs were determined experimentally and analytically, and they exceeded the AASHTO guidelines. The mobilization of strains in tensile reinforcement was adequately developed and full bending capacity of concrete section developed prior to diagonal shear failure.

Comparative performance of MMFX microcomposite reinforcing steel and other types of steel with respect to corrosion resistance and service life prediction in RC structures (AMEC Earth & Environmental, 2006)

A report by AMEC Earth & Environmental (2006) summarizes the usage of alternative reinforcement in bridge decks with respect to their performance and cost. There were various studies conducted by many universities and transportation agencies regarding this as summarized below.

In a study for the Virginia Transportation Research Council, Clemena and Virmani (2003) focused on MMFX2 micro-composite steel bars, R304 stainless steel bars, 2101 LDX duplex stainless steel bars, CB stainless steel-clad carbon steel bars, 316 L stainless steel bars, 2205 stainless steel bars, carbon steel with zinc coating, and epoxy-coated bars. Concrete blocks were made with different combinations of top and bottom reinforcements, as shown in Figure A.63.

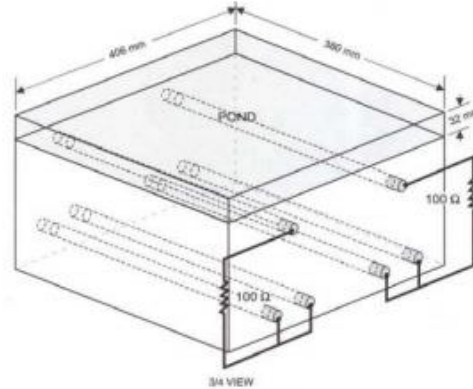


Figure A.63 Test Concrete Block (Clemena and Virmani (2003), as Presented in AMEC Earth & Environmental, 2006)

The test blocks were subjected to weekly cycles of 3 days of ponding with a saturated salt solution and 4 days of drying. Based on the polarization and open circuit potential measurements taken, the rate of corrosion was calculated using the Stern–Geary equation, and the following test results were achieved (Table A.9).

Table A.9 Various Corrosion Resistant Bars and the Corrosion Threshold

Bar	Time-to-Corrosion (day)	Chloride Threshold (ppm)	Threshold Ratio
CS (Straight & Bent)	90 to 95	460 to 580	1.0
316 LN (Straight)	> 895	> 5630	> 9.8 to 12.4
2205 (Straight)	> 895	> 5630	> 9.8 to 12.4
R304 (Straight)	> 895	> 5630	> 9.8 to 12.4
CB (Straight)	> 895	> 5630	> 9.8 to 12.4
MMFX-2 (Bent)	244 to 247	2700 to 2730	4.7 to 5.9
2101 LDX (Bent)	146 to 147	1550 to 1560	2.7 to 3.4
ZN-EC (Bent)	> 574	> 4630	> 8.0 to 10.1

Source: (Clemena and Virmani (2003), as presented in AMEC Earth & Environmental, (2006)).

The long-term costs of using different types of reinforcements were analyzed using the Life-365 service life model, based on the current rates specified by the Virginia Department of Transportation. At 100 years, the ZN-EC bars indicated the lowest cost, followed by the MMFX 2 bars, black steel, stainless clad bars; the 2101 LDX stainless bars had the highest cost. Estimation of life cycle did not include cracks on the bridge deck; if included, the curves would shift to the left, as shown in Figure A.64.

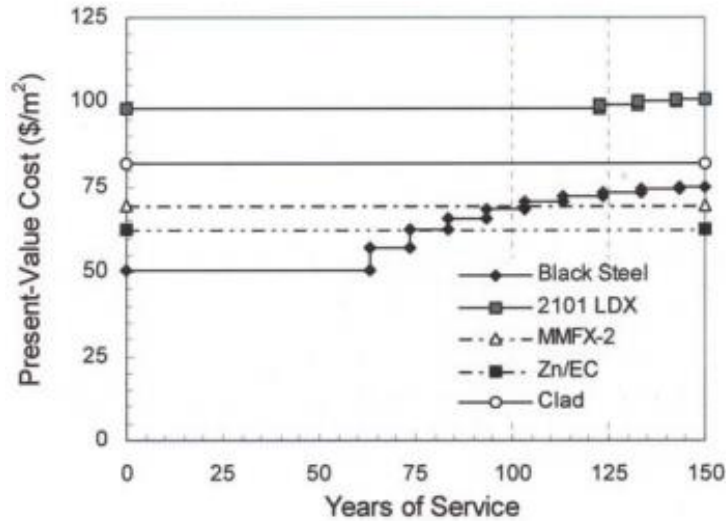


Figure A.64 Life Cycle Estimated from Life 365 Model (Clemena and Virmani (2003), as Presented in AMEC Earth & Environmental, (2006))

A.8 Summary of Literature Review

Cracking Due to Shrinkage and Freeze-Thaw

Shrinkage is the most common cause of early age cracking in bridge decks. The two main types of shrinkage are plastic (before hardening) and drying shrinkage (after hardening). The rate and severity of shrinkage are affected by several factors; these factors can be attributed to material properties, construction practices and design factors. When the tensile stresses exceed the concrete's modulus of rupture, cracking occurs.

Shrinkage reducing admixtures (SRA) reduce shrinkage by lowering the surface tension of pore water in both plastic and hardened concrete. There are two methods of application of SRA to concrete: one is impregnation or topical application, and the other is the integration of the SRA into the mix. Shrinkage reducing admixtures (SRA) and crack reducing admixtures (CRA) greatly reduce shrinkage with some side effects. Fiber is commonly used to mitigate shrinkage cracking in concrete. Its effect when used in combination with SRA or CRA is greatly advantageous. The addition of fiber significantly reduces the number and widths of cracks while improving freeze-thaw resistance and fatigue performance.

Structural Cracking

Many researchers and state transportation agencies have suggested the use of different concrete mixes, construction practices, placement procedures, and curing methods to reduce cracking, but the issue of cracking still remains widespread.

The crack width limitation equations proposed in ACI 224R-92, as well as current design specification provisions for flexural crack control (AASHTO 2012 and ACI 318-14) have been established with the maximum bar spacing specified to limit crack widths. However, merely satisfying these equations is inadequate for limiting crack widths to the corresponding

recommended values. Epoxy-coated bars cause wider cracking in bridge decks compared to conventional black bars. Repeated traffic loading causes these cracks to grow with time at a faster rate due to insufficient bond between the embedded bars and the surrounding concrete. Under sustained loading, the crack widths were observed to double over time, whereas the crack spacing remained unchanged (Nilson, 2010). Cyclic loading due to traffic volume causes the bars to slip from the surrounding concrete at the location of the cracks, leading to expansion of the cracks (Soltani, 2010). Use of fiber-reinforced concrete reduces crack widths significantly under flexural loading (Patnaik and Baah, 2015).

Corrosion of Slab Reinforcement

Defects caused on the epoxy coating of ECB during the site handling of bars lead to serious corrosion and peeling of the epoxy coating from the base steel (Patnaik and Gao, 2016). Corrosion of reinforcing bars affects the pull-out strength of the bars and will reduce the moment strength of reinforced concrete slabs. Addition of fiber to the concrete counteracts this deleterious effect and reduces the corrosion damage under sustained loading while providing significant resistance to crack formation and growth.

BIBLIOGRAPHY

- AASHTO (2012). AASHTO LRFD Bridge Design Specifications, Customary U.S. Units (6th Edition), American Association of State Highway and Transportation Officials, 4th Edition, Washington, D.C.
- AASHTO (2010). LRFD Bridge Design Specifications. 3rd Edition. American Association of State Highway and Transportation Officials, Washington, D.C.
- AASHTO PP34-99 (1999). “Standard Practice for Estimating the Cracking Tendency of Concrete.” American Association of State Highway and Transportation Officials, Washington, D.C.
- AASHTO T 22 “Standard Method of Test for Compressive Strength of Cylindrical Concrete Specimens.” American Association of State Highway and Transportation Officials, Washington, D.C. 2017.
- AASHTO T 161 “Standard Method of Test for Resistance of Concrete to Rapid Freezing and Thawing.” American Association of State Highway and Transportation Officials, Washington, D.C. January 2017.
- American Concrete Institute (ACI; 1966). “American concrete standards.” Detroit, Octavo, pp:300
- ACI 224.1R-93 “Causes, Evaluation and Repair of Cracks in Concrete Structures,” ACI Committee 224, American Concrete Institute, Farmington Hills, MI. (Reapproved 1998).
- ACI 224R.2R-92 “Cracking of Members in Direct Tension,” ACI Committee 224, American Concrete Institute, Farmington Hills, MI. (Reapproved 1997).
- ACI 224R-01 “Control of Cracking of Concrete Structures,” ACI Committee 224, American Concrete Institute, Farmington Hills, MI. 2008.
- ACI 224R-01 “Control of Cracking of Concrete Structures,” ACI Committee 224, ACI Manual of Concrete Practice, Part 2, American Concrete Institute, Farmington Hills, MI. 2003.
- ACI 318-95 “Building Code Requirements for Reinforced Concrete and Commentary,” American Concrete Institute, Farmington Hills, MI. 1995.
- ACI 318-08 “Building Code Requirements for Reinforced Concrete and Commentary,” American Concrete Institute, Farmington Hills, MI. 2008.
- ACI 318-11 “Building Code Requirements for Structural Concrete and Commentary,” American Concrete Institute, Farmington Hills, MI. 2011.
- ACI 318-14 “Building Code Requirements for Structural Concrete and Commentary,” American Concrete Institute, Farmington Hills, MI. 2014.
- Ah-Sha, H.H., Sanders, D.H., and Saiidi, M.S. (2001) Early Age Shrinkage and Cracking of Nevada Concrete Bridge Decks, Report No. RDT01-010, Nevada Department of Transportation, Carson City. October.

- Alonso, C., Andrade, C., Rodriguez, J., and Diez, J.M. (1998). Factors controlling cracking of concrete affected by reinforcement corrosion. *Materials and Structures*, 31(211): 435–441.
- Aly, T., Sanjayan, J.G., and Collins, F. (2008). Effect of polypropylene fibers on shrinkage and cracking of concretes. *Materials and Structures* 41:1741. Available at <https://link.springer.com/article/10.1617/s11527-008-9361-2>
- Alhozaimy, A.M., Soroushian, P., and Mirza, F. (1996). Mechanical properties of polypropylene fiber reinforced concrete and the effects of pozzolanic materials. *Cement and Concrete Composites*, 18(2): 85-92.
- AMEC Earth & Environmental (2006). Comparative performance of MMFX microcomposite reinforcing steel and other types of steel with respect to corrosion resistance and service life prediction in RC structures. AMEC Americas Limited, Burnaby, British Columbia. Available at: http://mmfx.com/doc2/Comparative_Performance_Morgan.pdf
- ASTM 39 “Standard Test Method for Compressive Strength of Cylindrical Concrete Specimens” ASTM International, West Conshohocken, PA. 2017. Available at <https://www.astm.org/Standards/C39.htm>
- ASTM A501 / A501M-14 “Standard Specification for Hot-Formed Welded and Seamless Carbon Steel Structural Tubing.” ASTM International, West Conshohocken, PA. 2014. Available at <https://www.astm.org/Standards/A501.htm>
- ASTM A955 (2009). “Standard Specification for Deformed and Plain Stainless-Steel Bars for Concrete Reinforcement.” ASTM International, West Conshohocken, PA.
- ASTM C143 / C143M-15a “Standard Test Method for Slump of Hydraulic-Cement Concrete.” ASTM International, West Conshohocken, PA. 2015. Available at <https://www.astm.org/Standards/C143.htm>
- ASTM C 157, “Standard Test Method for Length Change of Hardened Hydraulic-Cement Mortar and Concrete.” ASTM International, West Conshohocken, Pennsylvania
- ASTM C192 / C192M-16a “Standard Practice for Making and Curing Concrete Test Specimens in the Laboratory.” ASTM International, West Conshohocken, Pennsylvania. 2016. Available at <https://www.astm.org/Standards/C192.htm>
- ASTM C231 / C231M-17a “Standard Test Method for Air Content of Freshly Mixed Concrete by the Pressure Method.” ASTM International, West Conshohocken, Pennsylvania. 2017. Available at <https://www.astm.org/Standards/C231.htm>
- ASTM C469 “Standard Test Method for Static Modulus of Elasticity and Poisson’s Ratio of Concrete in Compression, ASTM International, West Conshohocken, Pennsylvania. 2014. Available at <https://www.astm.org/Standards/C469.htm>
- ASTM C490 “Standard Practice for Use of Apparatus for the Determination of Length Change of Hardened Cement Paste, Mortar, and Concrete.” ASTM International, West

- Conshohocken, Pennsylvania. 2017. Available at <https://www.astm.org/Standards/C490.htm>
- ASTM C496 “Standard Test Method for Splitting Tensile Strength of Cylindrical Concrete Specimens.” ASTM International, West Conshohocken, PA. 2011. Available at <https://www.astm.org/Standards/C496>
- ASTM C666 “Standard Test Method for Resistance of Concrete to Rapid Freezing and Thawing.” ASTM International, West Conshohocken, Pennsylvania. 2015. Available at <https://www.astm.org/Standards/C666.htm>
- ASTM C1116 “Standard Specification for Fiber-Reinforced Concrete.” ASTM International, West Conshohocken, Pennsylvania. 2015. Available at <https://www.astm.org/Standards/C1116.htm>
- ASTM C1581 “Standard Test Method for Determining Age at Cracking and Induced Tensile Stress Characteristics of Mortar and Concrete under Restrained Shrinkage.” ASTM International, West Conshohocken, Pennsylvania. 2016. Available at <https://www.astm.org/Standards/C1581.htm>
- ASTM G109 (2007). “Standard Test Method for Determining Effects of Chemical Admixtures on Corrosion of Embedded Steel Reinforcement in Concrete Exposed to Chloride Environments. ASTM International, West Conshohocken, Pennsylvania.
- Azad, A.K., Ahmad, S., and Azher, S.A. (2007). Residual strength of corrosion-damaged reinforced concrete beams. *ACI Materials Journal*, 104(1): 40–47.
- Babaei, K., and Purvis, R., (1994). “Prevention of Cracks in Concrete Bridge Decks: Report on Laboratory Investigation of Concrete Shrinkage,” Research Project No. 89-01, Pennsylvania Department of Transportation, Harrisburg, PA.
- Badawi, M., and Soudki, K. (2005). Control of corrosion induced damage in reinforce concrete beams under carbon fiber-reinforced polymer laminates. *Journal of Composites for Construction*, 9(2): 195–201.
- Bajaj et al., (2012). “Effect of corrosion on physical and mechanical properties of reinforced concrete,” Ohiolink, pp:169
- Balaguru, P., and Ramakrishnan, V. (1986). “Mechanical properties of superplasticized fiber reinforced concrete developed for bridge decks and highway pavements, ” American Concrete Institute, Special Publication SP- 93, Concrete in Transportation, ACI, Detroit, NH, 563–584.
- Ballim, Y., Reid, J.C., and Kemp, A.R. (2001). Deflection of RC beams under simultaneous load and steel corrosion. *Magazine of Concrete Research*, 53(3): 171–181.
- Ballim, Y., and Reid, J.C. (2003). Reinforcement corrosion and the deflection of RC beams - an experimental critique of current test methods. *Cement and Concrete Composites*, 25(6): 625–632.

- Bentz, D.P., Geiker, M.R., and Hansen, K.K. (2001). Shrinkage-Reducing Admixtures and Early Age Desiccation in Cement Pastes and Mortars. *Cement and Concrete Research* 31(7): 1075–1085.
- Bentz, D.P. (2007). A review of early-age properties of cement-based materials. *Cement and Concrete Research* 38:196–204.
- Bentz, D.P., and Peltz, M.A. (2008). Reducing Thermal and Autogenous Shrinkage Contributions to Early-Age Cracking. *ACI Materials Journal*, 105(4): 414–420.
- Berke, N.S., and Dallaire, M.P. (1997) “Drying shrinkage cement admixture.” U.S. Patent Number 5,622,558. April 22.
- Berkowski, P., and Kosior-Kazberuk, M. (2015). Effect of Fiber on the Concrete Resistance to Surface Scaling Due to Cyclic Freezing and Thawing. *Procedia Engineering* 111:121– 127.
- Bhagwat, Y. (2014). Effect on Super Structure of Integral Abutment Bridge under Fixed and Pinned Pile Head Connections. *Civil and Environmental Research*, 6(9): 97–107.
- Borosnyoi, A., and Balazs, G. L. (2005). Models for flexural cracking in concrete: the state of art. *Structural Concrete* 6(2): 53–62.
- Broms, B. B. (1965a), "Technique for Investigation of Internal Cracks in Reinforced Concrete Members," *ACI Journal, Proceedings*, Vol.62, No.1, pp. 35–43.
- Broms, B. B. (1965b), "Crack Width and Crack Spacing in Reinforced Concrete Members," *ACI Journal Proceedings*, Vol.62, No.10, pp. 1237–1255.
- Cairns, J., Du, Y., and Law, D. (2008). Structural performance of corrosion-damaged concrete beams. *Magazine of Concrete Research*, 60(5): 359–370.
- California Department of Transportation (CalTrans, 2015). “Loads and Load Combinations” In: *Bridge Design Practice*, California Department of Transportation, Sacramento, California. February.
- Carnate, G. (2014). Shrinkage Reducing Admixture Usage in Hawaii Bridge Decks. *Concrete Bridge Views*, 77(July/August).
- Castel, A., Vidal, T., Francois, R. and Arliguie, G. (2003). Influence of steel-concrete interface quality on reinforcement corrosion induced by chlorides. *Magazine of Concrete Research*, 55(2): 151–159.
- Cheng, T.T.H. and Johnston, D.W. (1985). Incidence Assessment of Transverse Cracking in Concrete Bridge Decks: Construction and Material Considerations, Report No. FHWA/NC/S5-002 Vol. 1, North Carolina State University at Raleigh, Department of Civil Engineering, 232 pp.
- China Standard, 2002c. Code for Design of Concrete Structure (GB/T50081-SD105-82).

- Cleary, D.B., and Ramirez, J.A. (1991). Bond of Epoxy-Coated Reinforcement. *ACI Materials Journal*, 88(2): 146–149.
- Clemena, G.G., and Virmani, Y.P. (2003). Comparison of Corrosion Resistance of Some New Metallic Reinforcing Bars in Concrete Blocks Exposed to Chloride Ions. Presented at Corrosion 2003, San Diego, California, 16–20 March. NACE International. Available at <https://www.onepetro.org/conference-paper/NACE-03298>
- Darwin, D., Browning, J., and Lindquist, W. (2004). “Control of Cracking in Bridge Decks: Observations from the Field,” *Cement, Concrete, and Aggregates*, 26(2):148–154.
- Darwin, A.B., Scantlebury, J.D. (2002). Retarding of corrosion processes on reinforcement bar in concrete with an FBE coating. *Cement and Concrete Composites*, 24(1): 73–78.
- Deepthi, V., Sabeena, M.V. (2016) Experimental and Analytical Study on Bond Performance of Reinforced Bars Embedded in Fibre Reinforced Concrete. *International Journal of Innovative Research in Science, Engineering and Technology*, 5(8): 14704–14714.
- El Maaddawy, T.A., and Soudki, K.A. (2003). Effectiveness of impressed current technique to simulate corrosion of steel reinforcement in concrete. *Journal of Materials in Civil Engineering*, 15(1): p. 41–47.
- El Maaddawy, T., Soudki, K., and Topper, T. (2005). Long-term performance of corrosion-damaged reinforced concrete beams. *ACI Structural Journal*, 102(5): 649–656.
- Elfgrén, L. and Gylltoft, K. (1977). “Statens rad för byggnadsforskning” (“Fatigue strength of infrastructures”), Publication no.R68:1977, Spångbergs Tryckerier AB (State Council for Building Research), Stockholm, Sweden, pp. 160. [In Swedish]
- Erdogdu, S., Bremner, T.W., and Kondratova, I. L. (2001). Accelerated testing of plain and epoxy-coated reinforcement in simulated seawater and chloride solutions. *Cement and Concrete Research*, 31(6): p. 861–867.
- Esfahani R, Rangan V. (1998). Bond between normal strength and high strength concrete and reinforcing bars in splices in beams. *ACI Structural Journal*, 95(3): 272–280.
- Fang, C.Q., Lundgren, K., Chen, L., and Zhu, C. (2004). Corrosion influence on bond in reinforced concrete. *Cement and Concrete Research*, 34(11): p. 2159–2167.
- Fanous, F., Wu, H., and Pape, J. (2000). Impact of deck cracking on durability, Center for Transportation Research and Education, Iowa State University, Ames, IA. March.
- Fickelson, M. (1988). “The impact of Robert L’Hermitte on the evolution of creep and shrinkage theory” in *Mathematical Modeling of Creep and Shrinkage of Concrete* (Z.P. Bazant , editor). Wiley, Chichester, N.Y.
- Folliard, K. J., and Berke, N. S. (1997). Properties of high-performance concrete containing a shrinkage-reducing additive. *Cement and Concrete Research*, 27(9), 1357–1364.

- François R., Arliguie G. (1998). Influence of service cracking on reinforcement steel corrosion. *Journal of Materials in Civil Engineering*, 10(1):14–20.
- French, C.E., Eppers, L.J., Le, Q.T., and Hajjar, J.F. (1999). "Transverse Cracking in Bridge Decks: Summary Report" Report No. MNIRC-1999-05, Minnesota Department of Transportation, St. Paul, Minnesota.
- Frosch, R.J. (1999). Another Look at Cracking and Crack Control in Reinforced Concrete. *ACI Struct. J.* 96 (3) 437–442.
- Frosch, R. J. (1999), "Another Look at Cracking and Crack Control in Reinforced Concrete," *ACI Structural Journal*, Vol. 96, No. 3, pp. 437-442.
- Gao, Z.C., Liang, R., and Patnaik, A.K. (2016a). Mass Loss and Capacity Loss of Reinforced Concrete Slabs with and without Polypropylene Fibers Corroded with Pre-existing Cracks and Sustained Loading. *NACE Corrosion Risk Management Conference*, Houston, Texas. p. 10.
- Gao Z., Liang, R.Y., and Patnaik, A.K. (2016b) Effects of sustained loading and pre-existing cracks on corrosion behavior of reinforced concrete slabs. *Construction and Building Materials*, 124: 776–785.
- Gergely, P. and Lutz, L. A., (1968) "Maximum Crack Width in Reinforced Flexural Members," Causes, Mechanisms and Control of Cracking in Concrete, ACI SP-20, American Concrete Institute, Detroit, pp. 87–117.
- Goto, Y. (1971). "Cracks Formed in Concrete around Deformed Tension Bars," *ACI Journal*, Proceedings, 68(4): 244–251.
- Goto, T., Sato, T., Sakai, K., and Ii, M. (1985). CEMENT-SHRINKAGE-REDUCING AGENT AND CEMENT COMPOSITION. U.S. Patent Number 4,547,223. October 15.
- Grzybowski, M., and Shah, S. P. (1990). Shrinkage cracking of fiber reinforced concrete. *ACI Materials Journal*, 87(2), 138–148.
- Hill, C., Chiaw, C.C., and Harik, I.E. (2003). Reinforcement Alternatives for Concrete Bridge Decks. *Kentucky Transportation Center Research Report*. 231. Report No. KTC-03-19/SPR215-00-1F. <http://dx.doi.org/10.13023/KTC.RR.2003.19>
- Hou, G., and Chen, S. (2017). Bent Connection Options for Curved and Skewed SMC Bridges in Low-to-Moderate Seismic Regions. *Practice Periodical on Structural Design and Construction*, 22(4):04017011.
- Ideker, J.H., Fu, T.F., and Deboodt, T. (2013). Development of Shrinkage Limits and Testing Protocols for ODOT High Performance Concrete, Report No. FHWA-OR-RD-14-09. Oregon Department of Transportation, Salem, Oregon. December.

- Iowa Department of Transportation (IowaDOT, 2006). OFFICE OF BRIDGES AND STRUCTURES. Retrieved from: <https://iowadot.gov/bridge/bridge-and-culvert-standards/bridge-standards>
- Issa, M. A. (1999). Investigation of cracking in concrete bridge decks at early ages. *Journal of Bridge Engineering*, 4(2), 116–124. DOI: [10.1061/\(ASCE\)1084-0702\(1999\)4:2\(116\)](https://doi.org/10.1061/(ASCE)1084-0702(1999)4:2(116))
- Kanakubo, T., Oyado, M., and Saito, Y. (2008). Study on local bond behavior between corroded reinforcement and concrete. Proceedings of the 3rd ACF International Conference Ho-Chi-Minh City, November, pp: 1146-1152. Kraii, P. P., (1985). “Proposed Test to Determine the Cracking Potential Due to Drying.” *Concrete Construction* 30 (9): 775–778.
- Karr, P.H., and Mattock, A.H. (1963). High-strength bars as concrete reinforcement – Part 4: Control of cracks. *Journal of the PCA Research Development Laboratories* 5 (1): 15–38.
- Kraii, P.P. (1985). A proposed test to determine the cracking potential due to drying shrinkage of concrete. Publication # C850775. The Aberdeen Group. Available at <http://www.concreteconstruction.net/view-object?id=00000153-8ba6-dbf3-a177-9fbfab6e0000>
- Krauss, P. D., and Rogalla, E. A., (1996) “Transverse Cracking in Newly Constructed Bridge Decks,” NCHRP Report 380, Transportation Research Board, National Research Council, Washington, D. C., USA.
- L’Hermite, R. (1988). Mathematical modeling of creep and shrinkage of concrete. Z. P. Bazant (Ed.). Chichester: Wiley.
- Li, V.C. (1992). Postcrack scaling relations for fibre reinforced cementitious composites. *Journal of Materials in Civil Engineering* 4(1):41–57.
- Li, B.X., Chen, M.X., Cheng, F., and Liu, L.P. (2004). The mechanical properties of polypropylene fiber reinforced concrete. *Journal of Wuhan University of Technology-Materials Science Edition*, 19(3): 68–71.
- Liu, Y.P., and Weyers, R.E., (1998). Modeling the time-to-corrosion cracking in chloride contaminated reinforced concrete structures. *ACI Materials Journal*, 95(6): 675–681.
- Lura, P., Pease, B., Mazzotta, G.B., Rajabipour, F., Weiss, J. (2007). Influence of shrinkage-reducing admixtures on development of plastic shrinkage cracks. *ACI Mater J.* 104 (2): 187–194.
- Maalej, M., Li, V.C., and Hashida, T. (1995). Effect of fibre rupture on tensile properties of short fibre composites. *Journal of Engineering Mechanics* 121(8):903–13.
- Maggenti, R., Knapp, C., and Ferreira, S. (2013). Controlling Shrinkage Cracking: Available technologies can provide nearly crack-free concrete bridge decks. *Concrete International* (July 2013): 36–41.

- Malumbela, G., Moyo, P., and Alexander, M. (2009). Behaviour of RC beams corroded under sustained service loads. *Construction and Building Materials*, 23(11): p. 3346-3351.
- Mangat, P.S., Elgarf, M.S. (1999). Flexural strength of concrete beams with corroding reinforcement. *ACI Structural Journal*, 96(1): 149–158.
- Mansoor, Y.A., and Zhang, Z.Q. (2013). The Reinforcement Bond Strength Behavior under Different Corrosion Condition. *Research Journal of Applied Sciences, Engineering and Technology* 5(7): 2346–2353.
- Matsumoto, T. (1998). Fracture mechanics approach to fatigue life of discontinuous fibre reinforced composites. Doctoral Thesis, Department of Civil and Environmental Engineering, University of Michigan, Ann Arbor, Michigan.
- McDonald, D. B., Krauss, P. D., and Rogalla, E.A., (1995) “Early-Age Transverse Deck Cracking,” *Concrete International*, 17(5): 49.
- Mimura, Y., Yoshitake, I., and Zhang, W. (2011). Uniaxial Tension Test of Slender Reinforced Early Age Concrete Members. *Materials* 4(8): 1345–1359.
- Minnesota Department of Transportation (2011). Bridge Deck Cracking. Transportation Research Synthesis 1105. Minnesota Department of Transportation, St. Paul, Minnesota. Available at <https://lrrb.org/media/reports/TRS1105.pdf>
- Mora-Ruacho, J., Gettu, R., and Aguado, A. 2009. Influence of Shrinkage-Reducing Admixtures on the Reduction of Plastic Shrinkage Cracking in Concrete. *Cement and Concrete Research*, 39 (3): 141–146.
- Neville, A.M., and Brooks, J.J. (1987) *Concrete Technology*. Longman Scientific and Technical, Harlow, England.
- Ng, P. L., Lam, J. Y. K., and Kwan, A. K. H. (2010). “Tension stiffening in concrete beams. Part 1: FE analysis.” *Proc., Institution of Civil Engineers, Structures and Buildings*, 163(1), 19–28.
- Nguyen, T., Martin, J.W., (2004). Modes and mechanisms for the degradation of fusion-bonded epoxy-coated steel in a marine concrete environment. *Journal of Coatings Technology and Research*, 1(2): 81-92.
- Nilson, A., Darwin, D., and Dolan, C. (2010) *Design of Concrete Structures*, 14th Edition, McGraw-Hill Book Co., New York.
- Nmai, C.K., Tomita, R., Hondo, F. and Buffenbarger, J. (1998). Shrinkage-reducing admixtures. *Concrete International*, 20 (4): 31–37.
- Nmai, C.K., Vojtko, D., Schaef, S., Attiogbe, E.K., and Bury, M.A. (2014). “Crack-Reducing Admixture”, *Concrete International*, Vol. 36, No. 1, pp 53–57.
- ODOT “Standard Drawing CS-01-03.” Ohio Department of Transportation, Columbus, OH. 2003.

- ODOT “Standard Drawing CS-01-08. Continuous Slab Bridge”. Ohio Department of Transportation, Columbus, OH. 2008. Available at <https://www.dot.state.oh.us/Divisions/Engineering/Structures/standard/Bridges/Standard%20Drawings/CS-1-08.pdf>
- ODOT QC/QA Concrete Pavement with Warranty. Supplemental Specification 896. Ohio Department of Transportation, Columbus, OH. April 15, 2015. Available at http://www.dot.state.oh.us/Divisions/ConstructionMgt/Specification%20Files/896_04152005_f or 2005.PDF
- Olsson, K., and Pettersson, J. (2010). Fatigue Assessment Methods for Reinforced Concrete Bridges in Eurocode. Master’s Thesis. Department of Civil and Environmental Engineering, Chalmers University of Technology, Göteborg, Sweden.
- Orangun, C.O., Jirsa, J.O., and Breen, J.E. (1977). Reevaluation of Test Data on Development Length and Splices. *ACI Journal, Proceedings*, 74 (3): 114–122.
- Paillère, A. M., Buil, M., and Serrano, J. J. (1989) “Effect of Fiber Addition on the Autogenous Shrinkage of Silica Fume Concrete,” *ACI Materials Journal*, Vol. 86, No. 2, Mar.-Apr., pp. 139–144.
- Palacios, M., and Puertas, F. (2007). Effect of shrinkage-reducing admixtures on the properties of alkali-activated slag mortars and pastes. *Cement and Concrete Research* 37: 691–702.
- Patnaik, A.K., Ramakrishnan, and V., Zellar, R., (2007) Plastic Shrinkage Reduction Potential of a new High Tenacity Monofilament Polypropylene Fiber, in American Concrete Institute ACI/CANMET Special Publication SP243 on Recent Advances in Concrete Technology - Editor: V.M. Malhotra, pp. 49-62.
- Patnaik. A. and P. Baah. (2015). “Cracking Behavior of Structural Slab Bridge Decks,” Report No. FHWA/OH-2015/4. Ohio Department of Transportation, Columbus, OH. January. Available at https://www.dot.state.oh.us/Divisions/Planning/SPR/Research/reportsandplans/Reports/2015/Structures/134708_FR.pdf
- Pedersen C. (1996). New production processes, materials and calculation techniques for fibre reinforced concrete pipes. PhD Thesis, Series R, No. 14, Department of Structural Engineering and Materials, Technical University of Denmark, Kongens Lyngby, Denmark.
- Pianca, F., and Schell, H. (2005), "The Long Term Performance of Three Ontario Bridges Constructed with Galvanized Reinforcement," Ontario Ministry of Transportation, Downsview, Ontario, 30 pp.
- Pipinato, A. (2015). *Innovative Bridge Design Handbook: Construction, Rehabilitation and Maintenance*. 1st Ed. Elsevier, New York.
- Portland Cement Association (PCA; 1970). “Durability of Concrete Bridge Decks,” Final Report of a Cooperative Study, No. EB067.01E.

- Poursaee, A., and Hansson, C.M. (2009). Potential pitfalls in assessing chloride-induced corrosion of steel in concrete. *Cement and Concrete Research* 39(5): p. 391–400.
- Qian, C., and Stroeven, P. (2000). Fracture properties of concrete reinforced with steel–polypropylene hybrid fibres. *Cement and Concrete Composites*, Volume 22, Issue 5, pp. 343–351.
- Rajabipour, F., Sant, G., and Weiss, J. (2008). Interactions between Shrinkage Reducing Admixtures and Cement Paste’s Pore Solution, *Cement and Concrete Research*, 38 (5) 606–615.
- Ramey, G. E., Wolff, A. R., and Wright, R. L., (1997). “Structural Design Actions to Mitigate Bridge Deck Cracking,” *Practice Periodical on Structural Design and Construction*, Vol. 2, No. 3, pp. 118–124.
- Rasidi, N., Soehardjono, A. M. D., and Zacoeb, A., (2013) “Crack width prediction in precast deck slab concrete structure,” *International Journal of Engineering and Technology*, 3 (1): 21–27.
- Rio, O., Andrade, C., Izquierdo, D., and Alonso, C. (2005). Behavior of patch-repaired concrete structural elements under increasing static loads to flexural failure. *Journal of Materials in Civil Engineering*, 17(2): 168–177.
- Russell, H.G. (2004). National Cooperative Highway Research Program Synthesis 333: Concrete Bridge Deck Performance, Transportation Research Board, Washington, D.C.
- Schmitt, T. R., and Darwin, D. (1995). “Cracking in Concrete Bridge Decks,” Report No. K-TRAN: KU-94-1, Final Report, Kansas Department of Transportation.
- Schmitt, T. R. and Darwin, D. (1999). “Effect of Material Properties on Cracking in Bridge Decks,” *Journal of Bridge Engineering*, ASCE, Vol. 4, No. 1, February, pp. 8–13.
- Shah, S., Marikunte, S., Yang, W., and Aldea, C. (1997). Control of Cracking with Shrinkage-Reducing Admixtures. *Transportation Research Record* 1574: 25–36.
- Shang, H.-S., and Yi, T.-H. (2013). Freeze-Thaw Durability of Air-Entrained Concrete. *Scientific World Journal*, Volume 2013, Article ID 650791, 6 pages. Available at <https://www.hindawi.com/journals/tswj/2013/650791/>
- Shing, P.B., and Abu-Hejleh, N. (1999). “Cracking in Bridge Decks: Causes and Mitigation,” Report No. CDOT-DTD-R-99-8. Colorado Department of Transportation, August.
- Sim and Frosch (2014). “Structural and Corrosion Performance of Concrete Bridge Decks Reinforced with Corrosion-Resistant Reinforcing Steel”, Ph.D. Thesis, Purdue University, USA.
- Soltani, A., (2010) “Bond and Serviceability Characterization of Concrete Reinforced with High Strength Steel,” Ph.D. Thesis, University of Pittsburgh, USA.

- Soltani, A., Harries, K.A., and Shahrooz, B.M. (2013). Crack Opening Behavior of Concrete Reinforced with High Strength Reinforcing Steel. *International Journal of Concrete Structures and Materials*, Volume 7, Issue 4, pp 253–264.
- Standards Association of Australia (2009) “SAA Concrete Structures Code,” AS 3600, Sydney, Australia.
- Standards New Zealand (1982). NZS 3101.1: Concrete structures standard - Code of practice for the design of concrete structures. New Zealand Ministry of Business, Innovation & Employment, Wellington, New Zealand.
- Stewart, C.F., and Gunderson, B.J. (1969). Factors Affecting the Durability of Concrete Bridge Decks. Interim Report No.2, Research and Development Section of Bridge Department, State of California, November 1969.
- Tada, H., Paris, P.C., and Irwin, G.R. (1985). *The Stress Analysis of Cracks Handbook*, 2nd edition. Paris Productions Corp and Del Research Corp.
- Torres-Acosta, A.A., Navarro-Gutierrez, S., and Terán-Guillén, J. (2007). Residual flexure capacity of corroded reinforced concrete beams. *Engineering Structures*, 29(6): 1145–1152.
- Transportation Research Board (TRB; 2004). National Cooperative Highway Research Program (NCHRP) Synthesis 333: Concrete Bridge Deck Performance examines previous and current design and construction practices designed to improve the performance of bridge decks. Transportation Research Board, Washington, D.C. DOI: [10.17226/17608](https://doi.org/10.17226/17608)
- Transportation Research Committee (TRC; 2006) Control of Cracking in Concrete: State of the Art. Bulletin No. E-C107. Transportation Research Board, Washington, D.C. October. TRS1105, 2011
- Treese, R. A., and Jirsa, J. O., (1989) “Bond Strength of Epoxy-Coated Reinforcing Bars,” *ACI Materials Journal*, Vol. 86, No. 2, Mar-Apr., pp. 167–174.
- Tritsch, N., Darwin, D. and Browning J. (2005) “Evaluating Shrinkage and Cracking Behavior of Concrete Using Restrained Ring and Free Shrinkage Tests,” SM Report No. 77, University of Kansas Center for Research, Inc., Lawrence, Kansas, January, pp. 178.
- Vaziri, N. (2016). 2d vs 3d Analysis of super-structure for curved box girder bridges and effect of curvature on bridge response. M.Sc. Thesis. California State University, Department of Civil Engineering, Sacramento, California. Available at: <https://csus-dspace.calstate.edu/bitstream/handle/10211.3/175536/2016VaziriNavid.pdf?sequence=1>
- Vidal, T., Castel, A., and Francois, R. (2007). Corrosion process and structural performance of a 17 year old reinforced concrete beam stored in chloride environment. *Cement and Concrete Research*, 37(11): p. 1551–1561.

- Weiss, W. J., and Berke, N. S., (2002) “Admixtures for Reducing Shrinkage and Cracking,” Early-Age Cracking in Cementitious Systems – State of the Art Report (A. Bentur, ed.).
- Whittmann, F. H. (1976). On the Action of Capillary Pressure in Fresh Concrete. *Cement and Concrete Research*, 6: 49–56.
- Xia, N., Ren, Q., Liang, R., Payer, J., and Patnaik, A. (2011). Nonuniform corrosion-induced stresses in steel-reinforced concrete. *Journal of Engineering Mechanics*, 138(4): 338–346.
- Xia, N., Liang, R.Y., Payer, J., and Patnaik, A. (2013). Probabilistic modelling of the bond deterioration of fully-grouted rock bolts subject to spatiotemporally stochastic corrosion. *Structure and Infrastructure Engineering*, 9(11): 1161–1176.
- Yoon, S., Wang K., Weiss, W.J., and Shah, S.P. (2000). Interaction between loading, corrosion, and serviceability of reinforced concrete. *ACI Materials Journal*, 97(6): 637–644.
- Yuan, Y.J., Ji, Y.S., and Mu, Y. (2007). Propagation and model of distribution for corrosion of steel bars in concrete. *China Civil Engineering Journal*, 40: 5–11.
- Yuan, Y.S., and Ji, Y.S. (2009). Modeling corroded section configuration of steel bar in concrete structure. *Construction and Building Materials*, 23(6): 2461–2466.
- Zhang, R.J., Castel, A., and Francois, R. (2010). Concrete cover cracking with reinforcement corrosion of RC beam during chloride-induced corrosion process. *Cement and Concrete Research*, 40(3): 415–425.
- Zhang, J., Stang, H., and Li, V.C. (1999). Fatigue life prediction of fiber reinforced concrete under flexural load. *International Journal of Fatigue* 21:1033–1049.
- Zuo, J., and Darwin, D. (2000). Splice Strength of Conventional and High Relative Rib Area Bars in Normal and High-Strength Concrete. *ACI Structural Journal*, 97 (4): 630–641.

Reduction of Bridge Deck Cracking through Alternative Material Usage

APPENDIX B CRACK SURVEYS OF BRIDGES

Prepared by:
Anil Patnaik, Ph.D.
and
Srikanth Marchetty

Prepared for:
The Ohio Department of Transportation,
Office of Statewide Planning & Research

State Job Number 135260
November 2017
Draft Final Report



TABLE OF CONTENTS

TABLE OF CONTENTS.....	1
LIST OF FIGURES	3
LIST OF TABLES.....	5
APPENDIX B.....	6
CRACK SURVEYS OF BRIDGES	6
B.1 CONCLUSIONS DRAWN FROM AN EARLIER PROJECT ON BRIDGE DECK CRACKING	6
B.2 BRIDGES CONSIDERED FOR SURVEY IN THE CURRENT PROJECT	8
B.3 CRACK SURVEY AND CRACK MAPPING OF BRIDGES INSPECTED	11
<i>B.3.1 Bridge FAI-37-7360 (District 5)</i>	15
<i>B.3.2 Bridge PER-668-1000 (District 5)</i>	16
<i>B.3.3 Bridge PER-668-9990 (District 5)</i>	17
<i>B.3.4 Bridge PER-22-12020 (District 5)</i>	18
<i>B.3.5 Bridge MUS-146-20920 (District 5)</i>	19
<i>B.3.6 Bridge COS-79-0160 (District 5)</i>	20
<i>B.3.7 Bridge MAD-323-15420 (District 6)</i>	21
<i>B.3.8 Bridge MAD-323-12230 (District 6)</i>	22
<i>B.3.9 Bridge MAD-323-14450 (District 6)</i>	23
<i>B.3.10 Bridge MAD-323-2800 (District 6)</i>	24
<i>B.3.11 Bridge MAD-38-18090 (District 6)</i>	25
<i>B.3.12 Bridge SHE-47-11520 (District 7)</i>	26
<i>B.3.13 Bridge CLA-235-2570 (District 7)</i>	27
<i>B.3.14 Bridge DAR-118-8490 (District 7)</i>	28
<i>B.3.15 Bridge DAR-722-6340 (District 7)</i>	29
<i>B.3.16 Bridge AUG-29-565 (District 7)</i>	30
<i>B.3.17 Bridge AUG-219-7210 (District 7)</i>	31
<i>B.3.18 Bridge DAR-705-0902 (District 7)</i>	32
<i>B.3.19 Bridge DAR-705-0947 (District 7)</i>	33
<i>B.3.20 Bridge DAR-705-10330 (District 7)</i>	34
<i>B.3.21 Bridge PRE-732-16580 (District 8)</i>	35

<i>B.3.22 Bridge PRE-503-21210 (District 8)</i>	36
<i>B.3.23 Bridge ATH-78-8310 (District 10)</i>	37
<i>B.3.24 Bridge VIN-278-8590 (District 10)</i>	38
<i>B.3.25 Bridge HOC-56-17960 (District 10)</i>	39
<i>B.3.26 Bridge HOC-56-16470 (District 10)</i>	40
<i>B.3.27 Bridge HOC-595-6040 (District 10)</i>	41
<i>B.3.28 Bridge HOL-83-15100 (District 11)</i>	42
<i>B.3.29 Bridge HOL-520-6440 (District 11)</i>	43
<i>B.3.30 Bridge BEL-148-3140 (District 11)</i>	44
B.4 SUMMARY AND CONCLUSIONS FOR BRIDGE INSPECTIONS	45
REFERENCES	46

LIST OF FIGURES

Figure B.1 Crack Widths at Various Depths from the Bridge Deck Surface (Patnaik and Baah, 2015)	8
Figure B.2 Bridge Inspection Pictures and Crack Map –FAI-37-7360	15
Figure B.3 Bridge Inspection Pictures and Crack Map – PER-668-1000	16
Figure B.4 Bridge Inspection Pictures and Crack Map – PER-668-9990	17
Figure B.5 Bridge Inspection Pictures and Crack Map – PER-22-12020	18
Figure B.6 Bridge Inspection Pictures and Crack Map – MUS-146-20920	19
Figure B.7 Bridge Inspection Pictures and Crack Map – COS-79-0160	20
Figure B.8 Bridge Inspection Pictures and Crack Map – MAD-323-15420	21
Figure B.9 Bridge Inspection Pictures and Crack Map – MAD-323-12230	22
Figure B.10 Bridge Inspection Pictures and Crack Map – MAD-323-14450	23
Figure B.11 Bridge Inspection Pictures and Crack Map – MAD-323-2800	24
Figure B.12 Bridge Inspection Pictures and Crack Map – MAD-38-18090	25
Figure B.13 Bridge Inspection Pictures and Crack Map – SHE-47-11520	26
Figure B.14 Bridge Inspection Pictures and Crack Map – CLA-235-2570.....	27
Figure B.15 Bridge Inspection Pictures and Crack Map – DAR-118-8940	28
Figure B.16 Bridge Inspection Pictures and Crack Map – DAR-722-6340	29
Figure B.17 Bridge Inspection Pictures and Crack Map – AUG-29-565	30
Figure B.18 Bridge Inspection Pictures and Crack Map – AUG-219-7210	31
Figure B.19 Bridge Inspection Pictures and Crack Map – DAR-705-0902	32
Figure B.20 Bridge Inspection Pictures and Crack Map – DAR-705-0947	33
Figure B.21 Bridge Inspection Pictures and Crack Map – DAR-705-10330	34
Figure B.22 Bridge Inspection Pictures and Crack Map – PRE-732-16580	35
Figure B.23 Bridge Inspection Pictures and Crack Map – PRE-503-21210	36
Figure B.24 Bridge Inspection Pictures and Crack Map – ATH-78-8310	37
Figure B.25 Bridge Inspection Pictures and Crack Map – VIN-278-8590.....	38
Figure B.26 Bridge Inspection Pictures and Crack Map – HOC-56-17960	39
Figure B.27 Bridge Inspection Pictures and Crack Map – HOC-56-16470	40
Figure B.28 Bridge Inspection Pictures and Crack Map – HOC-595-6040	41
Figure B.29 Bridge Inspection Pictures and Crack Map – HOL-83-15100	42

Figure B.30 Bridge Inspection Pictures and Crack Map – HOL-520-6440 43
Figure B.31 Bridge Inspection Pictures and Crack Map – BEL-148-3140 44
Figure B.32 Crack Widths Measured on Bridges in All ODOT Districts 45

LIST OF TABLES

Table B.1 Crack Widths Recorded for Bridges Surveyed from 2012–2014	6
Table B.1 Crack Widths Recorded for Bridges Surveyed from 2012–2014 (Continued)	7
Table B.2 Bridges Designed using ODOT Standard Drawing CS-01-08	9
Table B.2 Bridges Designed using ODOT Standard Drawing CS-01-08 (Continued)	10
Table B.3 Summary of the List of Bridges Inspected	12
Table B.3 Summary of the List of Bridges Inspected (Continued)	13
Table B.3 Summary of the List of Bridges Inspected (Continued)	14

APPENDIX B CRACK SURVEYS OF BRIDGES

ODOT has over 2700 bridges structural slab bridges in its inventory that have been built since the 1990s, ranging from a single span up to 34 spans. Three-span continuous structural slab bridges constitute the highest percentage of structural slab bridges in the ODOT bridge inventory.

B.1 Conclusions Drawn from an Earlier Project on Bridge Deck Cracking

A list of bridges inspected as part of a recently concluded project (Patnaik & Baah, 2015) are listed in Table B.1. These 13 bridges were chosen in consultation with ODOT subject matter experts (SMEs), considering numerous factors such as the number and length of spans, deck thickness, roadway width, number of lanes, skew effects, traffic conditions, and geographic location within the state. The decks of the selected bridges were all constructed between 1995 and 2012. The bridges have combinations of spans of various lengths, from 24–30–24 ft. to 44–55–44 ft. The deck thickness of the selected bridges ranged from 16 to 26 in. Different concrete mix designs were used in the construction of these bridge decks, including high performance concrete Class HP, Class S, and QC/QA concrete (specified in ODOT Supplemental Specification 896 (ODOT, 2015)). The study did not consider all cracks on the decks of the selected bridges; rather, it focused on the wide cracks, primarily those in the direction parallel to near the intermediate pier supports.

The CSS (continuous structural slab) bridges listed in Table B.1 were selected for crack surveys mainly to measure and map the cracks that had formed parallel to the pier lines (i.e., transverse cracks) on the bridge decks. These 13 bridges were inspected between December 2012 and July 2014. Cracks were identified and the crack lengths, crack widths, and distance between the cracks and the pier center lines were measured to develop crack maps. From the bridge inspection, it was found that these bridges had crack widths ranging from 0.04 inches to 0.13 inches, which are very wide when compared to the limit of 0.007 inches recommended by ACI 224R-01 for concrete exposed to deicing salts. The maximum crack widths recorded for the bridges are listed in Table B.1.

Table B.1 Crack Widths Recorded for Bridges Surveyed from 2012–2014
(Note: Based on ODOT Std. Drawing CS-1-93 or CS-1-03 using AASHTO Standard Specifications)

Bridge No.	ODOT Structure File No. (SFN)	Year Built/ Rebuilt	Length of Spans (ft.)	Deck Thickness (in.)	Skew Angle of Bridge Deck	Max. Recorded Crack Width (Dead load only) (in.)
ASD-42-0656	0301159	2009	40–50–40	24	12°10'	0.10
ASD-250-0377	0304697	2012	37–46.25–37	22.5	25°	0.03
WAY-30-1039	8501815	2006	44–55–44	26	30°	0.10

Table B.1 Crack Widths Recorded for Bridges Surveyed from 2012–2014 (Continued)

Bridge No.	ODOT Structure File No. (SFN)	Year Built/ Rebuilt	Length of Spans (ft.)	Deck Thickness (in.)	Skew Angle of Bridge Deck	Max. Recorded Crack Width (Dead load only) (in.)
POR-224-1172	6703900	2001	38–47.5–38	23	none	0.13
STA-225-076	7605943	2006	44–55–44	26	15°	0.10
MAH-62-0207	5001846	2008	28–35–28	18	10°	0.04
MAH-224-1619	5004837	2009	28–35–28	18	20°	0.05
POR-88-1250	6703607	2006	30–37.5–30	19	none	0.08
TRU-534-1516	7807457	2006	40–50–40	24	12°	0.10
TRU-45-2018	7802285	2003	40–50–40	24	10°	0.08
ATB-020-0326	0402087	2005	24.2–24.2	20	28°	0.08
ASD-250-1864	305006	1998	24.5–35–24.5	18	none	0.10
MED-162-2016	5206251	1995	24–30–24	16	30°	0.10

Note: These bridges were designed based on ODOT standard drawing CS-1-93 or CS-1-03 using AASHTO LRFD specifications.

One of the bridges (ASD-42-0656) was cored to determine the depth of the cracks in the negative moment region, as well as to determine the compressive strength and chloride content profile along the depth of the deck. It was found that the cracks penetrated deep into the deck with crack widths exceeding the ACI 224R-01 recommended limit of 0.007 inches as shown in Figure B.1. In addition, the chloride ion concentration in the deck was found to be 2% by weight of cement, which is about 20 times the recommended maximum value for black bars in ACI-318-11 for top bars in negative moment region. From the bridge crack surveys, it was observed that the crack widths ranged from 0.04 inches to 0.13 inches under dead load conditions only. These cracks increased over time and also resulted in cracking on the parapet walls over the negative moment regions.

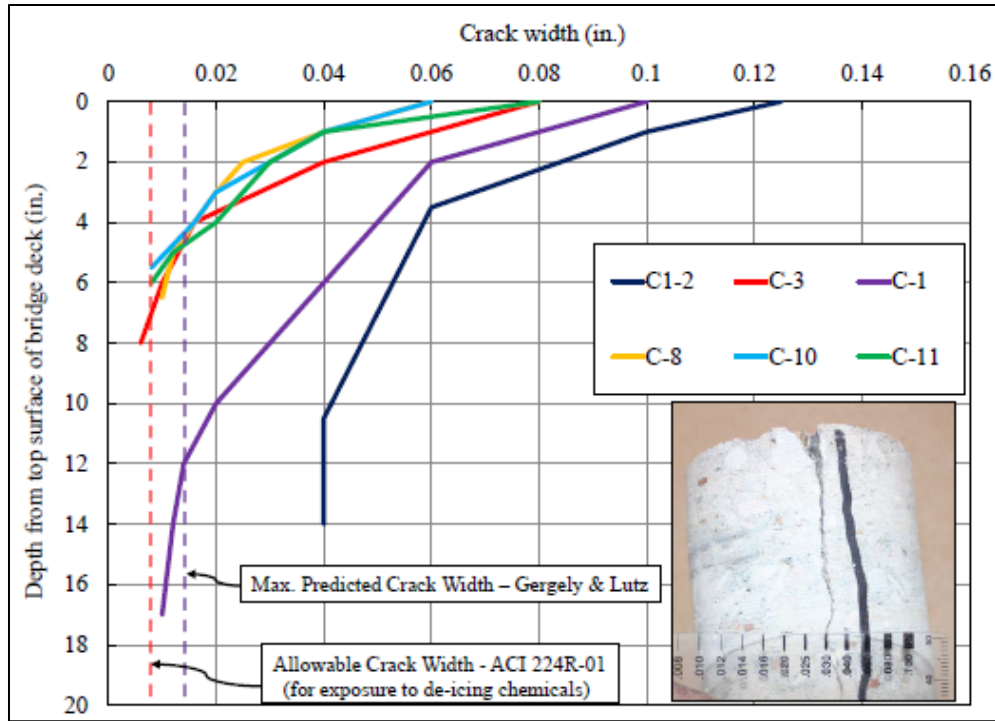


Figure B.1 Crack Widths at Various Depths from the Bridge Deck Surface (Patnaik and Baah, 2015)

B.2 Bridges Considered for Survey in the Current Project

As the previously inspected bridges were designed based on ODOT standard drawing before the introduction of CS-01-08 (ODOT, 2008), a list of three-span CSS bridges that were designed based on ODOT standard drawing CS-01-08 (ODOT, 2008) was compiled from ODOT bridge inventory. Sixty-three, three-span CSS bridges were proposed by ODOT SMEs in various districts (Table B.2). The spans of the bridges range from 16'-20'-16' to 46'-57.5'-46' with deck thicknesses ranging from 12 inches to 27 inches, respectively. The bridges were constructed or rebuilt between 2008 and 2016.

Table B.2 Bridges Designed using ODOT Standard Drawing CS-01-08

ODOT District	ODOT Structure File No. (SFN)	Bridge No.	Length of Spans (ft.)	Deck Thickness (in.)	Year Built
1	0201634	ALL-75-1000	26-32.5-26	17	2012
1	0201669	ALL-75-1000	26-32.5-26	17	2012
2	8703035	WOO-75-1800	*	*	*
3	1703617	CRA-598-70	28.83-34.875-28.83	18	2012
3	7002572	RIC-42-1020	30-37.5-30	19	2014
3	8501750	WAY-30-9350	24.75-29.5-24.75	16	2005
3	8501785	WAY-30-9350	24.75-29.5-24.75	16	2005
4	5006015	MAH-616-5880	*	*	*
5	1601482	COS-79-1600	32-40-32	20	2014
5	1601547	COS-79-3940	20-25-20	14	2014
5	2310000	FAI-37-7360	35.6-44.5-35.6	22	2015
5	4202260	KNO-62-18820	24-30-24	16	2013
5	4202597	KNO-95-5990	46-57.5-46	27	2011
5	4203739	KNO-661-2980	28-35-28	18	2014
5	4502566	LIC-62-3850	46-57.5-46	27	2010
5	4504542	LIC-70-28880	30-37.5-30	19.5	2013
5	4510001	LIC-661-158	20-25-20	14.5	2015
5	6002196	MUS-60-28870	20-25-20	14	2013
5	6003036	MUS-70-13060	36-45-36	16.25	2015
5	6004873	MUS-146-20920	24-30-24	16	2012
5	6005578	MUS-208-10410	16-20-16	12	2014
5	6006582	MUS-666-5710	16-20-16	12	2014
5	6402895	PER-668-1000	31-38.75-31	19.5	2010
5	6403166	PER-668-9990	37.2-46.5-37.2	21	2011
5	6410000	PER-22-12020	30-37.5-30	19.5	2015
6	4900456	MAD-38-18090	35-43.75-35	21.5	2011
6	4903943	MAD-323-2800	30-37.5-30	19	2013
6	4904168	MAD-323-12230	30-37.5-30	19	2010
6	4904214	MAD-323-14450	30-37.5-30	19	2010
6	4904222	MAD-323-15420	30-37.5-30	19	2010
6	4910000	MAD-665-3950	44-55-44	*	2014
6	8001634	UNI-36-890	32-40-32	20	2011

Note: * Indicates, the information on that bridge was not available

Table B.2 Bridges Designed using ODOT Standard Drawing CS-01-08 (Continued)

ODOT District	ODOT Structure File No. (SFN)	Bridge No.	Length of Spans (ft.)	Deck Thickness (in.)	Year Built
7	0600105	AUG-29-565	32-45-32	22	*
7	0603252	AUG-219-7210	20-25-20	14	2016
7	1200550	CLA-4-23120	20-25-20	14	2011
7	1205749	CLA-235-2570	26-32.5-26	17	2015
7	1901648	DAR-118-8490	24-30-24	18	2014
7	1903829	DAR-705-9020	16-20-16	12	2013
7	1903853	DAR-705-9470	16-20-16	12	2013
7	1903977	DAR-705-10330	16-20-16	12	2013
7	1904337	DAR-722-6350	31-38.75-31	19.5	2008
7	4604156	LOG-708-2080	26-32.5-26	18	2011
7	5705657	MOT-70-12190	46-57.5-46	27	2011
7	5708427	MOT-4-17620	*	*	*
7	7500556	SHE-47-11520	30-37.5-30	19	2008
7	7501064	SHE-65-8630	20-25-20	14	2015
8	6803911	PRE-503-21210	40-50-40	17	2014
8	6804969	PRE-732-16580	40-50-40	24	2014
10	0502863	ATH-78-8310	31-38.75-31	19.5	2011
10	0503576	ATH-329-14400	22-27.5-22	15	2012
10	2702924	GAL-218-13890	36-45-36	22	2011
10	3700968	HOC-33-15530	28-35-28	18	2012
10	3701514	HOC-56-16470	40-50-40	24	2011
10	3701573	HOC-56-17960	36-45-36	22	2013
10	3704343	HOC-595-6040	36-45-36	22	2010
10	5300975	MEG-124-1250	30.2-37.75-30.2	20	2001
10	5602769	MOE-379-4560	34-42.5-34	17.5	2013
10	8201994	VIN-278-8590	35-43.75-35	21.5	2010
10	8202419	VIN-327-12490	35-43.75-35	21.5	2010
10	8404461	WAS-550-10410	20-25-20	*	2012
11	0703761	BEL-148-3140	30-37.5-30	19	2011
11	3801888	HOL-83-15100	37-46.25-37	22.5	2012
11	3802728	HOL-520-6440	23-28.75-23	15.5	2013

Note: * Indicates, the information on that bridge was not available

B.3 Crack Survey and Crack Mapping of Bridges Inspected

From the list of proposed bridges, a total of 30 bridges was selected in various districts, based on the span length and deck thickness as listed in table B.3. The bridges were inspected in order to record the crack patterns, measure the crack widths, and crack locations relative to the center line of the pier caps. Crack measurements were omitted for some bridges, because some bridges had traffic levels too high for the survey team to safely remain on the bridge decks on the day of the survey.

Cracks widths were measured using a manual crack gage reader at various locations over the negative moment region to determine the average and maximum crack widths. Cracks were marked with chalk on the deck surface and were recorded at the site. Pictures were taken at each bridge to record the crack surveys. Crack maps were later developed in AutoCAD for all bridges where cracks could be measured. Details from the survey of each bridge are discussed in the subsections below and are presented in Figures B.2 to B.31. Crack width greater than 0.04 inches are highlighted in yellow. For bridges where no cracks were observed or where crack measurements could not be obtained at the time of survey, diagrams of the bridges are included in lieu of crack maps.

Table B.3 Summary of the List of Bridges Inspected

S.No.	District	Bridge Number	Spans	Deck Thickness (in.)	Year Built	Skew	Type of Substructure	Date & Time	Type of Traffic During Survey	Average Recorded Crack Width (in.)	Max Recorded Crack Width (in.)
1	5	COS-79-1600	32-40-32	20	2014	35 RF	Capped Pile Substructure	10/6/2016 2:50 PM	Low	0.004	0.008
2	5	FAI-37-7360	35.6-44.5-35.6	22	2015	14'50'48" RF	Capped Pile Substructure	9/15/2016 9:30 AM	Heavy	0.05	0.08
3	5	MUS-146-20920	24-30-24	16	2012	7'52'52"	Capped Pile Abutments and piers	10/5/2016 3:30 PM	Heavy	0.03	0.04
4	5	PER-668-1000	31-38.75-31	19.5	2010	30 RF	Concrete abutments and Piers	9/15/2016 10:30 PM	Low	0.02	0.04
5	5	PER-668-9990	37.2-46.5-37.2	21	2011	25	Capped Pile Pier and Abutments	9/15/2016 12:30 PM	Moderate	0.06	0.1
6	5	PER-22-12020	30-37.5-30	19.5	2015	30 LF	Capped Pile Substructure	9/15/2016 1:30 PM	Low	0.01	0.03
7	6	MAD-38-18090	35-43.75-35	21.5	2011	None	Capped Pile Substructure CIP RC Piles	10/4/2016 1:00 PM	Heavy	0.06	0.08
8	6	MAD-323-2800	30-37.5-30	19	2013	30 LF	Capped Pile Substructure	10/4/2016 11:20 AM	Low	0.02	0.03
9	6	MAD-323-12230	30-37.5-30	19	2010	15 RF	Capped Pile Substructure	10/4/2016 10:50 AM	Low	0.01	0.02

Table B.3 Summary of the List of Bridges Inspected (Continued)

S.No.	District	Bridge Number	Spans	Deck	Year Built	Skew	Type of Substructure	Date & Time	Type of Traffic During Survey	Average Recorded Crack Width (in.)	Max Recorded Crack Width (in.)
10	6	MAD-323-14450	30-37.5-30	19	2010	15 RF	Capped Pile Substructure	10/4/2016 10:20 AM	Low	0.02	0.03
11	6	MAD-323-15420	30-37.5-30	19	2010	15 RF	Capped Pile Substructure	10/4/2016 9:30 am	Low	0.01	0.03
12	7	AUG-29-565	32-45-32	22		10° LF	Capped Pile Piers and Abutments	10/10/2016 4:20 PM	Low	0.01	0.03
13	7	AUG-219-7210	20-25-20	14	2016	10° RF	Capped Pile Piers and Abutments	10/10/2016 4:40 PM	Low	0.01	0.02
14	7	CLA-235-2570	26-32.5-26	17	2015	30° LF	Capped Pile and Stub Abutments on Piles	10/11/2016 12:40 PM	Heavy	0.06	0.125
15	7	DAR-118-8490	24-30-24	18	2014	15° LF	Concrete Slab with Semi Integral Abutments and Cap and column Piers	11/13/2015 2:30 PM	Low	None	None
16	7	DAR-705-9020	16-20-16	12	2013	30° LF	Capped Pile Piers and Abutments	10/10/2016 5:30 PM	Low	None	None
17	7	DAR-705-9470	16-20-16	12	2013	None	Capped Pile Piers and Abutments	10/10/2016 5:40 PM	Low	None	None
18	7	DAR-705-10330	16-20-16	12	2013	30° RF	Capped Pile Piers and Abutments	10/10/2016 5:50 PM	Low	None	None
19	7	DAR-722-6350	31-38.75-31	19.5	2008	22° RF	Concrete Slab with Semi Integral Abutments and Cap and column Piers	11/13/2015 3:30 PM	Heavy	0.05	0.08
20	7	SHE-47-11520	30-37.5-30	19	2008	None	Capped Pile Substructure	10/11/2016 8:45 AM	Heavy	0.03	0.05
21	8	PRE-503-21210	40-50-40	17	2014	None	Capped Pile Abutments and piers	10/11/2016 10:30 AM	Moderate	0.03	0.04

Table B.3 Summary of the List of Bridges Inspected (Continued)

S.No.	District	Bridge Number	Spans	Deck	Year Built	Skew	Type of Substructure	Date & Time	Type of Traffic During Survey	Average Recorded Crack Width (in.)	Max Recorded Crack Width (in.)
22	8	PRE-732-16580	40-50-40	24	2014	30° RF	Concrete Cap and Column Piers on Drilled Shafts and Capped Pile Abutments	10/11/2016 11:45 AM	Moderate	None	0.125*
23	10	ATH-78-8310	31-38.75-31	19.5	2011	None	Capped Pile Abutments and piers	10/5/2016 5:20 PM	Heavy	0.06	0.125
24	10	HOC-56-16470	40-50-40	24	2011	25 LF	Capped Pile Abutments and piers	10/6/2016 11:23 AM	Moderate	0.04	0.05
25	10	HOC-56-17960	36-45-36	22	2013	30 RF	Capped Pile Abutments and piers	10/6/2016 10:30 AM	Moderate	0.03	0.05
26	10	HOC-595-6040	36-45-36	22	2010	25 LF	Capped Pile Pier	10/6/2016 12:20 PM	Moderate	0.035	0.04
27	10	VIN-278-8590	35-43.75-35	21.5	2010	None	Capped Pile Abutments and piers	10/6/2016 8:40 AM	Moderate	0.02	0.04
28	11	BEL-148-3140	30-37.5-30	19	2011	6° RF	Semi integral Abutments and wall type Piers	9/9/2016 3:45 PM	Moderate	0.02	0.04
29	11	HOL-83-15100	37-46.25-37	22.5	2012	None	Concrete Pile Abutments and Concrete capped pile piers	9/14/2016 2:30 PM	Heavy	0.06	0.1
30	11	HOL-520-6440	23-28.75-23	15.5	2013	15° LF	Capped Pile Pier and Abutments	9/14/2016 3:15 PM	Moderate	0.04	0.06

* Only longitudinal crack was observed

B.3.1 Bridge FAI-37-7360 (District 5)

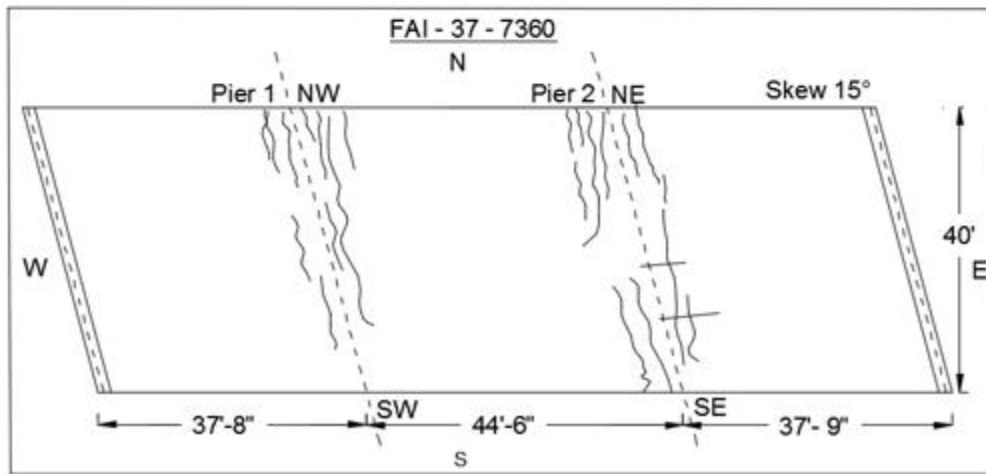


Figure B.2 Bridge Inspection Pictures and Crack Map –FAI-37-7360

B.3.2 Bridge PER-668-1000 (District 5)

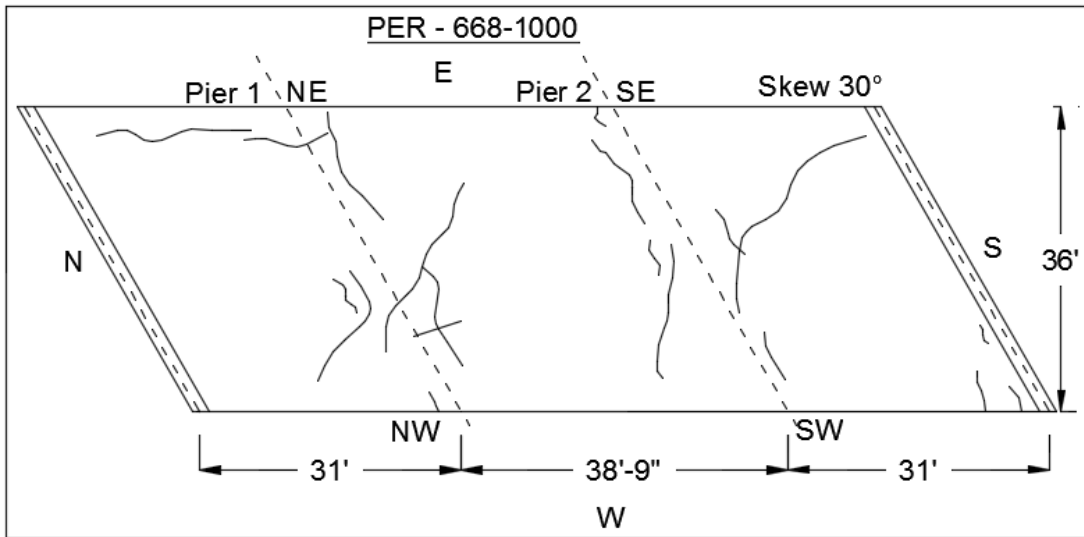


Figure B.3 Bridge Inspection Pictures and Crack Map – PER-668-1000

B.3.3 Bridge PER-668-9990 (District 5)

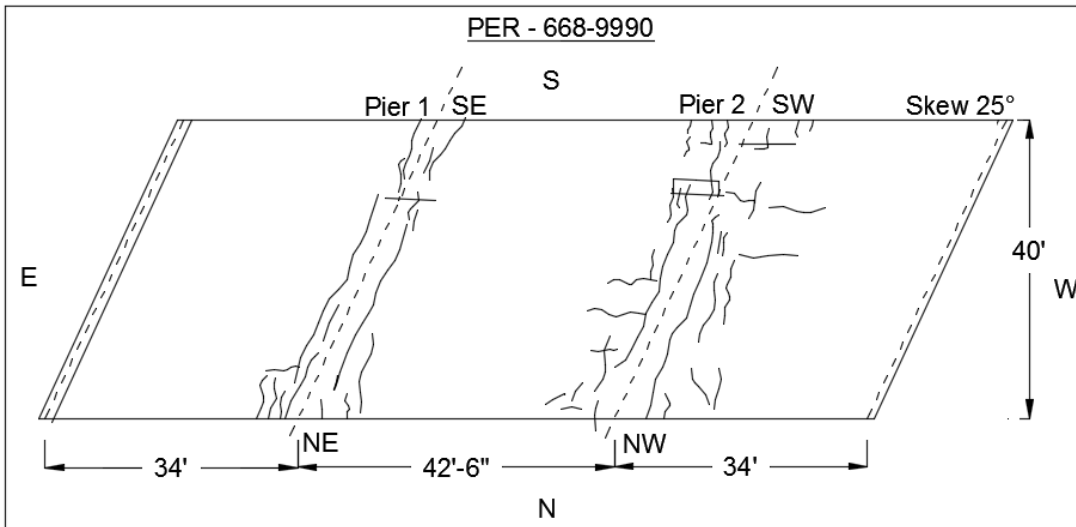


Figure B.4 Bridge Inspection Pictures and Crack Map – PER-668-9990

B.3.4 Bridge PER-22-12020 (District 5)

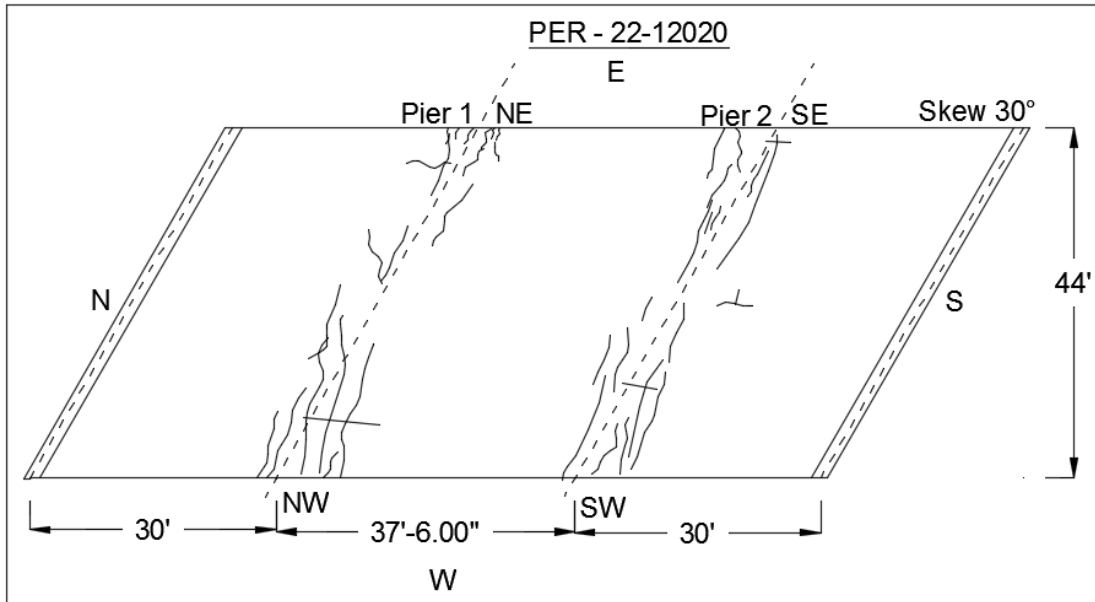


Figure B.5 Bridge Inspection Pictures and Crack Map – PER-22-12020

B.3.5 Bridge MUS-146-20920 (District 5)

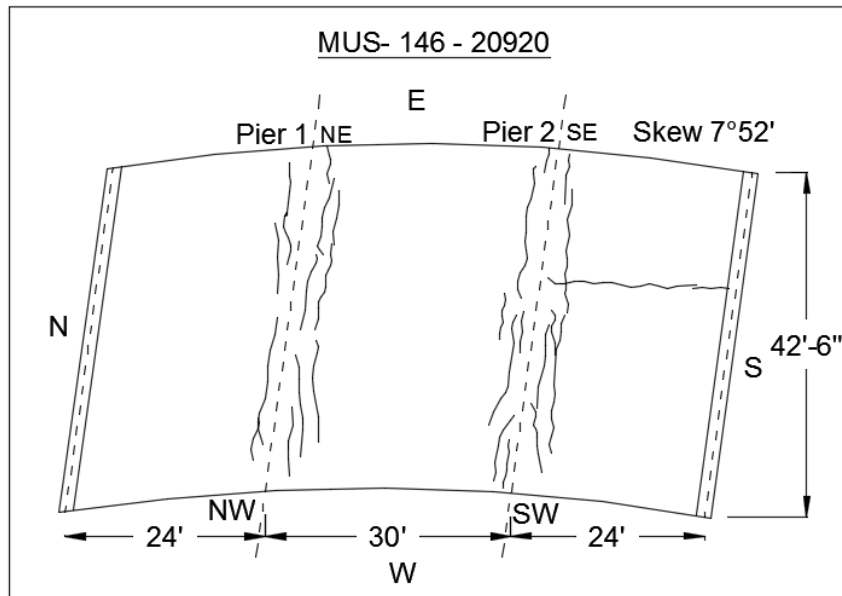


Figure B.6 Bridge Inspection Pictures and Crack Map – MUS-146-20920

B.3.6 Bridge COS-79-0160 (District 5)

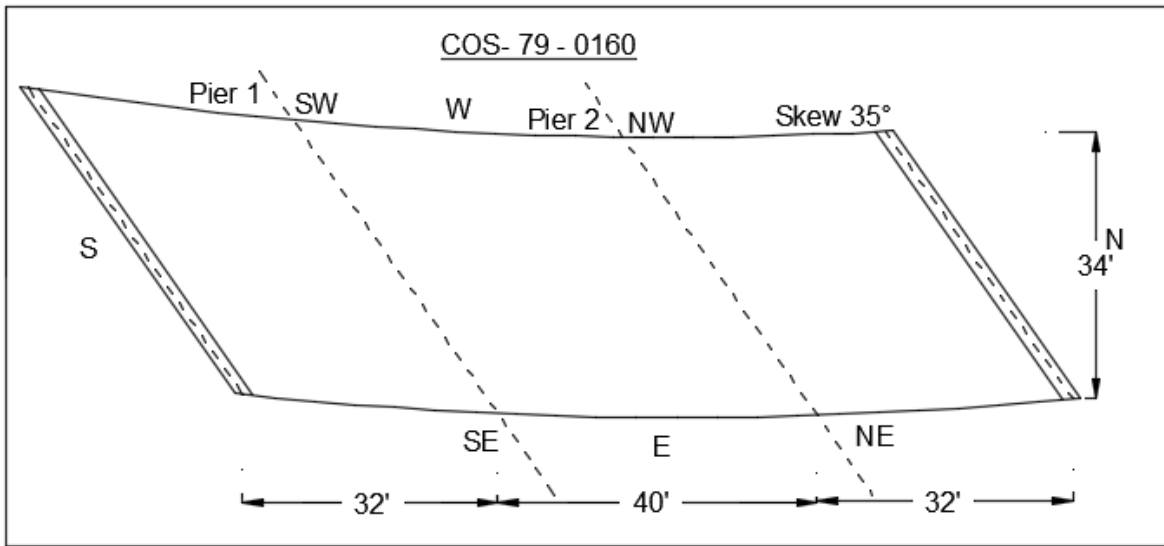


Figure B.7 Bridge Inspection Pictures and Crack Map – COS-79-0160

B.3.7 Bridge MAD-323-15420 (District 6)

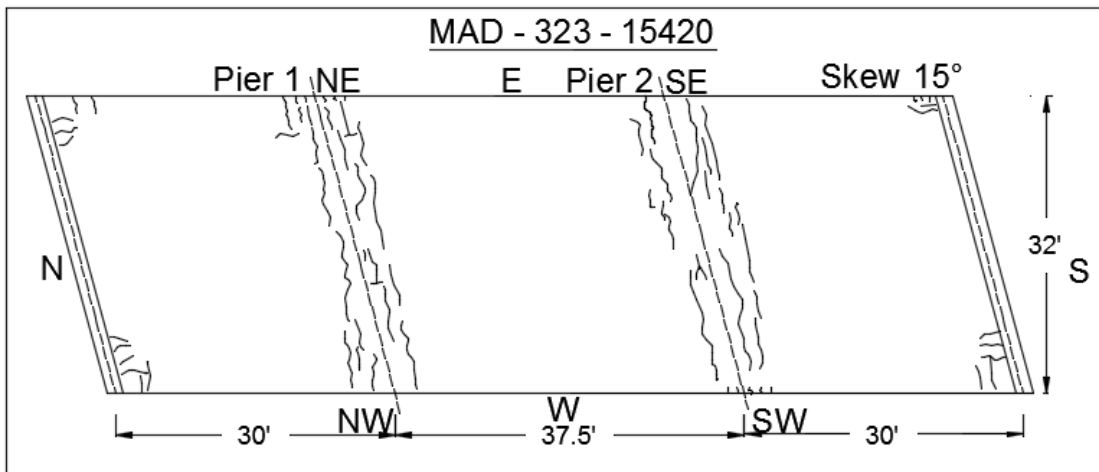


Figure B.8 Bridge Inspection Pictures and Crack Map – MAD-323-15420

B.3.8 Bridge MAD-323-12230 (District 6)

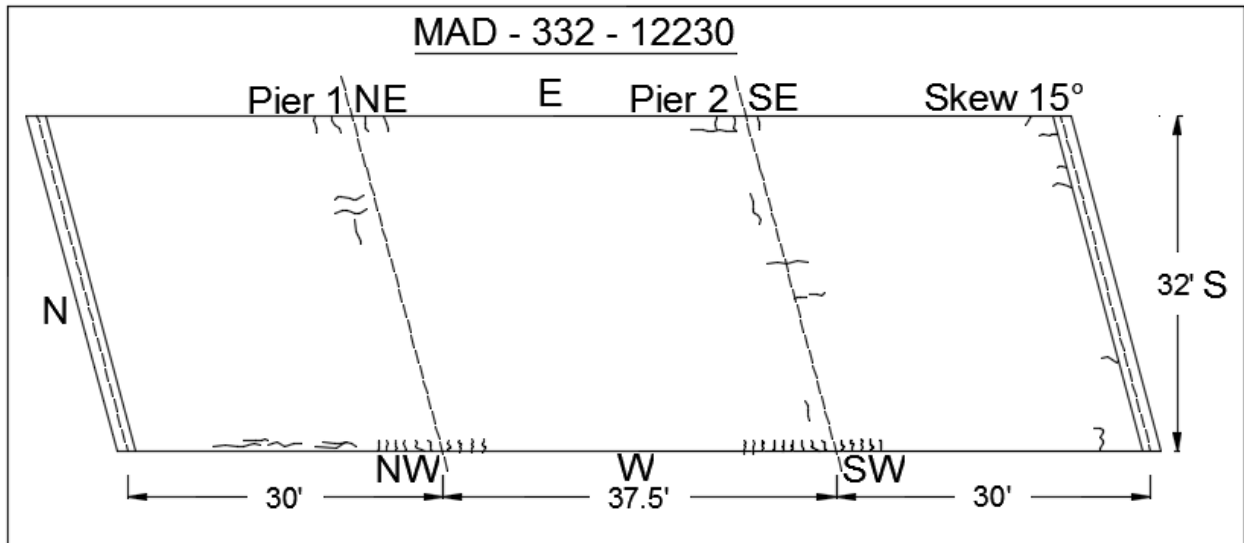


Figure B.9 Bridge Inspection Pictures and Crack Map – MAD-323-12230

B.3.9 Bridge MAD-323-14450 (District 6)

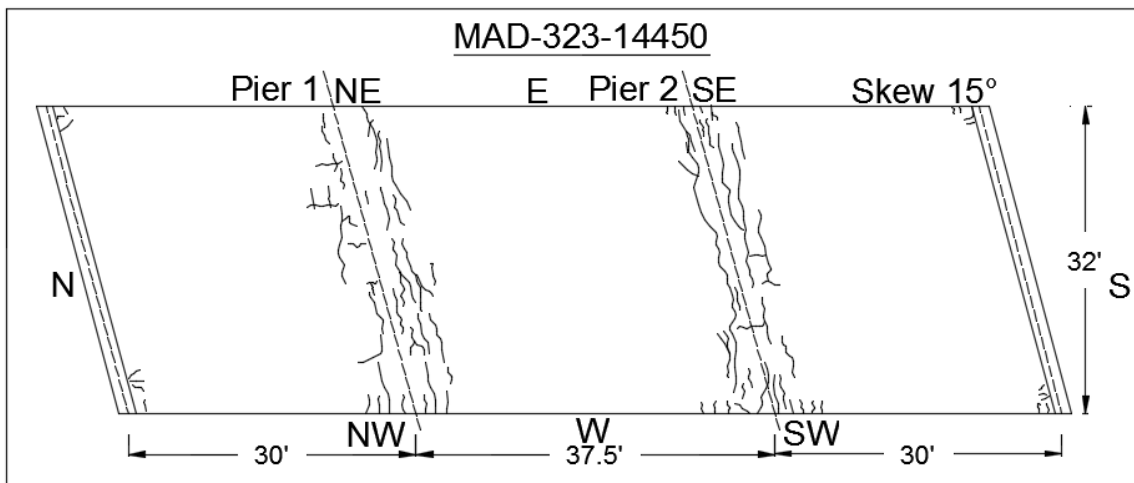


Figure B.10 Bridge Inspection Pictures and Crack Map – MAD-323-14450

B.3.10 Bridge MAD-323-2800 (District 6)

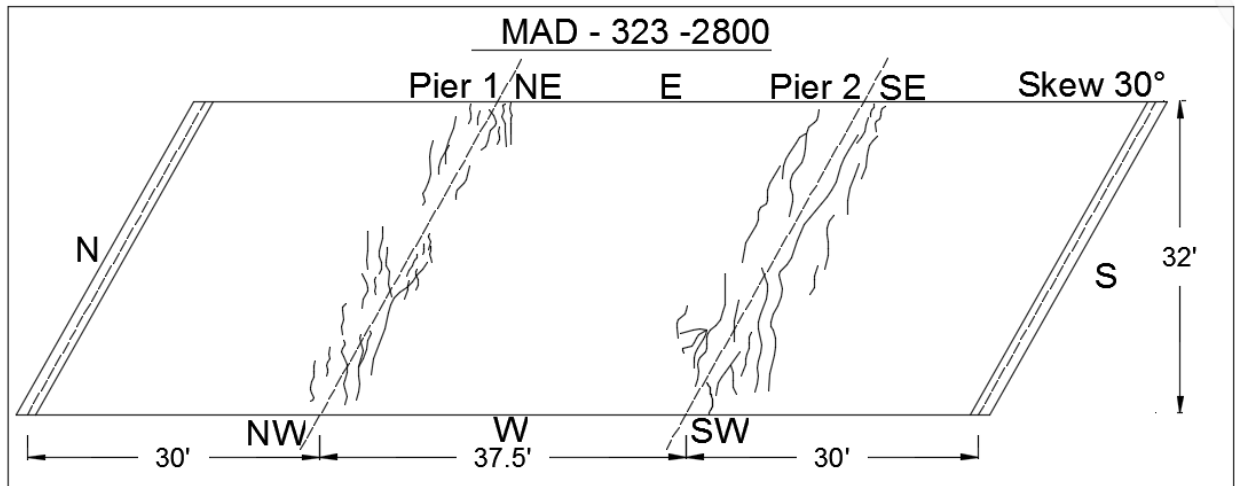


Figure B.11 Bridge Inspection Pictures and Crack Map – MAD-323-2800

B.3.11 Bridge MAD-38-18090 (District 6)

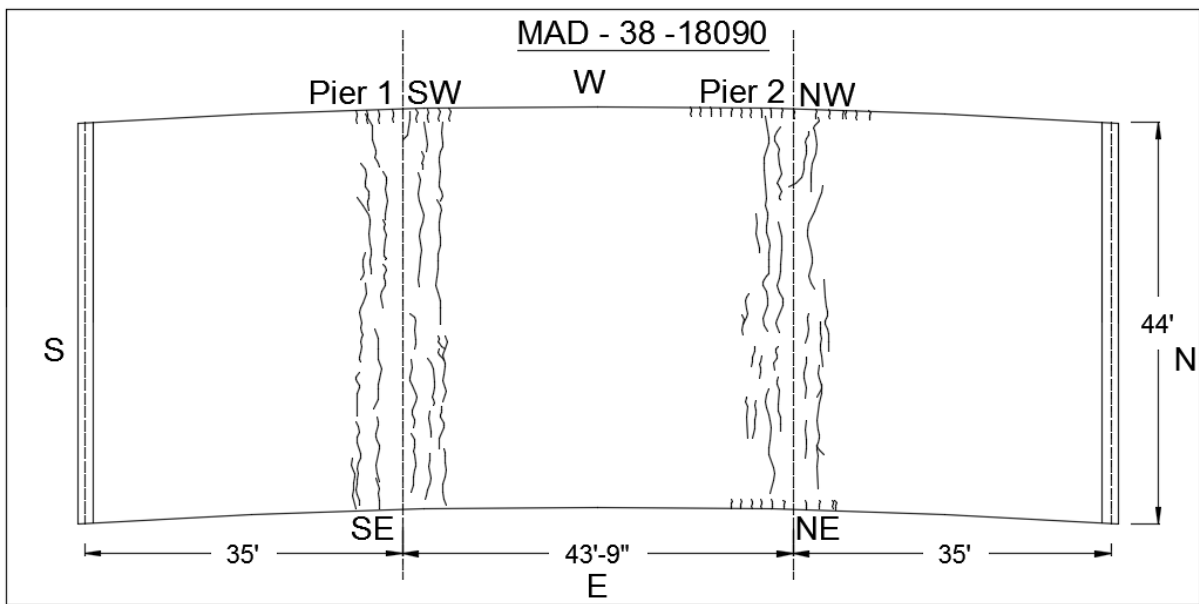


Figure B.12 Bridge Inspection Pictures and Crack Map – MAD-38-18090

B.3.12 Bridge SHE-47-11520 (District 7)

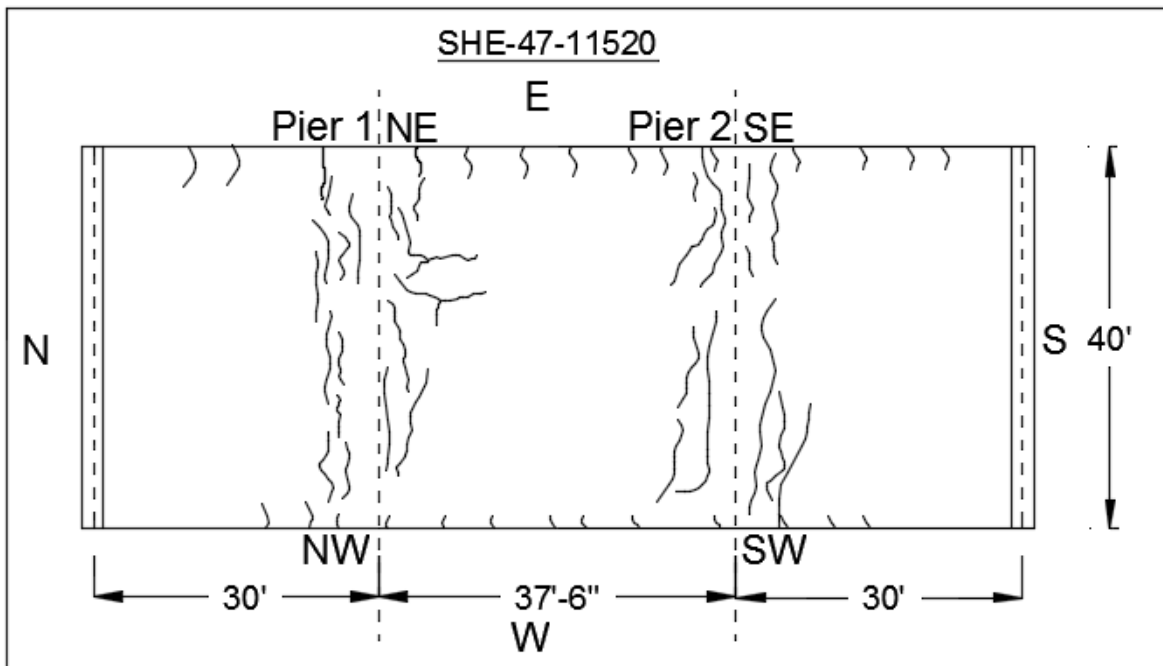


Figure B.13 Bridge Inspection Pictures and Crack Map – SHE-47-11520

B.3.13 Bridge CLA-235-2570 (District 7)

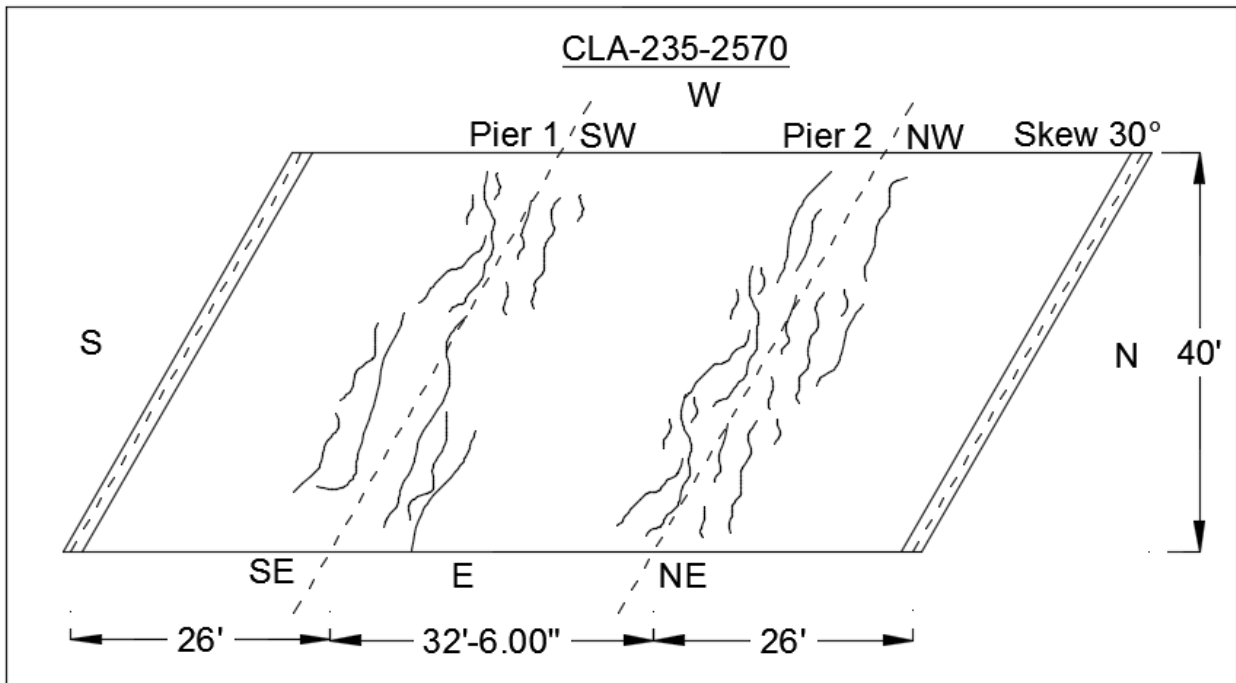


Figure B.14 Bridge Inspection Pictures and Crack Map – CLA-235-2570

B.3.14 Bridge DAR-118-8490 (District 7)

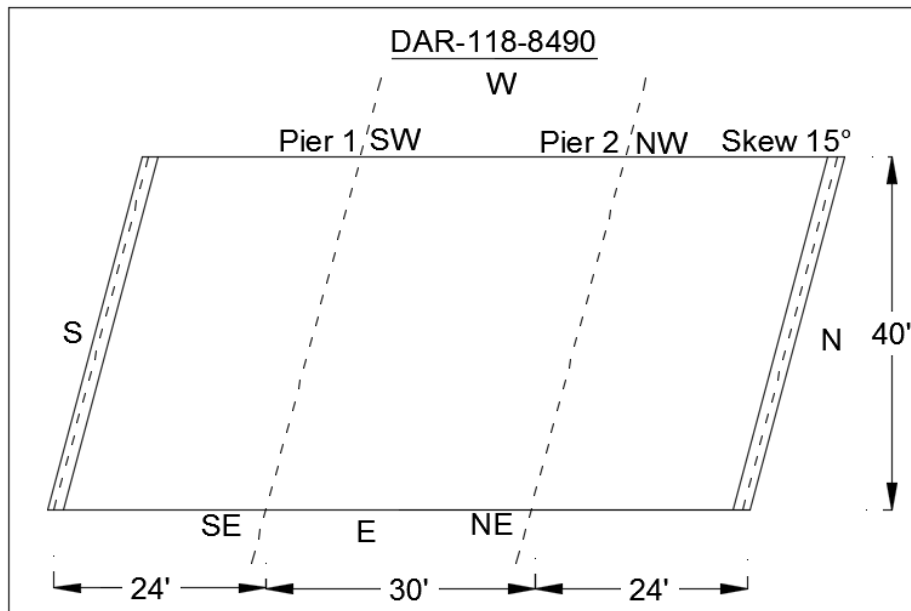


Figure B.15 Bridge Inspection Pictures and Crack Map – DAR-118-8940

B.3.15 Bridge DAR-722-6340 (District 7)

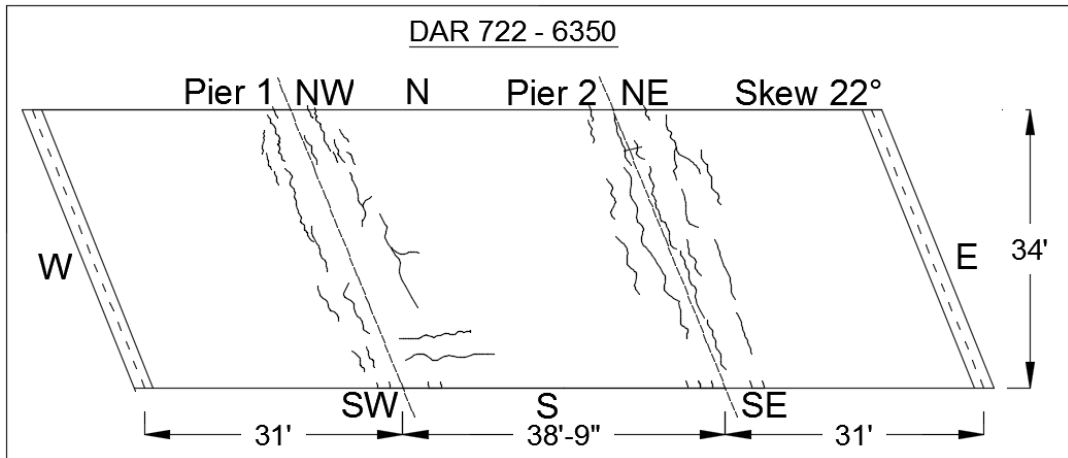


Figure B.16 Bridge Inspection Pictures and Crack Map – DAR-722-6340

B.3.16 Bridge AUG-29-565 (District 7)

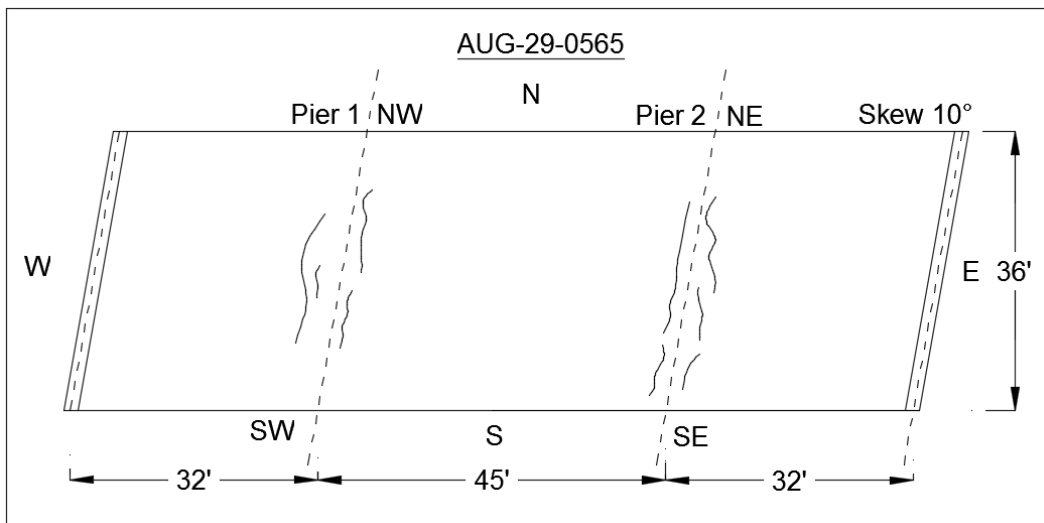


Figure B.17 Bridge Inspection Pictures and Crack Map – AUG-29-565

B.3.17 Bridge AUG-219-7210 (District 7)

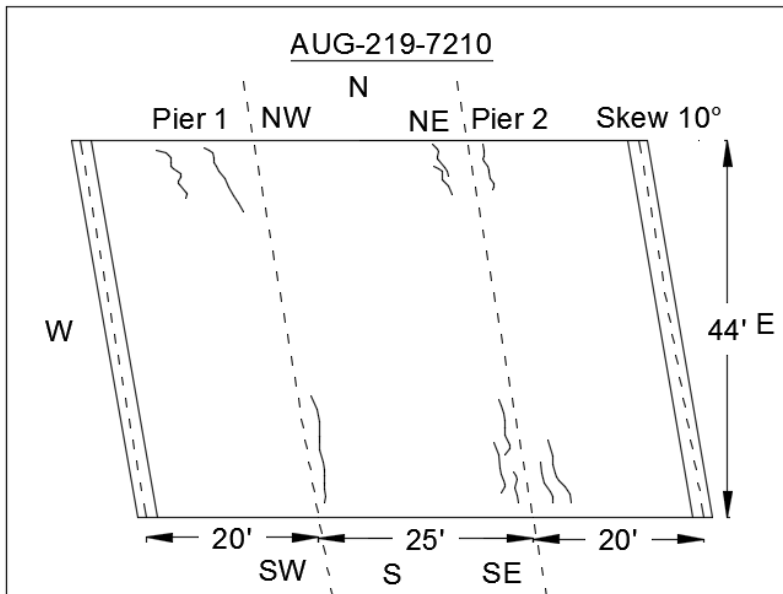


Figure B.18 Bridge Inspection Pictures and Crack Map – AUG-219-7210

B.3.18 Bridge DAR-705-0902 (District 7)

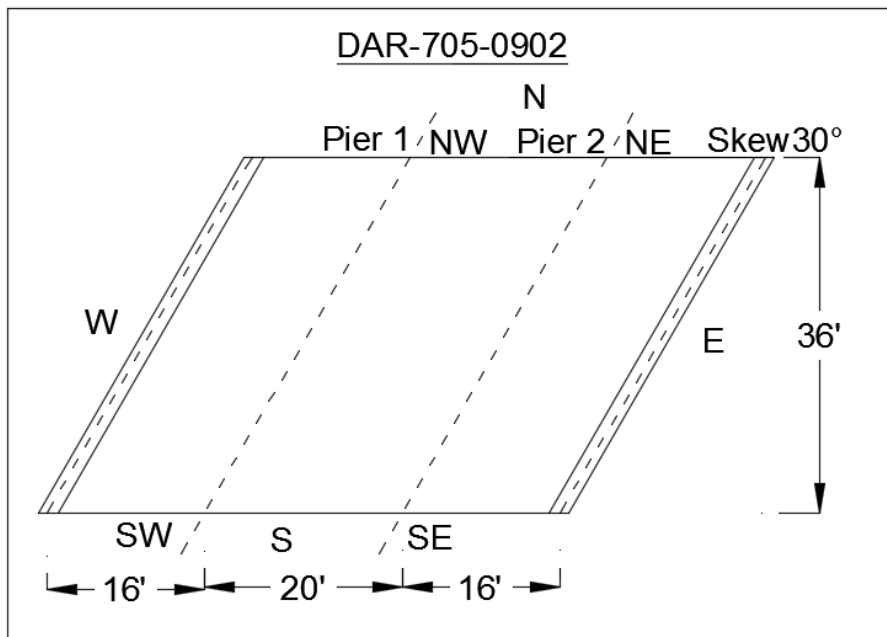
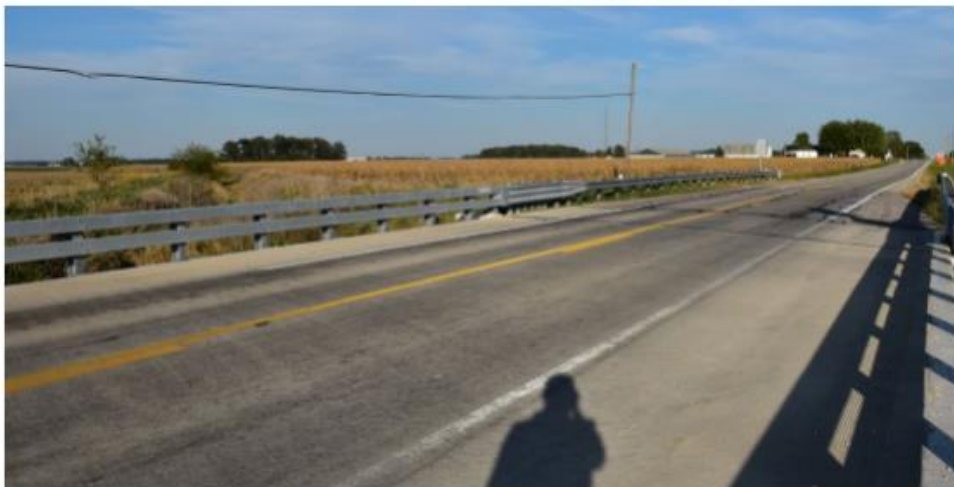


Figure B.19 Bridge Inspection Pictures and Crack Map – DAR-705-0902

B.3.19 Bridge DAR-705-0947 (District 7)

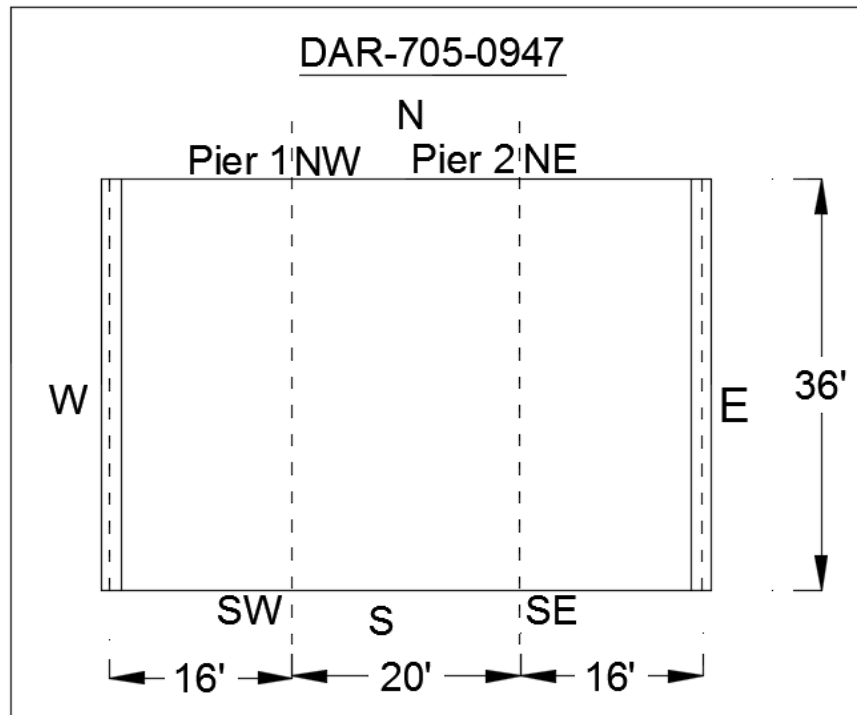


Figure B.20 Bridge Inspection Pictures and Crack Map – DAR-705-0947

B.3.20 Bridge DAR-705-10330 (District 7)

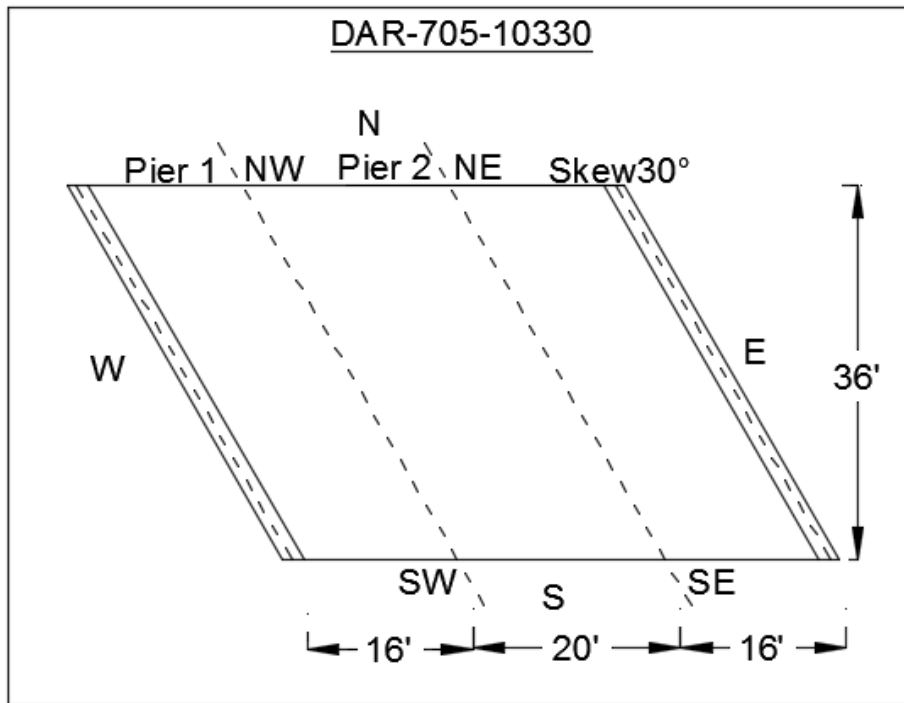


Figure B.21 Bridge Inspection Pictures and Crack Map – DAR-705-10330

B.3.21 Bridge PRE-732-16580 (District 8)

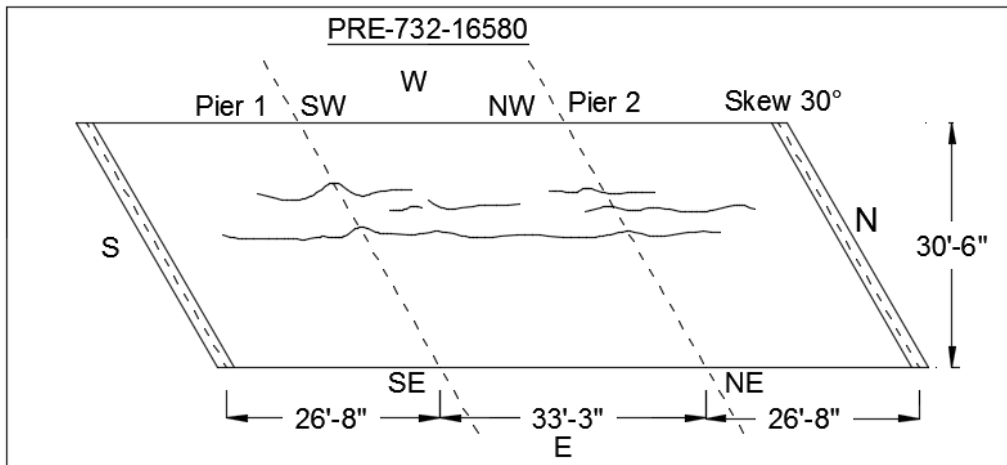


Figure B.22 Bridge Inspection Pictures and Crack Map – PRE-732-16580

B.3.22 Bridge PRE-503-21210 (District 8)

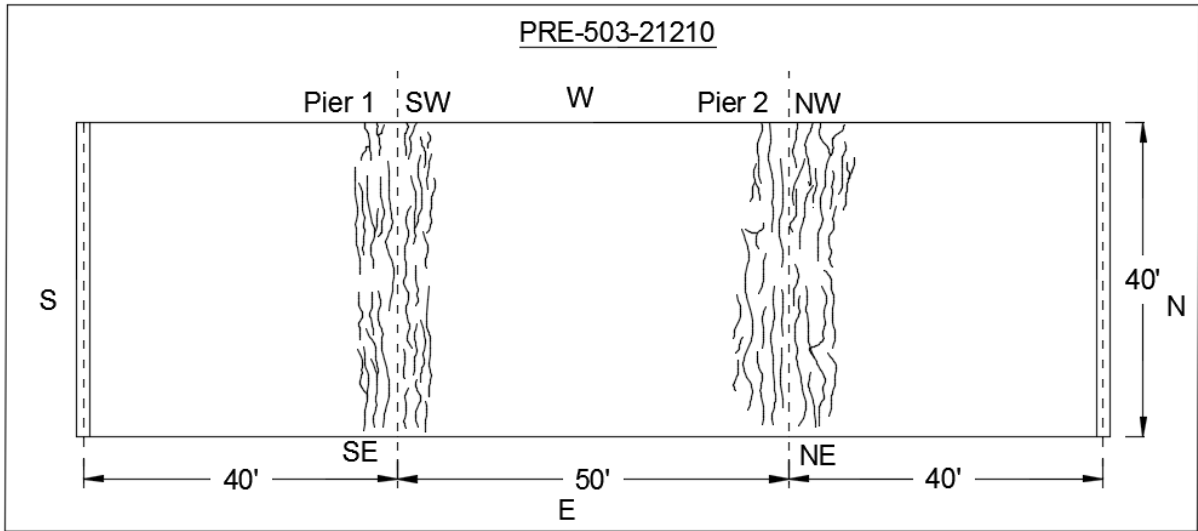


Figure B.23 Bridge Inspection Pictures and Crack Map – PRE-503-21210

B.3.23 Bridge ATH-78-8310 (District 10)

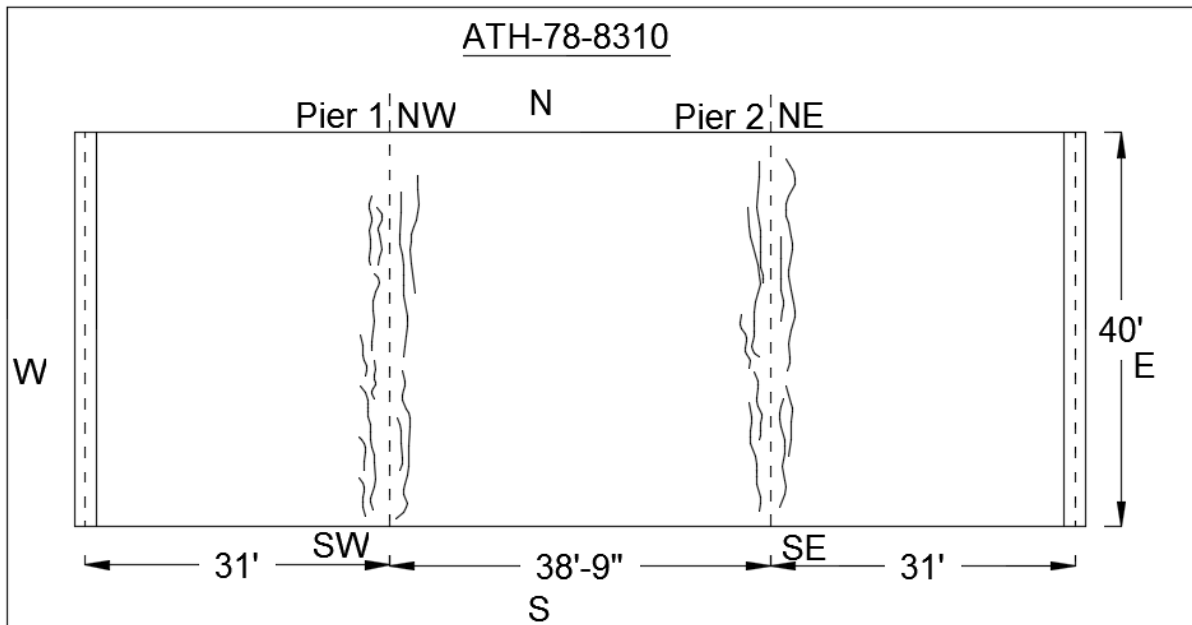


Figure B.24 Bridge Inspection Pictures and Crack Map – ATH-78-8310

B.3.24 Bridge VIN-278-8590 (District 10)

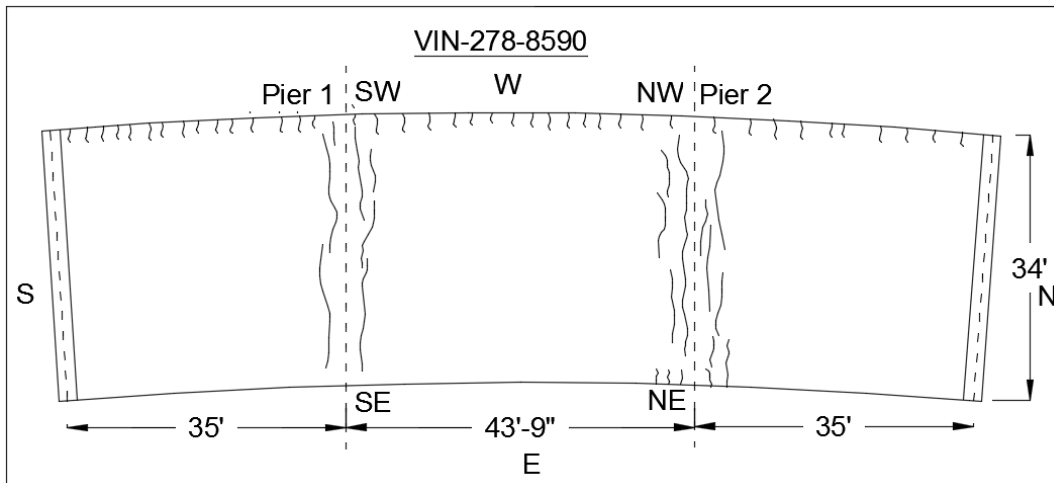


Figure B.25 Bridge Inspection Pictures and Crack Map – VIN-278-8590

B.3.25 Bridge HOC-56-17960 (District 10)

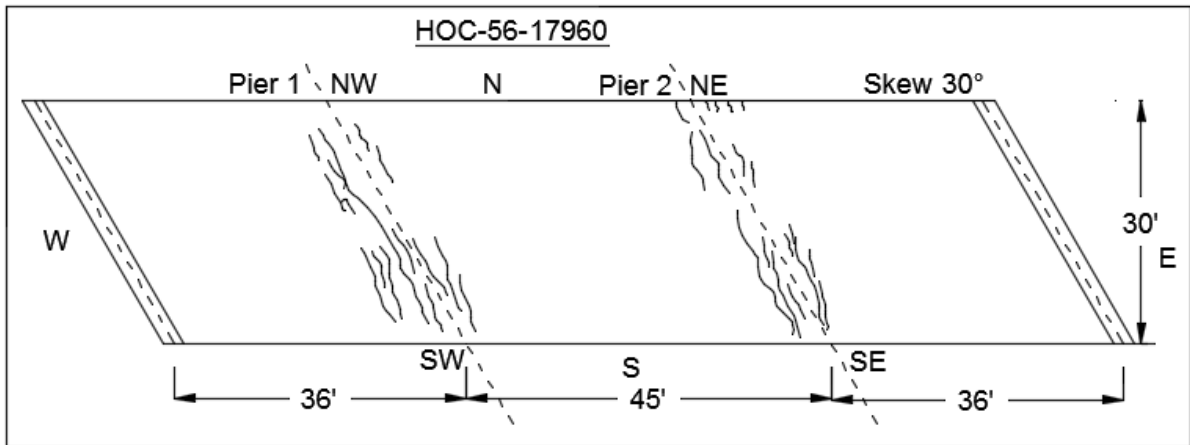


Figure B.26 Bridge Inspection Pictures and Crack Map – HOC-56-17960

B.3.26 Bridge HOC-56-16470 (District 10)

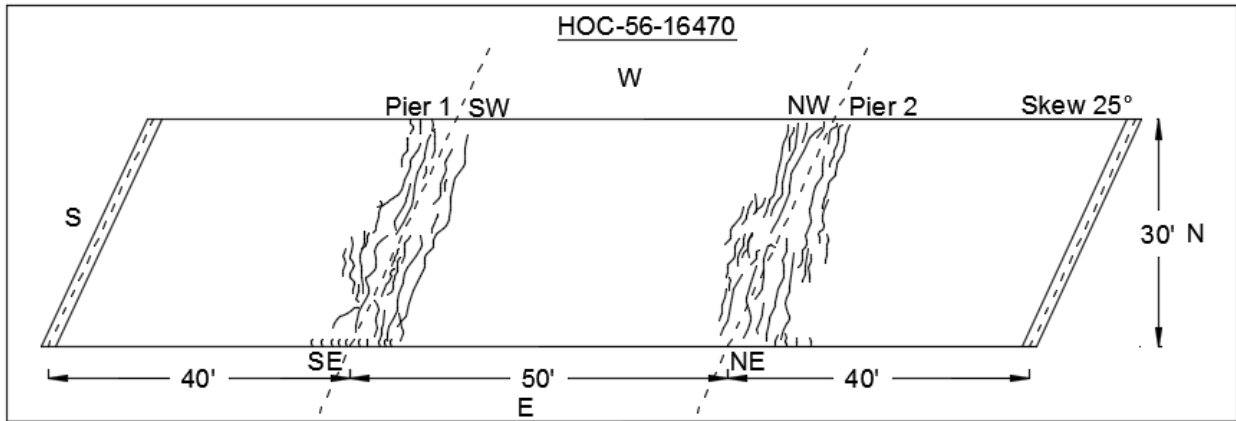


Figure B.27 Bridge Inspection Pictures and Crack Map – HOC-56-16470

B.3.27 Bridge HOC-595-6040 (District 10)

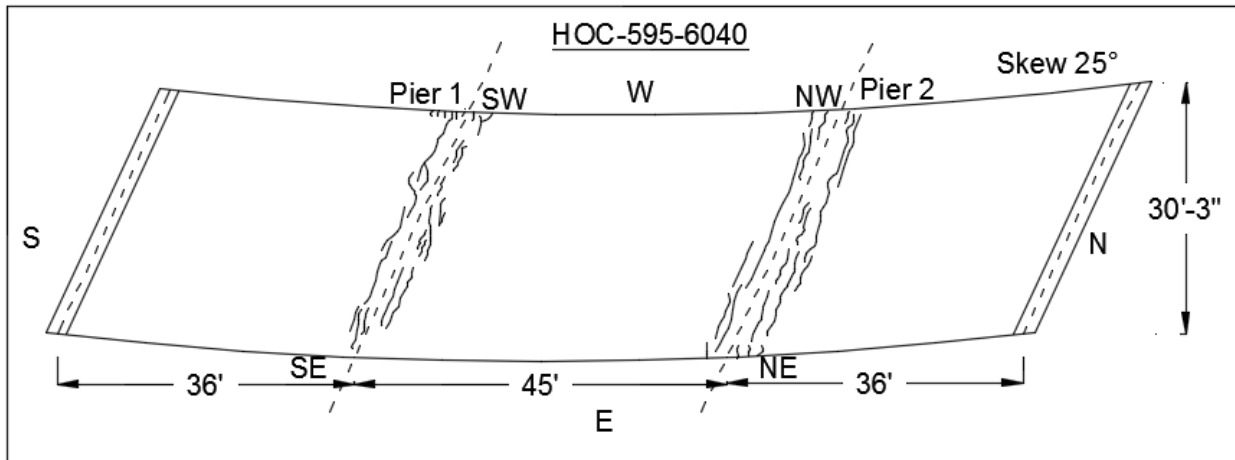


Figure B.28 Bridge Inspection Pictures and Crack Map – HOC-595-6040

B.3.28 Bridge HOL-83-15100 (District 11)

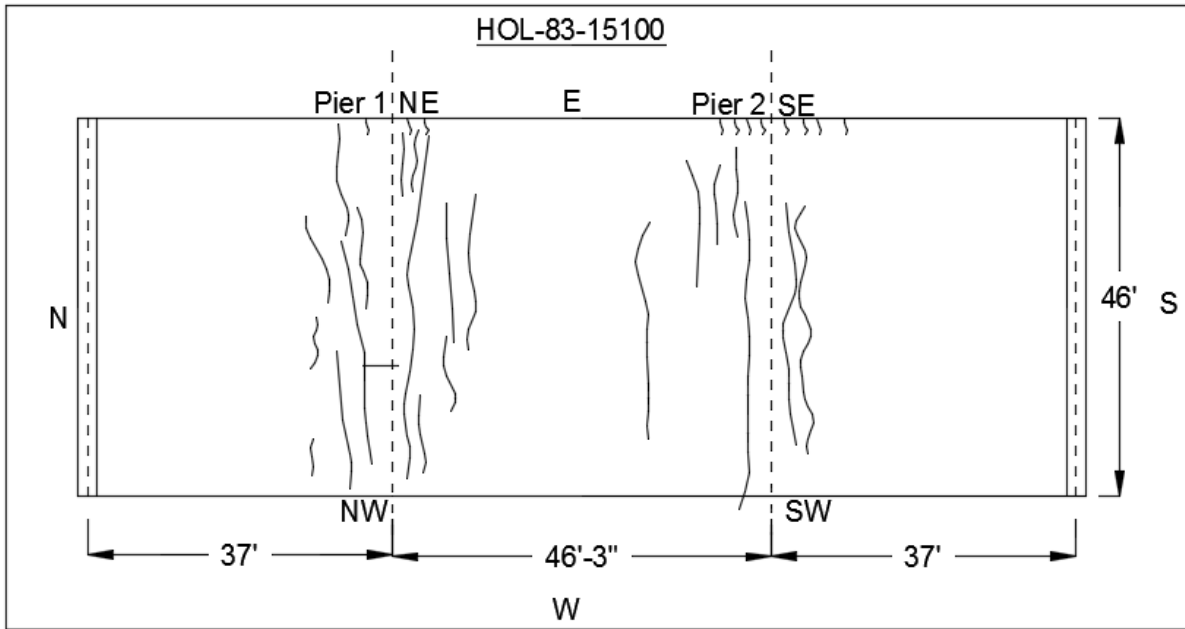


Figure B.29 Bridge Inspection Pictures and Crack Map – HOL-83-15100

B.3.29 Bridge HOL-520-6440 (District 11)

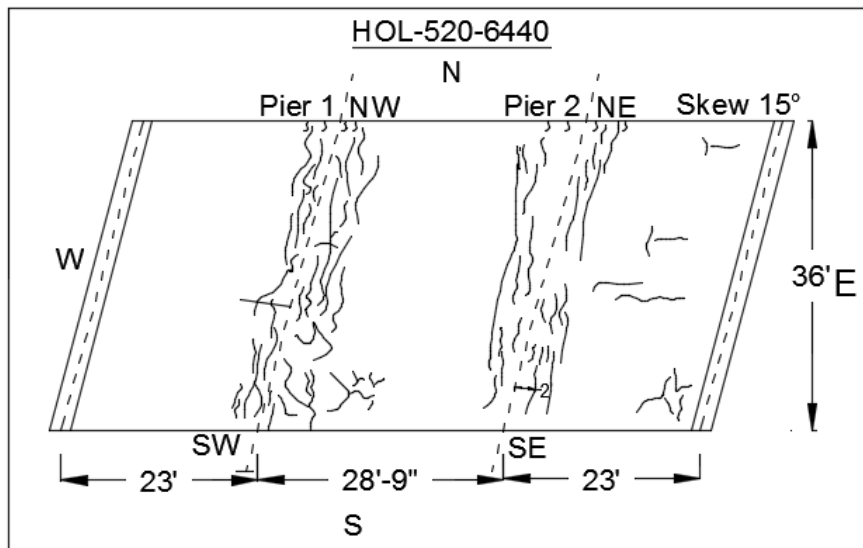


Figure B.30 Bridge Inspection Pictures and Crack Map – HOL-520-6440

B.3.30 Bridge BEL-148-3140 (District 11)

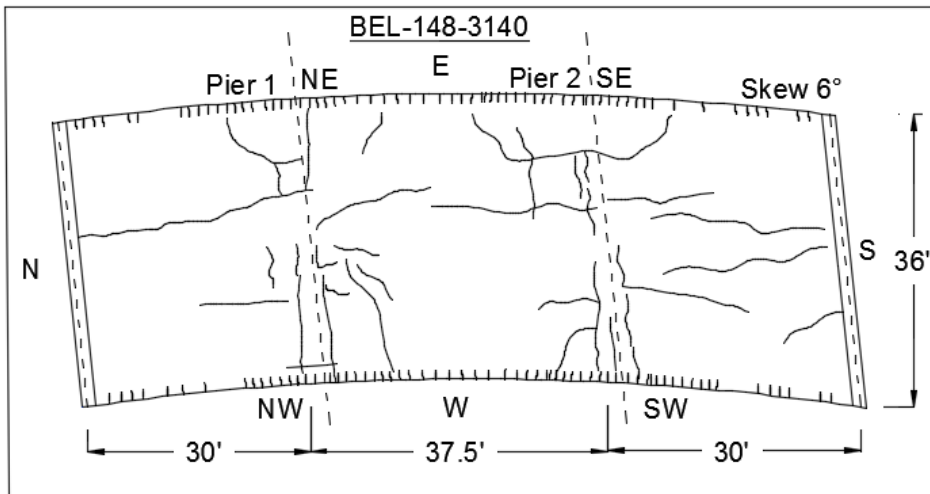


Figure B.31 Bridge Inspection Pictures and Crack Map – BEL-148-3140

B.4 Summary and Conclusions for Bridge Inspections

A total of 30 bridges out of the 63 three-span CSS bridges proposed by ODOT SMEs were surveyed for transverse cracks. The cracks on these bridge decks were mapped to record the crack patterns and the transverse crack widths in the negative moment region of the bridge decks, were measured. The cracks widths varied for bridges with different span lengths, traffic conditions, deck thicknesses, skew angles, and number of years in service.

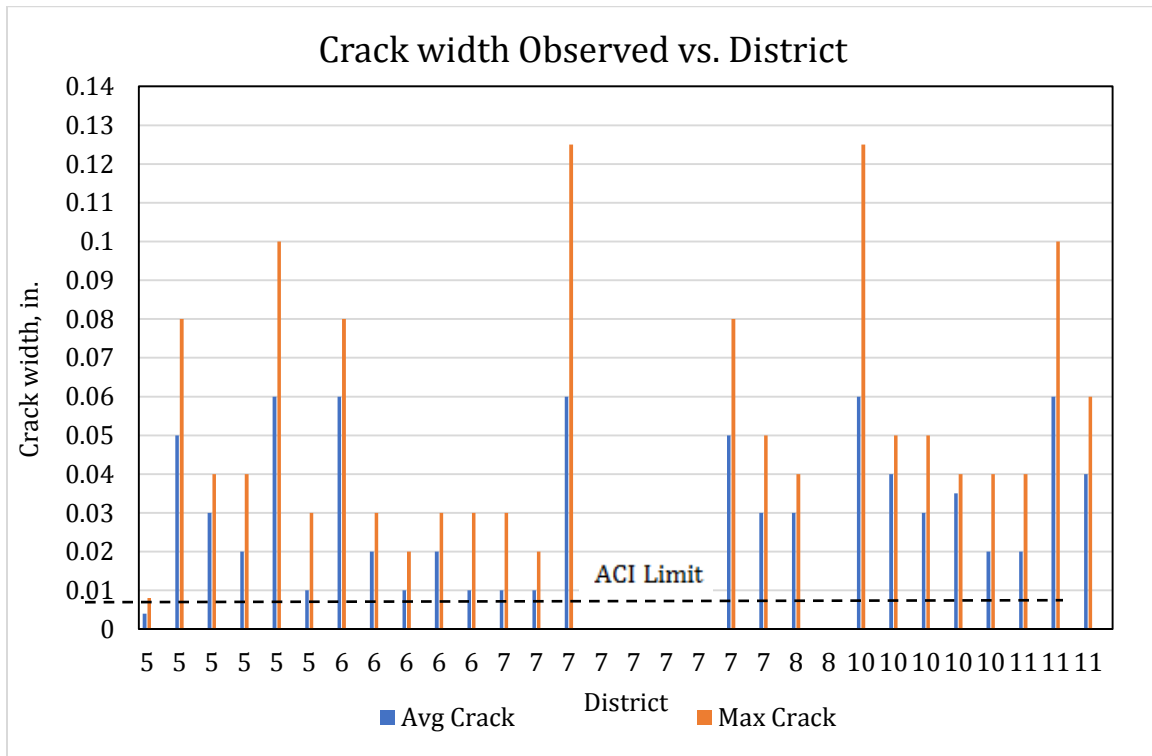


Figure B.32 Crack Widths Measured on Bridges in All ODOT Districts

Figure B.32 presents the average and maximum crack widths for all bridges surveyed in various ODOT districts. The maximum crack width ranging from 0.1 to 0.125 inches was observed on bridge decks.

Based on the findings of the crack inspections conducted on the 30 bridges surveyed in this study, the following conclusions are made:

- In District 7, the bridges with small spans (three bridges with maximum spans of 20 ft. and one bridge with a maximum span of 30 ft.) had no cracks. The bridge in District 7 with the longest span (45 ft.), already had cracks exceeding 0.03 inches in width after 8 years of service. This implies that the span length is a factor that needs to be considered to ensure the durability of structural slab bridges.
- For all bridges with measurable cracks, the observed crack widths greatly exceed the ACI allowable limit of 0.007 inches, which is indicated by a dashed line in Figure B.32. This finding suggests the limit by ACI is questionable.

REFERENCES

- ACI 224R-01 “Control of Cracking of Concrete Structures,” ACI Committee 224, American Concrete Institute, Farmington Hills, MI. 2008.
- ACI 318-11 “Building Code Requirements for Structural Concrete and Commentary,” American Concrete Institute, Farmington Hills, MI. 2011.
- ODOT QC/QA Concrete Pavement with Warranty. Supplemental Specification 896. Ohio Department of Transportation, Columbus, OH. April 15, 2015. Available at http://www.dot.state.oh.us/Divisions/ConstructionMgt/Specification%20Files/896_04152005_for_2005.PDF
- Patnaik. A. and P. Baah. (2015). “Cracking Behavior of Structural Slab Bridge Decks,” Report No. FHWA/OH-2015/4. Ohio Department of Transportation, Columbus, OH. January. Available at https://www.dot.state.oh.us/Divisions/Planning/SPR/Research/reportsandplans/Reports/2015/Structures/134708_FR.pdf

Reduction of Bridge Deck Cracking through Alternative Material Usage

APPENDIX C EVALUATION OF CRACK WIDTH EQUATIONS

Prepared by:
Anil Patnaik, Ph.D.
and
Srikanth Marchetty

Prepared for:
The Ohio Department of Transportation,
Office of Statewide Planning & Research

State Job Number 135260
November 2017
Draft Final Report



TABLE OF CONTENTS

TABLE OF CONTENTS..... 1
LIST OF TABLES 1
APPENDIX C 2
EVALUATION OF CRACK WIDTH EQUATIONS 2
REFERENCES 7

LIST OF TABLES

Table 10.1 Comparison of Spacing of Longitudinal Bars over the Pier Cap Region..... 6

APPENDIX C EVALUATION OF CRACK WIDTH EQUATIONS

Prior to 1999, ACI-318 adopted a crack control provision by following the well-known Gergely and Lutz equation as follows:

$$W_c = 0.076 \frac{h_2}{h_1} f_s \sqrt[3]{t_b A} \times 10^{-6} \text{ in.}$$

Where,

f_s = Stress in steel reinforcement (psi);

t_b = distance from extreme tension fiber to the center of the adjacent bar (inch);

t_s = distance from the side of the slab to the center of the bar (inch);

A = average effective area of concrete in tension around each reinforcing bar
= A_e/n

A_e is the rectangular concrete area of width, b and with same centroid as steel;

n = number of tension bars;

h_1 = the distance from centroid of top steel to the neutral axis (inch);

h_2 = distance from the extreme top tension fiber to the neutral axis (inch).

AASHTO adopted the Gergely and Lutz equation for controlling flexural cracking, but in a slightly rearranged form (AASHTO, 1998). The crack width variable and the β factor (the ration of h_2/h_1) were consolidated into a single Z-factor (which varies according to application and exposure conditions) to calculate the allowable stress in the bar. An approximate crack width of 0.016 in. and an average β factor of 1.2 were used to result in the following equation:

$$f_{sa} = \frac{Z}{\sqrt[3]{d_c A}} \leq 0.6f_y$$

Where,

f_{sa} = allowable reinforcement stress, ksi

Z = 170 for moderate exposure conditions,

= 130 for severe exposure conditions,

= 100 for precast box culverts,

= $\frac{155}{\beta}$ for cast-in-place box culverts;

d_c = distance from the tension face to centroid of nearest reinforcement layer, in.;

f_y = yield stress of reinforcement, (ksi);

With the remaining terms as defined above for Gergely and Lutz equation.

The equation proposed in AASHTO (1998) based on Z-factor approach resulted in impractical results for concrete covers over 3 inches and the computation for effective concrete area term A was cumbersome. Having such inadequacy in the above equation, AASHTO has specified to use 2 inches of concrete cover in design, regardless of the actual cover thickness. This change led to overall inaccuracy of the methodology.

On seeing this shortcoming based on the above equations, Frosch (1999), developed a simple equation to predict crack width that included the actual concrete cover:

$$w_c = 2 \frac{f_s}{E_s} \beta \sqrt{(d_c)^2 + \left(\frac{s}{2}\right)^2}$$

Where,

w_c = crack width, in.

f_s = stress in the steel reinforcement, ksi;

E_s = modulus of elasticity of steel reinforcement, ksi;

β = factor relating the strain at the tension face to the strain at the reinforcement layer;

d_c = distance from tension face to centroid of the nearest reinforcement layer, in.

s = reinforcement bar spacing, in.

This equation can be re-written to solve for maximum permitted reinforcement bar spacing for any limiting value of crack width, as follows:

$$s = 2 \sqrt{\left(\frac{w_c E_s}{2 f_s \beta}\right)^2 - (d_c)^2}$$

In 1999, the ACI 318 equation was modified from the long-held Gergely and Lutz equation to a simplified-version of Frosch's cracking model. This equation is currently being used to limit the maximum bar spacing.

$$s = \frac{540}{f_s} - 2.5c_c \leq \frac{432}{f_s}$$

Where,

c_c = clear concrete cover on the reinforcement nearest the tension face, in.

f_s = stress in the reinforcing bar, ksi

This simplified equation of the cracking model is based on the following assumption:

$\beta = 1 + 0.08 d_c$;

$w_c = 0.016$ in. limiting crack width, in.;

$d_c = c_c + 0.5$ in. (considering average bar diameter as #8)

The approach taken by ACI 318-05 was based on the following assumptions:

- The stress in steel (f_s) is equal of $0.67 f_y$
- Emphasis was on limiting the bar spacing and not on limiting the allowable stress
- No distinction was made between interior and exterior exposure
- No upper limit was given for the stress in the reinforcement f_s

AASHTO (2012) proposed one such equation based on the parametric studies comparing one various crack width predictive methods and developed an equation similar to the Frosch cracking model that was previously adopted by ACI 318-05.

$$s \leq \frac{(700\gamma_e)}{\beta_s f_{ss}} - 2d_c$$

where,

$$\beta_s = 1 + \frac{d_c}{0.7(h - d_c)}$$

Where,

- γ_e = exposure factor
 - = 1.00 for Class 1 exposure condition
 - = 0.75 for Class 2 exposure condition
- d_c = thickness of concrete cover measured from extreme fiber to center of the flexural reinforcement located closest thereto (in.);
- f_{ss} = tensile stress in steel reinforcement at the service limit state (ksi)
- h = overall thickness of the component (in.)
- s = spacing of reinforcement
- β_s = distance from the extreme compression fiber to the centroid of the extreme tension steel element (in.)

The Class 1 exposure condition is based on the assumed crack width of 0.017 inches and could be thought of as an upper bound in regards to crack width for appearance and corrosion. Areas that the “authority having jurisdiction” may consider a Class 2 exposure condition would include decks and substructures exposed to water. The crack width is directly proportional to γ_e exposure factor; therefore, if the individual authority with the jurisdiction desires a different crack width, the γ_e factor can be adjusted directly. For example, a γ_e factor of 0.5 will result in an approximate crack width of 0.0085 in.

The spacing equation given in ACI 318-14 was defined based on #8 bar diameter and clear concrete cover. Stress considered was $0.67f_y$. The accuracy of this equation for other bar diameters and different sections with different β factors is unknown.

Table 10.1 presents the comparison of actual spacing between the longitudinal bars over the pier cap region specified in ODOT standard drawing with the spacing determined from the above equations using ACI 318-14, Frosch (2001) and AASHTO (2012). Calculation parameters for individual columns are discussed below:

Column A: The spacing of the bar was also calculated using the ACI 318 equation with stress in the reinforcement as $0.67 f_y$ and clear concrete cover c_c .

Column B: In ODOT design calculations, AASHTO 5.7.3.4 is used to calculate the spacing between the bars. There is a reduction of 1 inch of concrete cover, which acts as sacrificial layer from the actual cover thickness; this leads to lowering of the β factor and results in larger spacing between the bars. The equation given in AASHTO uses effective concrete cover, and the β calculated uses the total thickness of the slab.

Column C: AASHTO 5.7.3.4 equation was used with actual stress in the reinforcement from ODOT design calculations and actual β of the section.

Column D: AASHTO 5.7.3.4 equation was used with $0.6f_y$ as stress in the reinforcement with actual β of the section.

Column E: Spacing between the bars was calculated using Frosch (2001) equation for a crack width of 0.016 inches and with a stress of $0.6f_y$.

As can be seen in the table, ODOT spacing is less than the maximum spacing determined from the AASHTO (2012) equation (Column B). However, the actual crack widths measured on the bridges inspected in this project were much larger than what is predicted from the use of these equations. Also, these crack width equations were derived primarily for black bars and are not necessarily applicable to other bars types, such as ECB.

Table 10.1 Comparison of Spacing of Longitudinal Bars over the Pier Cap Region

SLAB DATA									
SPANS	Thickness	Longitudinal Bars			A	B	C	D	E
		D BARS (Over The Pier Cap Region)			ACI	AASHTO	AASHTO	AASHTO	Frosch
(ft.)	(in.)	SIZE	SPACING (in.)	LENGTH	(in.)	(in.)	(in.)	(in.)	(in.)
14-17.50-14	11	8	7	21'	7.2	10.6	6.9	3.5	5.9
15-18.75-15	11.5	8	7	22'-3"	7.2	9.0	5.6	3.7	6.1
16-20-16	12	8	7	23'-6"	7.2	10.5	6.9	3.9	6.3
17-21.25-17	12.5	8	7	24'-9"	7.2	8.9	5.6	4.1	6.5
18-22.50-18	13	8	7	26'	7.2	9.0	5.7	4.2	6.7
19-23.75-19	13.5	8	7	27'-3"	7.2	8.9	5.6	4.4	6.9
20-25-20	14	8	7	28'-6"	7.2	8.9	5.7	4.5	7.1
21-26.25-21	14.5	8	7	29'-9"	7.2	8.9	5.7	4.6	7.2
22-27.50-22	15	8	7	24'-8"	7.2	8.6	5.5	4.8	7.4
23-28.75-23	15.5	8	7	25'-5"	7.2	9.0	5.9	4.9	7.5
24-30-24	16	8	6	26'-3"	7.2	8.8	5.7	5.0	7.6
25-31.25-25	16.5	8	6	27'-1"	7.2	8.5	5.5	5.1	7.7
26-32.50-26	17	8	6	27'-10"	7.2	8.9	5.9	5.2	7.8
27-33.75-27	17.5	8	6	28'-8"	7.2	8.9	5.9	5.3	7.9
28-35-28	18	8	6	29'-6"	7.2	8.5	5.5	5.3	8.0
29-36.25-29	18.5	8	6	30'-3"	7.2	9.5	6.5	5.3	8.0
30-37.50-30	19	9	7	31'-1"	7.2	9.4	6.5	5.3	8.1
31-38.75-31	19.5	9	7	31'-11"	7.2	9.7	6.8	5.4	8.1
32-40-32	20	9	7	32'-8"	7.2	9.8	6.9	5.5	8.2
33-41.25-33	20.5	9	7	33'-6"	7.2	8.9	6.1	5.5	8.3
34-42.50-34	21	9	7	34'-4"	7.2	9.2	6.4	5.6	8.4
35-43.75-35	21.5	9	6	35'-2"	7.2	8.9	6.0	5.7	8.4
36-45-36	22	9	6	35'-11"	7.2	10.0	7.1	5.7	8.5
37-46.25-37	22.5	9	6	36'-9"	7.2	9.8	7.0	5.8	8.6
38-47.50-38	23	9	6	37'-6"	7.2	9.9	7.1	5.8	8.6
39-48.75-39	23.5	9	6	38'-4"	7.2	11.2	8.3	5.9	8.7
40-50-40	24	9	6	39'-1"	7.2	11.1	8.2	5.9	8.7
41-51.25-41	24.5	10	6	39'-11"	7.2	9.9	7.1	6.0	8.8
42-52.50-42	25	10	6	40'8"	7.2	9.7	6.9	6.0	8.8
43-53.75-43	25.5	10	6	41'-6"	7.2	10.9	8.1	6.1	8.9
44-55-44	26	10	6	42'-4"	7.2	10.6	7.8	6.1	8.9
45-56.25-45	26.5	10	6	43'-1"	7.2	10.8	8.0	6.2	9.0
46-57.50-46	27	10	6	43'-10"	7.2	10.4	7.6	6.2	9.0

REFERENCES

- AASHTO "AASHTO LRFD Bridge Design Specifications," 2nd Edition, American Association of State Highway and Transportation Officials, Washington, D.C., 1998. p. 5-40.
- ACI 318-11 "Building Code Requirements for Structural Concrete and Commentary," American Concrete Institute, Farmington Hills, MI. 2011.
- ACI 318-14 "Building Code Requirements for Structural Concrete and Commentary," American Concrete Institute, Farmington Hills, MI. 2014.
- Destefano, R. J., J. Evans, M. K. Tadros, and C. Sun. 2003. "Flexural Crack Control in Concrete Bridge Structures." PCI Convention, October 19, 2003.
- Frosch, R.J. (1999). Another Look at Cracking and Crack Control in Reinforced Concrete. *ACI Struct. J.* 96 (3) 437–442.
- Gergely, P. and Lutz, L. A., (1968) "Maximum Crack Width in Reinforced Flexural Members," Causes, Mechanisms and Control of Cracking in Concrete, ACI SP-20, American Concrete Institute, Detroit, pp. 87–117.

Reduction of Bridge Deck Cracking through Alternative Material Usage

APPENDIX D

CORROSION RESISTANCE OF SLABS WITH DIFFERENT TYPES OF BARS

Prepared by:
Anil Patnaik, Ph.D.
and
Srikanth Marchetty

Prepared for:
The Ohio Department of Transportation,
Office of Statewide Planning & Research

State Job Number 135260
November 2017
Draft Final Report



TABLE OF CONTENTS

TABLE OF CONTENTS.....	1
LIST OF FIGURES	2
LIST OF TABLES	3
APPENDIX D CORROSION RESISTANCE OF SLABS WITH DIFFERENT TYPES OF BARS	4
D.1 INTRODUCTION	4
D.2 EXPERIMENTAL PROGRAM ON CORROSION SLABS	4
<i>D.2.1 Casting of Slab Specimens</i>	5
<i>D.2.2 Test Setup for Corrosion Testing</i>	7
<i>D.2.3 Accelerated Corrosion Process</i>	8
<i>D.2.4 Flexural Loading for Pre-Cracking</i>	9
<i>D.2.5 Corrosion Test Setup</i>	9
<i>D.2.6 Flexural Testing</i>	10
<i>D.2.7 Results of Corrosion Tests</i>	11
<i>D.2.8 Results of Flexural Testing</i>	13
<i>D.2.9 Metal Loss Results</i>	17
D.3 CORROSION OF PRISM SPECIMENS FOR PULLOUT TESTING.....	18
<i>D.3.1 Preparation of Formwork</i>	19
<i>D.3.2 Casting of Pullout Specimens</i>	19
<i>D.3.3 Curing of Pullout Specimens</i>	19
<i>D.3.4 Capping of Pullout Specimens</i>	20
<i>D.3.5 Accelerated Corrosion of Pullout Specimens</i>	20
<i>D.3.6 Testing of Pullout Specimens</i>	22
<i>D.3.7 Results of Pullout Tests</i>	23
D.4 SUMMARY AND CONCLUSIONS FROM CORROSION TESTING	27

LIST OF FIGURES

Figure D.1 Schematic of the Slab Specimen Designed for Corrosion Testing.....	5
Figure D.2 Wire and Defects Applied to the Epoxy-Coated Bars.....	6
Figure D.3 Formwork for Test Slabs with Various Types of Rebar.....	6
Figure D.4 Casting of Test Slabs for Corrosion Testing	7
Figure D.5 Typical Setup of Corrosion Tests for Slabs.....	8
Figure D.6 Pre-Cracking of Test Slabs in a Loading Frame Loading (left) and Marking of Pre-Cracks on the Slabs (right).....	9
Figure D.7 Schematic of the Corrosion Test Setup	10
Figure D.8 Typical Setup of Specimens Undergoing Accelerated Corrosion	10
Figure D.9 Flexure Test on Pristine Slab.....	11
Figure D.10 Surfaces of Slabs made with and without Fibers (Day 21)	12
Figure D.11 Flexural Capacity Loss of Non-Fiber Specimens Due to Corrosion	15
Figure D.12 Flexural Capacity Loss of Fiber Specimens Due to Corrosion	15
Figure D.13 Percentage Reduction in Capacity Loss of Slabs with and without Fibers	16
Figure D.14 Corroded Rebar from Slabs without Fibers (top) and with Fibers (bottom)	17
Figure D.15 Pullout Specimen Details.....	18
Figure D.16 Bond Breaker Applied on Bars.....	18
Figure D.17 Formwork of Pullout Specimens	19
Figure D.18 Pullout Specimens During and After Casting	19
Figure D.19 Curing of Pullout Specimens.....	20
Figure D.20 Capping of Pullout Specimens which are Subjected to Accelerated Corrosion.....	20
Figure D.21 Test Setup of Pullout Specimens Subjected to Accelerated Corrosion	21
Figure D.22 Corrosion on Specimen at 2 nd day (left) and 10 th day (Right)	22
Figure D.23 Test Setup for Pullout Specimens (left) and Dial Gage Setup (Right).....	22
Figure D.24 Tested Pullout Specimens with Fibers and Corroded.....	23
Figure D.25 Load versus Slip Curves of Non-Corroded Pullout Specimens	24
Figure D.26 Load versus Slip Curves of Corroded Pullout Specimens.....	25
Figure D.27 Peak loads of Non-Corroded Pullout Specimens	26
Figure D.28 Peak loads of Corroded Pullout Specimens.....	26

LIST OF TABLES

Table D.1 Testing Plan for Accelerated Corrosion Testing of Slab Specimens.....	5
Table D.2 Current Required for 14-Day Accelerated Corrosion Process.....	9
Table D.3 Flexural Capacity of Slabs without Fibers.....	13
Table D.4 Flexural Capacity of Slabs with Fibers.....	14
Table D.5 Test Matrix of Pullout Specimens.....	21

APPENDIX D

CORROSION RESISTANCE OF SLABS WITH DIFFERENT TYPES OF BARS

D.1 Introduction

Corrosion of reinforcing bars in bridge decks is a major problem for reinforced concrete (RC) bridges across the United States. Bridge decks are exposed to de-icing salts during the winter months. Cracks in bridge decks are the main pathway for de-icing salts to pass through the concrete cover and reach the reinforcing steel, leading to corrosion of the bars and loss of metal from the cross section of the bar. This is particularly true for continuous structural slab bridge decks, which are more prone to corrosion and subsequent degradation in the steel reinforcements because they have much wider cracks on the tension side on the top exposed to de-icing salts. Once the reinforcing steel starts corroding, the service life of the bridge deck will be reduced.

Another major problem with structural slab bridge decks is transverse cracking over the negative moment region. These cracks can greatly exceed the allowable limits recommended by ACI for different exposure conditions. Black conventional steel has been replaced by epoxy-coated bars in bridge reinforcements in recent decades to protect against corrosion. In the 1980s, most transportation agencies in the United States adopted epoxy-coated bars as the main reinforcing steel in structural applications where the reinforcing steel is more prone to corrosion. However, it has been well documented that bridges with epoxy-coated steel have wider cracks than conventional steel bridges. In addition, improper handling of epoxy-coated steel at the construction site can cause it to develop defects over the bar length. With wider cracks in the deck and defects present on the bars, bridges constructed using epoxy-coated steel have exhibited accelerated corrosion damage in bridges at localized locations.

Many researchers have conducted experiments to understand the behavior of RC slabs subjected to corrosion. Under actual conditions of the structural slab bridges during service, the dead load of the bridge is constantly acting and keeps the cracks open, providing a pathway for chlorides to reach the steel reinforcement. Service loads on the bridges allow these cracks to open further, leading to even more chlorides passing through the deck to the reinforcements. To replicate this condition in laboratory tests, the corrosion process on the bridge decks was simulated by using an accelerated corrosion process while the test specimens are subjected to sustained loading.

D.2 Experimental Program on Corrosion Slabs

Slab specimens that were 12 inches wide, 3 inches deep and 28 inches long were cast with conventional black steel as well as with several types of corrosion-resistant reinforcing bars (epoxy-coated bars, hot-dipped galvanized bars, stainless steel bars, and MMFX bars) in preparation for laboratory testing. The bar size selected was #4 rebar with a clear concrete cover of 0.5 inches. These slabs were cast using job mix formulas (JMFs) from ODOT projects for slabs with and without fibers. Figure D.1 shows the schematic of a slab specimen, and Table D.1 presents the test plan for corrosion testing.

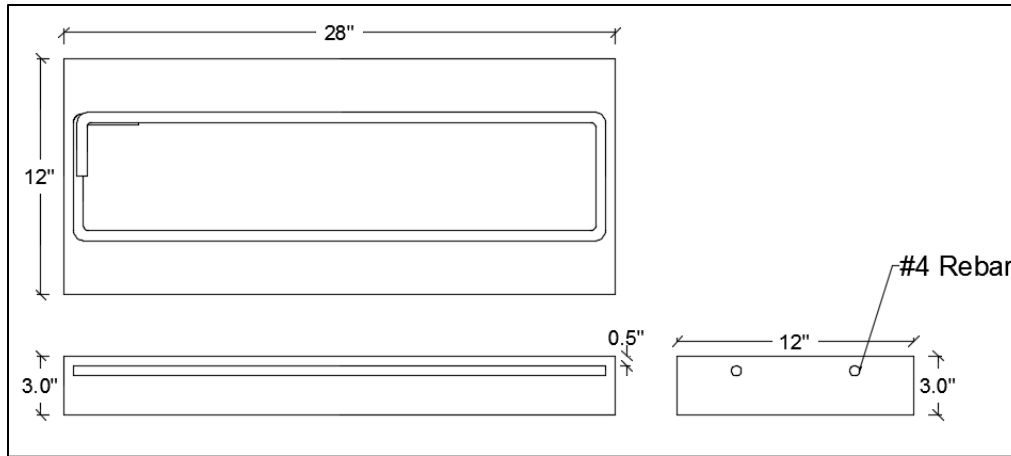


Figure D.1 Schematic of the Slab Specimen Designed for Corrosion Testing

Table D.1 Testing Plan for Accelerated Corrosion Testing of Slab Specimens

Type of Bar	Black Bar	Epoxy-Coated Bar	Hot-Dip Galvanized Bar	MMFX Bar	Stainless Steel Bar
Slabs (Uncorroded)	4 no fiber	4 no fiber	4 no fiber	4 no fiber	4 no fiber
	4 with fiber	4 with fiber	4 with fiber	4 with fiber	4 with fiber
Specimens (Cracked + Sustained Load + Corrosion)	4 no fiber	4 no fiber	4 no fiber	4 no fiber	4 no fiber
	4 with fiber	4 with fiber	4 with fiber	4 with fiber	4 with fiber
Total Specimens	16	16	16	16	16

D.2.1 Casting of Slab Specimens

A total of 80 slabs were cast in formwork that was made with 0.75-inch-thick plywood using a standard mix design commonly employed by ODOT for slabs with and without fibers, as discussed in Chapter F. The reinforcing bar was bent to the shape of a stirrup, and the ends of the hooks were welded so as to create hook action inside the slab (to prevent relative slipping of the reinforcement during testing). For the specimens that were to be subjected to corrosion, a 14-gage wire was connected to the reinforcement prior to casting and was covered with a hot shrink tube to protect it inside the concrete. The mix designs used are given in Table F.3. For specimens

constructed using epoxy-coated steel bars, a 5% defect was induced on the bars in order to replicate the defects that can occur on site during the handling process. Figure D.2 shows an epoxy-coated steel bar with manually applied defects.

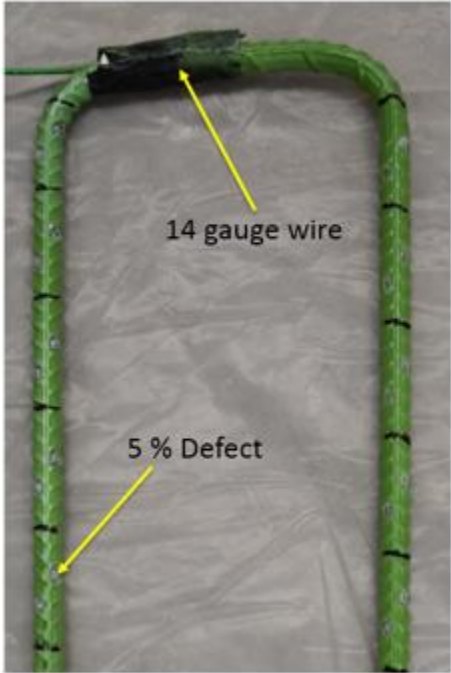


Figure D.2 Wire and Defects Applied to the Epoxy-Coated Bars

Figure D.3 presents the formwork constructed for the casting of test slabs. Each form could accommodate a total of 10 test slabs. Four sets of formworks were made to accommodate the 40 slabs cast without fibers, and an additional four sets of formworks were made for the remaining 40 slabs to be cast with fibers.



Figure D.3 Formwork for Test Slabs with Various Types of Rebar

After forty slabs were cast without fiber, the casting was repeated using the same mix design (Table F.3) with the addition of 10 lb/yd³ of polypropylene fibers. Figure D.4 shows the test slabs along with the cylinders made to determine the compression strength of the concrete during its curing period. These slabs were cured for 28 days, until a minimum of 4,500 psi of concrete strength was achieved.



Figure D.4 Casting of Test Slabs for Corrosion Testing

D.2.2 Test Setup for Corrosion Testing

The test setup for the corrosion testing was designed to replicate the actual conditions on the bridge decks. Each slab was supported in a specially fabricated test frame, and a constant sustained load was applied to the slab using a mechanical jack. A salt solution tank, which was assembled and glued to the tension face of the slab, contained a salt solution (5% NaCl) to act as an electrolyte and simulate a deicing salt on a bridge deck. A stainless-steel plate was placed in the salt solution tank to act as a cathode, and a wire from the stainless-steel plate was connected to the negative terminal of a direct current (DC) power supply. A second wire, which was connected at one end to the rebar of each specimen prior to casting, was connected at the other end to the positive terminal of the power supply during the test to form a closed circuit in order to accelerate the corrosion process. Figure D.5 shows the test setup for the accelerated corrosion of a typical test slab.

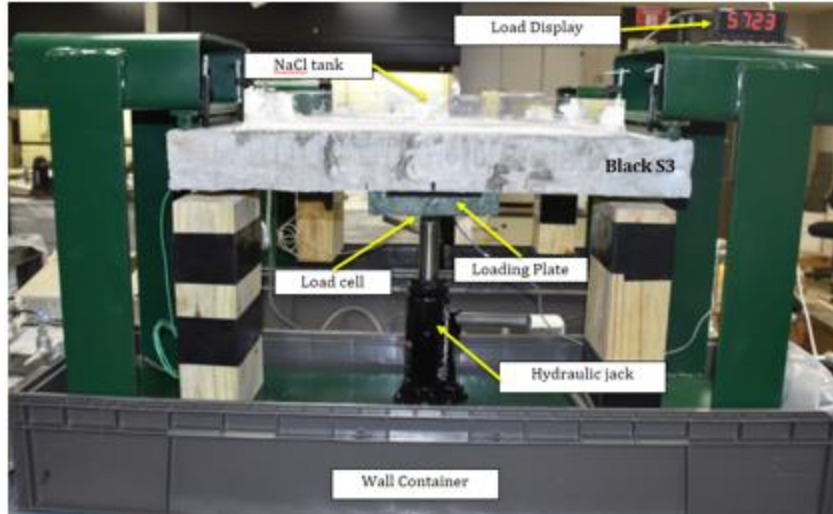


Figure D.5 Typical Setup of Corrosion Tests for Slabs

A 10-kip load cell along with a display was used to continuously monitor the load applied on the test slab, and a sustained load of 4.2 kips (i.e. 40% of the failure load of the slab) was maintained throughout the corrosion process. The applied load level was selected to replicate the dead load stresses that are constantly acting on the bridge decks.

D.2.3 Accelerated Corrosion Process

As the natural corrosion process occurs over a long period of time, it is unrealistic to investigate the behavior of corrosion-resistant bars embedded in RC slabs in laboratory tests using the same exposure period as a bridge exposed to environmental conditions during a given period of service. To minimize the time required to conduct laboratory tests, it is possible to accelerate the corrosion process by creating a corrosion cell and passing an electric current through the test specimens. The time and current for the accelerated corrosion process is calculated using Faraday's law to achieve a specific corrosion level. From prior tests performed by Gao and Patnaik (2016), it was observed that a higher percentage of corrosion had an observable effect on the structural strength of a concrete slab. Hence, a 15% corrosion level with a total corrosion time of 21 days was used in the tests conducted in this study. During the 21-day testing period, a cycle of two days of wetting followed by one day of drying was used, and the current was calculated for a two-week period (equivalent to 1,209,600 seconds) using Faraday's equation:

$$\Delta m = MIt/zF$$

where Δm is the mass of steel consumed (grams); M is the atomic weight of the metal (56 grams (0.1232 lb) for Fe); I is the current (amperes); t is time (seconds); z is the ionic charge (which is equal to 2); and F is Faraday's constant (96,500 amperes/second). Table D.2 presents the current calculated for a period of wetting cycle (14 days) to achieve a corrosion level of 15%.

Table D.2 Current Required for 14-Day Accelerated Corrosion Process

z	F	M (g)	t (sec.)	Unit Weight (lb/ft)	Percentage loss (%)	Rebar Exposed Length (in.)	I (amperes)
2	96,500	56	1,209,600	0.669	15	44	0.474

D.2.4 Flexural Loading for Pre-Cracking

Test slabs that are subjected to the corrosion process were cracked prior to the corrosion tests by applying a three-point load in a UTM of 300-kip capacity. The span of the test slabs was 24 inches, and a load between 40% and 50% of the capacity of the slab was applied to create cracks. Once the slab was loaded to the desired level, the slab surface was monitored to make sure a crack became visible. Figure D.6 shows the cracks induced on the test slabs before they were subjected to the accelerated corrosion process. The pre-cracks were marked on the slabs, and these locations were continuously monitored during the corrosion process. A total of three specimens for each bar type were pre-cracked and tested.

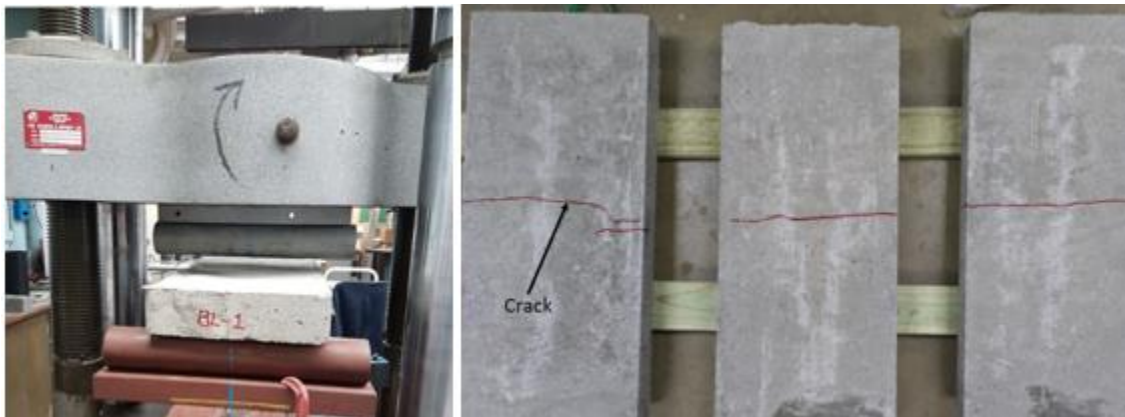


Figure D.6 Pre-Cracking of Test Slabs in a Loading Frame Loading (left) and Marking of Pre-Cracks on the Slabs (right)

D.2.5 Corrosion Test Setup

A salt solution tank made of plastic sheets was glued on the tension face of the pre-cracked slabs. Two rebar types were tested at one time for corrosion for a period of 21 days. The slabs were then placed in a setup in the testing frame with an applied sustained load of 4,200 kips throughout the corrosion process. The test load, which was calculated to replicate the dead load stresses that are typically observed on bridge decks, was applied to cause tension on the top of the slab using mechanical jacks. A load cell with a digital display was used to monitor the applied load to ensure that a constant load was maintained throughout testing. A 5% NaCl solution was prepared and used in the tanks to simulate exposure to deicing salts dissolved in water on the bridge deck. A stainless-steel plate was placed in the tank to act as a cathode. A wire from the specimen was connected to the positive terminal of a DC power supply, and a wire from the stainless-steel plate was connected to the negative terminal. The calculated current of 0.475A was applied during the

wetting cycle of the corrosion process. Figure D.7 shows a schematic of the setup as well as the flow of chloride ions during the corrosion process.

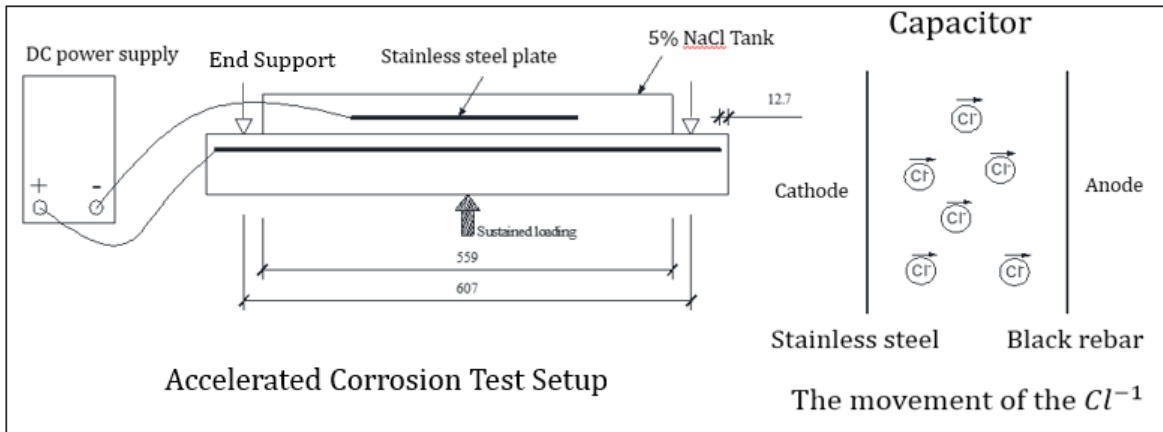


Figure D.7 Schematic of the Corrosion Test Setup

The tension face of the slab was divided into segments to facilitate monitoring the development of cracks over time during the corrosion process. The salt solution was removed on the third day, and the specimen was left to dry during the drying cycle. Pictures of the slab surface were taken and cracks patterns and widths were recorded. On fourth day, the salt solution was refilled in the tanks, and the process was repeated until the test duration reached a total of 21 days with 14 days of wetting cycles and 7 days of drying cycles. Figure D.8 shows the setup of a set of specimens undergoing corrosion.



Figure D.8 Typical Setup of Specimens Undergoing Accelerated Corrosion

D.2.6 Flexural Testing

Pristine slabs and corroded slab specimens were tested for flexural capacity loss after the corrosion process was completed. Three specimens for each set were tested to obtain the average

flexural capacity for pristine and corroded specimens. A universal testing machine was used to perform a three-point bending test using a load rate of 30 lbs/sec (13.6 kg/sec). This process was repeated for all the test slabs. Figure D.9 presents typical test setup for flexural capacity testing.



Figure D.9 Flexure Test on Pristine Slab

D.2.7 Results of Corrosion Tests

Three slabs of each bar type with and without fibers, were subjected to the accelerated corrosion process under similar conditions. It was observed that, the longitudinal cracks began to develop within the first three days, and the cracks grew slowly over a period of 21 days. Transverse cracks were initially formed and subsequently remained unchanged.

On comparison of slabs made with and without fibers at Day 21 (Figure D.10), it can be noticed that the surface condition of the slabs made with fibers was much better than that of the slabs made without fibers for all bar types. Both transverse and longitudinal crack widths were reduced drastically due to the addition of fibers, without much damage to the bars embedded within the concrete. It is concluded that the addition of fibers improved the performance of slabs under a highly accelerated corrosion process.



Figure D.10 Surfaces of Slabs made with and without Fibers (Day 21)

D.2.8 Results of Flexural Testing

Flexural testing was conducted on corroded and the corresponding pristine slab specimens to determine the loss in moment carrying capacity of the slabs due to corrosion. A three-point bending test was performed with a span of 24 inches on a UTM of 300-kip capacity universal testing machine. A load rate of 30 lbs /sec was applied during testing. The capacities of corroded and un-corroded slabs for slabs made with different reinforcing bar types were then compared. Results for the slabs made without fibers are presented in Table D.3.

Table D.3 Flexural Capacity of Slabs without Fibers

Serial No.	Specimen Type	Uncorroded Slab Capacity (Pounds)	Average Capacity Uncorroded (Pounds)	Corroded Slab Capacity (Pounds)	Average Capacity Corroded (Pounds)	Reduction in Capacity (%)
1	Black S1	9,200	9,400	7,100	7,133	24
2	Black S2	9,600		7,300		
3	Black S2	9,400		7,000		
4	Epoxy S1	9,000	9,033	6,100	6,150	32
5	Epoxy S2	9,200		6,200		
6	Epoxy S3	8,900		--		
7	HG S1	9,600	9,433	7,600	7,400	22
8	HG S2	9,500		7,200		
9	HG S3	9,200		7,400		
10	MMFX S1	11,500	11,373	9,648	9,689	15
11	MMFX S2	11,340		9,690		
12	MMFX S3	11,280		9,730		
13	Stainless Steel S1	10,800	10,767	8,700	8,793	18
14	Stainless Steel S2	10,600		8,690		
15	Stainless Steel S3	10,900		8,990		

Slabs cast with corrosion resistant reinforcing bars along with 10 lb/cubic-yard of fiber were also subjected to a three-point bending test to determine their corrosion performance under conditions similar to those of the specimens with no fibers. Results for un-corroded and corroded specimens with fibers and the flexural capacity loss are presented in Table D.4.

Table D.4 Flexural Capacity of Slabs with Fibers

Serial No.	Specimen Type	Uncorroded Slab Capacity (Pounds)	Average Capacity Uncorroded (Pounds)	Corroded Slab Capacity (Pounds)	Average Capacity Corroded (Pounds)	Reduction in Capacity (%)
1	Black Fiber S1	10,480	10,460	8,550	8,543	18
2	Black Fiber S2	10,650		8,630		
3	Black Fiber S2	10,250		8,450		
4	Epoxy Fiber S1	10,650	10,617	8,000	7,937	25
5	Epoxy Fiber S2	10,500		7,950		
6	Epoxy Fiber S3	10,700		7,860		
7	HG Fiber S1	10,200	10,250	8,600	8,517	17
8	HG Fiber S2	10,400		8,400		
9	HG Fiber S3	10,150		8,550		
10	MMFX Fiber S1	11,750	11,637	10,220	10,257	12
11	MMFX Fiber S2	11,540		10,180		
12	MMFX Fiber S3	11,620		10,370		
13	Stainless Steel Fiber S1	10,950	11,103	9,400	9,567	14
14	Stainless Steel Fiber S2	11,160		9,500		
15	Stainless Steel S3	11,200		9,800		

Figures D.11 and D.12 present charts showing the flexural capacity test results of slabs with no fibers and with fibers, respectively. These charts were developed to understand the performance of corrosion-resistant bars subjected to accelerated corrosion. As can be noticed in Figure D.11, epoxy-coated bars with 5% damage induced on the coating showed the greatest extent of corrosion compared to the other bar types, in terms of maximum flexural capacity loss due to loss in bond and reduced area of steel. MMFX bars showed the best corrosion resistance and the lowest bond loss. In hot-dip galvanized bars, the zinc coating protected the bar from corrosion for a few days; once the sacrificial layer was compromised, the base metal showed a similar effect as the black bars. Hence, the capacity loss for the slab with hot-dip galvanized bars is much closer to that of slabs with black bars. Slabs with stainless steel bars also showed better performance after corrosion as well as a smaller loss of flexural capacity due to corrosion.

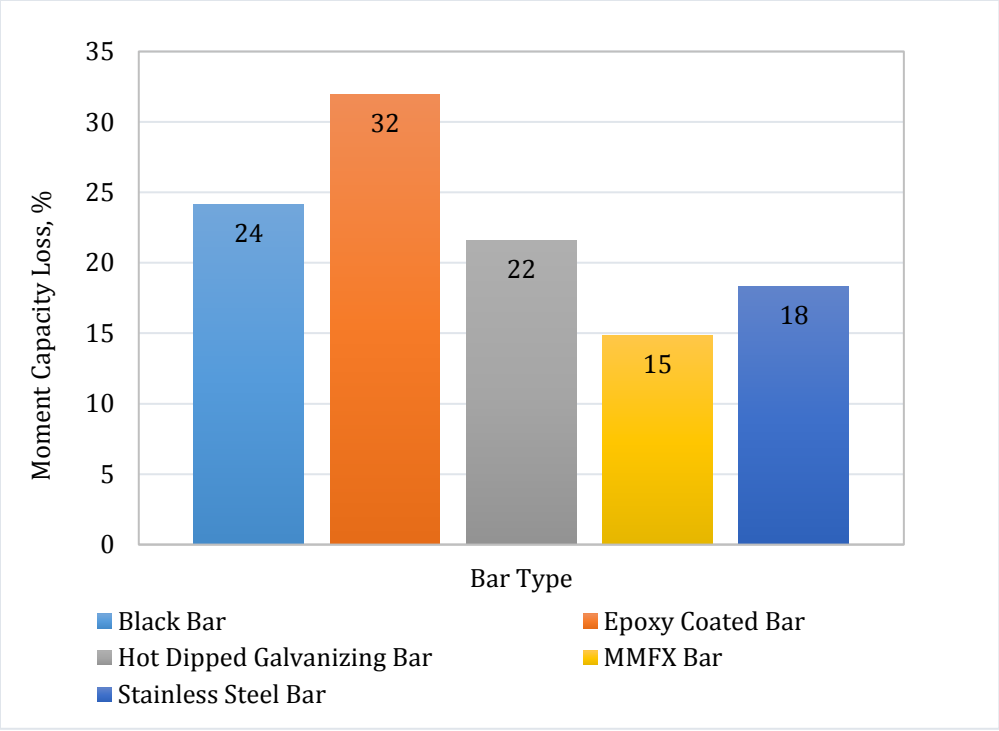


Figure D.11 Flexural Capacity Loss of Non-Fiber Specimens Due to Corrosion

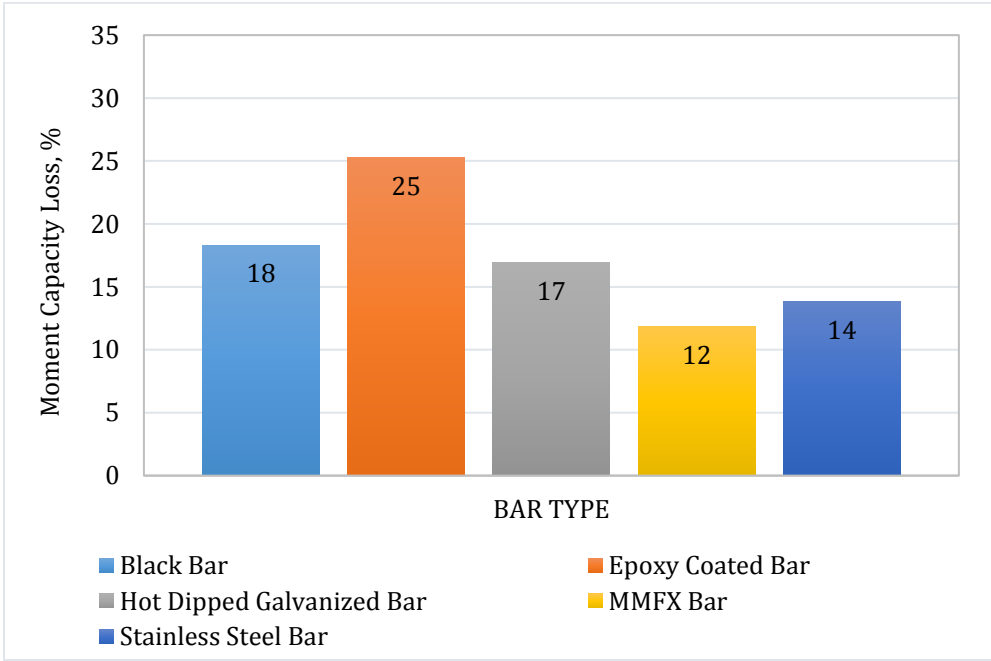


Figure D.12 Flexural Capacity Loss of Fiber Specimens Due to Corrosion

Figure D.13 shows the comparison of slabs with and without fibers in terms of percentage reduction in capacity loss. The performance of slabs with fibers was much better than the performance of slabs with no fibers but showed a similar trend in the percentage of capacity loss.

Slabs made with epoxy-coated bars with a 5% induced defect showed the most moment capacity loss, and the slabs made with MMFX showed the least moment capacity loss. It can be observed that the addition of fibers results in a smaller loss of capacity, even though the slabs have undergone an accelerated corrosion process.

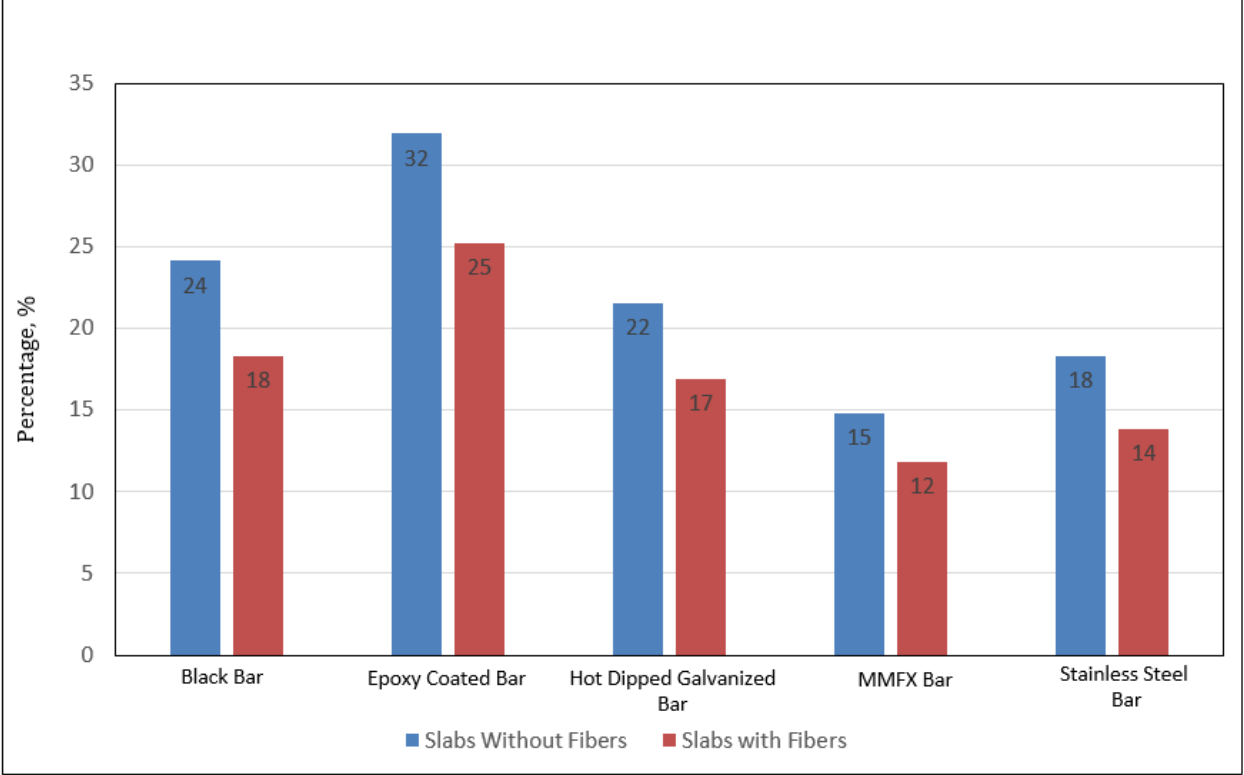


Figure D.13 Percentage Reduction in Capacity Loss of Slabs with and without Fibers

D.2.9 Metal Loss Results

The slabs that were tested for flexural capacity loss were then broken using sludge hammer. The condition of the rebar in all slabs were compared in order to observe the amount of metal lost during the corrosion process. Pictures of the bars made with and without fibers are shown in Figure D.14. After the corrosion process, all the types of bars seemed to have severe deterioration at the surface of the bars, regardless of the coatings on the bars. Addition of fiber doesn't seem to reduce the surface deterioration even though the structural flexural strength of slabs is better maintained due to the addition of fiber compared to slabs with no fiber.

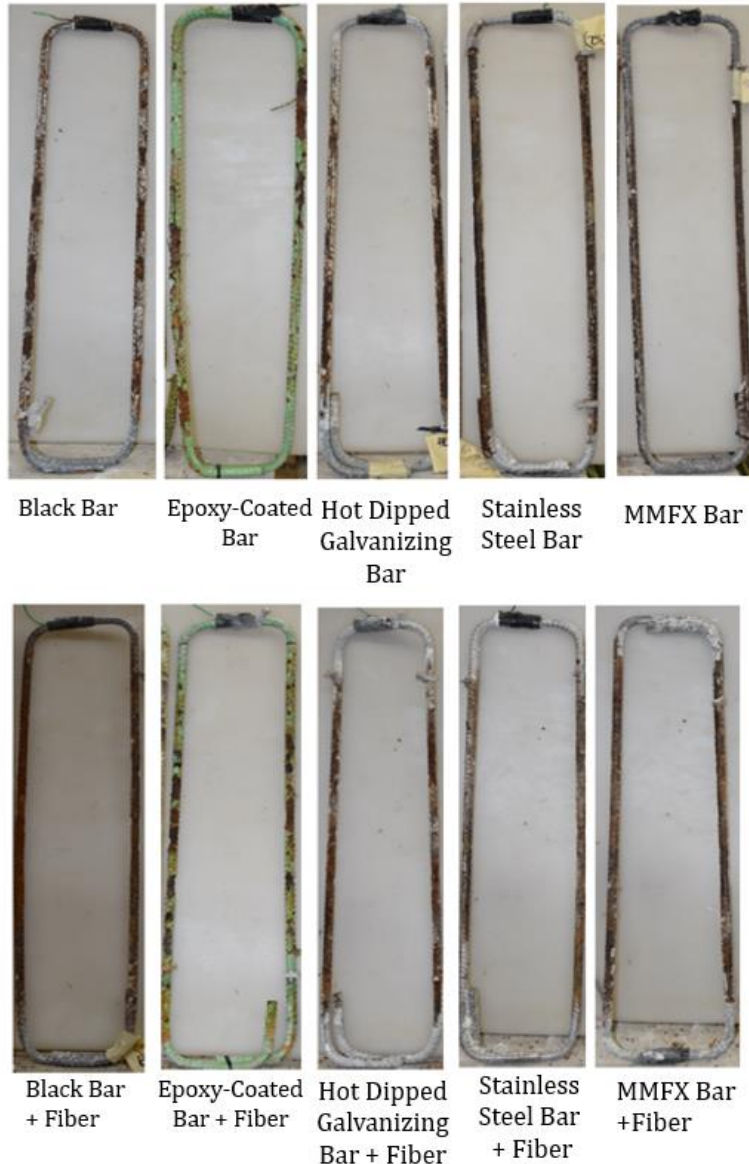


Figure D.14 Corroded Rebar from Slabs without Fibers (top) and with Fibers (bottom)

D.3 Corrosion of Prism Specimens for Pullout Testing

Corrosion of steel reinforcing bars causes volumetric expansion of steel causing cracks in cover concrete, and spalling of concrete leading to bond strength reduction. The behavior of pullout specimens cast with corrosion resistant bars was investigated. The casting and testing of prism specimens with different reinforcing bar types for corrosion-induced bond degradation is discussed.

Six reinforcing bar types as mentioned in Table F.1 were used to cast cube specimen with and without fibers. The specimens were cast with #5 bars, with an embedment length of 2.5 inches. The dimensions of the prisms are shown in Figure D.15. PVC pipe lengths of 1.75 inches were used as bond breaker outside the bonded length as shown in Figure D.16. Half-inch of bar length was protruded at the bottom of the specimen for accommodating the dial gage during testing to measure slip of bars relative to concrete cubes. The total length of the bar used was 30 inches so as to allow adequate length for gripping in the testing machine.

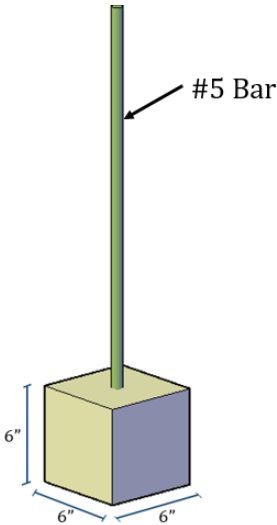


Figure D.15 Pullout Specimen Details



Figure D.16 Bond Breaker Applied on Bars

D.3.1 Preparation of Formwork

The formwork was prepared using 0.75-inch thick ply sheets. Molds of internal dimension 6-inch x 6-inch x 6-inch were made as shown in the figure D.17. The sidewalls were drilled to form 0.7-inch diameter holes to accommodate the reinforcing bar and align it at center.



Figure D.17 Formwork of Pullout Specimens

D.3.2 Casting of Pullout Specimens

The specimens were cast with standard QC2 mix design as mentioned in Table F.3. A total of 48 specimens were cast with and without fibers. Half of the total set served as non-corroded specimens and the remaining 24 specimens were subjected to accelerated corrosion to investigate the reduction in bond strength. Figure D.18 shows the casting of specimens.

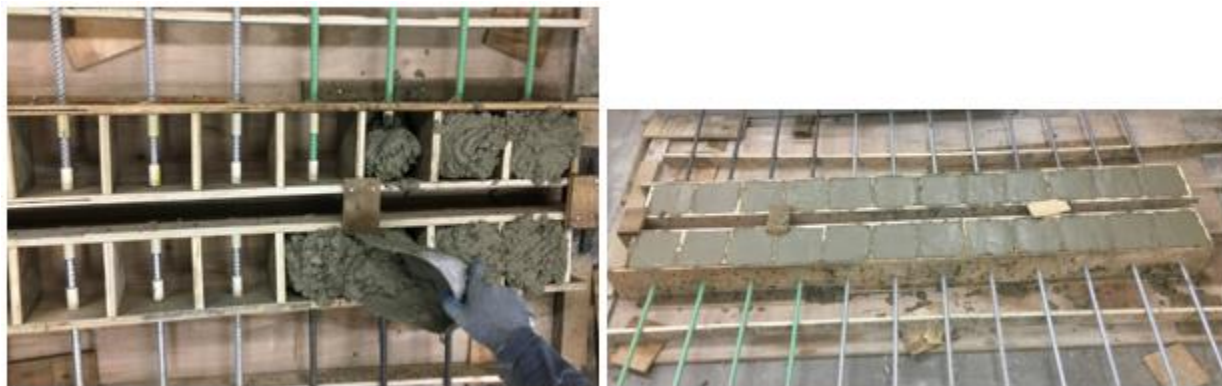


Figure D.18 Pullout Specimens During and After Casting

D.3.3 Curing of Pullout Specimens

The cast specimens were removed from the molds after 24 hours. Since the specimens had reinforcing bars extruded out, the specimens were cured outside the curing room at room temperature by covering them with wet burlaps as shown in Figure D.19. They were regularly

watered for a period of 21 days until a minimum compressive strength of 4500 psi was achieved on the companion cylinders.



Figure D.19 Curing of Pullout Specimens

D.3.4 Capping of Pullout Specimens

The specimens once cured, were ready for testing. The specimens that were subjected to corrosion were initially capped at the bottom surface to cover the half-inch protrusion of the rebar that was extruded during casting. The caps were applied using water resistant silicone to avoid corrosion of exposed bar as shown in Figure D.20.

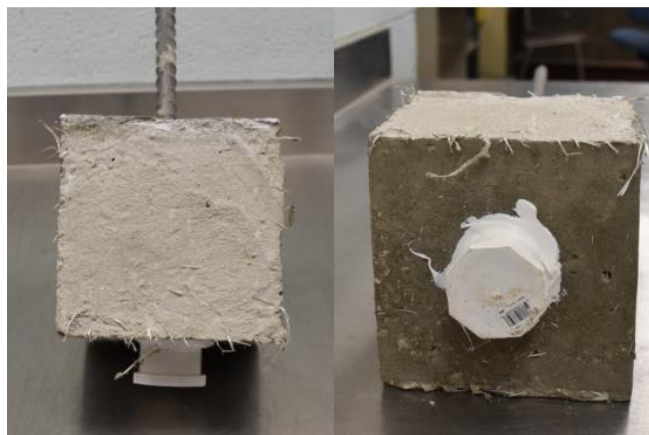


Figure D.20 Capping of Pullout Specimens which are Subjected to Accelerated Corrosion

D.3.5 Accelerated Corrosion of Pullout Specimens

Out of the 48 specimens mentioned in Table D.5., 24 specimens were subjected to accelerated corrosion for a period of 10 days. Five percent corrosion level was used as a basis and

the current intensity was calculated using Faraday’s equation for a period of 10 days. An impressed current of 0.02 A was applied to the bars, specially made casing using stainless steel plates was used as the cathode. A 5% NaCl solution was used as electrolyte in a plastic tank, in which the specimens were immersed until the solution just reached the top surface to avoid corrosion at the interface. A two-day wetting and one day drying cycle was used to increase the effect of corrosion. A typical test setup of corrosion process is shown in figure D.21.

Table D.5 Test Matrix of Pullout Specimens

Types of Reinforcing bar	Non-corroded		Corroded specimens	
	With	Without	With	Without
Black bar	2	2	2	2
Epoxy coated bar	2	2	2	2
MMFX bar	2	2	2	2
Stainless-steel bar	2	2	2	2
Hot-dipped	2	2	2	2
CGR-UAE bar	2	2	2	2
Total	12	12	12	12



Figure D.21 Test Setup of Pullout Specimens Subjected to Accelerated Corrosion

The progress of corrosion on the specimens was visually observed by monitoring the exposed surface of each specimen. A typical specimen with corrosion stains at the surface corrosion is shown in Figure D.22.

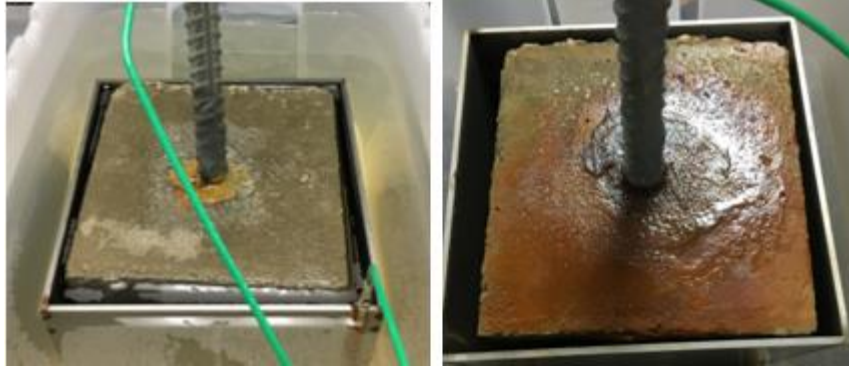


Figure D.22 Corrosion on Specimen at 2nd day (left) and 10th day (Right)

D.3.6 Testing of Pullout Specimens

Both Corroded and non-corroded specimens were tested for pullout strength using Baldwin universal testing machine with a capacity of 300 kips. The setup was arranged in such a way that, at least 6-inches reinforcing bar was clamped inside the jaws. A steel plate with a hole at center was used on the top surface of the specimen to load uniformly on the concrete surface, and a dial gage was used at the bottom side of the specimen to measure the slipping of the bar during testing. The load was applied at a constant rate of 30 to 35 lbs/sec. The dial gage measurements were recorded manually at every 250 lbs. A typical test setup of testing of pullout specimens is shown in Figure D.23. The load was applied until 1-inch of slip was observed in the dial gage.



Figure D.23 Test Setup for Pullout Specimens (left) and Dial Gage Setup (Right)

D.3.7 Results of Pullout Tests

The relative slip of the reinforcing bar with respect to the concrete cube of each test specimen for the entire range of loading was recorded. The loading curve increased to a peak value until a small slip was developed. Once the slipping started, the loading curve dropped rapidly causing larger slip at smaller loads. The typical tested specimens with fibers is shown in Figure D.24.



Figure D.24 Tested Pullout Specimens with Fibers and Corroded

Load versus slip plots were generated for all the specimens to compare the bond loss due to corrosion. The specimen with fibers showed higher bond strength than that of specimens without fibers. Fibers not only increased bond strength on non-corroded specimens but also reduced slippage of bars at similar loads. Typical load versus slip curves were shown in Figure D.25 and D.26. On comparison of the peak load values, it was observed that, the specimens with fiber had much higher peak load.

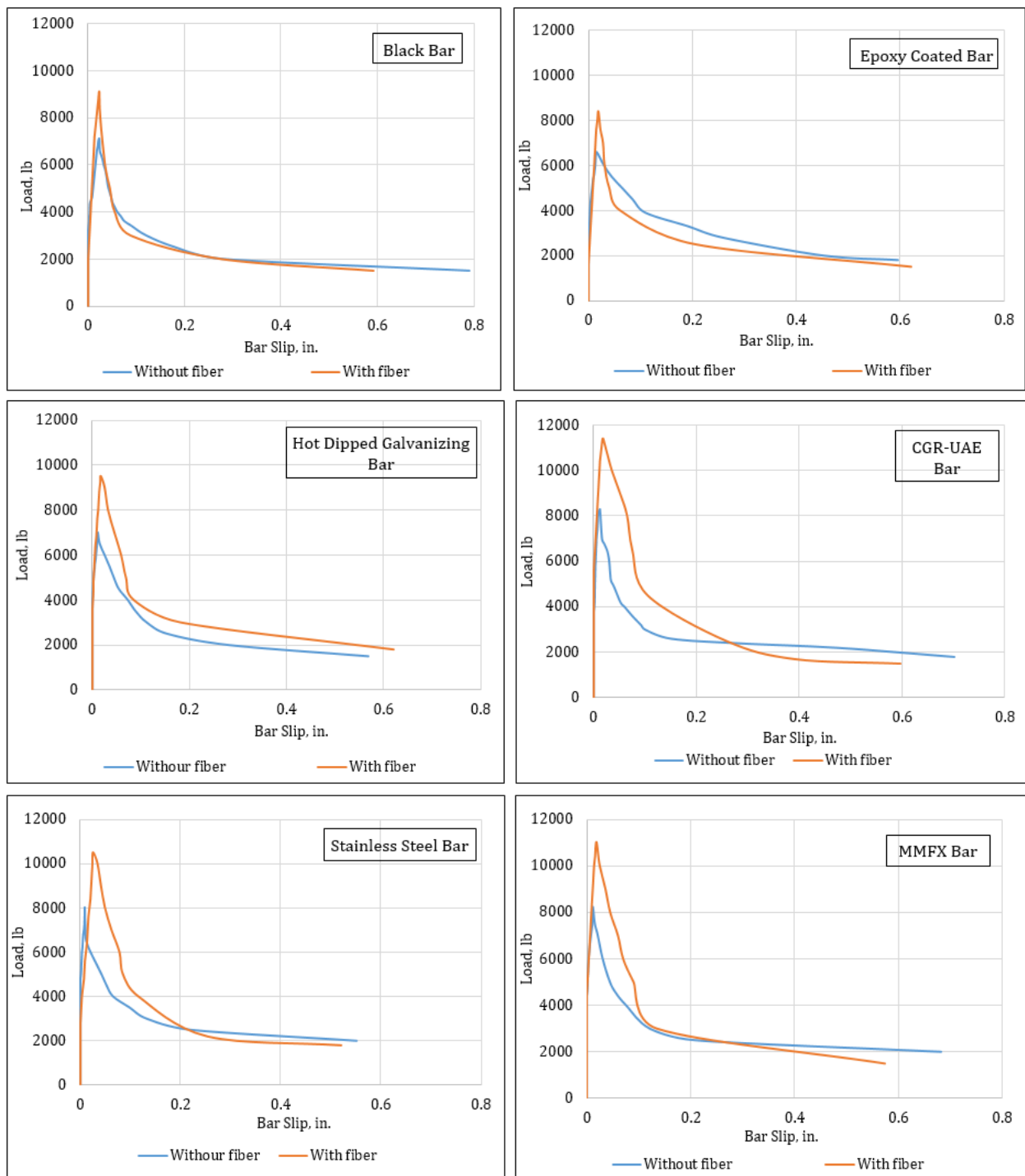


Figure D.25 Load versus Slip Curves of Non-Corroded Pullout Specimens

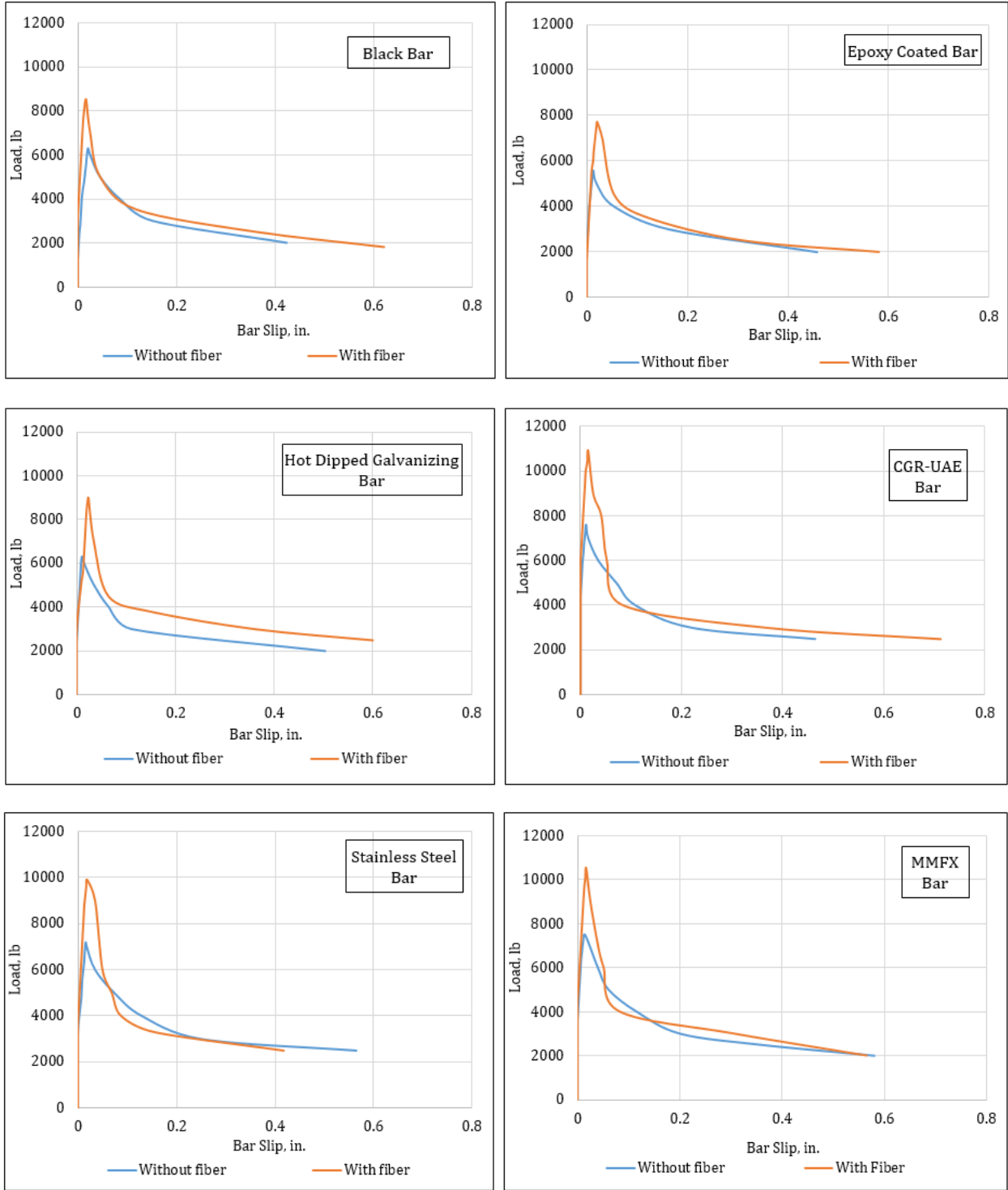


Figure D.26 Load versus Slip Curves of Corroded Pullout Specimens

The peak loads carried by the specimen before starting to slip were also recorded and plotted for comparison as shown in Figures D.27 and D.28.

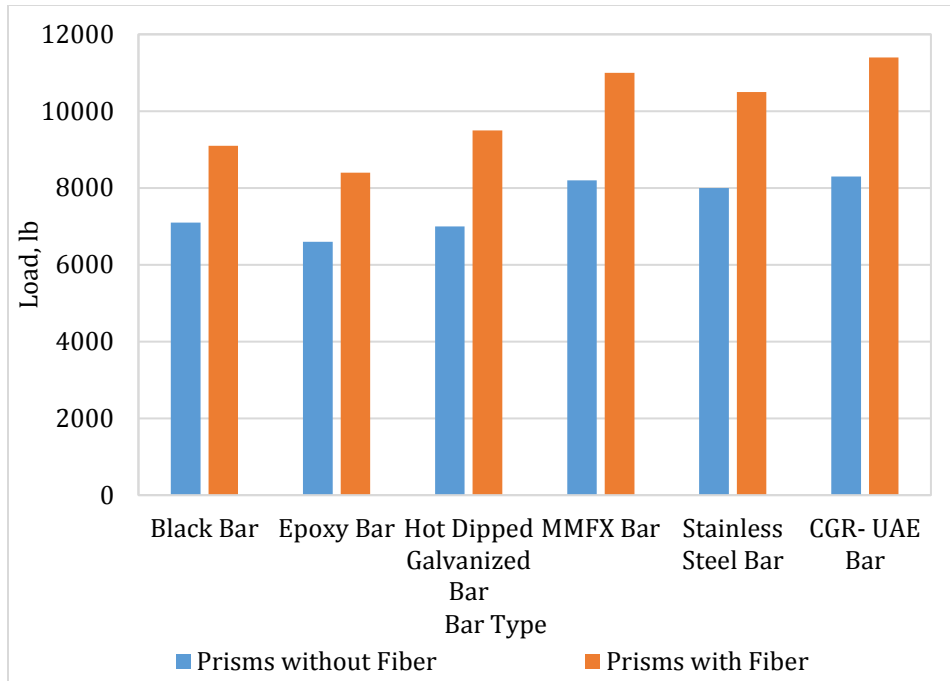


Figure D.27 Peak loads of Non-Corroded Pullout Specimens

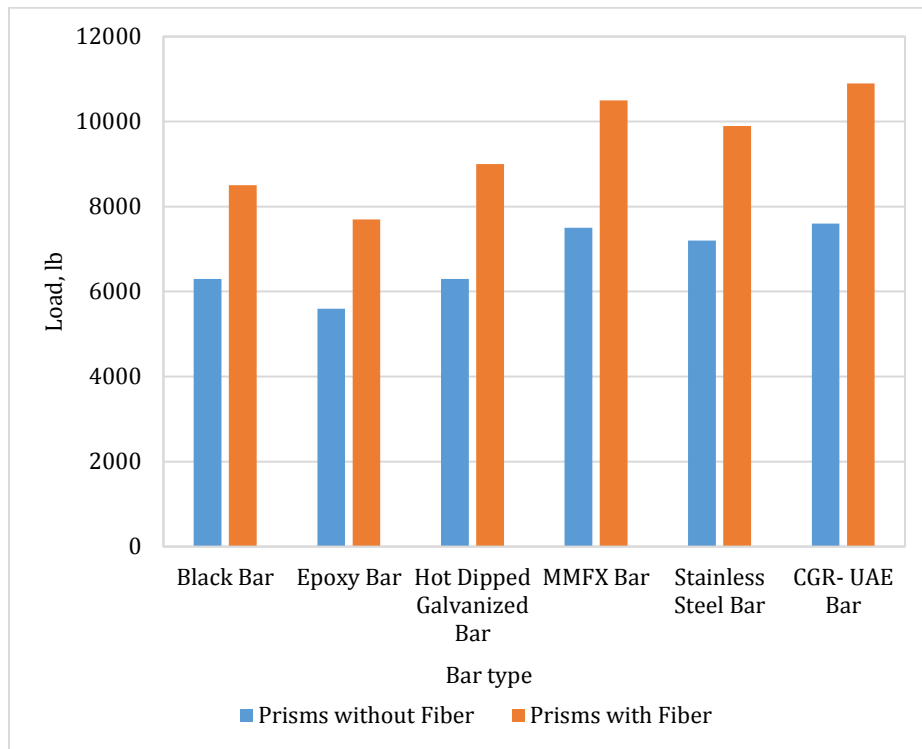


Figure D.28 Peak loads of Corroded Pullout Specimens

It was observed that 5% corrosion of the bars reduced the bond strength approximately by 12% in case of non-fiber specimens, whereas adding fibers improved the bond strength

significantly. The reduction in bond strength in case of specimens with fibers and subjected to accelerated corrosion was reduced to approximately 6%, i.e. addition of fibers reduced the bond strength loss by 50%.

D.4 Summary and Conclusions from Corrosion Testing

Continuous span structural slab bridges are constantly subjected to the dead loads of the bridge that keeps the cracks open in the tension region near the pier supports. These crack openings provide a pathway for chlorides to reach the embedded reinforcement. Service loads on the bridges allows these cracks to open further, leading to increase in the amount of chlorides passing through the deck to the reinforcement. To replicate this condition in laboratory tests, the corrosion process on the bridge decks was simulated by using an accelerated corrosion process while the test specimens are subjected to sustained loading to simulate the permanently acting dead loads.

Eighty slab specimens were cast with conventional black steel as well as with several types of corrosion-resistant reinforcing bars (epoxy-coated bars, hot-dipped galvanized bars, stainless steel bars, and MMFX bars). These slabs were cast using typical job mix formulas (JMFs) from ODOT projects for slabs without and with 10 lb/yd³ of polypropylene fiber. The test setup for the corrosion testing was designed to replicate the actual conditions on the bridge decks. Each slab was supported in a specially fabricated test frame, and a constant sustained load was applied to the slab using a mechanical jack. A salt solution tank, which was assembled and glued to the tension face of the slab, contained a salt solution (5% NaCl) to act as an electrolyte and simulate a deicing salt on a bridge deck. A stainless-steel plate was placed in the salt solution tank to act as a cathode, and a wire from the stainless-steel plate was connected to the negative terminal of a direct current (DC) power supply to complete the corrosion cell in order to accelerate the corrosion process. Figure D.5 shows the test setup for the accelerated corrosion of a typical test slab.

On visual comparison of slabs made with and without fibers, the surface condition of the slabs made with fibers had less deterioration than that of the slabs made without fibers for all bar types. Both transverse and longitudinal crack widths were reduced drastically due to the addition of fibers, without much damage to the bars embedded within the concrete for all bar types. It was evident that the addition of fibers substantially improved the performance of slabs under a highly accelerated corrosion process.

Slabs with epoxy-coated bars with 5% damage induced on the coating showed the greatest extent of corrosion compared to the other bar types, in terms of maximum flexural capacity loss due to corrosion. MMFX bars showed the best corrosion resistance and the lowest bond loss. In hot-dip galvanized bars, the zinc coating protected the bar from corrosion for a few days. However, once the sacrificial layer was compromised, the base metal showed a similar effect as the black bars. The capacity loss for the slab with hot-dip galvanized bars is much closer to that of slabs with black bars. Slabs with stainless steel bars also showed better performance after corrosion with a smaller loss of flexural capacity due to corrosion compared to epoxy-coated bars. Similar results and trends were obtained from pull-out tests. These tests demonstrated the increased corrosion resistance from the addition of 10 lb/yd³ of polypropylene fiber to concrete.

Reduction of Bridge Deck Cracking through Alternative Material Usage

APPENDIX E

EFFECTS OF FIBER ADDITION ON CRACKING DUE TO SHRINKAGE AND FREEZING AND THAWING

Prepared by:
Anil Patnaik, Ph.D.
and
Srikanth Marchetty

Prepared for:
The Ohio Department of Transportation,
Office of Statewide Planning & Research

State Job Number 135260
November 2017
Draft Final Report



TABLE OF CONTENTS

TABLE OF CONTENTS.....	1
LIST OF FIGURES	3
LIST OF TABLES.....	5
APPENDIX E	6
EFFECTS OF FIBER ADDITION ON CRACKING DUE TO SHRINKAGE AND FREEZING AND THAWING.....	6
E.1 INTRODUCTION	6
E.2 MATERIALS.....	6
<i>E.2.1 Cementitious Materials</i>	6
<i>E.2.2 Aggregates</i>	7
<i>E.2.3 Chemical Admixtures</i>	8
<i>E.2.4 Polypropylene Fibers</i>	8
E.3 CONCRETE MIXES	9
E.4 CONCRETE TESTING PROGRAM.....	11
<i>E.4.1 Concrete Mixing Procedure</i>	12
<i>E.4.2 Fresh Concrete Properties</i>	13
E.5 MECHANICAL TESTING	14
<i>E.5.1 Compressive Strength and Split Tensile Strength Test</i>	14
E.5.1.1 Compressive Strength Tests Results	15
E.5.1.2 Split Tensile Strength Tests Results	17
<i>E.5.2 Flexural Tensile Strength Test</i>	18
E.5.2.1 Flexure Tensile Strength Tests Results	18
<i>E.5.3 Shrinkage Tests</i>	20
E.5.3.1 Plastic Shrinkage Panel Tests	20
E.5.3.1a Plastic Shrinkage Panel Tests Results	22
E.5.3.2 Free Shrinkage Tests	24
E.5.3.2a Free Shrinkage Tests Results.....	26
E.5.3.3 Restrained Shrinkage Ring Tests.....	28
E.5.3.3a Restrained Shrinkage Tests Results.....	31
<i>E.5.4 Non-Cracked Freeze-Thaw Testing</i>	34

E.5.4.1 Freeze and Thaw Tests Results	37
<i>E.5.5 Freeze-Thaw Testing under Sustained Loading</i>	39
E.5.5.1 Results of Freeze-Thaw Test under Sustained Loading	42
E.6 SUMMARY AND CONCLUSIONS.....	43
REFERENCES	45

LIST OF FIGURES

Figure E.1 TUF-STRAND SF Polypropylene Fiber.....	9
Figure E.2 Slump Test Apparatus.....	13
Figure E.3 Air Content Test Apparatus	14
Figure E.4 Compressive Strength Testing	15
Figure E.5 Split Tensile Strength Testing.....	15
Figure E.6 Compressive Strength of Different Mixtures.....	16
Figure E.7 Split Tensile Strength of Different Mixtures	17
Figure E.8 Flexural Tensile Strength Test Setup.....	18
Figure E.9 Flexural Strength Test Data	19
Figure E.10 Formwork for Test Panels.....	21
Figure E.11 Shrinkage Panel Layout	21
Figure E.12 Panel Test Results	23
Figure E.13 Typical Crack Patterns in Non-Fiber Mixtures.....	23
Figure E.14 Typical Crack Patterns in Fiber-Reinforced Concrete Mixtures	24
Figure E.15 Free Shrinkage Specimen Molds	25
Figure E.16 Free Shrinkage Specimens	25
Figure E.17 Measurement of Free Shrinkage using ASTM C490.....	26
Figure. E.18 Free Shrinkage in Mixtures with No Fibers.....	26
Figure E.19 Free Shrinkage in Fiber-Reinforced Mixtures	27
Figure E.20 Free Shrinkage Tendency Diagram.....	27
Figure E.21 Dimensions of Ring used in this Study vs. AASHTO Standard Ring	29
Figure E.22 Ring Specimen Molds.....	29
Figure E.23 Casting of Concrete Rings	30
Figure E.24 Shrinkage Specimens Placed in Environmental Chamber.....	31
Figure E.25 Shrinkage Specimens Connected to Data Acquisition System.....	31
Figure E.26 Strains in Ring Specimens with No Fibers	32
Figure E.27 Strains in Fiber-Reinforced Ring Specimens.....	33
Figure E.28 Cracking in Control Specimen at 10 to 11 Days.....	33
Figure E.29 Cracking in SRA Specimen at 14 to 15 Days.....	34
Figure E.30 Freeze-Thaw Specimens inside the Environmental Chamber	35

Figure E.31 Freeze-Thaw Specimen Tray	35
Figure E.32 Curing of Freeze-Thaw Specimens.....	36
Figure E.33 Resonance Frequency Test.....	36
Figure E.34 Freeze-Thaw Cycle	37
Figure E.35 Tendency Diagrams for Freeze-Thaw.....	38
Figure E.36 Damage in Non-Fiber Freeze-Thaw Specimens after 60 Cycles	39
Figure E.37 Damage in Fiber-Reinforced Freeze-Thaw Specimens after 60 Cycles	39
Figure E.38 LC304-5k-TC1 Load Cell.....	40
Figure E.39 Loaded Freeze-Thaw Test Setup.....	40
Figure E.40 Freeze-Thaw Test Specimens	41
Figure E.41 Loaded Freeze-Thaw Test Setup inside the Chamber	41
Figure E.42 Setup for Loading.....	42
Figure E.43 Crack Growth Over Time of Slabs with Black Bar	43
Figure E.44 Crack Growth Over Time of Slabs with Epoxy Coated Bars	43

LIST OF TABLES

Table E.1 Properties and Chemical Contents of Type I Portland Cement..... 7

Table E.2 Gradation for #8 Limestone Coarse Aggregate (Sieve Analysis) 7

Table E.3 Gradation for Fine Aggregate (Sieve Analysis) 7

Table E.4 Mixes used for Plastic Shrinkage Panel Test 10

Table E.5 Mixes Used for Specimens Tested for Drying Shrinkage, Freeze/thaw and Mechanical Properties 11

Table E.6 Fresh and Hardened Property Tests..... 12

Table E.7 Compressive Strength Test Results 16

Table E.8 Split Tensile Test Results 17

Table E.9 Flexural Strength Test Results 19

Table E.10 Panel Test Results 22

Table E.11 Results of Free Shrinkage Tests 28

Table E.12 Restrained Shrinkage Results 32

APPENDIX E

EFFECTS OF FIBER ADDITION ON CRACKING DUE TO SHRINKAGE AND FREEZING AND THAWING

E.1 Introduction

Cracking due to shrinkage occurs early on bridge decks and continues to spread over the bridge lifecycle. The problem is exaggerated by expansion of cracks due to continuous freeze and thaw cycles and may lead to more serious impact on durability of bridge decks.

Details of restrained concrete ring tests, free shrinkage prism tests, plastic shrinkage panel tests and freeze-thaw tests are presented in this chapter. Tests were conducted to compare the shrinkage cracking, freeze-thaw durability and mechanical properties of several concrete mixes. Three sets of preliminary tests were conducted initially to validate the test procedures and make necessary adjustments to these procedures. The testing program evaluated a series of mixes subjected to identical environmental conditions.

Six mixes were used in the testing program: a control mix, two mixes that were similar to the control mix but contained admixtures—either MasterLife SRA (a shrinkage-reducing concrete admixture) or Masterlife CRA (a crack-reducing concrete admixture)—and three additional mixes that were similar to the control, SRA, and CRA mixtures, but with the addition of fibers. These mixes were based on typical ODOT mixes for bridge decks with minor modifications to suit the lab testing conditions. The test specimens used concrete cast with Type I Portland cement, slag, and limestone coarse aggregate and was cured for 24 hours prior to the initiation of drying. Freeze-thaw specimens were placed in a curing tank filled with lime water (diluted calcium hydroxide solution) for a period of 10 days.

E.2 Materials

The cementitious materials, aggregates, chemical admixtures, and fibers used in the concrete mix designs for the mixtures considered in this study are described in the following subsections.

E.2.1 Cementitious Materials

Two cementitious materials were used for the tests conducted in this portion of the testing program: Type I Portland cement (provided by the Cemex plant in Fairborn, Ohio) and Grade 100 slag (provided by the Lafarge Holcim plant in Cleveland, Ohio). The slag has a specific gravity of 2.89. The properties and chemical content of the Type I Portland cement are listed in Table E.1.

Table E.1 Properties and Chemical Contents of Type I Portland Cement

Type I Portland Cement	
Specific Gravity	3.15
SiO ₂ , %	1.5
Al ₂ O ₃ , %	0.9
Fe ₂ O ₃ , %	0.3
CaO, %	53.1
MgO, %	0.8
SO ₃ , %	0.1
Loss on Ignition	2.6
Limestone	3

E.2.2 Aggregates

The #8 limestone coarse aggregate used in this study were provided by W. L. Tucker Supply Company (Cuyahoga Falls, Ohio). The specific gravity of the aggregate was 2.67. The gradation for the coarse aggregates is presented in Table E.2.

Table E.2 Gradation for #8 Limestone Coarse Aggregate (Sieve Analysis)

Sieve	Cumulative % Passing
1/2"	100.0
3/8"	98.5
1/4 "	67.8
#4	37.7
#8	3.0
#16	0.4

Fine aggregate was also provided by the W. L. Tucker Supply Company. The fine river sand aggregate met ODOT sand requirements. The specific gravity of the fine aggregate was 2.65. The detailed gradation is listed in Table E.3.

Table E.3 Gradation for Fine Aggregate (Sieve Analysis)

Sieve	Cumulative % Retained	Cumulative % Passing
3/8"	0	100.0
1/4"	0.5	99.5
#4	1.8	97.7
#8	13.4	84.3
#16	23.3	61.0
#30	18.8	42.2
#50	24.5	17.7
#100	13.6	4.1
#200	1.9	2.2

E.2.3 Chemical Admixtures

Five types of chemical admixtures were used in this study: air entraining admixture (AEA), Type A water reducer (WR), high-range water reducing admixture (HRWRA), shrinkage reducing admixture (SRA), and crack reducing admixture (CRA).

- Eucon Air Mix 200, an air-entraining admixture from Euclid Chemical, was used to ensure proper air content (between 6% and 7%) in all the concrete mixes. According to the product information from the manufacturer, this admixture contains a concentrated aqueous solution of modified resins and can be used for proper air control under a wide range of temperatures. The dosage used for mixtures in this study was based on the recommended addition rate from the product instructions and was adjusted after several laboratory trials.
- Eucon WR-91 Type-A – a liquid, water-reducing and plasticizing admixture for concrete produced by Euclid Chemical – was adopted in this study to achieve the desired slump value (around 6-8 in.) as well as to reduce the water content in all concrete mixes. This product is intended for use in applications prone to shrinkage cracking, especially concrete floors and bridge decks with large surface areas. The dosage for this admixture was determined based on the product instructions and was adjusted after laboratory trials.
- Eucon 1037 Type-F high-range water-reducing admixture from Euclid Chemical is a polycarboxylate-based admixture that is formulated without added chlorides and is specifically designed for use by the concrete industry. This admixture was adopted in the study to achieve adequate workability in the fiber-reinforced mixes as well as to reduce the water content, as this product is reported to provide excellent slump increase and retention in concrete mixtures having a low water-to-cement ratio. Its dosage was determined according to the product instructions and was adjusted after several trials.
- MasterLife SRA-035 shrinkage-reducing admixture from BASF Corporation (Beachwood, Ohio) was added to two mixes to test its ability to reduce concrete shrinkage during drying. It was developed specifically to reduce drying shrinkage in concrete and mortar, and thus reduce the potential for subsequent cracking. This admixture functions by reducing the capillary tension of pore water, which is a primary cause of drying shrinkage. The dosage for the admixture was based on the recommended addition dosage from the manufacturer and was adjusted after several laboratory trials. When shrinkage reducing admixture (SRA) was added to a mixture, the amount of water required for the mix was reduced by an equivalent amount.
- MasterLife CRA-007 crack-reducing admixture from BASF Corporation was added to two mixes to test its ability to reduce concrete shrinkage during drying and to reduce subsequent cracking. The amount to be added was from the recommended dosage given in the product instructions and adjusted after laboratory trials. When crack reducing admixture (CRA) was added to a mixture, the amount of water required for the mix was reduced by an equivalent amount.

E.2.4 Polypropylene Fibers

TUF-STRAND SF polypropylene fiber from Euclid Chemical was used for the fiber reinforced specimens (Figure E.1). This product can be used in a wide variety of applications, it

complies with ASTM C1116 (“Standard Specification for Fiber Reinforced Concrete and Shotcrete”), and it was designed to provide equivalent tensile, bending and abrasion resistance similar to conventional reinforcements. It also helps mitigate the formation of plastic shrinkage cracking in concrete. This fiber has specific gravity of 0.92, a typical length of 2”, an aspect ratio of 74, a typical tensile strength between 87 and 94 ksi, a modulus of elasticity 1380 ksi, and it has a distinctive white color. As the dosage rates will vary depending upon the reinforcement requirements, the dosage rate used for specimens in this study were based on the intended use in the pilot bridge deck planned in this study.



Figure E.1 TUF-STRAND SF Polypropylene Fiber

E.3 Concrete Mixes

A variety of concrete mixes were used to evaluate the effects of the use of shrinkage-reducing admixture, crack-reducing admixture and polypropylene fibers to study shrinkage cracking, mechanical properties of the fresh as well as hardened concrete, and also to predict the concrete’s freeze-thaw durability. The preliminary testing used a basic concrete mix that was expected to have a normal cracking tendency. In this program, the ODOT mix represents a typical concrete mix for bridge decks used by the agency.

Some modifications were made to the basic mix to make it more suitable for lab testing conditions. The rest of the mixes included in the testing program were developed in the laboratory. The water-cement ratio (w/c) was held constant at 0.5 for the control mixes to ensure a high potential for cracking, while a w/c value of 0.6 was used for the panel shrinkage mixes and a w/c value of 0.48 was used for mixes with SRA and CRA. The mixes developed in the laboratory had a desired air content of 6 to 7%, a desired slump of 150 mm (6 in.), and contained a maximum aggregate size of $\frac{3}{8}$ ". A cement content of 450 lb/yd³ and a slag content of 150 lb/yd³ was used for all mixes, with the exception of the panel shrinkage mixes, where a cement content of 960 lb/yd³ was used.

Details of the mixing, casting, curing, and drying of the concrete specimens are provided in Section E.4.1. Table E.4 lists the six different mixes used in this study for plastic shrinkage panel tests, and Table E.5 lists the mixes used for all other tests.

Table E.4 Mixes used for Plastic Shrinkage Panel Test

Material	Series I (Control)	Series II (SRA)	Series III (CRA)	Series IV (PP Fibers)	Series V (Fibers + SRA)	Series VI (Fibers + CRA)
Cement Type I (lb/yd ³)	960	960	960	960	960	960
#8 Limestone Aggregate (lb/yd ³)	1,185	1,185	1,185	1,185	1,185	1,185
River Sand (lb/yd ³)	1,185	1,185	1,185	1,185	1,185	1,185
Water (lb/yd ³)	576	576	576	576	576	576
W/C Ratio	0.6	0.6	0.6	0.6	0.6	0.6
BASF MasterLife SRA 20 (gal/yd ³)	--	1	--	--	1	--
BASF MasterLife CRA 007 (gal/yd ³)	--	--	1	--	--	1
PolyPropylene Fibers (lb/yd ³)	--	--	--	10	10	10

Table E.5 Mixes Used for Specimens Tested for Drying Shrinkage, Freeze/thaw and Mechanical Properties

Material	Series I (Control)	Series II (SRA 1 gal/yd ³)	Series III (CRA 1 gal/yd ³)	Series IV (PP Fibers)	Series V (Fibers + SRA)	Series VI (Fibers + CRA)
Cement Type I (lb/yd ³)	450	450	450	450	450	450
Slag Grade 100	150	150	150	150	150	150
#8 Limestone Aggregate (lb/yd ³)	1,750	1,750	1,750	1,750	1,750	1,750
River Sand Fine Aggregate (lb/yd ³)	1,195	1,195	1,195	1,195	1,195	1,195
Water (lb/yd ³)	300	288	288	300	288	288
W/C Ratio	0.5	0.48	0.48	0.5	0.48	0.48
Eucon WR 91 Water Reducer (oz/yd ³)	20	20	20	20	20	20
Eucon AM 200 Air Entrainer (oz/yd ³)	4.5	4.5	4.5	4.5	4.5	4.5
Eucon 1037 High- Range Water Reducer (oz/yd ³)	--	--	--	40	40	40
BASF MasterLife SRA 20 (gal/yd ³)	--	1	--	--	1	--
BASF MasterLife CRA 007 (gal/yd ³)	--	--	1	--	--	1
Polypropylene Fibers (lb/yd ³)	--	--	--	10	10	10

E.4 Concrete Testing Program

This section describes the test methods used in this study for determining the fresh, hardened, shrinkage and freeze-thaw properties for the various concrete mix designs. A number of tests were conducted in order to evaluate several early age properties for each mix. According to

the state of the concrete at the time of testing, these tests can fall into one of two categories: fresh concrete tests or hardened concrete tests.

Fresh concrete property tests evaluated the air content and slump. The hardened concrete property tests were further divided into three sub-classes. The first sub-class considered the early-age properties of concrete and included tests such as compression strength, flexural strength, and split tensile strength. The second sub-class considered the plastic and drying shrinkage of concrete and included tests for panel shrinkage, free shrinkage and restrained ring shrinkage. The third sub-class focused on testing the freeze-thaw durability of different mixes, which were measured by tests for two properties: weight loss and resonance frequency change. The candidate mixture(s) with the best overall mechanical, shrinkage cracking resistance, and freeze-thaw resistance were selected in order to develop a concrete mix performance test matrix. The tests conducted in this study for each concrete mix are summarized in Table E.6.

Table E.6 Fresh and Hardened Property Tests

Concrete property	Test Method
Fresh Concrete Properties	
Slump	ASTM C 143/AASHTO T 119
Air Content	ASTM C 231/AASHTO T 152
Hardened Concrete Properties	
Compressive Strength	ASTM C 39/AASHTO T 22
Split Tensile Test	ASTM C 496
Flexural Shear Strength	ASTM C 78/AASHTO T97
Plastic Shrinkage	Shrinkage Panel Test (Kraai, 1985)
Drying Shrinkage (Free)	ASTM C 157 AASHTO T 160
Drying Shrinkage (Restrained)	ASTM C1581 AASHTO PP34-99
Freeze-Thaw Durability	ASTM C666 AASHTO T-161
Cracked Freeze-thaw	Loaded and Cracked Panels Under Freeze-Thaw

E.4.1 Concrete Mixing Procedure

Twelve mixes were prepared using the mix proportions outlined in Tables E.4 and E.5. All mixing was done in a mixer with a capacity of 0.15 m³ (5.0 ft³). The cementitious materials, aggregates, chemical admixtures and fibers were all weighed accurately and kept in separate plastic containers. The mixer was then “buttered” with a mixture of cement, sand, and water. Next, coarse aggregate was placed in the mixer. The sand and two-thirds of the water were then added and mixed for one minute. Type I cement and Grade 100 slag were then added along with the

remaining one-third of the water. All chemical admixtures were diffused into the mixing water shortly before addition. For fiber-reinforced mixes, the fibers were added after all other ingredients were thoroughly combined. After addition of the fibers, the mixture was mixed for three minutes, which was followed by a three-minute rest period. A final mixing was performed for a total of two minutes to ensure that the fibers are evenly distributed.

Since the mixes exhibited a flowing consistency, no problems were encountered during the mixing and placement. Some vibration was used to ensure that the concrete was adequately consolidated. For the fiber-reinforced mixes, the fibers were distributed uniformly and blended well in the mixture. No segregation or balling of the fibers was observed in any of the mixes. Six different mixes were produced on a single day for conducting panel tests, while the preparation of the other mixes was divided into two phases: in the first phase, which consisted of mixes in Series I through III, no fibers were used; in the second phase, which consisted of mixes in Series IV through VI, fibers were added. After each mixing, the mixing drum was thoroughly cleaned and buttered before the next mix was prepared. All the mixes were prepared under identical conditions. Because of higher cement and water content as well as the use of super plasticizers, the slump achieved in each batch was greater than 150 mm (6 inches). No reduction in slump due to the addition of fibers was detected, mainly due to the use of Type-F high-range water reducer. The fresh concrete test results were then documented.

E.4.2 Fresh Concrete Properties

Slump was tested for every trial mix design following the standards of ASTM C143 (“Standard Test Method for Slump of Hydraulic-Cement Concrete”). Figure E.2 shows the test apparatus for the slump test.



Figure E.2 Slump Test Apparatus

All mixes were also tested for air content according to ASTM C231 (“Standard Test Method for Air Content of Freshly Mixed Concrete by the Pressure Method”). Results for the air content test are summarized. The test apparatus for the air content tests is shown in Figure E.3.



Figure E.3 Air Content Test Apparatus

The slump tests and air content tests were conducted as quality control of concrete fresh properties in this series of tests. The slump test followed ASTM C 143/AASHTO T 119 “Slump of hydraulic cement concrete and for air content test”. The pressure method was used to measure the air content. The method followed AASHTO T 152/ASTM C 231 “Air Content of Freshly-mixed Concrete by the Pressure Method”.

The slump test results ranged from 6.5 in. to 8.5 in., and the air content test results ranged from 6.5% to 8.6%. Because of the slightly high w/c ratio in addition to several chemicals being added to the concrete mix, the slump for some concrete mixes was greater than 5 to 6 in. range.

The addition of SRA and CRA did not seem to have any significant effect on either the slump or air content. All mixes achieved desirable flow and were placed and consolidated without problems. When using fiber, the addition of superplasticizer was required in order to maintain desirable workability. Fiber-reinforced concrete mixtures with superplasticizer had slightly higher slump than non-fiber mixtures. And the air content was similar to that of non-fiber mixtures.

E.5 Mechanical Testing

Six cylinders with diameter of 4 inches and a height of 8 inches were prepared for each of the mixes according to the ASTM C39 test procedures. Cylinders of all mixes were tested at 3, 15 and 28 days of curing to determine the compressive strength, and cylinders were tested at 28 days to determine the split tensile strength. Additional 4 in. × 4 in. × 14 in. prisms were cast to determine the flexural tensile strength at 28 days for each mix.

E.5.1 Compressive Strength and Split Tensile Strength Test

ASTM C 39/AASHTO T 22 was used to determine the compressive strength of the concrete mixes, and ASTM C 469 was used to determine the static modulus of elasticity. The tests were conducted using a Forney hydraulic press test apparatus (shown in Figure E.4, E.5) at a constant load rate of 30–40 psi/s. For each mix, a total of six-cylinder specimens with a 4-in. diameter and an 8-in. height were cast; two specimens were tested after curing for 3 days, and the four remaining specimens were tested at 28 days. The displacements and corresponding loads were recorded and were used to calculate the compressive strength. The specimens were then loaded until failure, and all displacements and load data were recorded.



Figure E.4 Compressive Strength Testing



Figure E.5 Split Tensile Strength Testing

E.5.1.1 Compressive Strength Tests Results

ASTM C 39/AASHTO T 22 “Compressive Strength of Cylindrical Concrete Specimens” was followed for the compressive test of concrete cylinder specimens. Specimens were tested for compressive strength at 3, 15 and 28 days. The compressive strength test results were relatively low compared to the minimum ODOT 28-day compressive strength requirements of around 5,000 psi, this is due to the high water/cement ratio (48-50%) used in the different mixes to ensure maximum shrinkage potential. The test results are presented in Table E.7 and graphically in Figure E.6.

Table E.7 Compressive Strength Test Results

Mixture	Series I (psi)	Series II (psi)	Series III (psi)	Series IV (psi)	Series V (psi)	Series VI (psi)
3 days	1,682	2,019	3,049	1,640.5	1,885	2,905
15 days	2,828	3,293	5,009	2,720	2,807	4,118
28 days	2,977	3,625	5,149	2,742	3,003	4,838

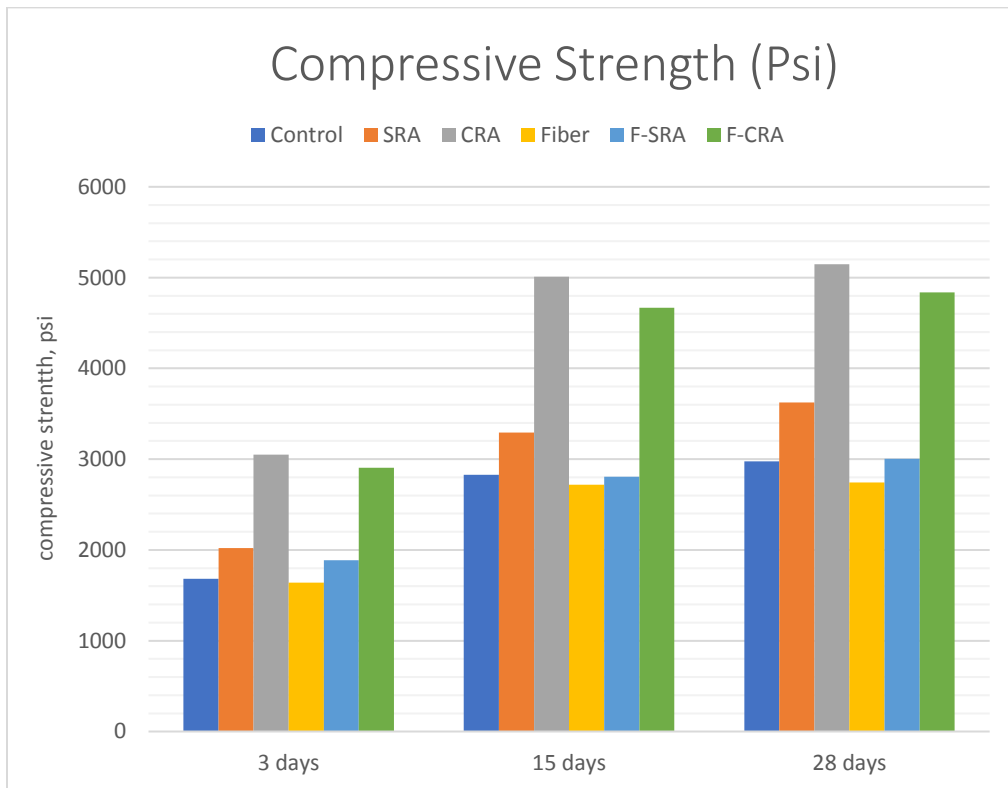


Figure E.6 Compressive Strength of Different Mixtures

A comparison among the test results for different mixes shows that the addition of SRA leads to a slight increase in compressive strength at all ages (around 20%). This can be mainly due to the lower water content specified by the producer and conforms to observations from literature. The addition of CRA, however, leads to a much more significant increase in compressive strength (between 65-70%) at all ages, which is more than can be accounted for by only the reduction in water content.

Fiber-reinforced concrete mixtures were found to have relatively lower compressive strength at early ages. This conforms to observations by Aly et. al (2008) in which it was concluded that the use of polypropylene fibers in concrete mixtures containing slag can cause a slight reduction in mechanical properties initially.

E.5.1.2 Split Tensile Strength Tests Results

ASTM C496 “Standard Test Method for Splitting Tensile Strength of Cylindrical Concrete Specimens” is followed for split tensile test of cylinder specimens. The test results are presented in Table E.8 and shown graphically in Figure E.7

Table E.8 Split Tensile Test Results

Specimens Type	Split Tensile Strength (Psi)	
	Without Fibers	With Fibers
Control	282	269
SRA	365	342
CRA	433	408

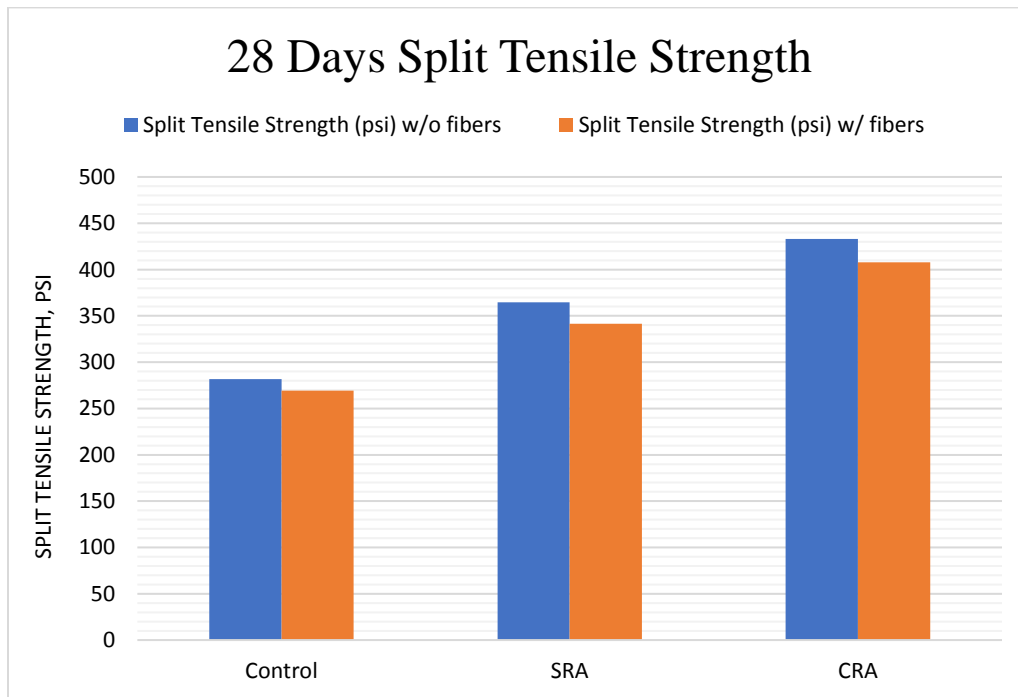


Figure E.7 Split Tensile Strength of Different Mixtures

Results from split tensile tests reflect those of compressive strength tests, with mixtures containing CRA having split tensile strength significantly higher than those of Control and SRA. Fiber-reinforced concrete mixtures marginally suffer from reduced split tensile strength compared to those without fibers.

E.5.2 Flexural Tensile Strength Test

ASTM C 78/AASHTO T97 procedures were followed to determine the flexural strength of concrete beam specimens. Each concrete beam specimen is 4 in × 4 in × 14 in. A span of 12 in. was used for the support blocks, which made the height of the beam (4 in.) equivalent to one-third of the span length (12 in.), as shown in Figure E.8. This test was conducted using an Instron 400HVL hydraulic testing machine, using a loading rate of 125–175 psi/min.



Figure E.8 Flexural Tensile Strength Test Setup

E.5.2.1 Flexure Tensile Strength Tests Results

AASHTO T 97/ASTM C 78 “Standard Method of Test for Flexural Strength of Concrete (Using Simple Beam with Four-Point Loading)” is followed for the flexural strength test of beam specimens. The flexural strength of all the concrete mix designs were tested at 28 days. The test results are presented in Table E.9 and graphically in Figure E.9.

Table E.9 Flexural Strength Test Results

Mixture	Control	SRA	CRA	Fibers	F + SRA	F + CRA
Load At Failure (lbs)	2760	2729	3610	3081	2786	3316
28-days Modulus of Rupture (psi)	518	512	677	578	522	622

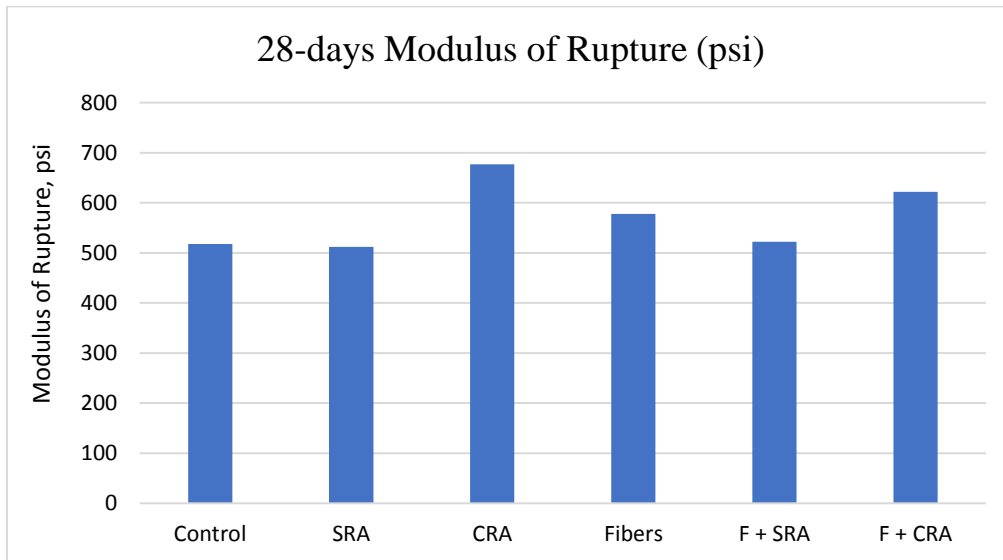


Figure E.9 Flexural Strength Test Data

Results from flexural strength tests are generally higher than split tensile test. Mixtures containing CRA have a significantly higher strength than those of Control and SRA. Fiber-reinforced concrete mixtures showed better performance than non-fiber mixtures for control mix without SRA or CRA. SRA mixtures seem to have slightly lower strengths compared to control.

E.5.3 Shrinkage Tests

Shrinkage tests were performed to evaluate the concrete mix design in terms of its tendency for cracking, amount of shrinkage over time and improving the performance by altering the mix design.

E.5.3.1 Plastic Shrinkage Panel Tests

Tests were conducted using slabs with a thickness of 25 mm (1 inch), length of 0.9 meter (3 ft.), and width of 0.6 meter (2 ft.). The slabs were restrained around the perimeter using wire mesh. The slab size was selected so as to be similar to the slab size currently used for plastic shrinkage testing of concrete in various studies in the literature.

Since shrinkage testing is a qualitative comparative study, the slab size is not expected to influence the test results. Slabs were placed on a flat surface (the laboratory floor) and were subjected to a wind velocity of about 22 km/hour (14 mph), using high-velocity fans. Six slabs (one slab of each trial mix type) were made and tested simultaneously under identical environmental conditions to ensure that a true comparison of shrinkage cracking was obtained. Wire mesh and rebar were used at the perimeter (panel edges to achieve restraints to ensure the panels did not shrink freely).

The formwork for the shrinkage panels is shown in Figure E.10. The figure shows the molds prepared prior to placing the concrete. One mold was used for the control mix (concrete without any admixtures or fibers) and the other five were used for concrete mixed with fiber and admixtures. Freshly mixed concrete was placed in the molds with proper care taken to fill around the wire mesh that was placed at the side runners at the periphery. The concrete was lightly tamped and leveled using trowels. The top surface of the concrete slabs as then finished with a straight-edge wooden float. To maintain consistency in the surface finish of all the test slabs, the same research assistant finished all the test slabs in this project.

Figures E.11 shows the prepared test specimens subjected to testing. After 24 hours of testing, crack widths and distributions were measured for all panels.



Figure E.10 Formwork for Test Panels



Figure E.11 Shrinkage Panel Layout

Since the main objective was to study the influence of admixtures and fiber addition on the plastic shrinkage, it was necessary to make concrete with a very high potential for shrinkage cracking. A high cement content as well as high water-cement ratio (0.6) were used to maximize the cracking potential. The testing conditions—such as the ambient temperature, the humidity and the wind velocity of 22 km/hour (14 mph)—were kept constant for each set of test slabs.

E.5.3.1a Plastic Shrinkage Panel Tests Results

The average crack widths and lengths were measured for all the cracks that appeared on the top surface of each test slab after 24 hours. The 24-hour duration was chosen so as to make sure that all the cracks had developed and stabilized. The crack widths were measured at a number of locations along the length of each crack. The lengths of cracks were measured for each crack. Area of each crack was calculated by multiplying the length of the crack by the average width. Total crack area for a given slab was calculated by summing the areas of all the cracks on the slab. The crack area of control slab was considered as 100 percent for comparison of the effectiveness of the materials. The crack areas of the other panels were expressed as a percentage of the crack area of the corresponding control slab. Table E.10 lists the results of panel testing. Crack widths and distributions are shown in Figure E.12. Crack distributions obtained for concrete mixtures without fiber and for different fiber-containing mixes are shown in Figures E.13 and E.14, respectively.

Table E.10 Panel Test Results

Mix	Series I	Series II	Series III	Series IV	Series V	Series VI
Maximum Crack Width (in.)	0.04	0.03	0.012	0.007	0.012	0.007
Crack Density (in/in ²)	0.181	0.103	0.05	0.06	0.024	0.022
Reduction in Crack Distribution (%)	0	43	72	67	87	88

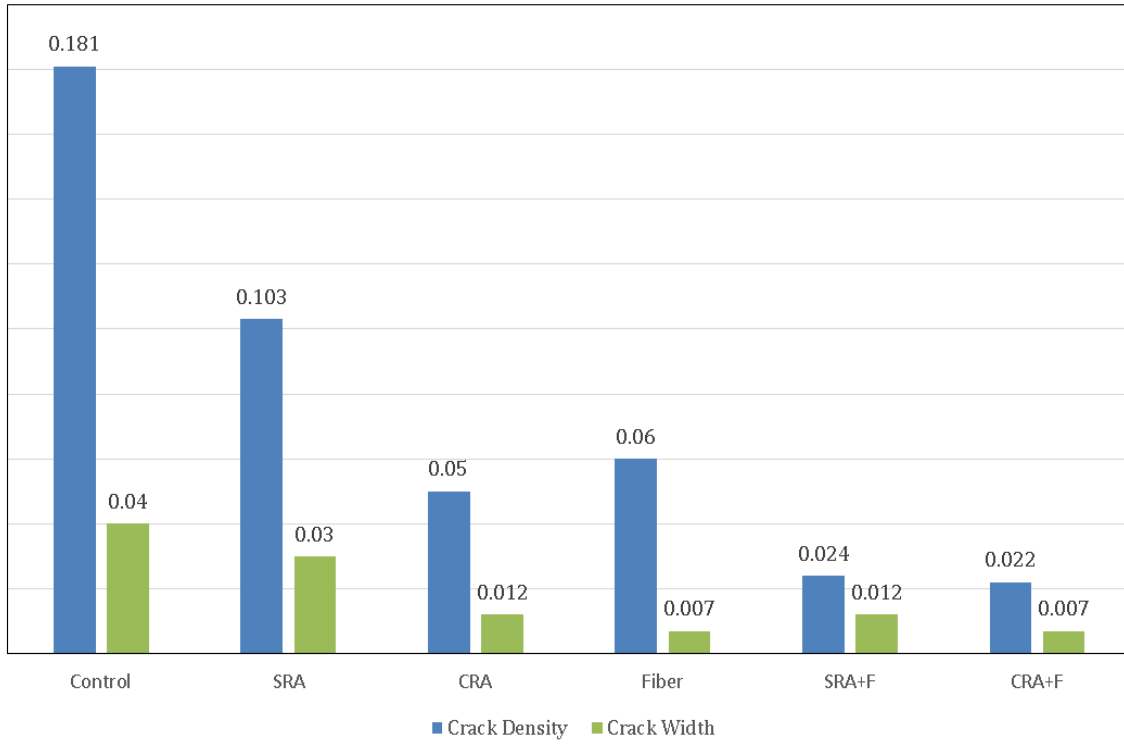


Figure E.12 Panel Test Results

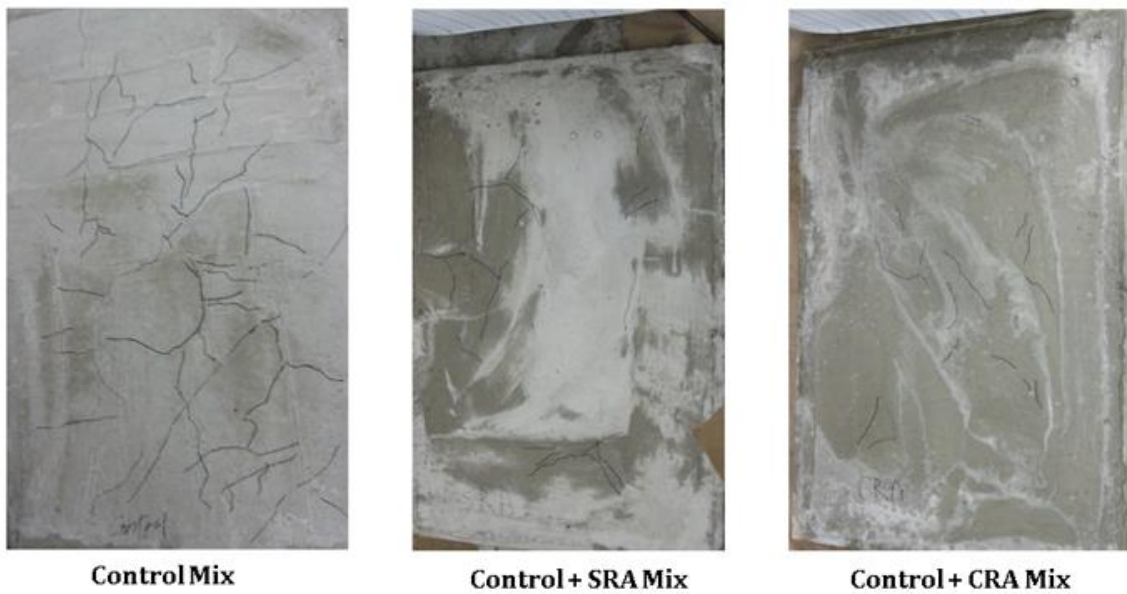


Figure E.13 Typical Crack Patterns in Non-Fiber Mixtures

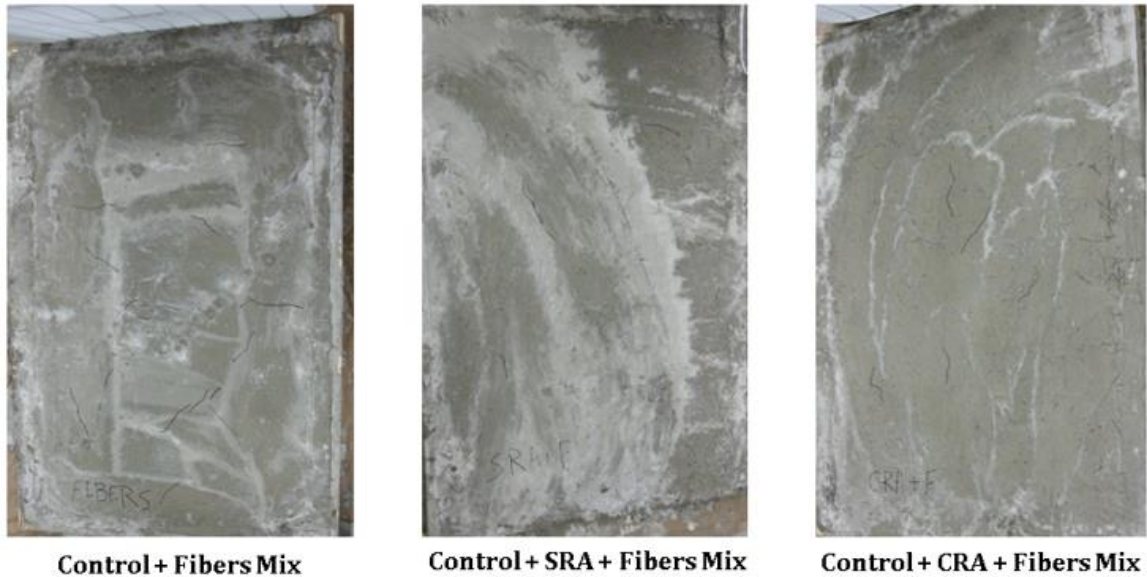


Figure E.14 Typical Crack Patterns in Fiber-Reinforced Concrete Mixtures

E.5.3.2 Free Shrinkage Tests

The free shrinkage tests were carried out following ASTM C157/C157M and AASHTO T160 “Length Change of Hardened Hydraulic-Cement Mortar and Concrete”. A total of three 3-in. × 3-in. × 11.25-in. prisms were cast using the same concrete batch for both the free shrinkage and restrained shrinkage specimens in every mix design. The prisms were cast into steel molds manufactured specifically for length change tests and supplied by Humboldt. Each mold has a replaceable gage stud at each end, providing the gage length of 10 in. specified by ASTM C490. Figure E.15 shows the molds before casting the specimens, and Figure E.16 shows the specimens after casting. The prisms were demolded 24 hours after casting and placed in an environmental chamber at the same time as the ring specimens.

The inside of the chamber was maintained at a temperature of $23 \pm 1^\circ\text{C}$ and a relative humidity of $50 \pm 4\%$. A shrinkage frame with an electronic dial gage was used to monitor the free shrinkage, as shown in Figure E.17. A dial meter was installed to record the shrinkage value at different ages. The specimen’s initial shrinkage values were measured using the shrinkage frame shown in Figure E.17 immediately after demolding and before placing in the chamber. Readings were then taken every 24 hours for the first seven days, and then on Days 14, 21, and 28.



Figure E.15 Free Shrinkage Specimen Molds



Figure E.16 Free Shrinkage Specimens



Figure E.17 Measurement of Free Shrinkage using ASTM C490

E.5.3.2a Free Shrinkage Tests Results

Free shrinkage tests followed AASHTO T 160 (ASTM C 157) “Length Change of Hardened Hydraulic Cement Mortar and Concrete”. Free shrinkage data were collected at 1, 2, 3, 4, 5, 6, 7, 14, 21, and 28 days, respectively, from which the free shrinkage tendency diagrams were drawn for all concrete mixes. The free shrinkage data is listed in Table E.11; results for free shrinkage of mixtures without fibers and with fibers are shown in Figures E.18 and E.19, respectively. A free shrinkage tendency diagram is shown in Figure E.20.

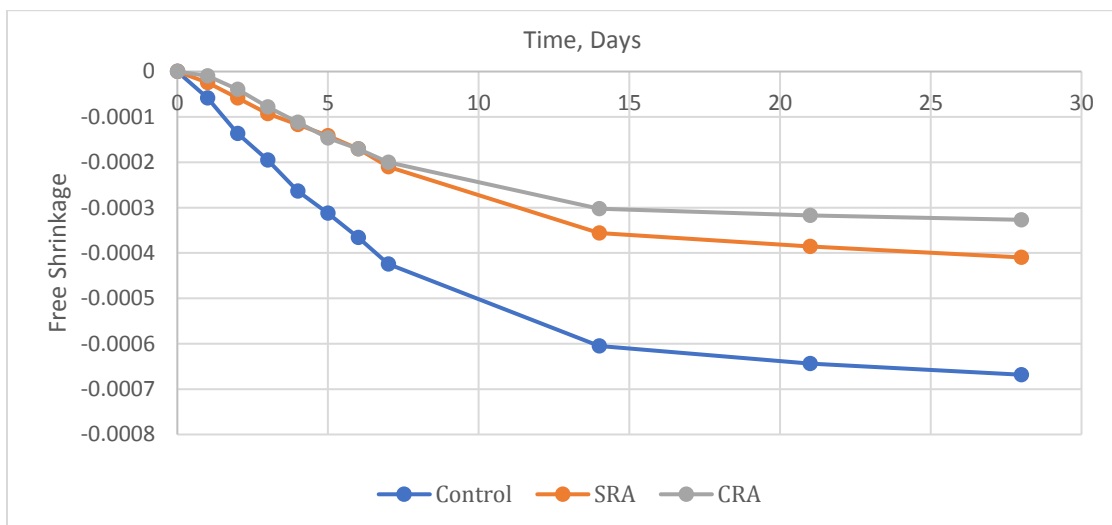


Figure. E.18 Free Shrinkage in Mixtures with No Fibers

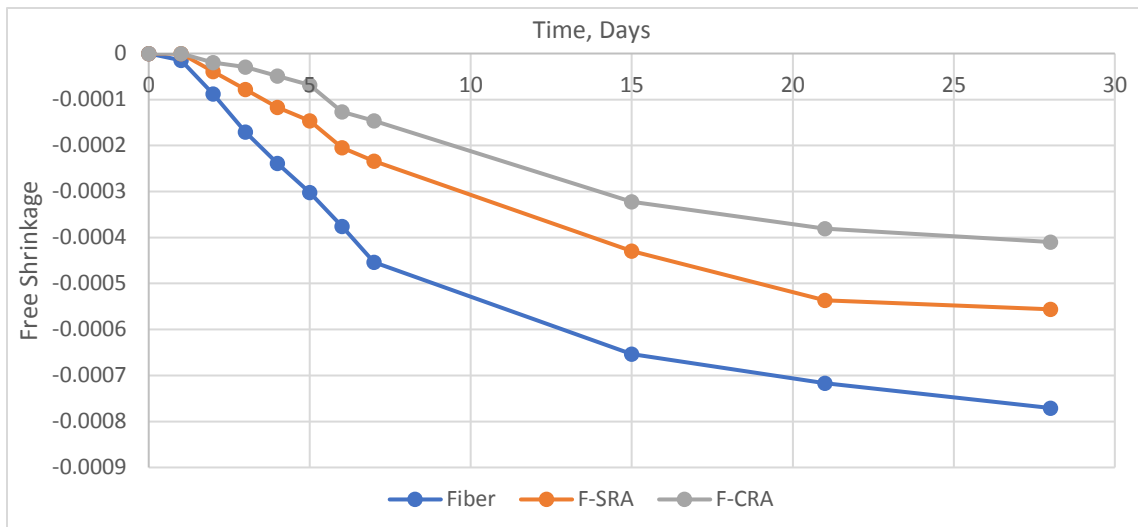


Figure E.19 Free Shrinkage in Fiber-Reinforced Mixtures

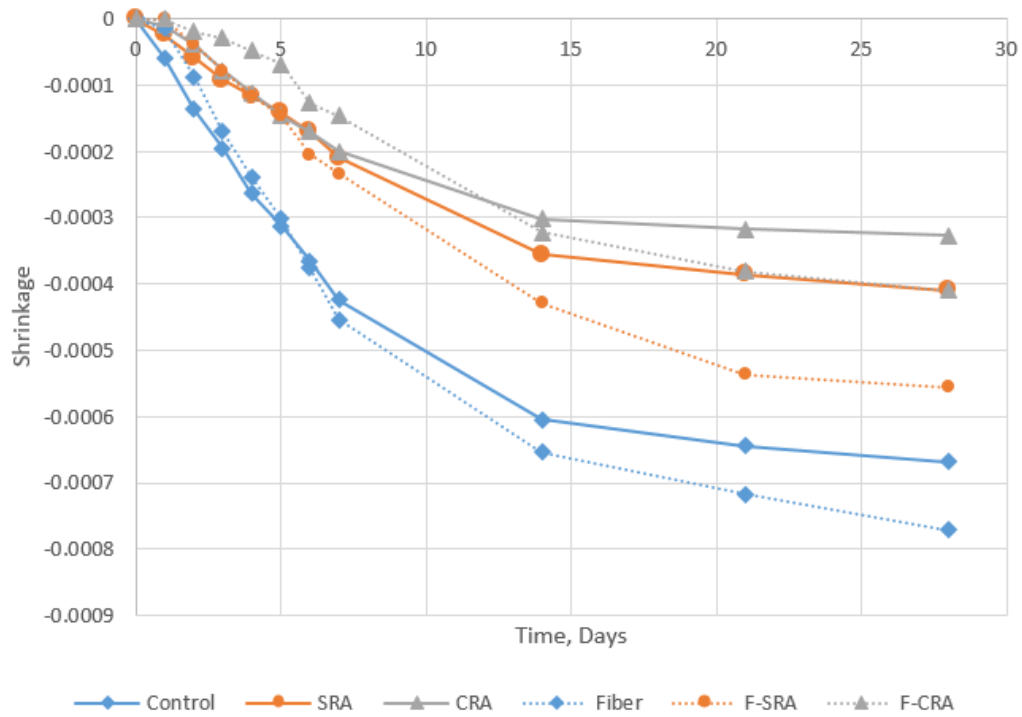


Figure E.20 Free Shrinkage Tendency Diagram

Table E.11 Results of Free Shrinkage Tests

Day	Series I	Series II	Series III	Series IV	Series V	Series VI
0	0	0	0	0	0	0
1	-5.9E-05	-2.4E-05	-9.7561E-06	-1.46341E-05	0	0
2	-0.00014	-5.9E-05	-3.90244E-05	-8.78049E-05	-3.9024E-05	-2E-05
3	-0.0002	-9.3E-05	-7.80488E-05	-0.000170732	-7.8049E-05	-2.9E-05
4	-0.00026	-0.00012	-0.000112195	-0.000239024	-0.00011707	-4.9E-05
5	-0.00031	-0.00014	-0.000146341	-0.000302439	-0.00014634	-6.8E-05
6	-0.00037	-0.00017	-0.000170732	-0.00037561	-0.00020488	-0.00013
7	-0.00042	-0.00021	-0.0002	-0.000453659	-0.00023415	-0.00015
14	-0.0006	-0.00036	-0.000302439	-0.000653659	-0.00042927	-0.00032
21	-0.00064	-0.00039	-0.000317073	-0.000717073	-0.00053659	-0.00038
28	-0.00067	-0.00041	-0.000326829	-0.000770732	-0.0005561	-0.00041

Figures E.18 through E.19 show that the use of SRA and CRA reduces the amount of free shrinkage at 28 days by 38% and 52%, respectively, the use of CRA seems to greatly reduce the amount of shrinkage during the first 2 to 3 days, with minimal or no shrinkage occurring during this period. The use of fibers, while effective in reducing the amount of shrinkage in the first 7 to 10 days, was found to cause an increase in free shrinkage at later ages.

This can be explained through the work of Aly et al. (2008) in which it was found that the use of polypropylene fibers in concrete mixtures containing slag can cause increased shrinkage compared to non-fiber mixtures. This is due to an increase in the number of nano-sized pores in the microstructure, which influence the rate of drying shrinkage. The high porosity is likely due to the increase in the mesoporous zone at the vicinity of PP fibers.

E.5.3.3 Restrained Shrinkage Ring Tests

The restrained shrinkage tests performed in this study adopted the AASHTO ring and followed AASHTO PP34-99 (“Estimating the Cracking Tendency of Concrete”). The test apparatus in this study was fabricated using a modified ring with a smaller thickness than the ring specified by AASHTO.

Structural steel pipe conforming to ASTM A 501 or A 53M/A 53 extra-strong pipe with a length of 12-in, an outside diameter of 324 mm (12-¾ in.) and wall thickness 13 mm (½ in.) was used to fabricate the inner steel ring (see Figures E.21 and E.22).

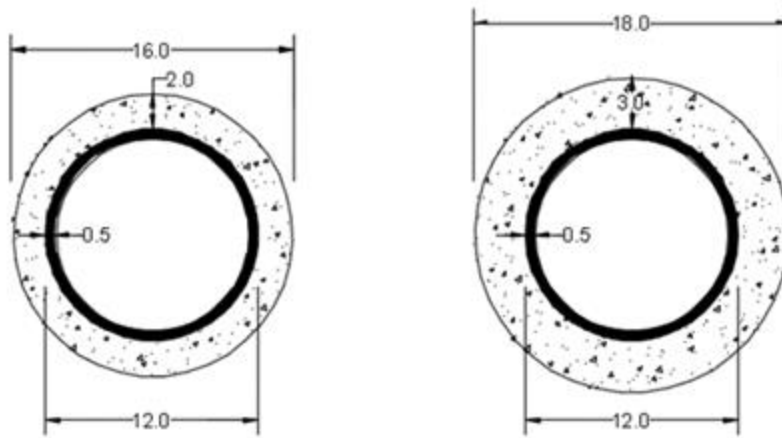


Figure E.21 Dimensions of Ring used in this Study vs. AASHTO Standard Ring



Figure E.22 Ring Specimen Molds



Figure E.23 Casting of Concrete Rings

The outer ring is made of Sono tube board provided by Whitecap Supply (Figure E.23). It had an inside diameter of 406 mm (16 in.). Two strain gages were mounted on the inner surface of the steel ring at equidistant points at mid height. Data acquisition system from Vishay Company is used for the strain instrumentation, and it automatically recorded each strain gage every 60 minutes independently. Data acquisition system was a Vishay Measurements Group System-9000 DAQ connected to a PC with StrainSmart software installed (See Figure E.25).

Wooden forms were made from a 21-in. \times 21-in. sheet of $\frac{3}{4}$ -in.-thick plywood, and the top surface was covered with polyurethane sheet to ensure that the concrete rings were able to shrink freely. Two ring specimens were cast for each mix design, both were 6 in. tall. The outer forms were removed at an age of 12 h., and then the specimens were moved to the environmental chamber for conditioning (Figure E.24) with a constant air temperature of $23 \pm 1^\circ\text{C}$ and $50 \pm 4\%$ relative humidity. Temperature and humidity were maintained using an environmental chamber manufactured by Darwin Chambers Company in St. Louis, Missouri. The data from the strain gages were recorded every 60 minutes, and review of the strain and visual inspection of cracking were conducted daily.



Figure E.24 Shrinkage Specimens Placed in Environmental Chamber



Figure E.25 Shrinkage Specimens Connected to Data Acquisition System

E.5.3.3a Restrained Shrinkage Tests Results

ASTM C1581/AASHTO PP34-99 was followed for the restrained shrinkage test. The test results are presented in Table E.12 and are plotted in Figures E.26 and E.27 for ring specimens without fibers and with fibers, respectively. Pictures of cracking in control and SRA specimens are presented in Figures E.28 and E.29, respectively.

Table E.12 Restrained Shrinkage Results

	Non-fiber-reinforced		Fiber-Reinforced	
	Time of First Crack (Days)	Crack Width (in.)	Time of First Crack (days)	Crack Width (in.)
Control	10–11	0.02	none	none
SRA	14–15	0.01–0.012	none	none
CRA	none	none	none	none

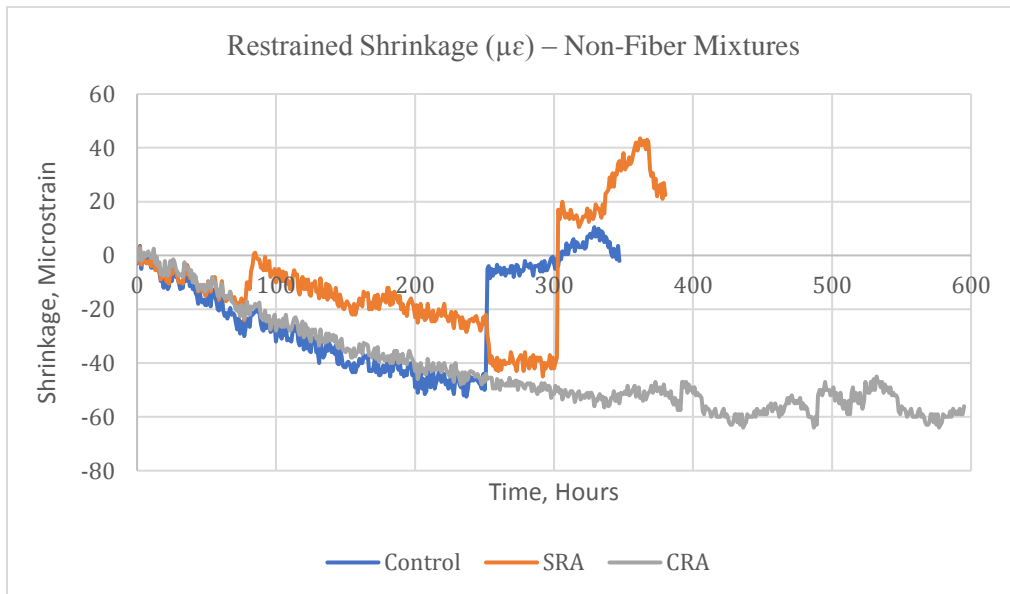


Figure E.26 Strains in Ring Specimens with No Fibers

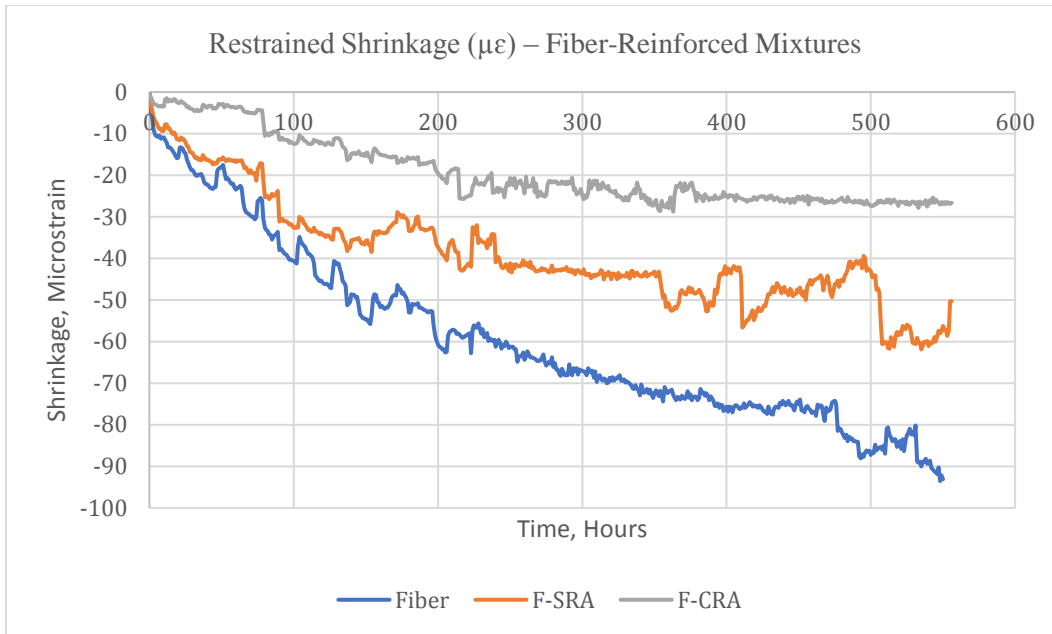


Figure E.27 Strains in Fiber-Reinforced Ring Specimens

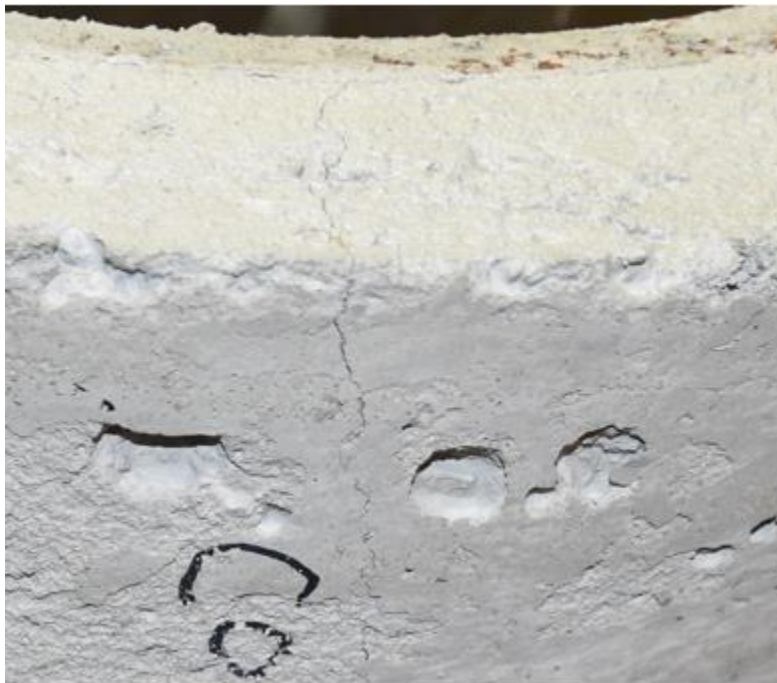


Figure E.28 Cracking in Control Specimen at 10 to 11 Days



Figure E.29 Cracking in SRA Specimen at 14 to 15 Days

Of the six mixtures considered in this study, the specimen made with the control mix was the first to crack at around 10 to 11 days (Figure E.28), followed by the SRA mix at 14 to 15 days (Figure E.29), with the SRA mixture exhibiting a smaller crack width than the control. No cracks were found in the CRA mix even after 28 days.

In the fiber-reinforced concrete mixtures, none of the rings showed cracking by the end of the testing period of 28 days. The use of SRA and CRA was found to reduce the strains due to shrinkage by 40–50% and 60–70%, respectively. The use of CRA seems to greatly reduce the strains due to shrinkage during the first 2 to 3 days, with minimal or no shrinkage occurring during this period. The use of fibers was found to cause an increase in strains due to shrinkage, which agrees with the findings in Aly et. al (2008).

E.5.4 Non-Cracked Freeze-Thaw Testing

The objective of this part of the investigation was to evaluate durability characteristics of ODOT concrete mixtures containing SRA and CRA using the freezing and thawing of concrete test (ASTM C 666 procedure A). The objective also was to compare the performance of the fiber reinforced concrete mixes with polypropylene fiber compared to that of control mixes.

Figure E.30 shows the test specimens inside the chamber. A freeze-thaw chamber model TH-055 manufactured by Darwin chambers was used for this study. Each specimen was placed inside a galvanized steel tray fabricated specifically for freeze-thaw testing. Figure E.31 shows the dimensions of each tray.



Figure E.30 Freeze-Thaw Specimens inside the Environmental Chamber

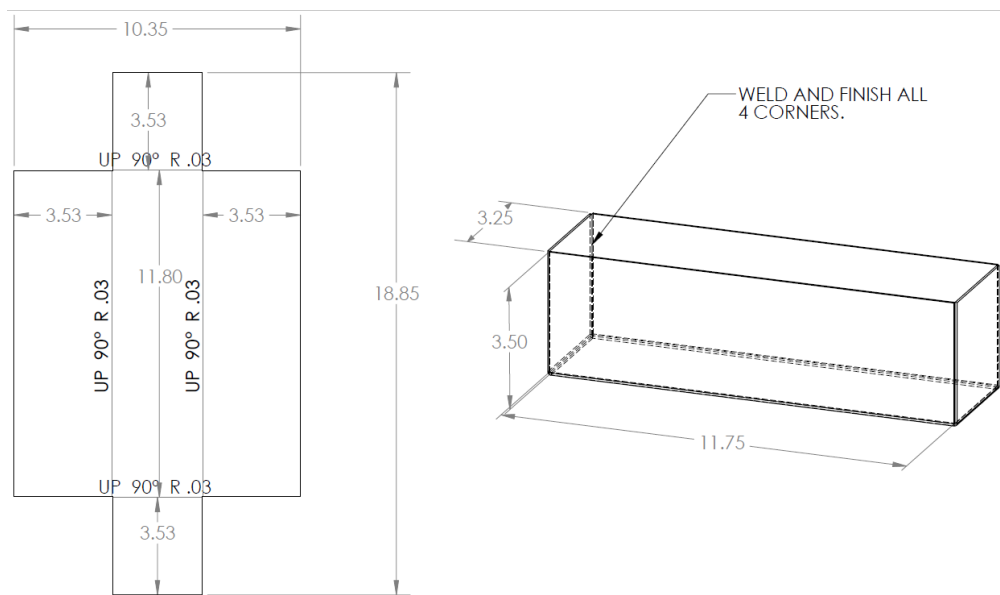


Figure E.31 Freeze-Thaw Specimen Tray

All specimens were 11.25 in. \times 3 in. \times 3 in. The tray's dimensions are slightly larger to allow for all the faces to be covered by at least $\frac{1}{8}$ " of water at all times. Specimens were submerged for 14 days in a tank filled with lime water as shown in Figure E.32.



Figure E.32 Curing of Freeze-Thaw Specimens

After curing, initial readings of weight and resonance frequency were taken for each specimen (Figure E.33). Specimens were then moved to the freeze-thaw chamber where they are placed inside the tray and covered with a 5% salt solution. The temperature changes between -15°C and 15°C , over a cycle of 12 hours. Reading for weight loss and change in resonance frequency were taken every 10 cycles (5 days). The test was stopped after 60 cycles (30 days). Figure E.34 shows the cycle time.

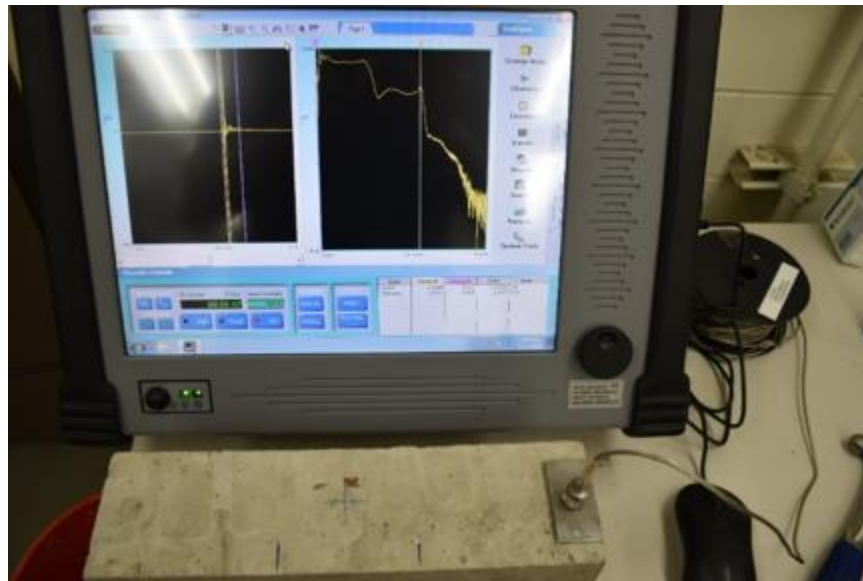


Figure E.33 Resonance Frequency Test

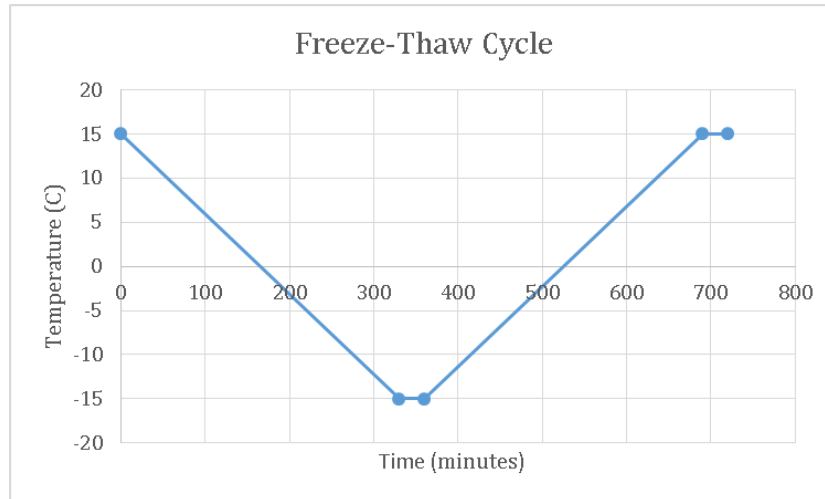
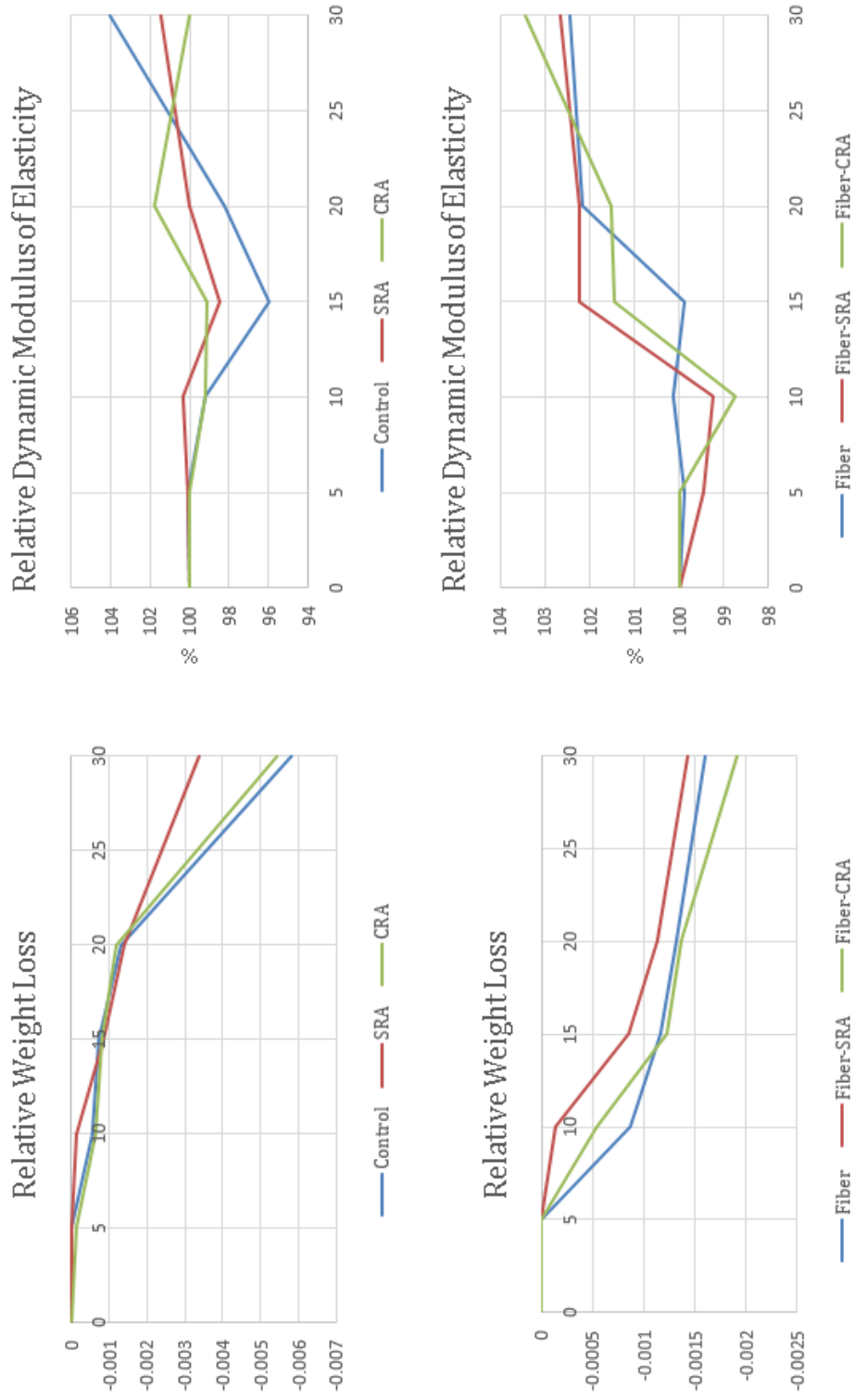


Figure E.34 Freeze-Thaw Cycle

E.5.4.1 Freeze and Thaw Tests Results

Freeze-thaw tests followed AASHTO T 161/ASTM C666 (“Standard Method of Test for Resistance of Concrete to Rapid Freezing and Thawing”), and weight loss and resonance frequency data were collected every 10 cycles (5 days). Diagrams showing the freeze-thaw resistance tendency for all concrete mixes is presented in Figure E.35. A visual comparison of the damage due to freeze-thaw in fiber-reinforced concrete specimens and specimens with no fibers can be made from the pictures shown in Figures E.36 and E.37.

Figure E.35 Tendency Diagrams for Freeze-Thaw



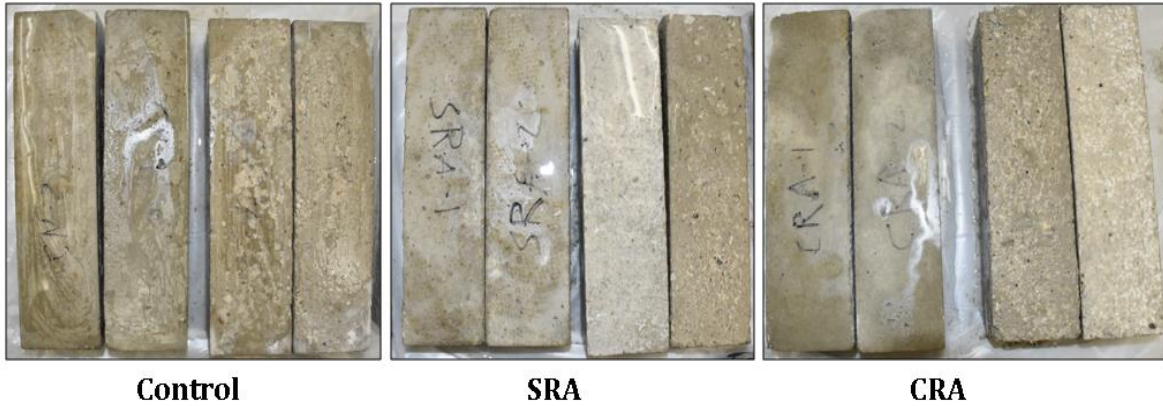


Figure E.36 Damage in Non-Fiber Freeze-Thaw Specimens after 60 Cycles

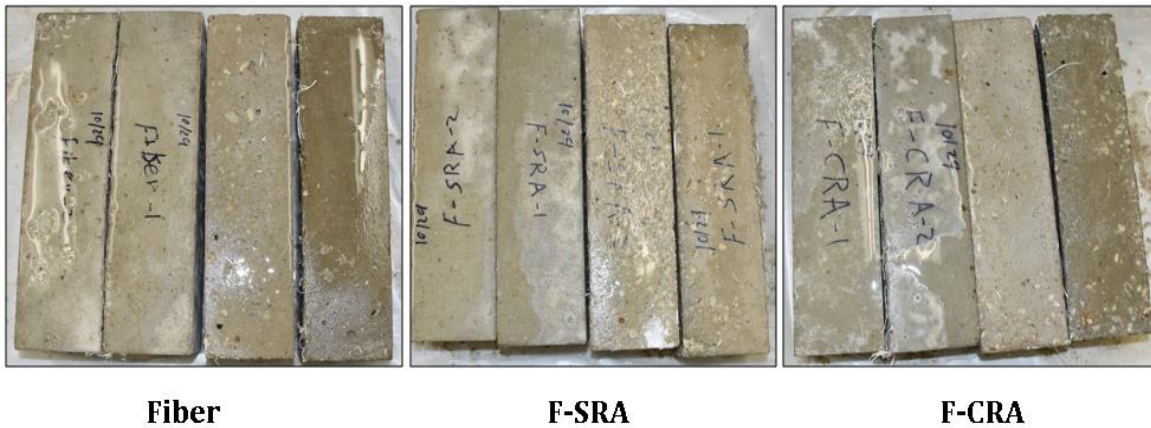


Figure E.37 Damage in Fiber-Reinforced Freeze-Thaw Specimens after 60 Cycles

While some weight loss due to surface scaling was detected in all specimens, the resonance frequency for the specimens remained relatively unchanged throughout the test duration, implying that no internal damage was occurring. This finding is attributed to the high air content (6–8%) used for all mixes.

Results from the freeze-thaw tests show that the use of SRA and CRA has no significant impact on the damage due to freezing or thawing. The addition of CRA seems to increase the scaling in both fiber and non-fiber mixtures compared to the addition of SRA, with less of an effect for the fiber-reinforced mixtures. The addition of polypropylene fibers was found to reduce the weight loss for all mixes, which implies improved resistance to scaling in the fiber-reinforced concrete mixtures compared to those without fibers.

E.5.5 Freeze-Thaw Testing under Sustained Loading

Experimental work was carried out to test the effects of freeze-thaw on crack development in reinforced concrete bridge decks. Four reinforced concrete slab specimens were tested under loaded freeze thaw conditions in 2 stages. First stage was a concrete mixture without fiber and the second stage was for fiber-reinforced concrete mixture. Two specimens were tested in each stage,

one reinforced with black bar and the other with epoxy-coated bar. For this, the specimens were initially cracked by loading the specimens in a test frame. Tank containing 5% salt solution were fixed on top of the cracked region of each test specimen. These specimens are then placed inside the freeze-thaw chamber under loaded conditions and subjected to the same freeze-thaw cycles as shown in Figure E.34. The load was generated using threaded jacks and monitored using specially modified load cells capable of operating under extreme freezing temperatures. The load cells were of model LC304-5k-TC1 supplied by Omega Engineering (Figure E.38).



Figure E.38 LC304-5k-TC1 Load Cell

The freeze-thaw cycle was planned to continue for a period of 4 weeks for each stage. First stage will have consisted of 2 reinforced concrete slabs without fibers. One specimen reinforced using black #4 rebar, and the other one using epoxy coated rebar. The expansion of the crack was measured every 24 hours. The process was then repeated for the second stage with the difference being the use of fiber reinforced concrete. Figure E.39 shows the test setup for the loaded freeze-thaw tests. Figures E.40 through E.42 are pictures of the specimens and the loading of specimens in the test frame.

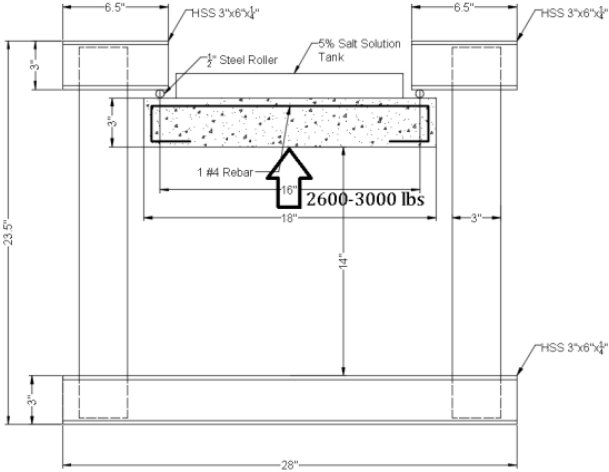


Figure E.39 Loaded Freeze-Thaw Test Setup



Figure E.40 Freeze-Thaw Test Specimens



Figure E.41 Loaded Freeze-Thaw Test Setup inside the Chamber



Figure E.42 Setup for Loading

E.5.5.1 Results of Freeze-Thaw Test under Sustained Loading

For loaded freeze-thaw tests, the results show that the initial crack width as well as the rate of crack widening for epoxy-coated reinforcements are much higher than those observed in black rebar.

Slabs with black and epoxy coated bars were subjected to 60 freeze–thaw cycles. During the testing, the load on the display was monitored to keep it constant at 2600 pounds. Cracks were measured manually using crack microscope, at the beginning of the test (i.e. zero cycles) and at every 10 cycle intervals. Crack growth over the number of cycles was monitored and plot showing crack growth is presented in Figures E.43 and E.44 for slabs with black bar and slabs with epoxy coated bars for both fiber and non-fiber specimens.

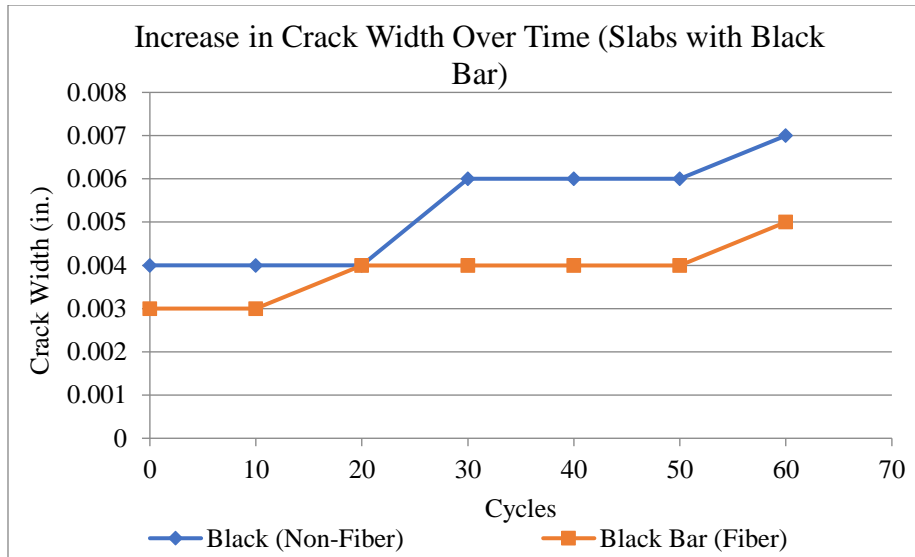


Figure E.43 Crack Growth Over Time of Slabs with Black Bar

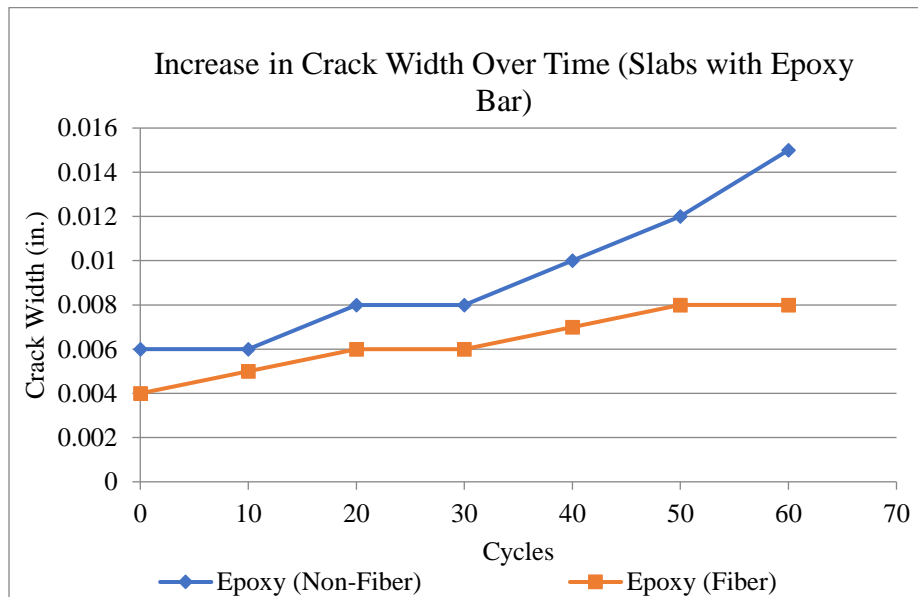


Figure E.44 Crack Growth Over Time of Slabs with Epoxy Coated Bars

E.6 Summary and Conclusions

Shrinkage cracking on bridge decks starts shortly after concrete placement and continues for years. The problem is exacerbated due to crack expansion from freeze and thaw, and fatigue load cycles. Restrained concrete ring tests, free shrinkage prism tests, plastic shrinkage panel tests and freeze-thaw including those with sustained loading were conducted in this project. Six mixes were used in the testing program: a control mix, two mixes that were similar to the control mix but contained admixtures—either MasterLife SRA or Masterlife CRA - and three additional mixes that were similar to these control, SRA, and CRA mixtures, but with the addition of fibers. These mixes were based on typical ODOT mixes for bridge decks with minor modifications to suit the

laboratory testing conditions. The test specimens used concrete cast with Type I Portland cement, slag, and limestone coarse aggregate and was cured for 24 hours prior to the initiation of drying. Freeze-thaw specimens were placed in a curing tank filled with lime water (diluted calcium hydroxide solution) for a period of 10 days. The complete details of the test procedures and results are presented in Appendix E.

From shrinkage panel tests, the addition of fiber to concrete was found to reduce plastic shrinkage cracking by a factor of 8.5. The use of SRA and CRA reduces the amount of free shrinkage (based on AASHTO T160 test or ASTM C 157 test) at 28 days by 38% and 52%, respectively; the use of CRA seems to greatly reduce the amount of shrinkage during the first 2 to 3 days, with minimal or no shrinkage occurring during this period. The use of fibers, while effective in reducing the amount of shrinkage in the first 7 to 10 days, was found to cause an increase in free shrinkage at later ages. The use of polypropylene fibers in concrete mixtures containing slag can cause this type of increased shrinkage compared to non-fiber mixtures. Therefore it is useful to minimize the amount of slag to offset this effect in mixes that also include polypropylene fiber.

Restrained shrinkage tests performed using AASHTO PP34-99 or ASTM C1581 ring tests showed that the concrete mixture with SRA developed a smaller crack width than that of the control mix in 28 days. The mixes with CRA did not develop any cracks even after 28 days in the environmental chamber. In the fiber-reinforced concrete mixtures, none of the rings showed cracking by the end of the testing period of 28 days. The use of SRA and CRA was found to reduce the strains due to shrinkage by 40–50% and 60–70%, respectively. The use of CRA seems to greatly reduce the strains due to shrinkage during the first 2 to 3 days, with minimal or no shrinkage occurring during this period. The use of fibers was found to cause an increase in strains due to shrinkage, which was similar to the observation from free shrinkage tests.

Results from the freeze-thaw tests conducted similar to the procedure given in AASHTO T161 and ASTM C666 (modified to suit the available freeze-thaw chamber) show that the use of SRA and CRA had no significant impact on the damage due to freezing or thawing. The addition of CRA seems to increase the scaling in both fiber and non-fiber mixtures compared to the addition of SRA, with less of an effect for the fiber-reinforced mixtures. The addition of polypropylene fibers was found to reduce the weight loss for all mixes, implying improved resistance to scaling in the fiber-reinforced concrete mixtures compared to those mixes without fibers.

From the freeze-thaw tests performed while maintaining the sustained load that is comparable to the service load in typical bridge decks, the initial crack widths as well as the rate of crack widening in slabs with ECB and no fiber were higher by a factor of 2.3 compared to those with black bars under identical test conditions. Addition of 10 lb/yd³ of fiber reduced crack widths by a factor of 2 for slabs with ECB in such freeze-thaw tests with sustained loading.

REFERENCES

- AASHTO T 22 “Standard Method of Test for Compressive Strength of Cylindrical Concrete Specimens.” American Association of State Highway and Transportation Officials, Washington, D.C. 2017.
- AASHTO T 161 “Standard Method of Test for Resistance of Concrete to Rapid Freezing and Thawing.” American Association of State Highway and Transportation Officials, Washington, D.C. January 2017.
- ASTM 39 “Standard Test Method for Compressive Strength of Cylindrical Concrete Specimens” ASTM International, West Conshohocken, PA. 2017. Available at <https://www.astm.org/Standards/C39.htm>
- Aly, T., Sanjayan, J.G., and Collins, F. (2008). Effect of polypropylene fibers on shrinkage and cracking of concretes. *Materials and Structures* 41:1741. Available at <https://link.springer.com/article/10.1617/s11527-008-9361-2>
- ASTM C143 / C143M-15a “Standard Test Method for Slump of Hydraulic-Cement Concrete.” ASTM International, West Conshohocken, PA. 2015. Available at <https://www.astm.org/Standards/C143.htm>
- ASTM C 157, “Standard Test Method for Length Change of Hardened Hydraulic-Cement Mortar and Concrete.” ASTM International, West Conshohocken, Pennsylvania
- ASTM C231 / C231M-17a “Standard Test Method for Air Content of Freshly Mixed Concrete by the Pressure Method.” ASTM International, West Conshohocken, Pennsylvania. 2017. Available at <https://www.astm.org/Standards/C231.htm>
- ASTM C469 “Standard Test Method for Static Modulus of Elasticity and Poisson’s Ratio of Concrete in Compression, ASTM International, West Conshohocken, Pennsylvania. 2014. Available at <https://www.astm.org/Standards/C469.htm>
- ASTM C496 “Standard Test Method for Splitting Tensile Strength of Cylindrical Concrete Specimens.” ASTM International, West Conshohocken, PA. 2011. Available at <https://www.astm.org/Standards/C496>
- ASTM C666 “Standard Test Method for Resistance of Concrete to Rapid Freezing and Thawing.” ASTM International, West Conshohocken, Pennsylvania. 2015. Available at <https://www.astm.org/Standards/C666.htm>

Reduction of Bridge Deck Cracking through Alternative Material Usage

APPENDIX F STRUCTURAL TESTS

Prepared by:
Anil Patnaik, Ph.D.
and
Srikanth Marchetty

Prepared for:
The Ohio Department of Transportation,
Office of Statewide Planning & Research

State Job Number 135260
November 2017
Draft Final Report



TABLE OF CONTENTS

TABLE OF CONTENTS.....	1
LIST OF FIGURES	3
LIST OF TABLES.....	6
APPENDIX F.....	7
STRUCTURAL TESTS.....	7
F.1 INTRODUCTION.....	7
F.2 TENSILE STRENGTH TESTING OF #5 REINFORCEMENT BARS	7
F.3 DIRECT TENSION CRACKING OF PRISMS.....	9
<i>F.3.1 Testing of Trial I and Trial II Prism Specimens</i>	<i>9</i>
<i>F.3.2 Testing of Trial III Slender Prism Specimens</i>	<i>14</i>
F.3.2.1 Trial III – Direct Tension Test Results	15
<i>F.3.3 Testing of Long Prism Specimens</i>	<i>18</i>
F.3.3.1 Long Tension Prism Test Results – Direct Tension Cracking	21
F.4 DESIGN AND PREPARATION OF SLAB SPECIMENS TO TEST FOR FLEXURE CRACKING.....	29
<i>F.4.1 Details for the Full-Scale and Half-Scale Slab Specimen</i>	<i>31</i>
<i>F.4.2 Preparation of Slab Specimens</i>	<i>32</i>
F.5 STRUCTURAL TESTS CONDUCTED ON FULL-SCALE SLAB SPECIMENS.....	33
<i>F.5.1 Results on Full-Scale Slab Testing for Flexural Cracking</i>	<i>34</i>
F.6 PREPARATION AND TESTING OF REDUCED-SCALE SLAB SPECIMENS	39
<i>F.6.1 Casting of Reduced-Scale Trial Slab Specimens</i>	<i>40</i>
<i>F.6.2 Testing of Reduced-Scale Trial Slab Specimens</i>	<i>41</i>
F.6.2.1 Results of Reduced Scale Slab Specimens	42
F.7 REDUCED-SCALE SLAB SPECIMENS WITH DIFFERENT TYPES OF REINFORCEMENT	44
<i>F.7.1 Preparation of Reduced-Scale Slabs with Different Types of Reinforcement.....</i>	<i>45</i>
<i>F.7.2 Testing of Slabs with and without Fibers for Flexural Cracking.....</i>	<i>46</i>
F.7.2.1 Results of Slabs with and without Fibers with Different Types of Reinforcement.....	46
<i>F.7.3 Testing of Slabs with and without Fibers for Crack Widening Due to Fatigue.....</i>	<i>51</i>
F.7.3.1 Results on Crack Widening Due to Cyclic Loading.....	52
F.8 SUMMARY AND CONCLUSIONS.....	55
F.9 SAMPLE CALCULATIONS	57

<i>F.9.1 Flexural Crack Width Calculations for Slabs</i>	57
F.9.1.1 Section Properties for a Typical Slab	57
F.9.1.2 Cracking and Yielding and Ultimate Load Calculations for Slabs.....	57
<i>F.9.2 Calculation of Deflection for Slabs Using Moment Curvature Relation</i>	60
<i>F.9.3 Calculation of Deflection for Slabs Using Elastic Equation</i>	61
<i>F.9.4 Direct Tension Crack Width Calculations for Prisms</i>	62
F.9.4.1 Calculation of Cracking Load for Specimen using ACI-224.2R-92	63

LIST OF FIGURES

Figure F.1 Various Reinforcement Bars Machined at the Center for Tensile Strength Testing.....	7
Figure F.2 Attachment of Extensometer to Collect Strain Measurements (Left); Failure of a Specimen (Right)	8
Figure F.3 Stress vs. Strain Curves for #5 Bars of Various Types	8
Figure F.4 Prism Specimen with a 7" × 7" Section	10
Figure F.5 Prism Specimen with a 5.5" × 5.5" Section	10
Figure F.6 Compressive Strength for Concrete Mix over 28 Days	12
Figure F.7 Prism Specimens with 7" × 7" Sections.....	12
Figure F.8 Casting of 7" × 7" Specimens	13
Figure F.9 Testing of Prisms in Trial I (Left) and Trial II (Right)	13
Figure F.10 Specimens Tested in Trial I.....	14
Figure F.11 Slender 3.5" × 3.5" Prism Specimen.....	14
Figure F.12 Testing of Slender Prisms (Left) and Cracked Specimens (Right)	15
Figure F.13 Testing of Trial III Prism Specimens	16
Figure F.14 Cracks Formed on Specimens during Testing in Trial III.....	16
Figure F.15 Load vs. Crack Width for 3.5" × 3.5" Prisms	17
Figure F.16 Stress vs. Crack Width for 3.5" × 3.5" Prisms.....	17
Figure F.17 Sectional Details of Long Prism Specimens	18
Figure F.18 Test Setup for Long Prisms	19
Figure F.19 Formwork and Rebar for Casting of Long Prisms	20
Figure F.20 Typical Casting of Long Specimens	20
Figure F.21 Test setup for Testing of Long Prisms	21
Figure F.22 Load vs. Crack Width for Prisms without Fibers.....	22
Figure F.23 Stress vs. Crack Width for Prisms without Fibers	22
Figure F.24 Load vs. Crack Width for Prism Specimens with Fibers	24
Figure F.25 Stress vs. Crack Width for Prisms Specimens with Fibers	24
Figure F.26 Plots Showing Stress Versus Crack Widths of Prisms with Different Bar Types with and without Fiber	25
Figure F.27 Cracks on Prism Specimens without Fibers with Black, Epoxy-Coated and Hot-Dipped Galvanized Bars	27

Figure F.28 Cracks on Prism Specimens without Fibers with CGR-UAE Bars, MMFX and Stainless-Steel Bars.....	28
Figure F.29 Cracks on Prism Specimens with Fibers with Black, Epoxy-Coated and Hot-Dipped Galvanized Bars	28
Figure F.30 Cracks on Prism Specimens with Fibers with CGR-UAE Bars, MMFX and Stainless-Steel Bars.....	29
Figure F.31 Bending Moment Diagram Showing Points of Inflection Points.....	30
Figure F.32 Bridge POR-88-1250: Transverse Sectional Details (Top), Observed Cracks (Bottom).....	30
Figure F.33 Slab Section Representing the Negative Moment Region of Bridge (left) and Typical Cross Sections Details of the Test Specimen (Right)	31
Figure F.34 Formwork and Reinforcing Cage for Slab Specimens.....	32
Figure F.35 Placing of Concrete into the Formwork	33
Figure F.36 Curing of Slab Specimens	33
Figure F.37 Test Setup for Testing of a 16-ft. Slab	34
Figure F.38 Load vs. Deflection Plot for a 15-ft.-Span Slab with Black Bars	35
Figure F.39 Load vs. Deflection Plot for a 15-ft.-Span Slab with Epoxy-Coated Bars.....	36
Figure F.40 Stress vs. Crack Width for a Slab with Black Bars.....	37
Figure F.41 Stress vs. Crack Width for Slabs with Epoxy-Coated Bars	38
Figure F.42 Stress vs. Crack Width for 7.5-ft. Slabs with Black Bars and Epoxy-Coated Bars ..	38
Figure F.43 Crack Patterns on Slabs with Black Bars and Epoxy-Coated Bars (Black Bars in Foreground and Epoxy-Coated Bars in the Back)	39
Figure F.44 Schematic of Reduced-Scale Slab Sections	40
Figure F.45 Longitudinal Section of the Reduced-Scale Slab.....	40
Figure F.46 Formwork and Reinforcement for Reduced-Scale Slab Specimens	40
Figure F.47 Casting for Reduced-Scale Trial Slab Specimens.....	41
Figure F.48 Typical Test Setup for Trials using Reduced-Scale Slab Specimens.....	41
Figure F.49 Stress vs. Crack Width for 13" × 6" Slab with Black Bar	42
Figure F.50 Stress vs. Crack Width for 13" × 8" Slabs with Black Bar.....	43
Figure F.51 Stress vs. Crack Width for Full-Scale and Reduced-Scale Slabs with Black Bars...	43
Figure F.52 Failed 13" × 8" Slab Specimen Showing Crack Pattern	44

Figure F.53 Sections Details of the 14" × 8" Slab.....	44
Figure F.54 Typical Reinforcement Cages for Black (Left, at Top of Image), Epoxy-Coated (Left, at Bottom of Image), and Stainless-Steel Bars (Right).....	45
Figure F.55 Formwork Showing Black Bars (Left) and Stainless-Steel Bars (Right).....	46
Figure F.56 Stress vs. Crack Widths for Slabs with Different Bar Types (Non-Fiber).....	47
Figure F.57 Stress vs. Crack Widths for Slabs with Different Bar Types (Fiber).....	47
Figure F.58 Plots Showing Stress versus Crack Width of 14"x8" Slabs with and without Fiber	48
Figure F.59 Comparison of Crack Widths for Slabs with Black Bars, Epoxy-Coated Bars and Zinc-Galvanized Bars	49
Figure F.60 Load vs. Deflection Curves for Slabs without Fibers	50
Figure F.61 Load vs. Deflection Curves for Slabs with Fibers	50
Figure F.62 Tested Slab Specimens.....	51
Figure F.63 Fatigue Loading on a Slab to Monitor Crack Widening	52
Figure F.64 Slab Showing LVDTs to Measure Deflection (Left) and Crack Width (Right)	52
Figure F.65 Average Increase in Crack Width for Slabs with and without Fibers over Time	53
Figure F.66 Average Increase in Deflection for Slabs with and without Fiber over Time.....	54
Figure F.67 Longitudinal and Cross (only top bars shown) Section of Typical Slab.....	57
Figure F.68 Loading of Slab from the Bottom	60

LIST OF TABLES

Table F.1 Yield and Ultimate Strength of #5 Reinforcing Bars	9
Table F.2 Details of Trial I and II Prism Specimens	11
Table F.3 Class QC2 Concrete Mix Design used for All Specimens	12
Table F.4 Trial III Prisms with the Same Reinforcement Ratio as an Actual Bridge.....	15
Table F.5 Specimen Types for Long Prisms.....	19
Table F.6 Crack Spacing on Prism Specimens without Fibers	23
Table F.7 Crack Spacing on Prism Specimens with Fibers	26
Table F.8 Percentage Reduction in Crack Widths at a Stress of 40 ksi for Specimens with and without Fibers	27
Table F.9 Slab Specimen Details	31
Table F.10 Test Matrix for Slabs with Different Reinforcing Types for Flexure and Fatigue Testing.....	45
Table F.11 Percentage Reduction in Crack Widths on Slabs with Fibers at 40 ksi.....	49
Table F.12 Percentage Increase in Crack growth and Deflection over Time	54

APPENDIX F STRUCTURAL TESTS

F.1 Introduction

This chapter presents details on the experimental program conducted to understand the factors that cause structural cracking in bridge decks and to reduce cracking with the use of alternative materials such as various corrosion-resistant reinforcements as well as the incorporation of polypropylene fibers in concrete. The tests included direct tension tests on prism specimens, flexural testing of slab sections, fatigue tests on slabs to study crack widening, pullout tests to understand the bond behavior of reinforcing bar with concrete, and a test on the connection between the slab and a pier cap.

The reinforcement bars validated in the experimental program were black steel bars (control), epoxy-coated bars, grade 2304 stainless steel bars, MMFX corrosion-resistant alloy steel bars, hot-dipped galvanized bars, and zinc galvanized bars (CGR-UAE). As very little research has been performed on the use of corrosion-resistant reinforcing steel as a means for reducing cracks on bridge decks, various experiments were designed to gain insight into the effects of each reinforcement type on bridge deck cracking.

F.2 Tensile Strength Testing of #5 Reinforcement Bars

Tension tests were performed to initially determine the material properties such as yield strength, tensile strength and stress-strain behavior. Tests were conducted on #5 bars (with a nominal diameter of 0.625 in.). Bar specimens were cut to a length of 17 inches, and the cross section at the middle region of each bar was reduced to approximately 0.30 inches as per ASTM E8 standards to ensure that failure would occur in that region (Figure F.1).



Figure F.1 Various Reinforcement Bars Machined at the Center for Tensile Strength Testing

Axial tension testing was conducted using an Instron (UTM-HYD type with Model #1000HDX) axial-tension testing machine. The end portions of each reinforcing bar specimen were clamped between the jaws of the machine, and the middle region was fitted with a 2-inch extensometer to capture the strain data. Displacement was applied at a strain rate of 0.005 in./in./min. until failure. Figure F.2 shows the setup for the tensile testing of reinforcing bars.

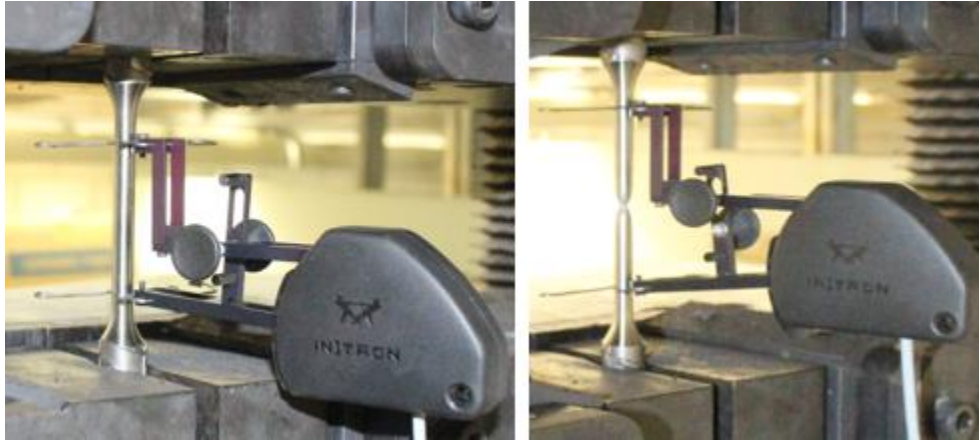


Figure F.2 Attachment of Extensometer to Collect Strain Measurements (Left); Failure of a Specimen (Right)

Stress-strain curves for all the bars were developed and are plotted in Figure F.3, and the test results are presented in Table F.1. The results showed linear stress-strain profile until 70 ksi.

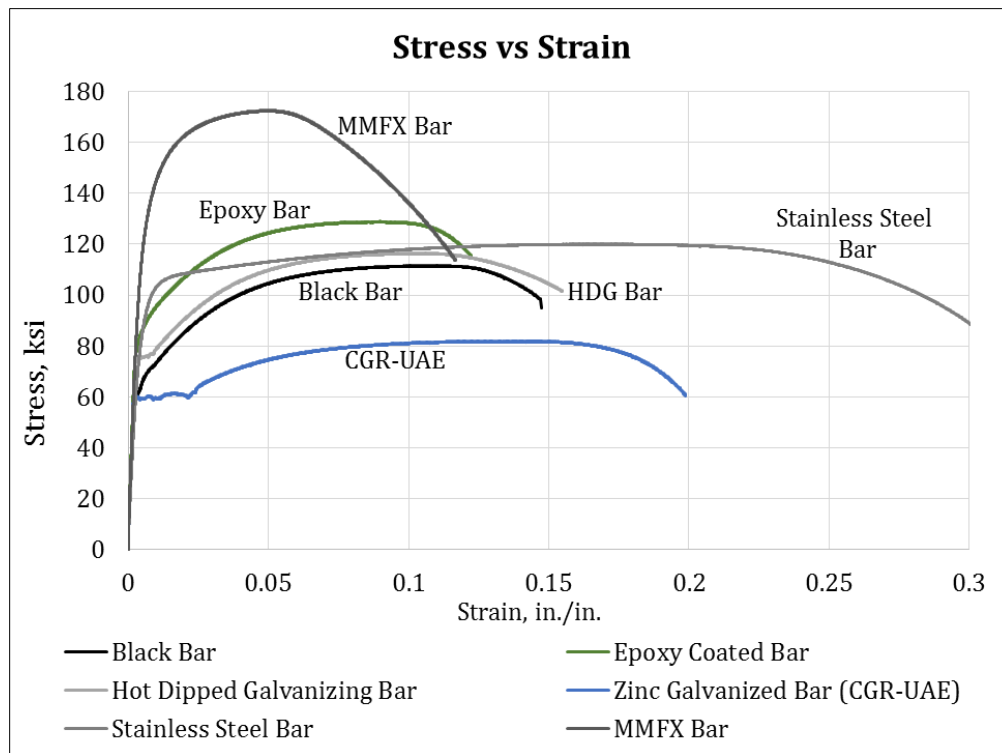


Figure F.3 Stress vs. Strain Curves for #5 Bars of Various Types

Table F.1 Yield and Ultimate Strength of #5 Reinforcing Bars

Serial No.	Type of Rebar	Specimen #	Yield Strength (ksi)	Average Yield Strength (ksi)	Tensile Strength (ksi)	Average Tensile Strength (ksi)
1	Black Bar	S1	64	65	110	111
		S2	66		112	
2	Epoxy-Coated Bar	S1	76	75.5	128	128.5
		S2	75		129	
3	Hot-Dipped Galvanized Bar	S1	70	70.5	115	116.5
		S2	71		118	
4	CGR-UAE Bar	S1	62	61.5	83	82.5
		S2	60		82	
5	Stainless-Steel Bar	S1	95	95.5	123	120.5
		S2	96		118	
6	MMFX Bar	S1	125	128	168	170.5
		S2	131		173	

F.3 Direct Tension Cracking of Prisms

Direct tension tests were performed to study cracking in prism specimens with different type of reinforcing bars embedded centrally. These tests were performed to determine how well the reinforcing bar is bonded to the concrete and to determine the crack widths and the distribution of cracks along the length of the prism. The parameters considered in this test are applied load, stress in the bar, crack widths, and crack spacing.

F.3.1 Testing of Trial I and Trial II Prism Specimens

The prism specimens used for Trials I and II were 44 inches long with 30 inches of embedment length and 7 inches of rebar projecting on either side. These specimens were designed so as to allow the specimen to be gripped between the jaws of the testing machine. Two trial sections were tried during the testing of prisms.

In Trial I, four types of reinforcing bars were used, and a total of eight specimens were cast. A 7-in. × 7-in. section with a clear cover of 3.18 in. was used. The intention was to simulate an effective concrete cover similar to that of an actual bridge deck. The #5 reinforcing bar was

placed centrally and was aligned horizontal to avoid any skew along the length of the specimen. The rebar was fitted with three strain gages along its length, as shown in Figure F.4.

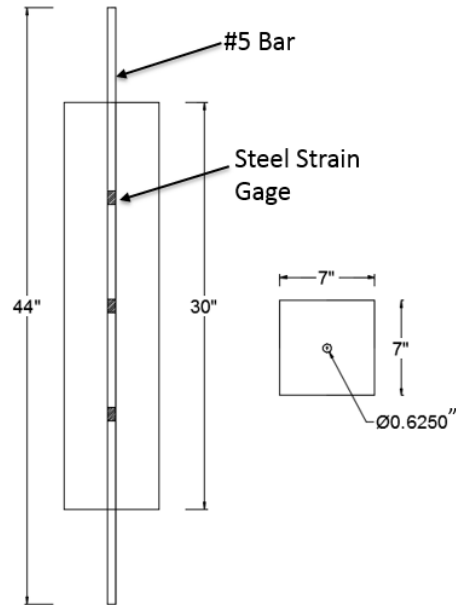


Figure F.4 Prism Specimen with a 7" × 7" Section

For the Trial II specimens, the dimensions of the section were modified and stirrups were added at the ends of the prism to prevent splitting cracks from developing. In this trial, six reinforcing bar types were used, and a total of 12 specimens were cast. A 5.5 in. × 5.5 in. section with a clear cover of 2.47 inches was used, as shown in Figure F.5. The 7" x 7" section was modified because it was found that the reinforcement ratio was very low.

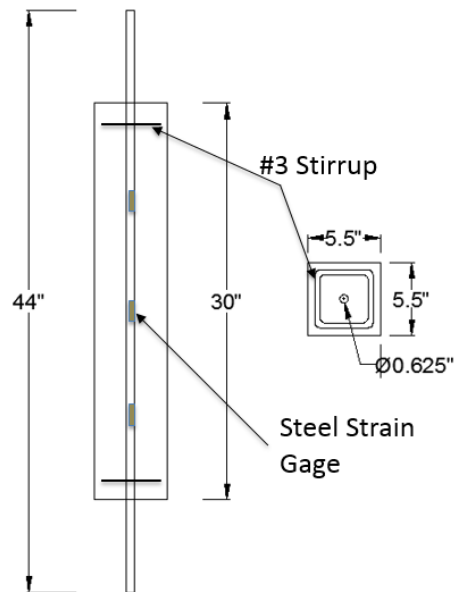


Figure F.5 Prism Specimen with a 5.5" × 5.5" Section

Table F.2 Details of Trial I and II Prism Specimens

Trial	Rebar Type	# of Specimens	Cross Section (in.)	Reinforcement Ratio
I	Black Bar	2	7 × 7	0.00633
	Epoxy-Coated Bar	2	7 × 7	0.00633
	Dual-Coated Z-Bar	2	7 × 7	0.00633
	Stainless Steel Bar	2	7 × 7	0.00633
II	Black Bar	2	5.5 × 5.5	0.0102
	Epoxy Bar	2	5.5 × 5.5	0.0102
	Dual-Coated Z- Bar	2	5.5 × 5.5	0.0102
	Stainless Steel Bar	2	5.5 × 5.5	0.0102
	Hot-Dipped Galvanized Bar	2	5.5 × 5.5	0.0102
	CGR-UAE	2	5.5 × 5.5	0.0102

The prism specimens were cast in formwork made from 3/4-inch-thick plywood. A 0.625-in.-diameter hole was made in the plywood ends to accommodate reinforcing bar at the centerline of each prism, as shown in Figure F.7. Prior to installation, each piece of reinforcing bar was ground at three locations along the embedded length so that strain gages could be attached. Once the reinforcing bar was placed in the form, three strain gages (designated as “top”, “middle” and “bottom”) were wired to facilitate data collection. Class QC2 concrete mix design was selected (Table F.3) to achieve a 28-day compressive strength of 5,000 psi.

Although the Trial I and Trial II prisms have different dimensions and Trial II prisms have stirrups, both specimen types use reinforcing bar with the same embedment length, and the strain gages were installed at the same locations along the length. In addition to the prism specimens, cylinders were also cast to monitor the compressive strength of concrete over 28 days; a typical plot of development of the compressive strength is shown in Figure F.6. Polypropylene fibers were added to the QC2 mix at a rate of 10 lb/yd³ to prepare additional specimens with fiber reinforced concrete for comparison purposes. Minor adjustments to the super plasticizer and the air content were made in the fiber reinforced concrete mixtures to obtain a minimum slump of 4 inches and an air content of 6 to 8%.

Table F.3 Class QC2 Concrete Mix Design used for All Specimens

Material	Design Quantity (1 yd ³)
Coarse Aggregate #57	1,210 lb.
Coarse Aggregate #8	650 lb.
Sand	1,220 lb.
Cement	472 lb.
Ground Slag	117 lb.
Sika Super Plasticizer	45 oz.
Air	5 oz.
WR 91 Water Reducing Admixture	5 oz.
Water–Cement Ratio	0.4

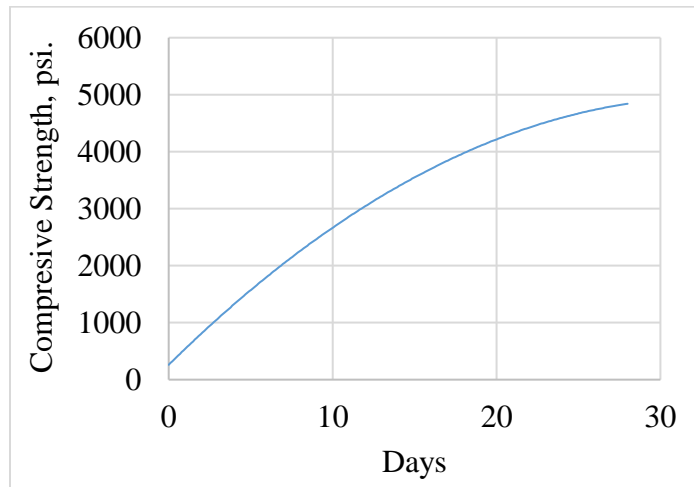


Figure F.6 Compressive Strength for Concrete Mix over 28 Days



Figure F.7 Prism Specimens with 7" × 7" Sections



Figure F.8 Casting of 7'' × 7'' Specimens

Prism specimens were installed in an Instron machine with a capacity of 220 kips for direct tension cracking, as shown in Figure F.9. This machine was able to accommodate prism specimens having a maximum length of 36 inches with 6 inches protrusion at each end, which is needed to grip in the machine and to clamp the specimen in place while aligning in a vertical position as axial tension is applied by the hydraulic system. The wires to the strain gages on the reinforcing bar were attached to a data acquisition system through channels so that the strains could be recorded. During the test, loading was applied as displacement control at a rate of 0.05 in./in./min. The machine was operated using Instron software, and loading was recorded and exported to Microsoft Excel. StrainSmart data acquisition software (provided by Micro-Measurements) was used to record the strains during the test. In addition, crack widths were recorded at 2 kip intervals using a manual crack gage; these measurements were later used for generating plots against respective strain in the reinforcing bar. The failed prism specimens are shown in figure F.10.



Figure F.9 Testing of Prisms in Trial I (Left) and Trial II (Right)



Figure F.10 Specimens Tested in Trial I

F.3.2 Testing of Trial III Slender Prism Specimens

When the specimens in Trial I and Trial II underwent direct tension cracking tests, it was observed that the desired extent of cracking did not occur. This may be because the reinforcement ratio in the prism specimens was very low. Therefore, it was decided to modify the test specimens with a reinforcement ratio matching the ratio for the tension zone in an actual bridge section. The section was sized for the target reinforcement ratio using #5 rebar, keeping the 1:1 ratio of the sides of the prism as well as the 30" length of the specimen the same as in the Trial I and Trial II specimens. The resulting design for the Trial III section was a slender prism. The details of the revised specimen are shown in Figure F.11 and are summarized in Table F.4.

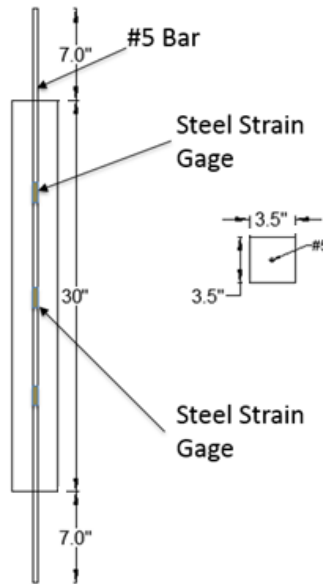


Figure F.11 Slender 3.5" × 3.5" Prism Specimen

Table F.4 Trial III Prisms with the Same Reinforcement Ratio as an Actual Bridge

Trial	Rebar Type	# of Specimens	Cross Section (in.)	Reinforcement Ratio
III	Black Bar	2	3.5 × 3.5	0.0253
	Epoxy-Coated Bar	2	3.5 × 3.5	0.0253

Prisms with only black (uncoated bar) and epoxy-coated bars were cast and tested for direct tension cracking. The rate of loading for the Trial III specimens was identical to the rate used in previous tests, and the crack widths and strains were recorded. Figure F.12 shows the testing of these prisms and images of the cracked specimens. It was observed that prisms made with epoxy-coated bars showed wider cracks than that those made with black (uncoated) bars. In addition, it was noted that the crack spacing was closer (i.e. more distributed cracks were observed) on the prisms with epoxy-coated bars.

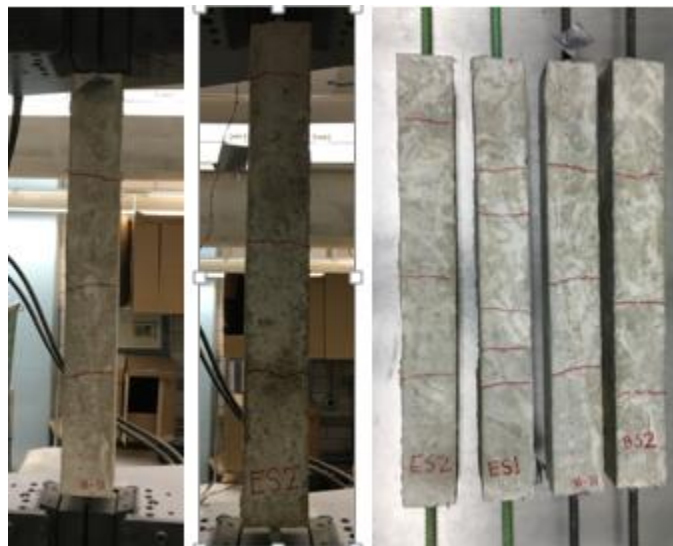


Figure F.12 Testing of Slender Prisms (Left) and Cracked Specimens (Right)

F.3.2.1 Trial III – Direct Tension Test Results

In Trial III, four slender specimens with black bars and epoxy-coated bars were cast and tested in a 220-kip Instron testing machine, as shown in Figure F.13. Loading was applied vertically, in line with the longitudinal axis of the member, by clamping the bar at the two ends of each specimen in the jaws of the machine. Strains and crack widths were recorded during the testing. Figure F.14 shows test specimens with cracks that formed during testing. Plots showing load versus crack width and stress versus crack width were presented in Figures F.15 and F.16. The concrete compressive strength was 4,800 psi at the time of testing.



Figure F.13 Testing of Trial III Prism Specimens



Figure F.14 Cracks Formed on Specimens during Testing in Trial III

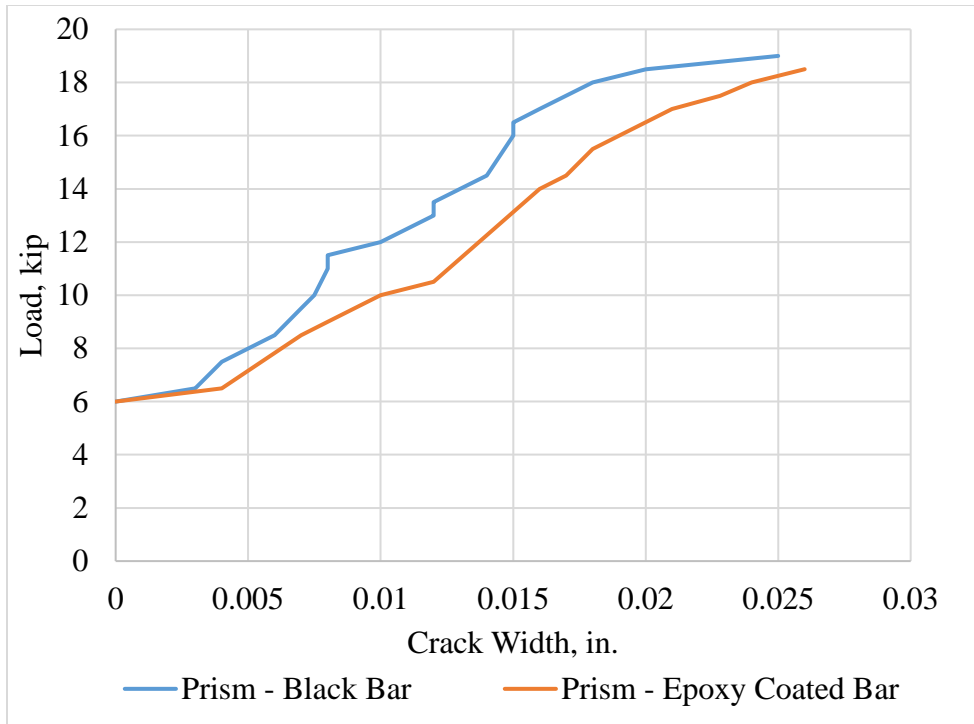


Figure F.15 Load vs. Crack Width for 3.5" × 3.5" Prisms

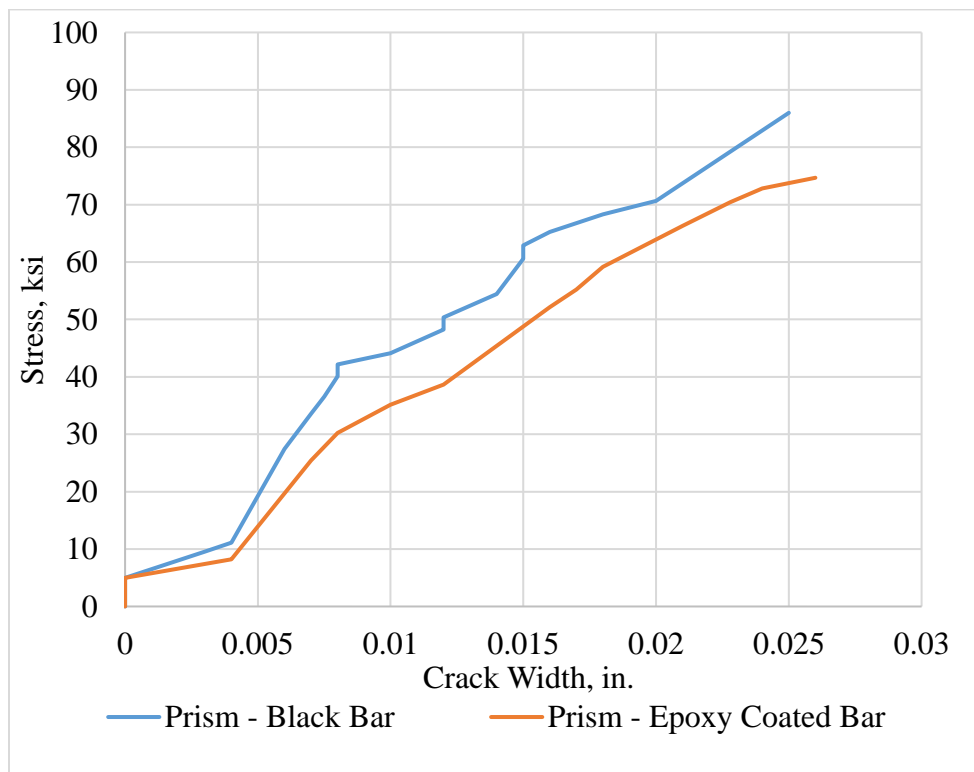


Figure F.16 Stress vs. Crack Width for 3.5" × 3.5" Prisms

From Figures F.15 and F.16, the average increase in crack widths due to the use of epoxy coated bars compared to those with the black bars was found to be about 20% near the service load level.

These tests were preliminary tests and therefore compare crack widths of prisms with epoxy-coated bars with those with black bars. The results of prism tests with different types of bars are presented in the next section.

F.3.3 Testing of Long Prism Specimens

When comparing the sections of slender prisms to prisms with larger cross-sectional area (Trials I and II), it was observed that the strain gages in the previous test setup were not yielding meaningful values. The test setup was subsequently modified to accommodate longer, more slender prisms with a larger number of strain gages and to perform axial testing of the prisms while placing them in a horizontal position rather than in a vertical one. A modified test setup was used for the modified prisms specimens that would give a more clear understanding of structural cracking under loading conditions.

For the next set of tests, 90-inch-long prism specimens were designed that maintained the same reinforcement ratio and the same ratio for the sides as in the tension zone of an actual bridge section. The section details of the resulting prism specimen are shown in Figure F.17.

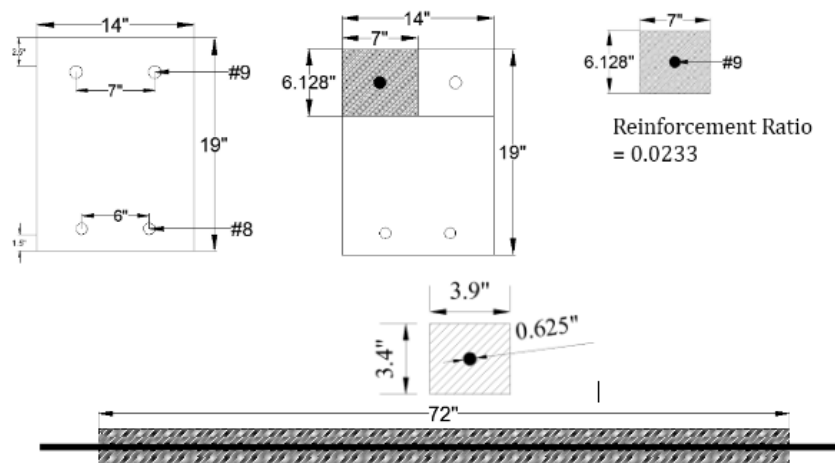


Figure F.17 Sectional Details of Long Prism Specimens

The test setup was modified to accommodate the long prisms and to apply tension force axially as shown in Figure F.18. Two 4 ft. long sections of 8" × 8" Hollow Structural Sections were used at the ends, and 2.5-inch-diameter holes were drilled vertically to secure the HSS sections to the strong floor with threaded anchor rods and nuts. On the webs of the HSS, 1.25-inch-diameter holes were drilled horizontally to accommodate the threaded rods attached to the ends of the prisms. Each end of the prism was welded with a 2.5-inch-long threaded rod. One of the ends of each prism attached with a threaded rod passing through the HSS and hydraulic jack with long nut. The other end had the HSS section and also accommodated the load cell to read the load applied. Two jack posts were placed in between the HSS sections to transfer the load in such a way that it would not affect the threaded rods that were used to ground the HSS sections.

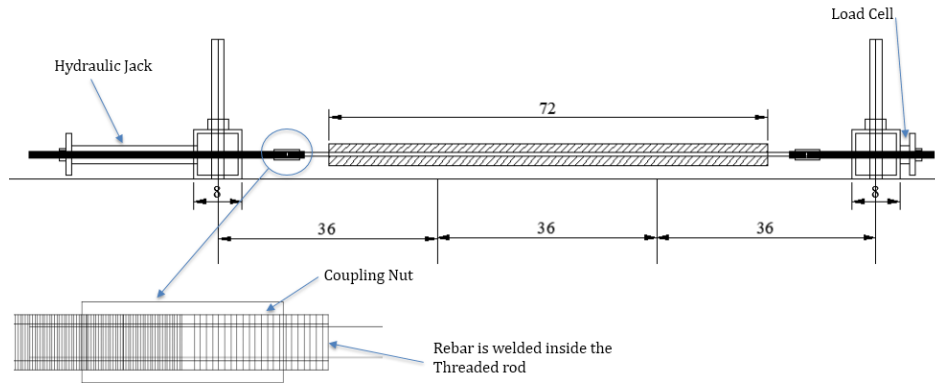


Figure F.18 Test Setup for Long Prisms

A total of 24 long prisms (two specimens each of six reinforcing bar types, with and without fibers) were cast, as summarized in Table F.5. The embedment length of the reinforcing bar was 72 inches. Five strain gages were attached on the reinforcing bar at a distance of 18 inches apart. The concrete mix design used was the standard QC2 mix (shown in Table F.3) to achieve a minimum strength of 4,500 psi at 28 days. Images showing the formwork and casting of the long prism specimens are shown in Figures F.19 and F.20.

Table F.5 Specimen Types for Long Prisms

Concrete Type	Rebar Type	# of Specimens	Cross Section (in.)	Reinforcement Ratio
Without Fibers	Black Bar	2	3.4 × 3.9	0.0233
	Epoxy-Coated Bar	2	3.4 × 3.9	0.0233
	Dual-Coated Z-Bar	2	3.4 × 3.9	0.0233
	Stainless Steel Bar	2	3.4 × 3.9	0.0233
	Hot-Dipped Galvanized Bar	2	3.4 × 3.9	0.0233
	CGR-UAE	2	3.4 × 3.9	0.0233
With Fibers	Black Bar	2	3.4 × 3.9	0.0233
	Epoxy-Coated Bar	2	3.4 × 3.9	0.0233
	Dual-Coated Z-Bar	2	3.4 × 3.9	0.0233
	Stainless Steel Bar	2	3.4 × 3.9	0.0233
	Hot-Dipped Galvanized Bar	2	3.4 × 3.9	0.0233
	CGR-UAE	2	3.4 × 3.9	0.0233

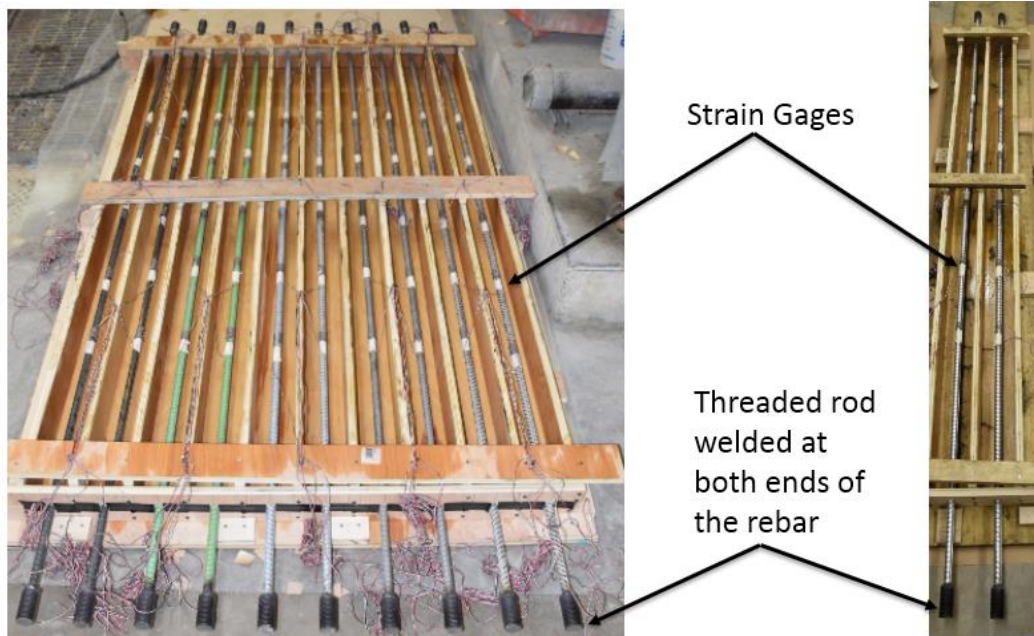


Figure F.19 Formwork and Rebar for Casting of Long Prisms



Figure F.20 Typical Casting of Long Specimens

Specimens were tested for axial direct tension cracking after 28 days. The average concrete strength was 4,800 psi on the day of testing. The specimens were installed in the frame, and the ends were joined with the threaded rod using coupling nuts. The typical test setup for the long specimen testing is shown in Figure F.21. The loading was applied manually using a hydraulic jack, and the applied load was read using a load cell. The wires from the strain gages and the load cell were connected to a data acquisition system, and the strains in the reinforcing bar and the load were recorded using StrainSmart software. Crack widths were measured and recorded manually using crack gage at every 0.5 kips. The measurement included in this test were strain in the reinforcing bar, crack widths, and the spacing of cracks over the length of the specimen. Two

specimens of each type of reinforcing bar were tested, and the results were averaged. Results are presented in section F.3.3.1.

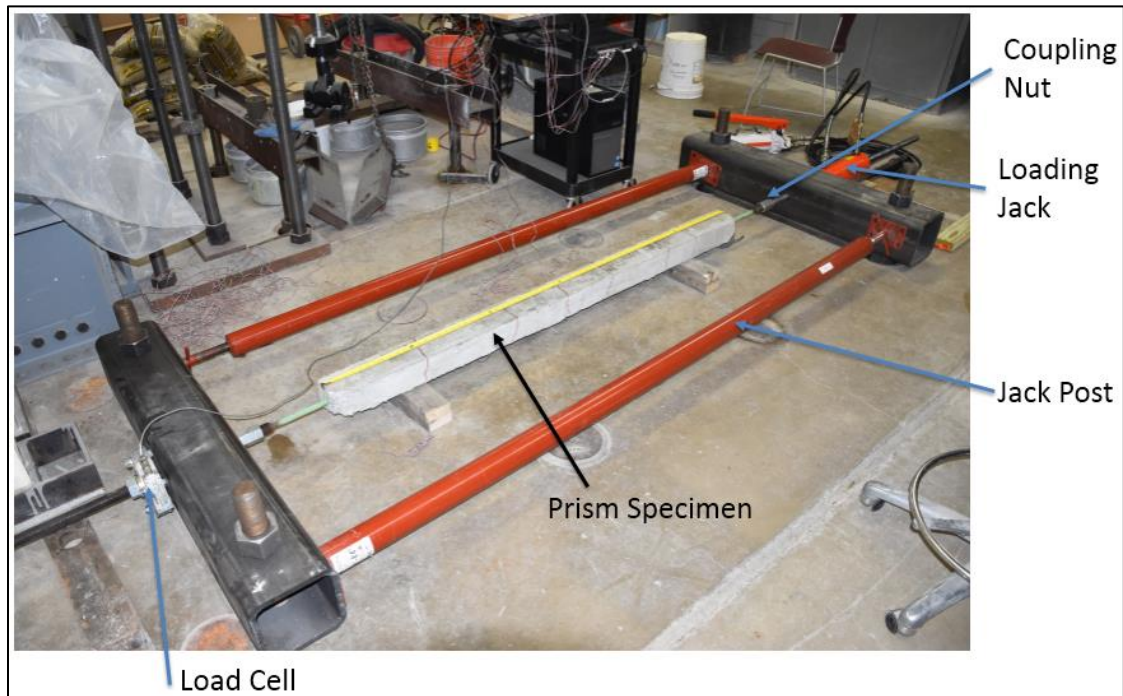


Figure F.21 Test setup for Testing of Long Prisms

F.3.3.1 Long Tension Prism Test Results – Direct Tension Cracking

Twenty-four prism specimens with different reinforcing bars, both with and without fibers were tested for direct tension cracking under axial loading. The specimens were tested in a horizontal position with five strain gages attached along the embedment length. The strains along the length of the specimen, the crack widths, the crack spacing, and the crack patterns were recorded during these tests. Plots showing load versus crack width and stress versus crack width of the specimens without fibers are presented in Figure F.22 and Figure F.23, respectively.

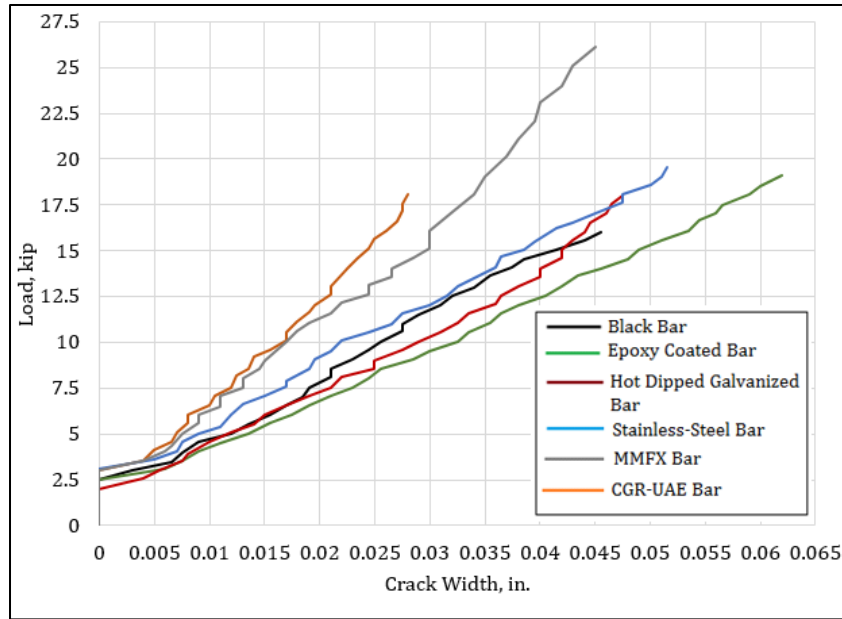


Figure F.22 Load vs. Crack Width for Prisms without Fibers

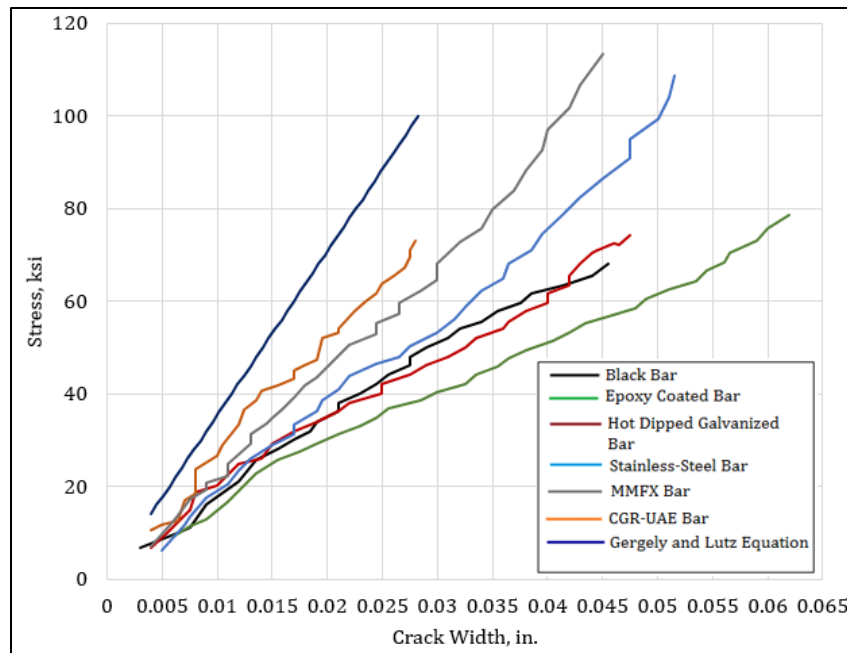


Figure F.23 Stress vs. Crack Width for Prisms without Fibers

From the test results, it was observed that the specimens with epoxy-coated bars showed wider cracks at a given load or stress level compared to specimens with other types of bars, whereas prism specimens with MMFX and zinc-galvanized bars (CGR-UAE) showed smaller crack widths. The straight line in the Figure F.23 indicates the theoretical crack width prediction by using Gergely and Lutz equation. Specimens with black bars and hot-dipped galvanized bars showed similar cracking behavior. Crack spacing on specimens with different bars is presented in Table F.6. The theoretical crack spacing given by ACI 224R-92 was calculated using the equation $4 \cdot d_c$,

where d_c is the concrete cover. Also, the theoretical cracking load was calculated using an equation provided in ACI 224R-92. All specimens cracked between 3.0 and 4.0 kips compared to the calculated theoretical crack load of 4.2 kips. It was observed that the average crack spacing ranged between 7 to 10 inches.

Table F.6 Crack Spacing on Prism Specimens without Fibers

Serial No.	Bar Type	Specimen #	Crack Spacing (in.)			# of Cracks	ACI Theoretical Crack Spacing (in.)	Theoretical Cracking Load (per ACI 224R-92)	Experimental Cracking Load
			Min	Max	Avg		(4* d_c)		
1	Black	S1	5	9	7.5	7	7	4.2	3.5
2	Black	S2	6	12	7.7	8	7	4.2	3.25
3	Epoxy-Coated	S1	6	13	9.4	6	--	4.2	3.15
4	Epoxy-Coated	S2	8	15	10.2	6	--	4.2	3.1
5	Hot Dip Galvanized	S1	6	9	8.2	7	--	4.2	3.0
6	Hot Dip Galvanized	S2	7	11	9	7	--	4.2	3.5
7	CGR-UAE	S1	6	9	6.5	9	--	4.2	4.0
8	CGR-UAE	S2	7	11	7.5	8	--	4.2	3.5
9	Stainless Steel	S1	6	10	7.4	9	--	4.2	3.5
10	Stainless Steel	S2	5	9	7	9	--	4.2	3.45
11	MMFX	S1	5	11	8	8	--	4.2	3.45
12	MMFX	S2	6	11	8.3	8	--	4.2	3.5

The crack widths versus load and crack width versus stresses were plotted for specimens with fibers and presented in Figures F.24 and F.25. The crack widths on specimens with epoxy-coated bars were wider compared to the specimens with other types of bars, whereas specimens with MMFX and CGR-UAE bars showed smaller crack widths. A similar trend was observed in specimens without fibers, but the crack widths for specimens with fibers were much smaller. All the cracks occurred between 3 and 3.5 kips with an average crack spacing ranging between 6 to 10.2 inches, as presented in Table F.7.

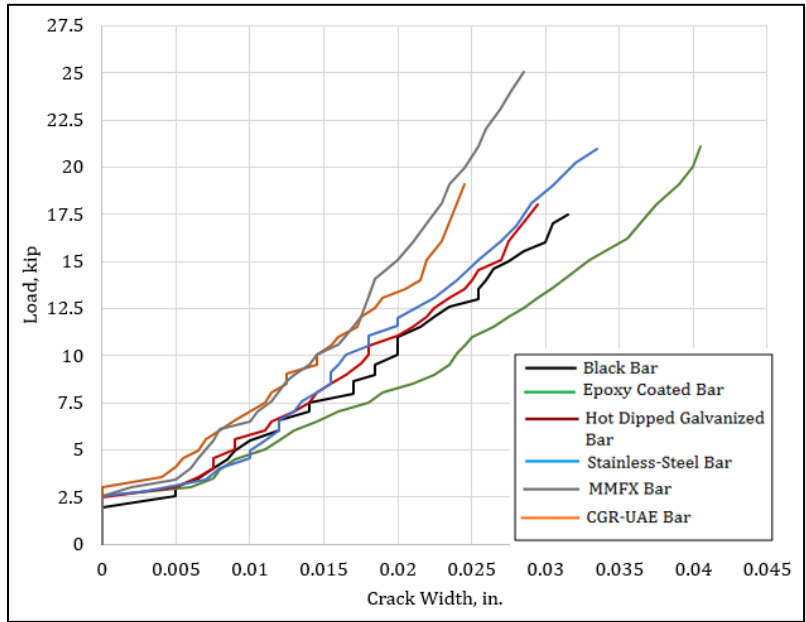


Figure F.24 Load vs. Crack Width for Prism Specimens with Fibers

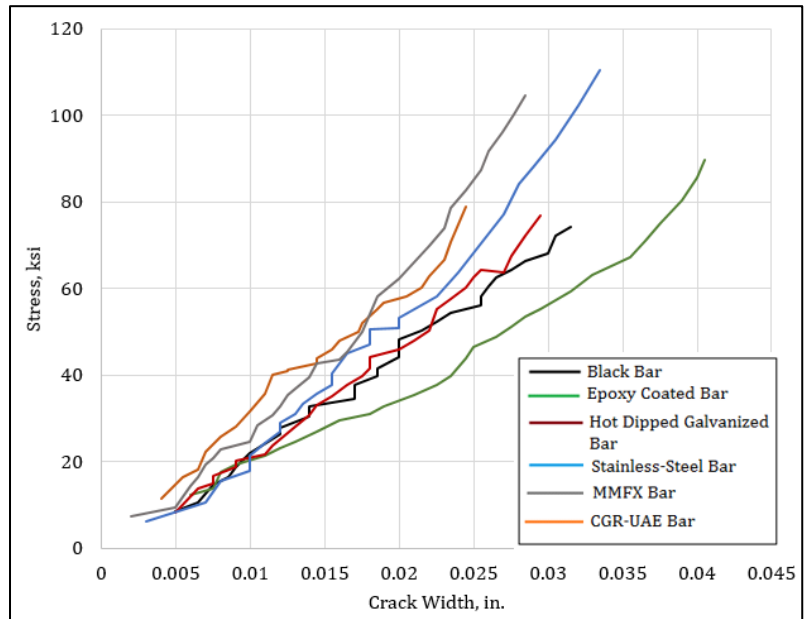


Figure F.25 Stress vs. Crack Width for Prisms Specimens with Fibers

Plots showing, stress versus crack width of prisms with and without fibers in Figure F.26 and compared with Gergely and Lutz equation for each bar type.

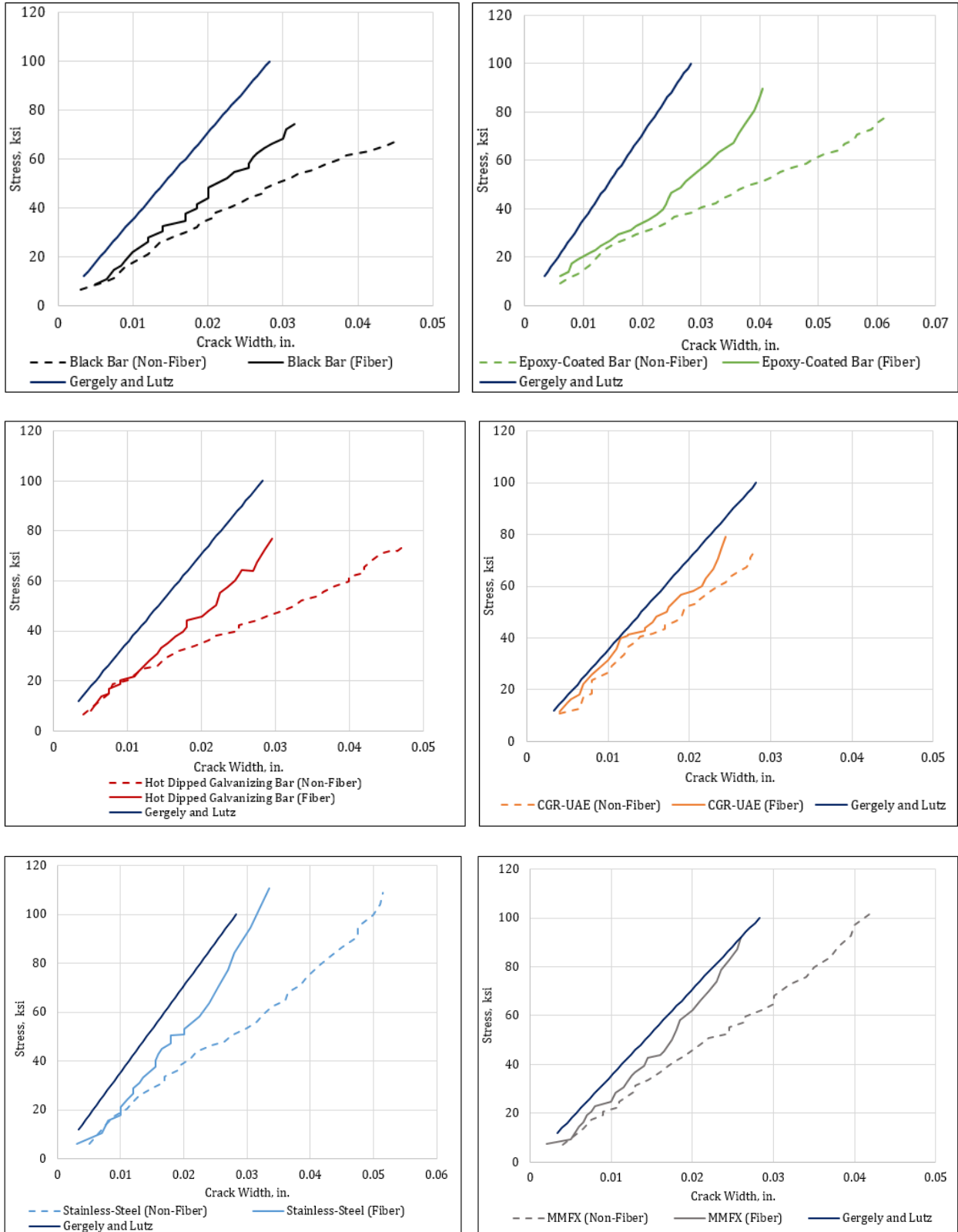


Figure F.26 Plots Showing Stress Versus Crack Widths of Prisms with Different Bar Types with and without Fiber

Table F.7 Crack Spacing on Prism Specimens with Fibers

Serial No. #	Bar Type	Specimen #	Crack Spacing (in.)			# of Cracks	ACI Theoretical Crack Spacing (in.)	Theoretical Cracking Load (per ACI - 224R-92)	Experimental Cracking Load
			Min.	Max.	Avg.		(4*dc)		
1	Black	S1	4	11	7.2	10	7	4.2	3.0
2	Black	S2	6	8.5	7.1	9	7	4.2	3.0
3	Epoxy-Coated	S1	4	9	6.6	10	--	4.2	3.0
4	Epoxy-Coated	S2	5	10	7.3	9	--	4.2	3.0
5	Hot-Dip Galvanized	S1	5	15	7.8	8	--	4.2	3.0
6	Hot-Dip Galvanized	S2	8	12	10.5	6	--	4.2	3.0
7	CGR-UAE	S1	5	7	6.2	10	--	4.2	3.43
8	CGR-UAE	S2	5	8	7	9	--	4.2	3.56
9	Stainless Steel	S1	4	12	6.5	10	--	4.2	3.0
10	Stainless Steel	S2	4	10	7.6	9	--	4.2	3.42
11	MMFX	S1	5	10	7.1	9	--	4.2	3.6
12	MMFX	S2	5.5	9	7.4	10	--	4.2	3.0

The crack widths were reduced by about 25% for specimens with fibers compared to the corresponding specimens without fibers, as the fibers could arrest the cracks at higher loads. (Table F.8).

Table F.8 Percentage Reduction in Crack Widths at a Stress of 40 ksi
for Specimens with and without Fibers

Serial No.	Bar Type	Crack width of Non-Fiber Slab (in.)	Crack Width of Slab with Fiber (in.)	% Reduction in Crack Width
1	Black	0.023	0.0175	24 %
2	Epoxy-Coated	0.03	0.0235	21.6 %
3	Hot-Dip Galvanized	0.025	0.019	24 %
4	CGR-UAE	0.014	0.011	21.4 %
5	Stainless-Steel	0.021	0.0155	26.2 %
6	MMFX	0.017	0.013	23.5 %

The crack patterns formed on the specimens were marked, and the crack spacing was estimated as presented in Tables F.6 and F.7. Figures F.27 and F.28 show the crack patterns formed on specimens without fibers and Figure F.29 and F.30 shows cracks that are formed on specimens with fibers.



Figure F.27 Cracks on Prism Specimens without Fibers with Black, Epoxy-Coated and Hot-Dipped Galvanized Bars

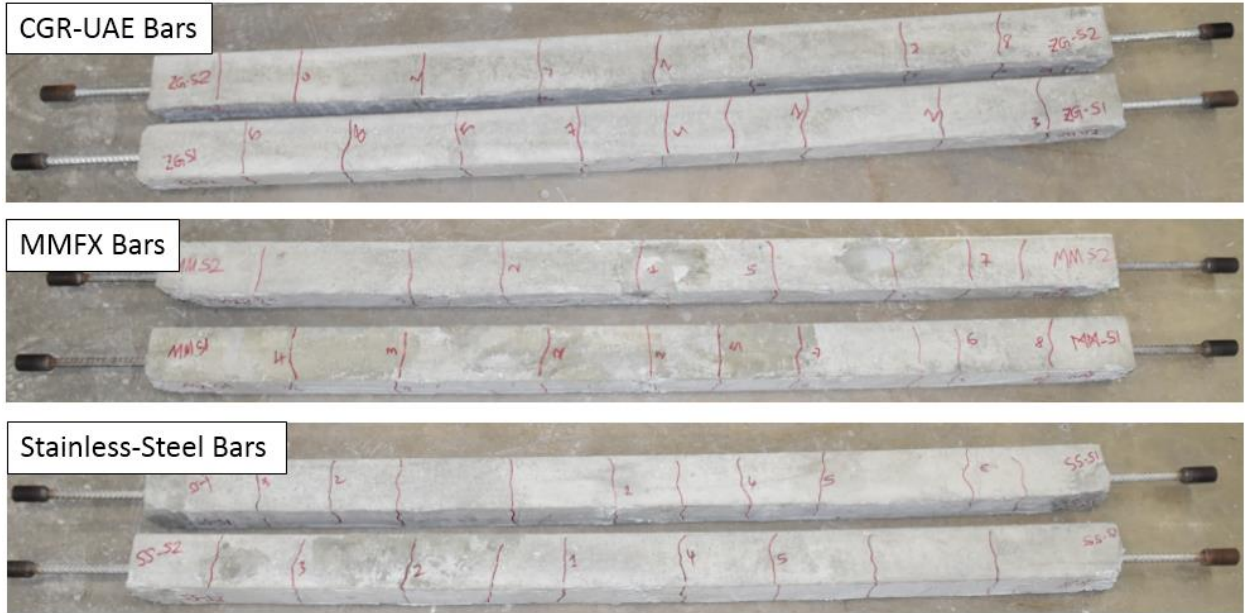


Figure F.28 Cracks on Prism Specimens without Fibers with CGR-UAE Bars, MMFX and Stainless-Steel Bars



Figure F.29 Cracks on Prism Specimens with Fibers with Black, Epoxy-Coated and Hot-Dipped Galvanized Bars

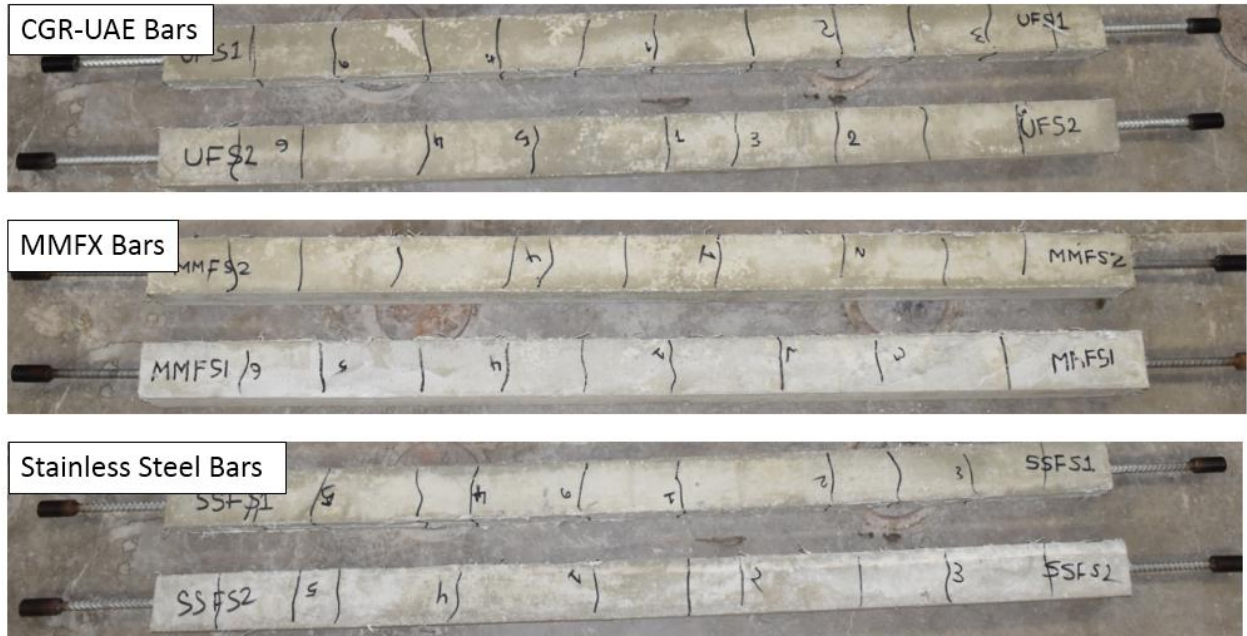


Figure F.30 Cracks on Prism Specimens with Fibers with CGR-UAE Bars, MMFX and Stainless-Steel Bars

F.4 Design and Preparation of Slab Specimens to Test for Flexure Cracking

Conducting tests on a full-scale bridge section is a tedious and expensive process. Therefore, there was a need to establish a relation to scale down the specimen size so the specimen could be easily tested under laboratory conditions, and the results could be extrapolated to the actual scale of the bridge.

The span lengths of the standard ODOT three span continuous slab bridges are designed in such a way that the span length of exterior spans is 0.8 times of that of interior span. If “ L ” is designated as the span length of the middle span, then the span lengths of the left and right spans are $0.8 L$. The analysis was performed using SAP2000 structural analysis software considering only the dead load on the slab to find the distance between the inflection points near the pier caps, as shown in Figure F.31.

The distance between inflection points for several of the bridges surveyed in the previous project (Patnaik and Baah et al. 2015, Ganapuram et al. 2013) were estimated and of these bridges, a three-span continuous slab bridge in Portage County (POR-88-1250) was selected to investigate transverse cracking on the deck slab at the negative moment region and to understand the effect of scaling down the slab specimen. This bridge has spans of 30'-37.5'-30'.

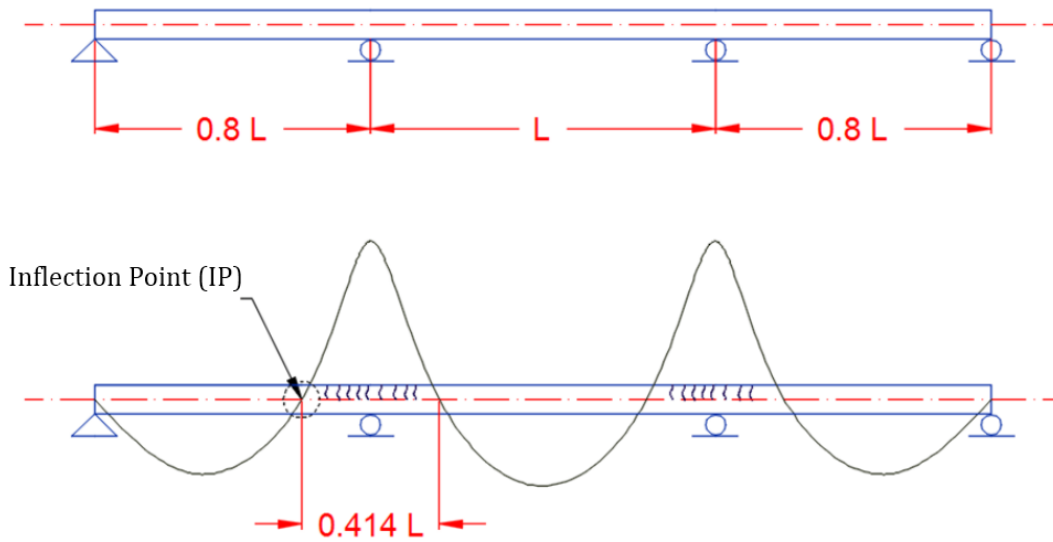


Figure F.31 Bending Moment Diagram Showing Points of Inflection Points

Bridge POR-88-1250 was constructed in 2006, and the sectional details of this bridge are presented in the ODOT standard drawing as shown in Figure F.32. A crack survey was performed by Patnaik and Baah et al. (2015) and Ganapuram et al. (2013) when the bridge had been in service for 8 years. It was found that the bridge had extensive longitudinal and transverse cracking, with a maximum surface crack width of 0.08 inches near the negative moment region, as shown in Figure F.32.

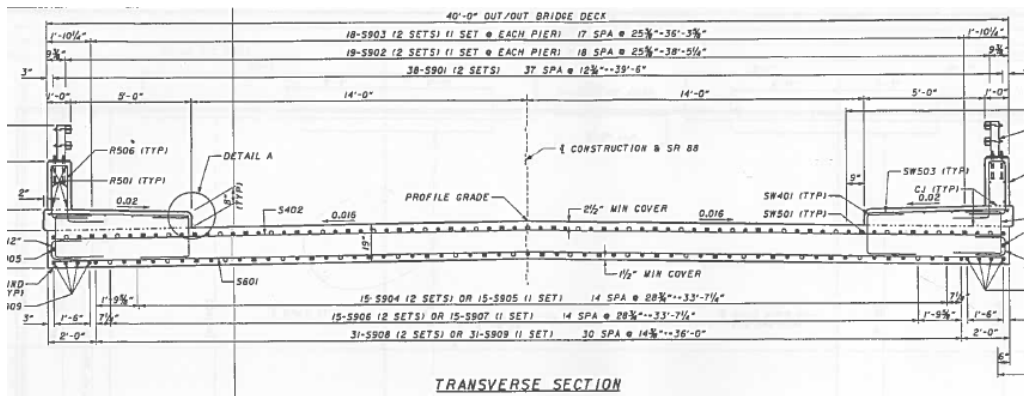


Figure F.32 Bridge POR-88-1250: Transverse Sectional Details (Top), Observed Cracks (Bottom)

The span between the inflection points over the negative moment region for Bridge POR-88-1250 was estimated to be 15.5 ft. and rounded to 15 ft. Since these inflections points have zero bending moment, they can be considered as simple supports in designing the test specimens representing bridge decks for subsequent testing in this study.

F.4.1 Details for the Full-Scale and Half-Scale Slab Specimen

A full-scale section of the bridge POR-88-1250 with a total length of the slab of 16 ft. and a span of 15 ft. was selected for full scale testing. The reinforcement details were the same as those of the actual bridge deck, with the same reinforcement ratio, cover thickness and section details (Figure F.33). The spacing of the compression steel was adjusted to be same as that of tension steel to accommodate stirrup near the support regions.

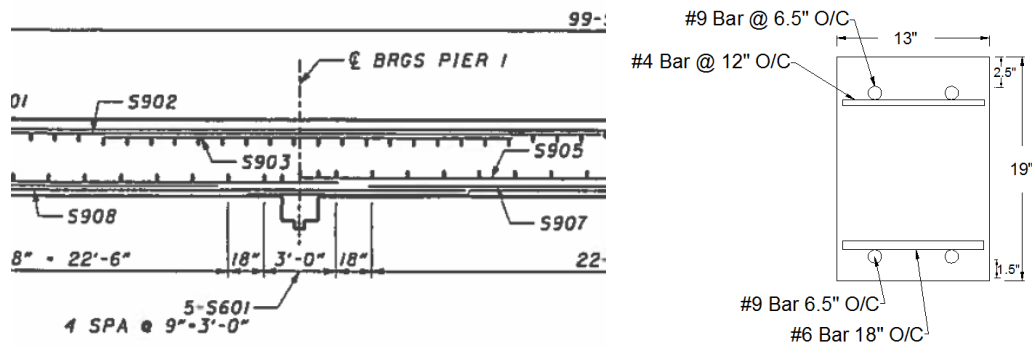


Figure F.33 Slab Section Representing the Negative Moment Region of Bridge (left) and Typical Cross Sections Details of the Test Specimen (Right)

Two slabs that were 16 ft. in length, 13 inches wide to accommodate two #9 bars at a spacing of 6.5", and 19 inches deep were cast as full-scale specimens to replicate the negative moment region of the bridge deck between the inflection points. One specimen was cast with uncoated black bars and the other was cast with epoxy-coated bars. Four additional specimens (two with uncoated reinforcement and two with epoxy-coated reinforcement) were also cast with the same reinforcement and section details but using only half the span length (i.e. 8 ft). All specimens were cast using the same mix design (Class QC2 concrete mix) to understand the cracking behavior for the full-span and half-span slab specimens and the scaling effects. A summary of the specimens that were cast for these tests is provided in Table F.9.

Table F.9 Slab Specimen Details

Serial No.	Slab Length	Slab Section	Type of Reinforcement	No. of Specimens
1	16 ft.	13 in. × 19 in.	Uncoated Bar	1
2	16 ft.	13 in. × 19 in.	Epoxy-Coated Bar	1
3	8 ft.	13 in. × 19 in.	Uncoated Bar	2
4	8 ft.	13 in. × 19 in.	Epoxy-Coated Bar	2

F.4.2 Preparation of Slab Specimens

The formwork for casting the slabs was made with $\frac{3}{4}$ -inch plywood. The top main reinforcing bars were ground at the mid-span and quarter-span locations before the cage was placed in the formwork. The cage was then positioned in the formwork so as to achieve a bottom clear cover of 1.5 inches and a top clear cover of 2.5 inches. The formwork and the rebar cage for the slab specimens is shown in Figure F.34.



Figure F.34 Formwork and Reinforcing Cage for Slab Specimens

To prepare the tension reinforcement for the application of strain gages, the top two tension reinforcing bars were ground at locations 4 inches apart at the mid-span and at the quarter-span so as to attach strain gages. Prior to the application of the strain gages, the surface of the bar was cleaned following a procedure suggested by Micro-Measurements.

Standard ODOT mix design was used to prepare the concrete for all the slab specimens. This concrete was supplied by a local company, ACE Ready-Mix Concrete Co. (Norton, Ohio). The design compressive strength at 28 days was 4,500 psi. A water-to-cement ratio of 0.45 that results in a concrete slump of 4 inches was used, and Sika 2100 super plasticizer was added to increase the workability of the mix. The mixture proportions are presented in Table F.3.

The concrete was filled into the forms with the help of chute of the truck. The concrete flowed easily, and no vibration was required. Once all the slab forms were filled, the surface was leveled and smoothed, as shown in Figure F.35.



Figure F.35 Placing of Concrete into the Formwork

Once the concrete was leveled and smoothed, it was left for 24 hours to harden. The slabs were covered with wet burlap and plastic sheeting to retain moisture. The test slabs were wet cured for 21 days and achieved a minimum compressive strength of 4,500 psi. The curing of the slab specimens is shown in Figure F.36.



Figure F.36 Curing of Slab Specimens

F.5 Structural Tests Conducted on Full-Scale Slab Specimens

The slabs were placed in a frame that was specially fabricated to test for flexural cracking by applying load from the bottom (i.e., on the compression side of the slab) while the supports were provided at the ends from the top. The crack data, deflections and the strain in the bars were the parameters monitored during the applied load.

The specially designed frame used for testing of the full-scale slabs is shown in Figure F.37. The supports were made from threaded rods connected to 2-inch-thick steel base plate, and 1-inch plates were used at the bottom to hold the beam in correct position. A 2-inch-thick plate with a 2-inch-diameter bar welded to it on the top acting as a roller support. The slab, when loaded, was designed to react against the $\frac{3}{4}$ " bars at the ends that was acting as roller support on the tension side. The span for the testing was 15 ft.

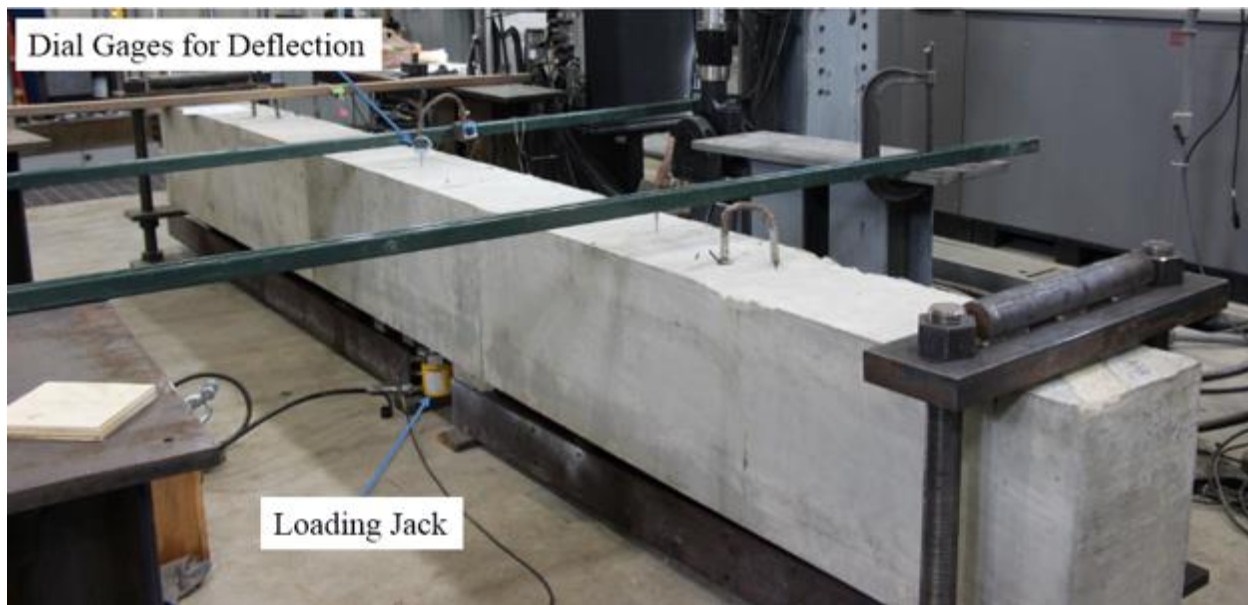


Figure F.37 Test Setup for Testing of a 16-ft. Slab

During testing, each test slab was supported at the ends, and was applied at the mid-span with two rollers to spread the load 8 inches apart. The load was applied by using a manually operated 30-ton hydraulic jack and pump system (as shown in Figure F.37), where the hydraulic jack was placed below the slab near the mid-span location. A 200-kip Interface load cell was placed over the jack to read the applied load in the data acquisition system. A rectangular steel plate was placed over the load cell with two long bars symmetrically spaced 8 inches apart, and load was transferred from the jack to the slab, at two points.

A System 5000 data acquisition unit supplied by Vishay (Micro-Measurements) was used during the test to capture the strains in the reinforcing steel and the load applied. Wires from the strain gages and the load cell were connected to the system through conduits. The strains and load values were recorded using StrainSmart software. Crack widths, deflection measurements were recorded manually at every 500 lbs.

Dial gages (shown in Figure F.37) were used to manually read the deflections at the mid-span and quarter-span locations for each load increment. Crack data such as crack widths, crack patterns, and crack spacing were also collected during the testing. The crack widths were measured manually using crack gages, and the crack patterns was noted by measuring and locating the cracks.

F.5.1 Results on Full-Scale Slab Testing for Flexural Cracking

Tests were performed on two full-scale slabs to understand the effect of scaling of the slabs. These specimens were detailed to have the same reinforcement as needed for a typical three-span bridge with spans of 30 ft. – 37.5 ft. – 30 ft. The specimens were 16 ft. in length, which is between the points of inflections of the actual bridge moment envelope. Four specimens with black bars and epoxy-coated bars with half the span (i.e. 8 ft. in length) were also tested to understand the cracking

behavior of reduced-sized spans. Load was applied using a manually operated hydraulic jack, and the strains and applied loads were recorded continuously. The deflections at the mid-span and the quarter-span were manually recorded using dial gages. The load versus deflection plots for slabs with 15 ft. spans are shown in Figure F.38 and F.39.

The theoretical deflection at the mid-span was also calculated, and it was found that both the theoretical and experimental mid-span were mostly close for the slab with black bars and slightly off for the slab with epoxy-coated bars. The deflection plots for slabs with black bars and epoxy-coated bars are shown in appendix.

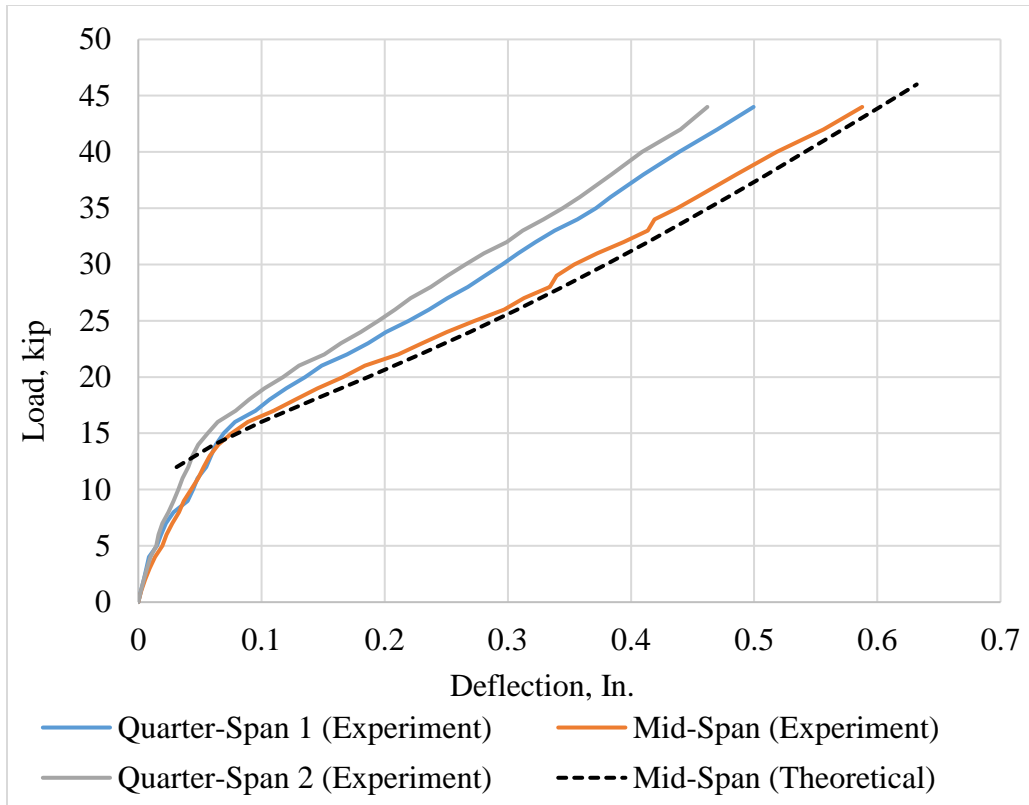


Figure F.38 Load vs. Deflection Plot for a 15-ft.-Span Slab with Black Bars

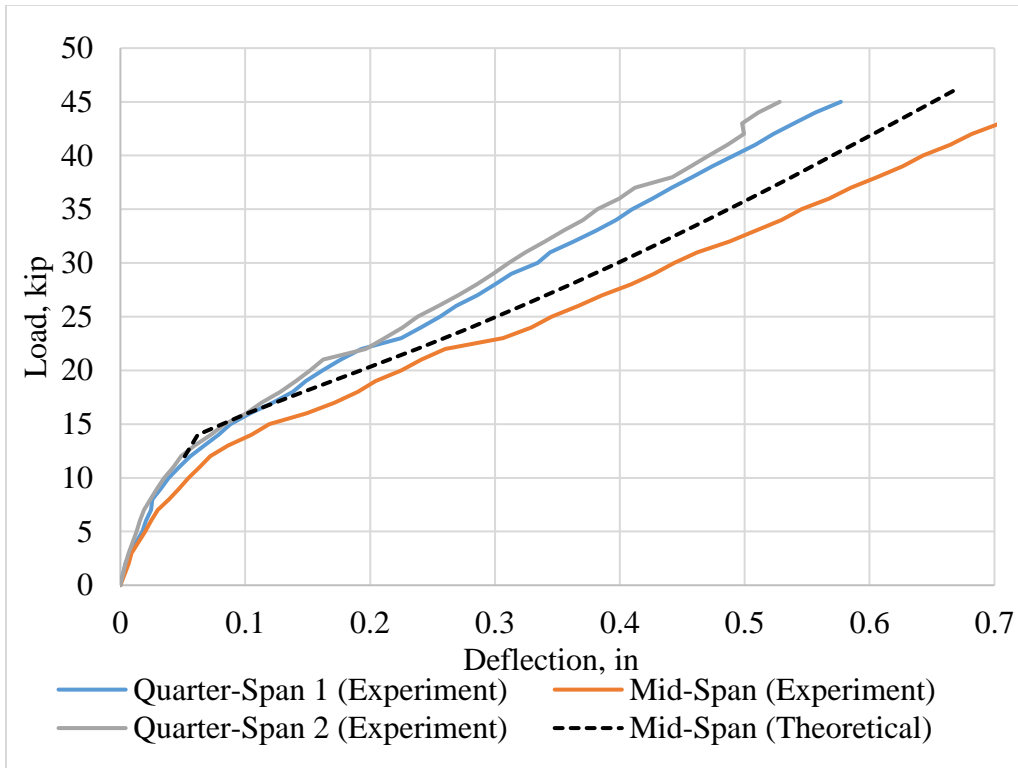


Figure F.39 Load vs. Deflection Plot for a 15-ft.-Span Slab with Epoxy-Coated Bars

Crack widths were measured on the tension side of the slabs using a crack gage. Crack data was collected at regular load intervals while the strain in the bars and the applied load were recorded using a data acquisition system. Plots of crack width versus stress were generated, and the observed crack widths were compared with the theoretical equation of Gergely and Lutz (1968) and Kim, B., and Kim, Y., et. al., (1987). The crack width plots of slabs with 15-ft. spans and 7.5-ft. spans that were made with black-bars were compared to study the cracking behavior under similar levels of stress, as shown in Figure F.40.

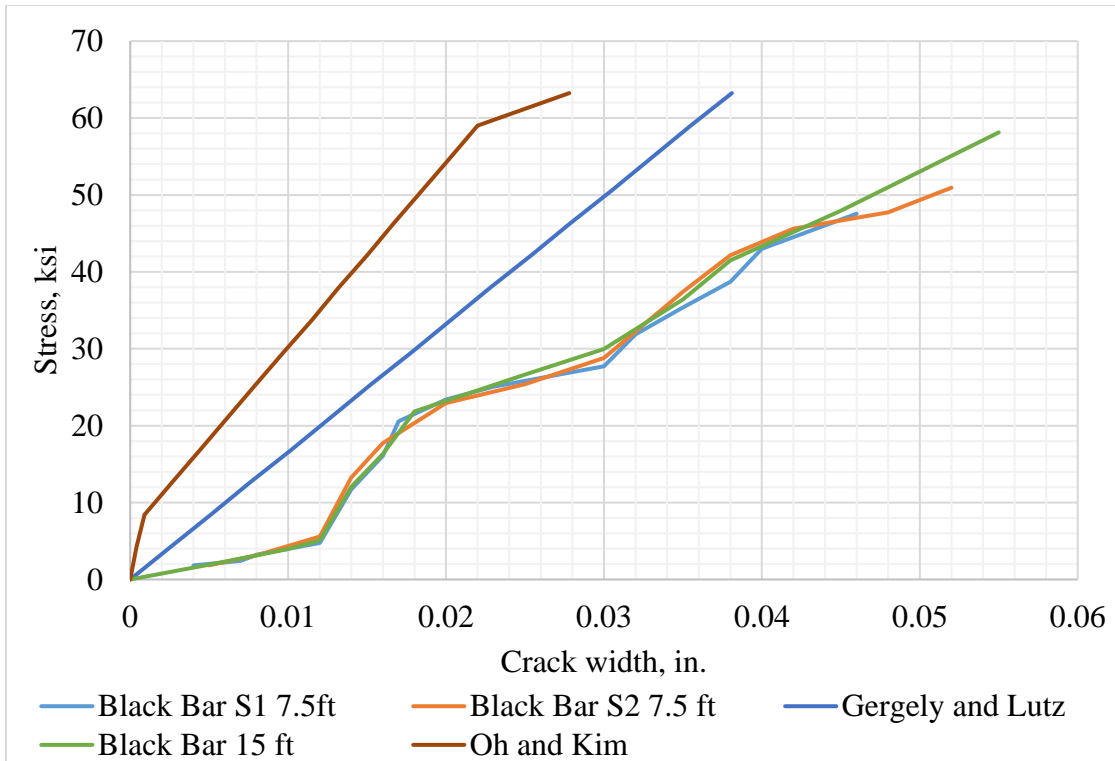


Figure F.40 Stress vs. Crack Width for a Slab with Black Bars

On comparison, it was observed that the crack widths on both the slabs with a 15 ft.-span and a 7.5-ft. span were mostly similar at the same stress level. However, the theoretical crack predictions were found to underestimate the crack widths of this section. Hence, for further study, slabs with 7.5-ft. spans were chosen.

Similar curves were developed for slabs with epoxy-coated bars for comparison between the slabs with a 15-ft. span and those with a 7.5-ft. span. A similar trend as that for slabs with black bars was observed, with a slight scatter in the data, as crack widths. The plots for stress vs. crack width of slabs with epoxy-coated bars is shown in Figure F.41.

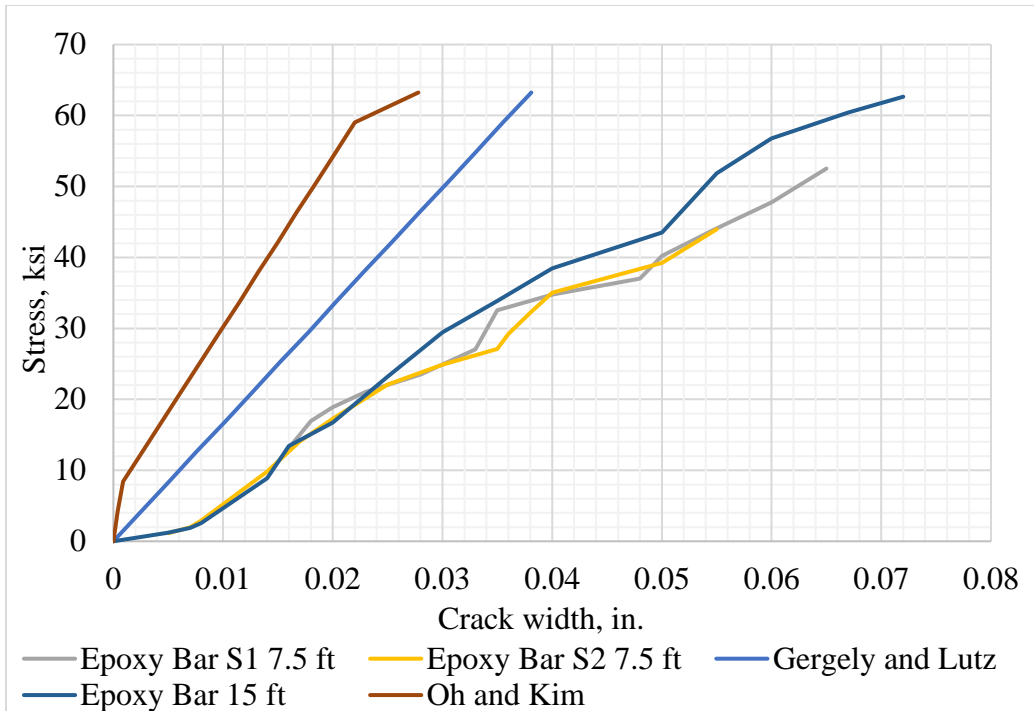


Figure F.41 Stress vs. Crack Width for Slabs with Epoxy-Coated Bars

The crack widths on slabs with black bars and epoxy-coated bars for 7.5-ft. spans were compared, as shown in Figure F.42. Slabs with epoxy-coated bars had wider cracks than slabs with black bars.

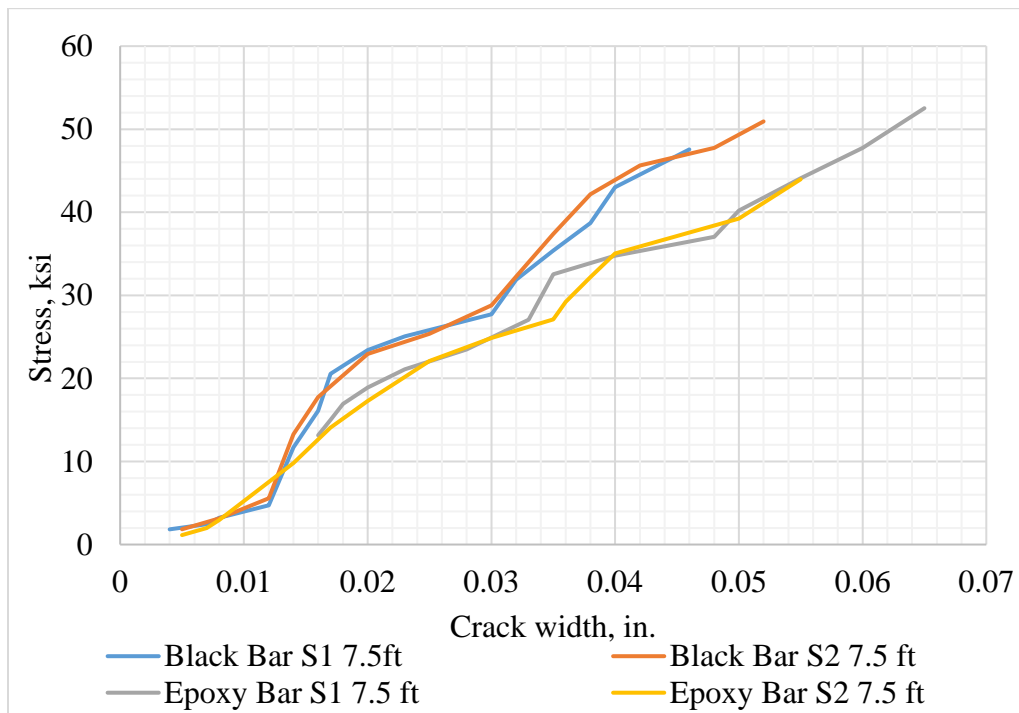


Figure F.42 Stress vs. Crack Width for 7.5-ft. Slabs with Black Bars and Epoxy-Coated Bars

The crack spacing was also measured and found to be more uniform in case of specimens with both bar types as shown in Figure F.43. The crack pattern was documented and found to be similar for specimens of both types.



Figure F.43 Crack Patterns on Slabs with Black Bars and Epoxy-Coated Bars (*Black Bars in Foreground and Epoxy-Coated Bars in the Back*)

F.6 Preparation and Testing of Reduced-Scale Slab Specimens

To understand total scaling effect, the full-scale slab designs were modified to create smaller sections, keeping the length of the slab as 8 ft. These sections were designed in such a way that the tension reinforcement ratio would be the same as that for the full-scale slab specimen. The diameter of the tension steel (#5 bars) was 0.625 inches, and the diameter of the compression steel (#4 bars) was 0.5 inches, with similar spacing between the bars as that of the full-scale slab specimen. Two sections, one with the same effective concrete cover as that of an actual bridge and the other with a reduced concrete cover, were designed. These two sections differ only in the depth of the concrete cover, and all the remaining details are identical. The reinforcement details of the reduced-size slab specimens are shown in Figure F.44 and F.45.

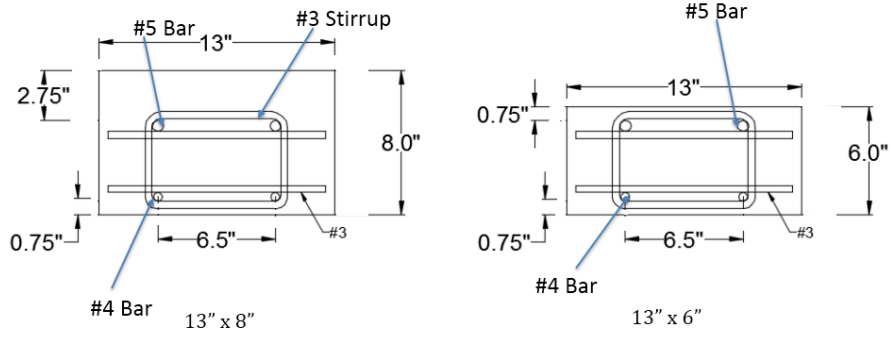


Figure F.44 Schematic of Reduced-Scale Slab Sections

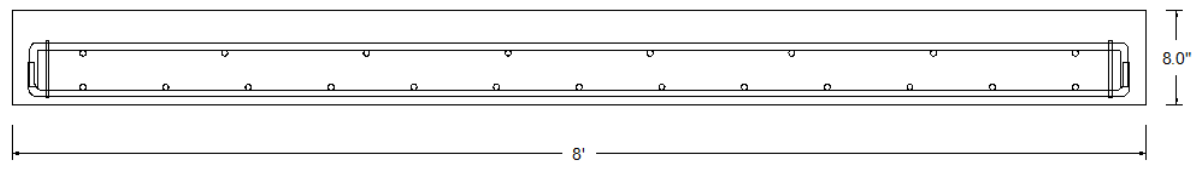


Figure F.45 Longitudinal Section of the Reduced-Scale Slab

F.6.1 Casting of Reduced-Scale Trial Slab Specimens

Two 8-ft.-long slabs—one 13 inches wide by 6 inches deep, and the other 13 inches wide by 8 inches deep—were cast. The formwork was made using 3/4-inch plywood as described in Section F.5.2. The reinforcing cage was constructed with #5 bars on the tension side and #4 bars on the compression side, with lateral ties using #3 bars (Figure F.46). Four strain gages (two on each bar on the tension side) were attached to collect strain measurements during the tests.



Figure F.46 Formwork and Reinforcement for Reduced-Scale Slab Specimens

A similar concrete mix design to that given in Table F.3 was prepared in the laboratory. Strain gages were attached to both the tension steel and the compression steel at a distance of 4

inches from center on either side to collect measurements that helped to establish a clear relationship between the applied load and the strain or stress in the bar during the testing of the slabs. The cast specimens are shown in Figure F.47.



Figure F.47 Casting for Reduced-Scale Trial Slab Specimens

F.6.2 Testing of Reduced-Scale Trial Slab Specimens

After the slabs were cured for a period of 28 days, the reduced-scale slabs were tested in a way that was similar to that for the full-scale specimens. The reduced-scale slabs were loaded using a 30-kip hydraulic jack that was operated using a manual hydraulic pump. The slab was loaded with four-point loading at the mid-span, with load points 8 inches apart. Crack widths and crack spacing were measured manually, deflections were measured using dial gages and were recorded manually. The strains in the bars were monitored and recorded continuously using the data acquisition system. A typical test setup is shown in Figure F.48.

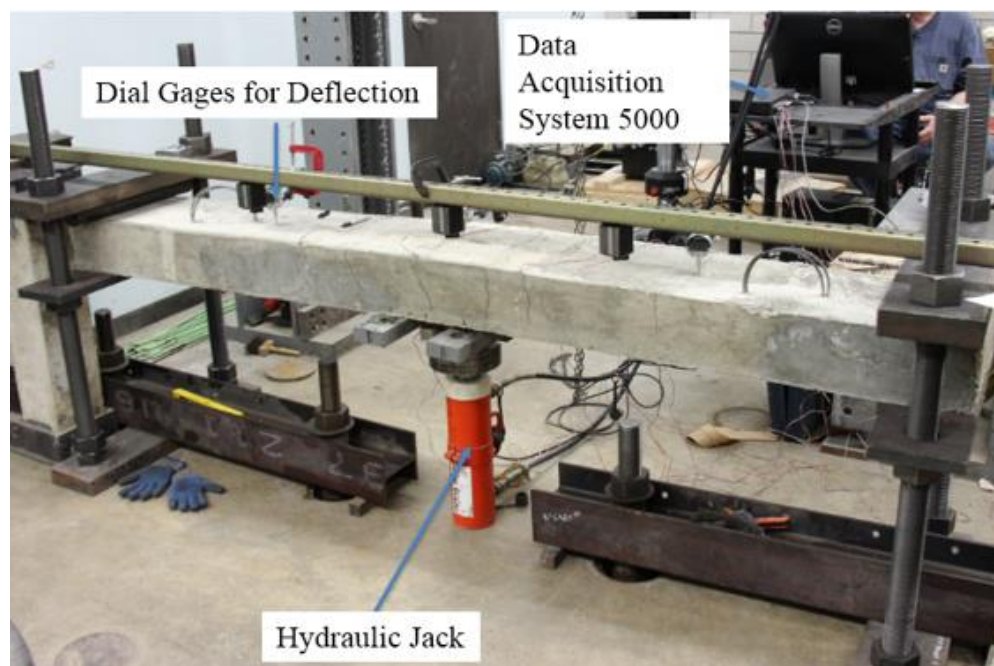


Figure F.48 Typical Test Setup for Trials using Reduced-Scale Slab Specimens

F.6.2.1 Results of Reduced Scale Slab Specimens

From the full-scale and reduced scale testing, it was evident that the reduced-scale slab specimens showed similar cracking at each stress level as the full-scale specimens. To reduce the effort of making test specimens casting, sections were designed with a reduced depth for the slab, while keeping the same effective concrete cover and tension reinforcement ratio. Three specimens were tested: two 13-inch \times 8-inch specimens and one 13-inch \times 6-inch specimen (the details for these specimens were included in Section F.6). Crack widths, applied load, and stress in the bars were the parameters considered. The stress versus crack width for the 13" \times 6" slab and the 13" \times 8" slabs with black bars are shown in Figures F.49 and F.50, respectively. For both slab sizes, the crack widths predicted by Gergely and Lutz (1968) equation underestimated the actual cracks observed in the slabs.

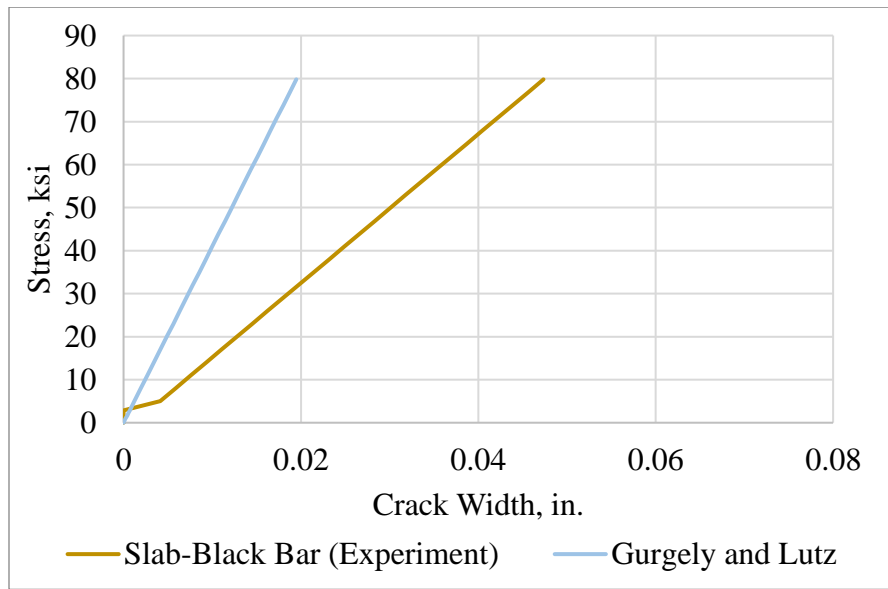


Figure F.49 Stress vs. Crack Width for 13" \times 6" Slab with Black Bar

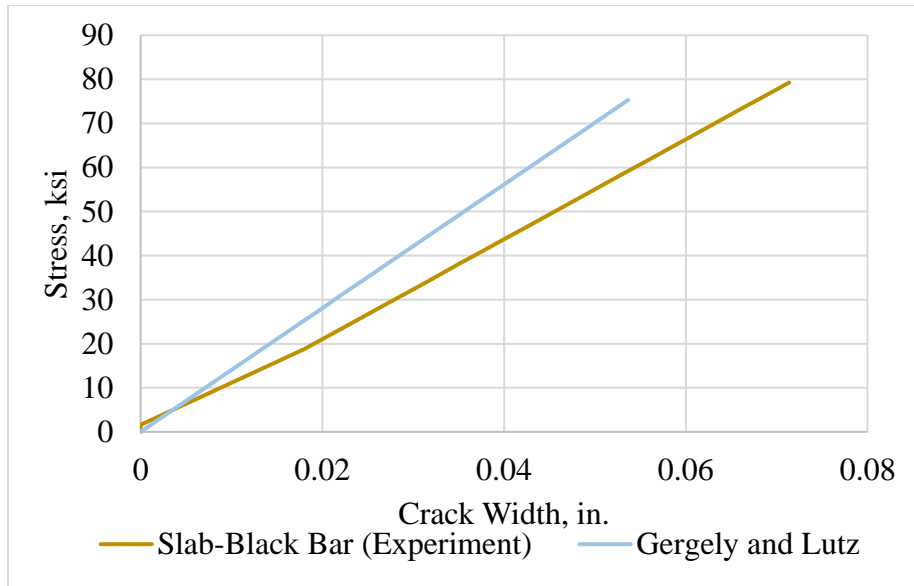


Figure F.50 Stress vs. Crack Width for 13'' x 8'' Slabs with Black Bar

On comparing the crack data from the reduced-scale slab specimens with that of the full-span and half-span specimens (i.e. 13-in. x 19-in. section with 15 ft. spans and the 13-in. x 8-in. with 7.5 ft. span) it was observed that the reduced-scale 13-inch x 8-inch sections showed similar crack widths, whereas 13-inch x 6-inch sections showed smaller crack widths as the effective concrete cover was smaller. A trendlines for stress versus crack widths for 13-in. x 19-in. slabs with black bars and for the reduced-scale sections (i.e., 13-in. x 8-in. and 13-in. x 6-in. were plotted for comparison purposes, as presented in Figure F.51. Figure F.52 shows the failed 13-in. x 8-in. slab specimen and the generated crack pattern.

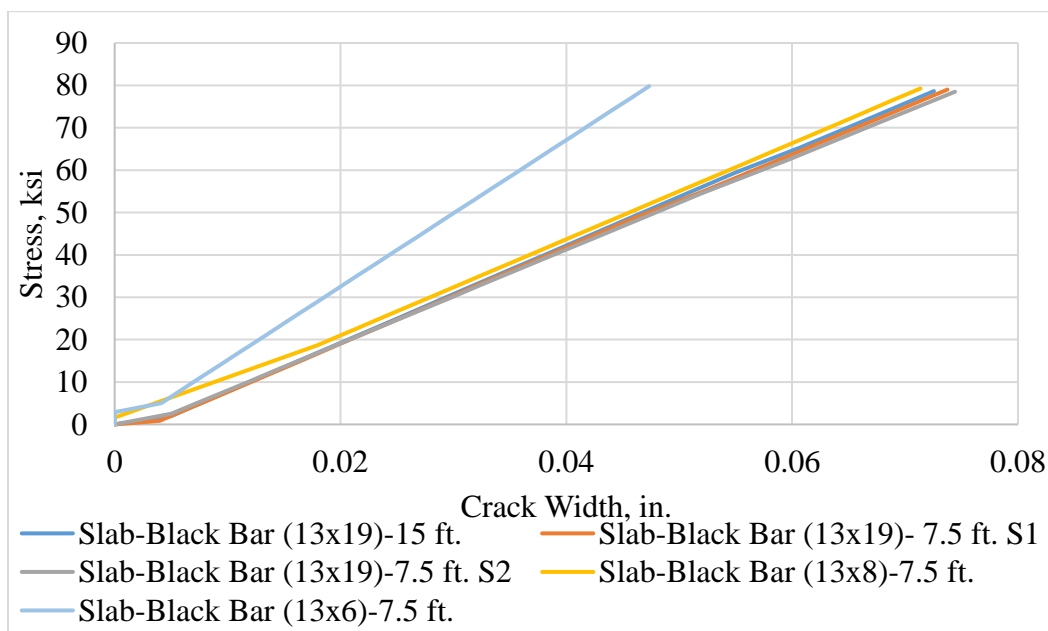


Figure F.51 Stress vs. Crack Width for Full-Scale and Reduced-Scale Slabs with Black Bars

It was observed that, when using the same tension reinforcement ratio and the same effective cover, the crack widths at a given stress level on the reduced-scale slab section were similar to the crack widths on a full-scale slab section. Based on this finding, a 13-in. \times 8-in. section with a span length of 7.5 ft. was chosen for further study of crack widths on slabs with corrosion-resistant reinforcing bars.



Figure F.52 Failed 13" \times 8" Slab Specimen Showing Crack Pattern

F.7 Reduced-Scale Slab Specimens with Different Types of Reinforcement

Based on the results from the trial testing of the 13-inch \times 8-in. slab specimens, it was decided to use this section size for further testing of slabs with different types of reinforcement. The section was slightly modified to 14 in. \times 8 in. to meet current CS-01-08 standards, with all steel details remaining the same and the span length set at 7.5 ft. The sectional details of the slabs with 14-inch \times 8-in. cross section is shown in Figure F.53.

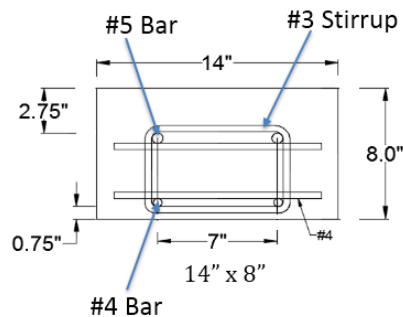


Figure F.53 Sections Details of the 14" \times 8" Slab

Six different reinforcing bar types were used on the tension side of the test slabs, while the compression steel (#4 black bars) were kept the same for all slabs. Slabs with and without fibers were cast, with two slabs for each bar type. A total of 24 slab specimens with and without fibers were cast to test for flexure cracking and 8 slabs with and without fibers were cast for fatigue testing with black and epoxy-coated bars as presented in Table F.10.

Table F.10 Test Matrix for Slabs with Different Reinforcing Types for Flexure and Fatigue Testing

Specimen Type	Black Bar	Epoxy-Coated Bar	Hot-Dip Galvanized Bar	Stainless Steel Bar	Zinc-Galvanized Bar (CGR)	MMFX Bar
Slabs without Fiber	4	4	2	2	2	2
Slabs with Fiber	4	4	2	2	2	2
Total	8	8	4	4	4	4

F.7.1 Preparation of Reduced-Scale Slabs with Different Types of Reinforcement

The tension steel was #5 bar of different types of reinforcement whereas the compression steel was #4 black bar in all specimens. The spacing of the reinforcing bar was 7 inches with #3 stirrups at the ends to hold the steel cage in place. A #4 black bar 13 inches long was used for both top and bottom reinforcement to maintain the spacing between the longitudinal bars. The top lateral bars were placed at 12 inches apart whereas the bottom lateral bars were 7 inches apart. The typical reinforcement cages for black, epoxy-coated and stainless-steel bars are shown in Figure F.54.

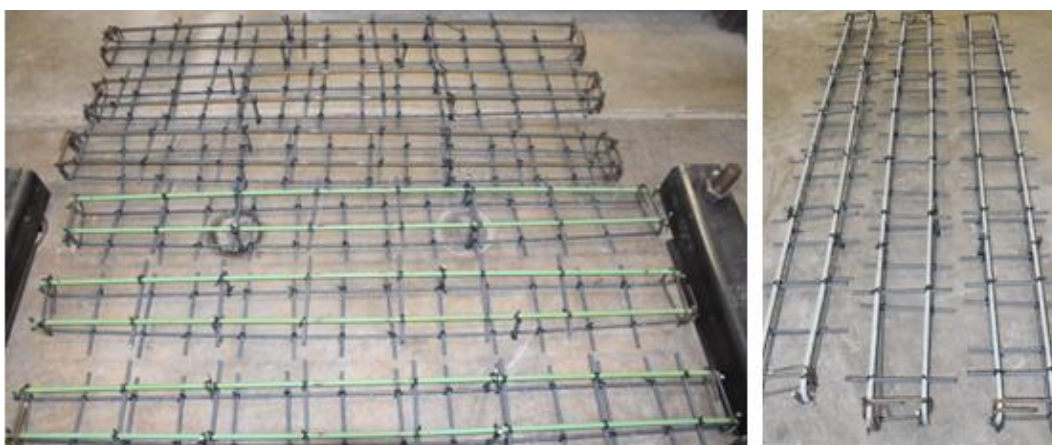


Figure F.54 Typical Reinforcement Cages for Black (*Left, at Top of Image*), Epoxy-Coated (*Left, at Bottom of Image*), and Stainless-Steel Bars (*Right*)

A total of 24 flexure specimens with six reinforcement types and 8 fatigue specimens with black and epoxy-coated bars were cast. Concrete mix design mentioned in Table F.3 was used with slabs without fibers and a 10 lbs/yd³ of polypropylene fibers was added to the concrete to cast

slabs with fibers. The concrete was obtained from concrete plant situated in Akron, Ohio. Formwork was made similar to as mentioned in Section F.6.1, with four strain gages attached on the tension steel (top bars) 4 inches apart from center. A typical formwork setup and of slabs with and without fibers are shown in Figures F.55.



Figure F.55 Formwork Showing Black Bars (*Left*) and Stainless-Steel Bars (*Right*)

F.7.2 Testing of Slabs with and without Fibers for Flexural Cracking

A total of 24 slabs with various reinforcement types with and without fibers were tested for flexure cracking similar to that mentioned in Section F.6.2. Applied load, stress in the bar, crack widths, deflections were monitored and recorded continuously during the testing. Two specimens of each bar type were tested to average the results. The test setup was similar to as shown previously in Figure F.48.

F.7.2.1 Results of Slabs with and without Fibers with Different Types of Reinforcement

Slab specimens designed based on CS-01-08 standards (as mentioned in Section F.7) were tested for flexural cracking. A total of 24 slabs with six reinforcement types, both with and without fibers, were tested. Two specimens of each bar type were tested to obtain average values. Deflections, crack spacing, crack widths, and stresses in the bar for different levels of applied load were the parameters considered in the test. A test setup as described in Section F.6.2 was adopted for the testing of the specimens. Data acquisition was used to capture the strains and applied load during the test, whereas deflections, crack spacing and crack widths were measured manually. The crack widths were averaged from the results of two specimens of each bar type. Figure F.56 shows the stress versus crack widths of slab specimens without fibers, whereas Figure F.57 shows the results for slab specimens with fibers.

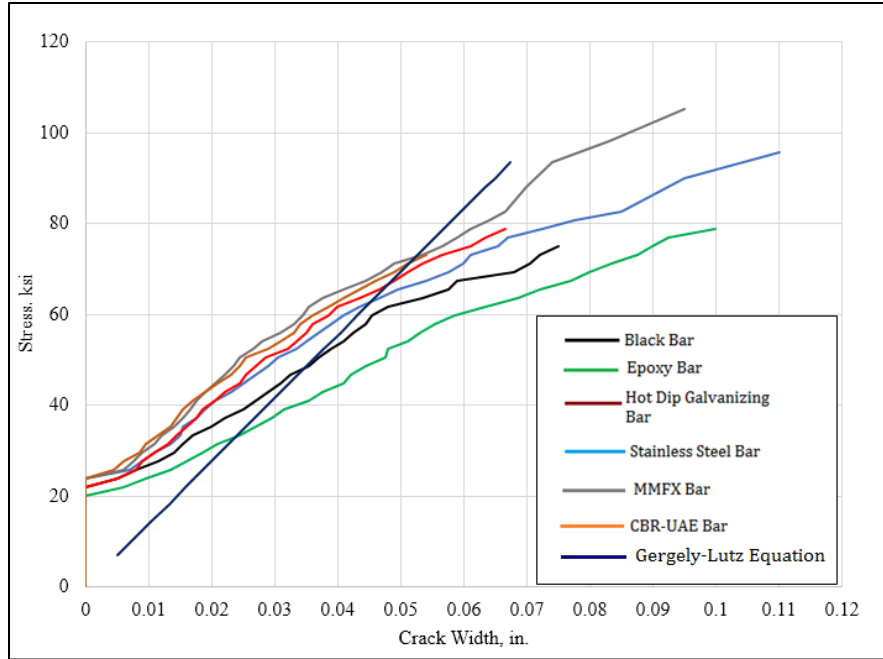


Figure F.56 Stress vs. Crack Widths for Slabs with Different Bar Types (Non-Fiber)

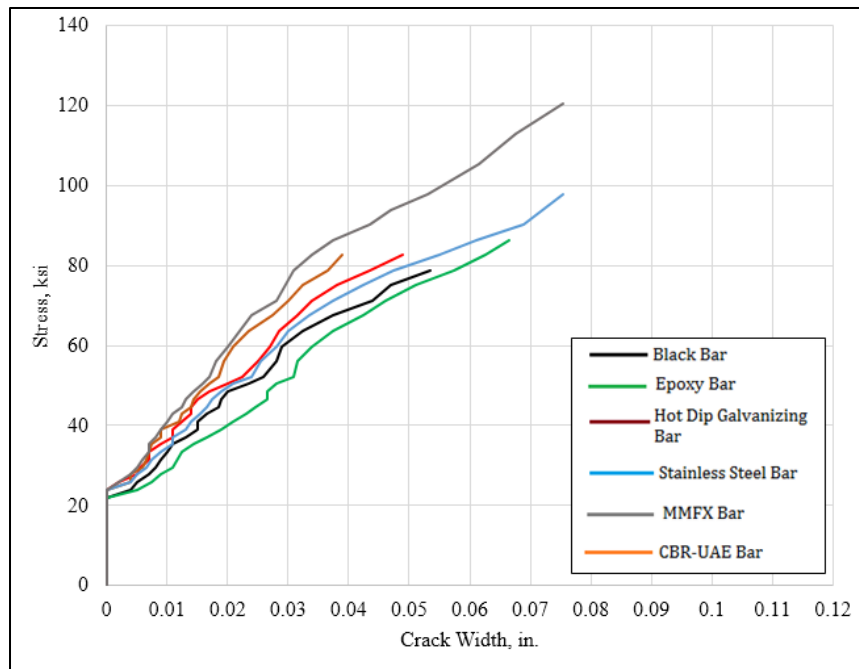


Figure F.57 Stress vs. Crack Widths for Slabs with Different Bar Types (Fiber)

Plots showing stress versus crack widths for specimens with and without fibers individually are shown in Figure F.58.

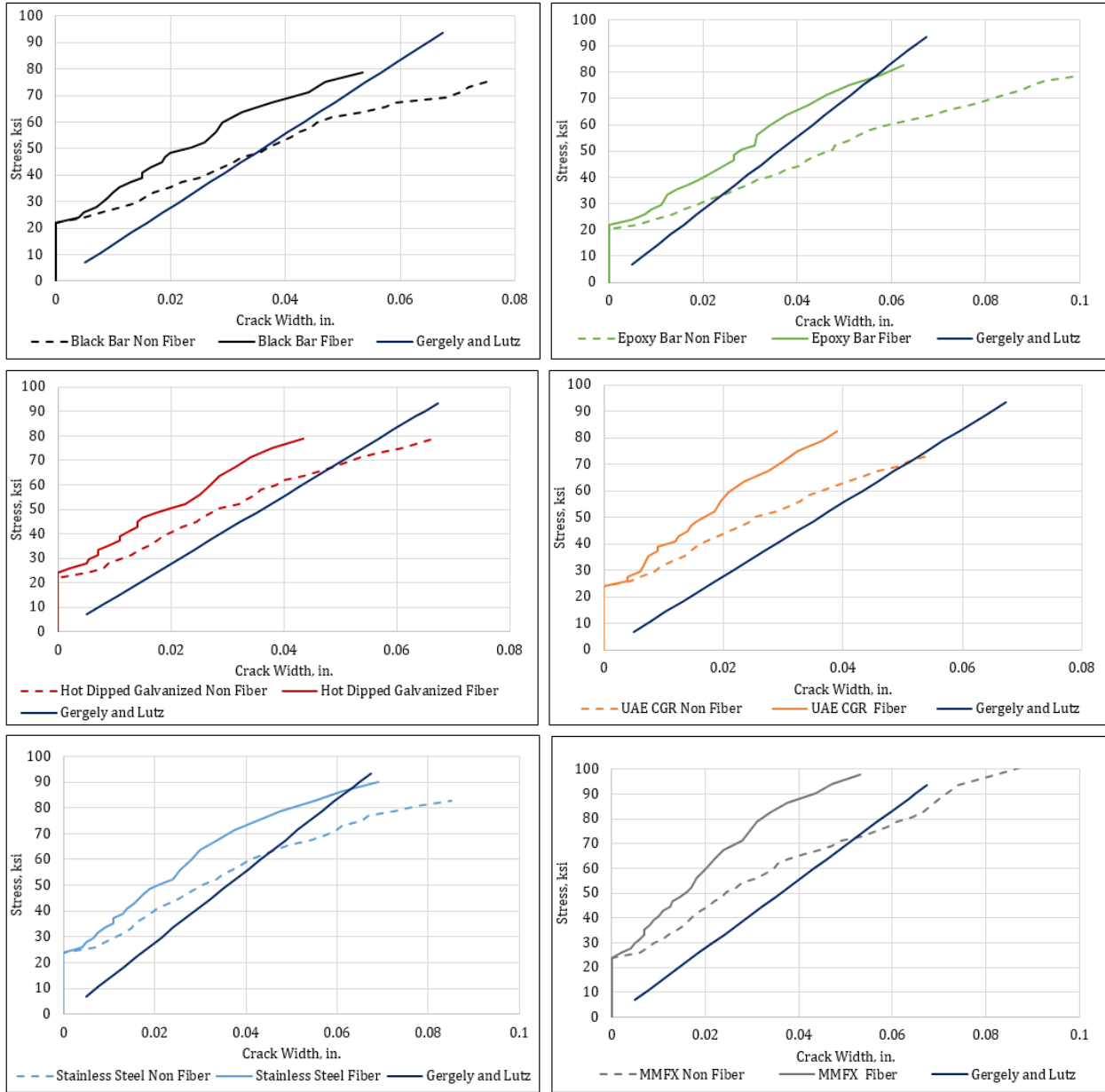


Figure F.58 Plots Showing Stress versus Crack Width of 14"x8" Slabs with and without Fiber

Stress versus crack widths were compared for slabs with black bars, epoxy-coated bars, and zinc-galvanized bars both with and without fibers for clear understanding as shown in Figure F.59.

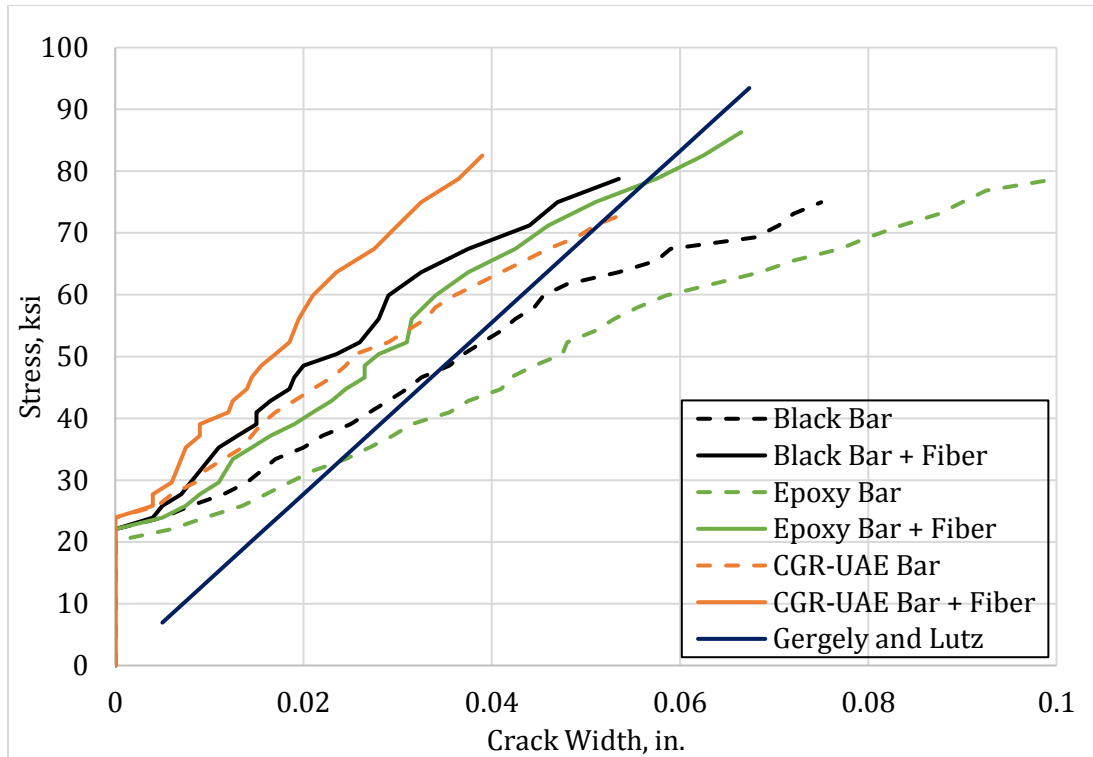


Figure F.59 Comparison of Crack Widths for Slabs with Black Bars, Epoxy-Coated Bars and Zinc-Galvanized Bars

In the case of slabs without fibers, the slabs with epoxy-coated bars showed wider cracks compared to those with other bar types, whereas slabs with MMFX and zinc-galvanized bars showed smaller crack widths. In case of slabs with fibers, a similar trend was observed, with much closer values for most bar types and crack widths that were minimized by 35 to 48% by using polypropylene fibers. The crack widths observed for slabs with and without fibers are compared at 40 ksi stress and are presented in Table F.11.

Table F.11 Percentage Reduction in Crack Widths on Slabs with Fibers at 40 ksi

Serial No.	Bar Type	Crack Width of Non-Fiber Slab	Crack Width of Slab with Fiber	% Reduction in Crack Width
1	Black	0.027	0.015	44.4%
2	Epoxy-Coated	0.035	0.020	42.8 %
3	Hot-Dip	0.0205	0.012	41.4 %
4	CGR-UAE	0.0155	0.01	35.5 %
5	Stainless Steel	0.0205	0.013	36.6 %
6	MMFX	0.017	0.009	47 %

The load versus deflection plots were compared for all the slabs with and without fibers to determine for difference in deflections. Figure F.60 and Figure F.61 shows plots of load versus

deflection for slabs without and with fibers, respectively. The curves were compared with the theoretical mid-span deflection and was found to be in line with the experiment data. All curves seem closer to each other and not much difference was observed between the deflections of slabs with different bar type. In the case of slabs with fibers, the slabs with MMFX and zinc-galvanized bar types showed smaller deflections compared to other bar types. The failed slab specimens are shown in Figure F.62.

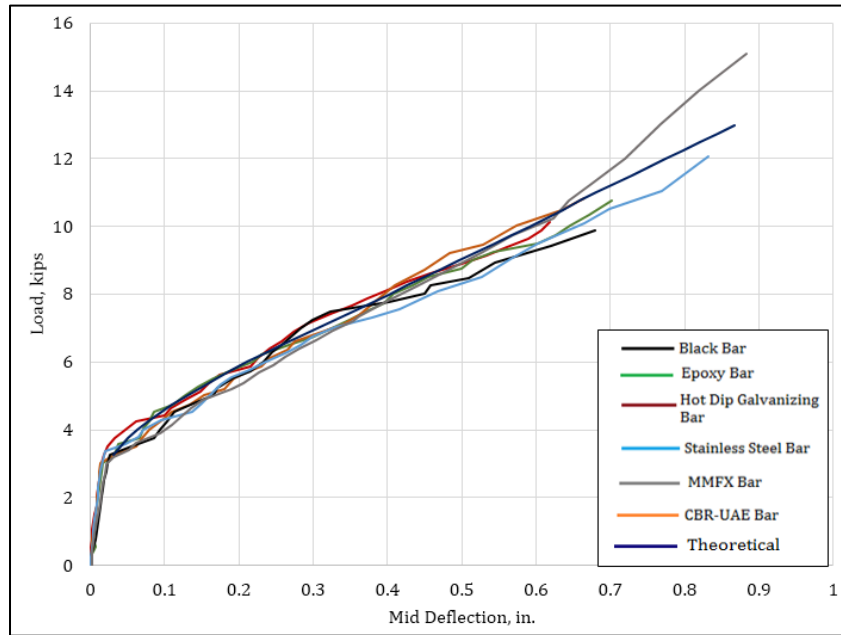


Figure F.60 Load vs. Deflection Curves for Slabs without Fibers

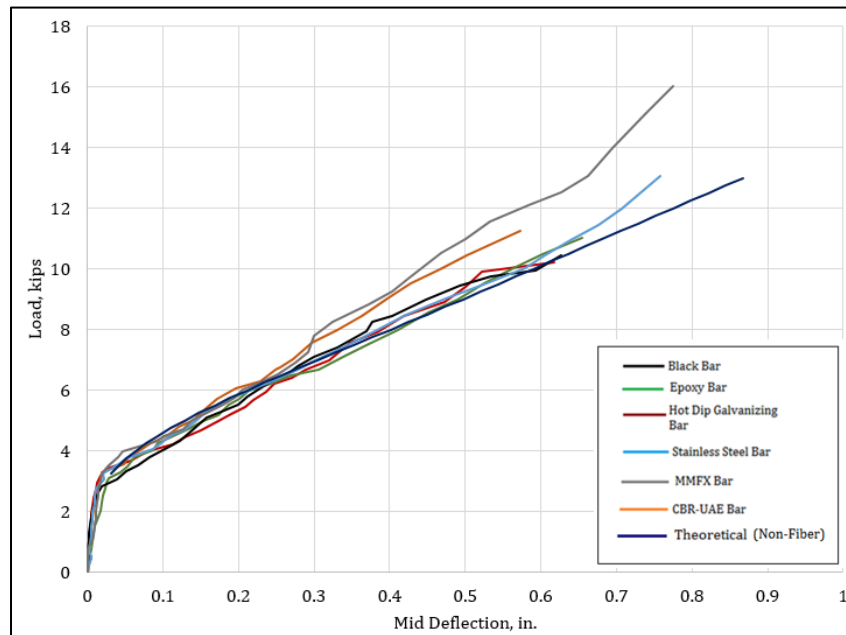


Figure F.61 Load vs. Deflection Curves for Slabs with Fibers



Figure F.62 Tested Slab Specimens

F.7.3 Testing of Slabs with and without Fibers for Crack Widening Due to Fatigue

Reduced scale slabs with details presented in Figure F.53, were tested to understand the crack widening due to cyclic loading caused due to moving traffic on bridges. Slabs with epoxy-coated bars with and without fibers were tested. The slabs were tested with tension side facing down and the four-point load applied on the compression face using of a 22-kip actuator. MTS machine was used to apply the fatigue load with 2 Hz (cycles per second) frequency with a minimum load of 1850 lbs and maximum load of 5250 lbs. Two linear variable displacement transducers (LVDTs) with 1-inch travel were used to measure the deflection of the slab at the mid-span and two LVDTs with 0.25-inch travel were glued to the concrete surface on the tension side near the crack to measure the crack opening and closing during the fatigue loading as shown in Figure F.64. The load limit was determined to maintain the stresses in the slab close to that of the service load stresses in the actual bridge. The loading was limited to a total of 2 million cycles due to time limit to perform all the tests. The strain gage measurement, crack widening, and deflections were continuously recorded using StrainSmart software. A typical test setup of slab subjected to dynamic loading is shown in Figure F.63.



Figure F.63 Fatigue Loading on a Slab to Monitor Crack Widening



Figure F.64 Slab Showing LVDTs to Measure Deflection (*Left*) and Crack Width (*Right*)

F.7.3.1 Results on Crack Widening Due to Cyclic Loading

Four slabs (two slabs with epoxy-coated bars without fibers and two slabs with epoxy-coated bars and fibers) with sectional details the same as those used for flexure cracking were tested for crack widening due to cyclic fatigue loading. The test setup was designed in such a way that the applied load, mid-span deflections, crack widths, and strains were continuously recorded using a data acquisition system. The frequency of loading was set to 2 Hz after initial trials. The peak maximum and minimum loads were set to cause stresses in the slab similar to that in the actual bridge deck over the negative moment region. The load was applied downward, causing cracks at the bottom side of the slab. The StrainSmart software was set to record deflections, crack widths, and strains at 3-hour intervals. The specimens were subjected to a total of 2 million cycles

over a period of 14 days. Plots showing an average increase in crack widths and also an average increase in deflections with time are presented in Figure F.65 and Figure F.66 for two specimens of each bar type and slabs without and with fibers, respectively.

In the case of slabs without fibers, the cracks grew at an increasing rate, whereas in case of slabs with fibers, the cracks grew at slower rate until 150 hours and then the curve was more flattened. A similar trend was observed in the case of deflections at the mid-span. The percentage increase in crack growth and the deflection from initial stage to final was calculated, and a summary of the percentage increase is provided in Table F.12.

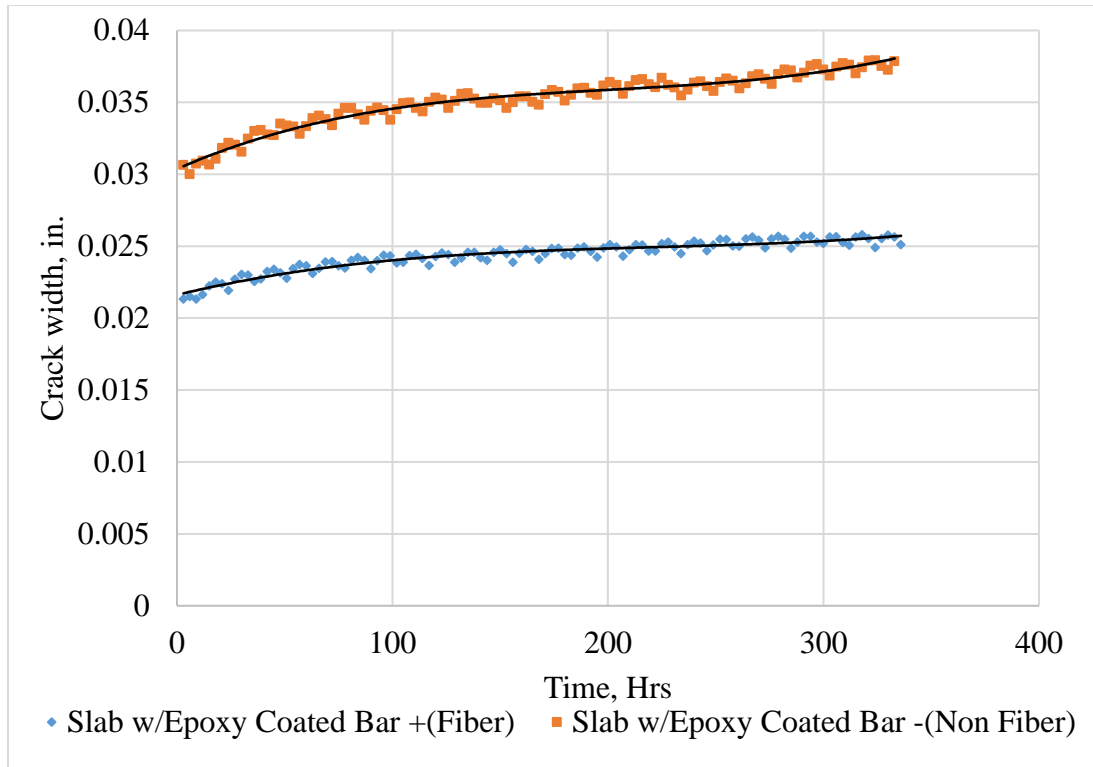


Figure F.65 Average Increase in Crack Width for Slabs with and without Fibers over Time

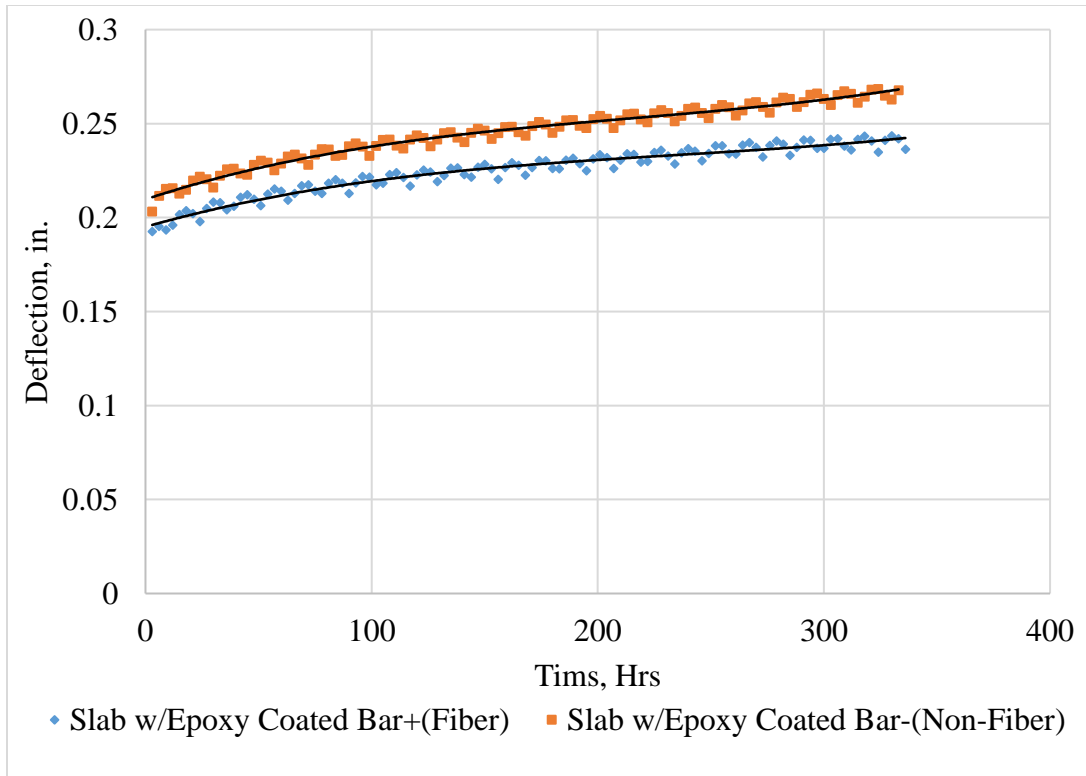


Figure F.66 Average Increase in Deflection for Slabs with and without Fiber over Time

Table F.12 Percentage Increase in Crack growth and Deflection over Time

Specimen Type	Initial Crack Width	Final Crack Width	Initial Deflection	Final Deflection	% Increase in Crack Width	% Increase in Deflection
Slab with Epoxy-Coated Bars (Non-Fiber)	0.0307	0.0378	0.213	0.263	23	23.4
Slabs with Epoxy-Coated Bars + Fiber	0.0224	0.0253	0.205	0.238	13	16

F.8 Summary and Conclusions

An extensive and elaborate experimental program was designed to develop insight into the factors that cause structural cracking in bridge decks and to reduce cracking with the use of alternative materials such as various corrosion-resistant bars as well as the incorporation of polypropylene fibers in concrete. The tests included direct tension tests on prism specimens (Figure F.21), flexural testing of full-scale and reduced-scale slab specimens, fatigue tests on slabs to study crack widening, pullout tests to understand the bond behavior of reinforcing bar with concrete, and tests on the connection between typical slab and pier caps. The reinforcing bars validated in the experimental program were black steel bars (control), epoxy-coated bars (ECB), grade 2304 stainless steel bars, MMFX corrosion-resistant alloy steel bars, hot-dipped galvanized bars, and zinc galvanized bars (CGR). As very little research has been performed on the use of corrosion-resistant bars as a means for reducing cracks on bridge decks, various experiments were designed to gain insight specifically into the effects of each reinforcement type on bridge deck cracking.

The prism specimens showed that the crack widths on specimens with epoxy-coated bars were wider compared to the specimens with other types of bars, whereas specimens with MMFX and CGR bars showed smaller crack widths. A similar trend was observed in specimens with fibers; crack widths were reduced by about 25% for specimens with fibers compared to the corresponding specimens without fibers.

Two slabs that were 16 ft. in length, 13 inches wide to accommodate two #9 bars at a spacing of 6.5", and 19 inches deep were cast as full-scale specimens to replicate the negative moment region of a typical bridge deck between the inflection points. These specimens were detailed to have the same reinforcement as needed for a typical three-span bridge with spans of 30 ft. – 37.5 ft. – 30 ft. The specimens were 16 ft. in length, which is the distance between the points of inflections of the actual bridge moment diagram. One specimen was cast with uncoated black bars and the other was cast with epoxy-coated bars. Four additional specimens (two with uncoated reinforcement and two with epoxy-coated reinforcement) were also cast with the same reinforcement and section details but using only half the span length (i.e. 8 ft). All specimens were cast using the same mix design (Class QC2 concrete mix) to understand the cracking behavior for the full-span and half-span slab specimens and the scaling effects. Load was applied using a manually operated hydraulic jack (Figure F.48), and the strains and applied loads were recorded continuously. The deflections at the mid-span and the quarter-span were recorded. Crack data such as crack widths, crack patterns, and crack spacing were also collected during the testing.

The crack widths measured on both the types of slabs with a 15 ft. span and a 7.5-ft. span were mostly similar at the same steel stress level for the same bar type as long as the steel reinforcement ratio and the concrete cover were the same.

After establishing the lack of scaling effect on smaller slabs, a total of 24 slabs with six reinforcement types, both with and without fibers, were tested. Two specimens of each bar type were tested to obtain average values. Deflections, crack spacing, crack widths, and stresses in the bars for different levels of applied load were the parameters considered in the test. A test setup as

shown in Figure F.48 was adopted for the testing of these slabs. Data acquisition was used to capture the strains and applied load during the test, whereas deflections, crack spacing and crack widths were measured manually. The crack widths were averaged from the results of two specimens of each bar type. Figure F.59 shows the stress versus crack widths of slab specimens without and with fibers. In the case of slabs without fibers, the slabs with epoxy-coated bars showed wider cracks compared to those with other bar types, whereas slabs with MMFX and CGR showed smaller crack widths. In case of slabs with fibers, a similar trend was observed, with much smaller crack widths for most bar types with about 35 to 48% reduction due to the use of polypropylene fibers.

Four slabs with epoxy-coated bars with and without fibers were also tested under fatigue loading at 2 Hz (cycles per second) frequency for 2 million cycles. The load was cycled through a minimum that corresponds to the permanent dead load on a typical bridge and a maximum that corresponds to the bridge live load. Plots showing an average increase in crack widths and also an average increase in deflections with time are presented in Figures F.65 and F.66 for two specimens of each bar type and slabs without and with fibers, respectively. In the case of slabs without fibers, the cracks grew at an increasing rate, whereas in case of slabs with fibers, the cracks grew at slower rate. A similar trend was observed in the case of deflections at the mid-span. These figures demonstrate that the crack widths and deflections increase with fatigue loading over time, and also that the rate of such increase of crack widths can be reduced by a factor of about 1.5 with the addition of fiber.

F.9 Sample Calculations

F.9.1 Flexural Crack Width Calculations for Slabs

In this section, the cracking load, moment capacity, average crack spacing and maximum crack width are calculated for Slab U.

F.9.1.1 Section Properties for a Typical Slab

All slabs were loaded from the bottom, and the top of the slab was in tension. Figure A.1 Shows the cross section and longitudinal and section of a typical slab. The two loading points were 8 inches apart.

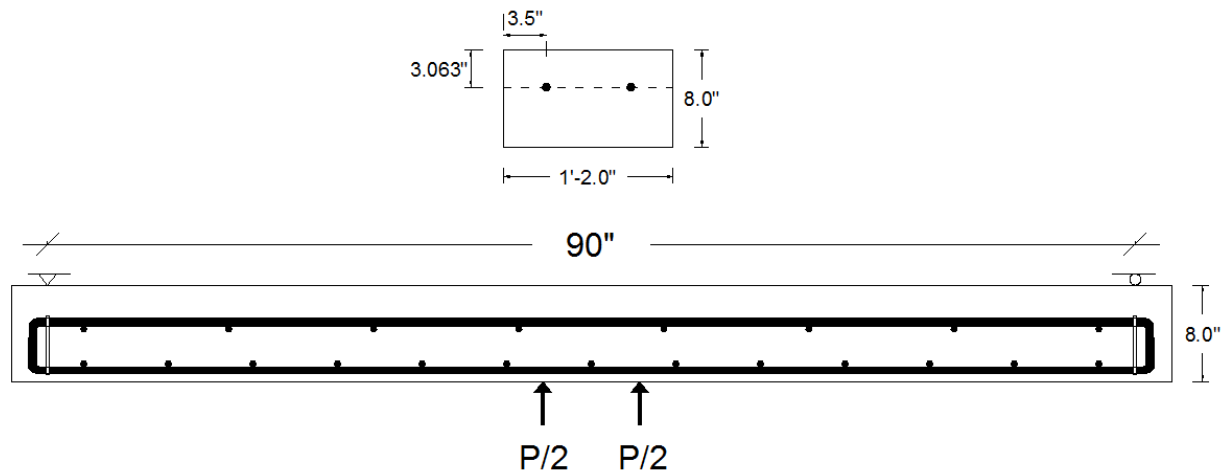


Figure F.67 Longitudinal and Cross (only top bars shown) Section of Typical Slab

Section properties of a typical slab:

Cross-section area, $A = 112 \text{ in.}^2$

Effective span = 7.5 ft.

Distance from load to support, $a = 41 \text{ in.}$

Distance between the two loading points, $z = 8 \text{ in.}$

Concrete compressive strength on day of test, $f'_c = 4500 \text{ psi}$

Specified tensile strength of steel reinforcement, $f_y = 75 \text{ ksi}$

Width, $b = 14 \text{ in.}$

Effective depth, $d = 4.937 \text{ in.}$

Overall depth, $h = 8 \text{ in.}$

Area of steel for 2 Nos. of #6 bars, $A_s = 0.62 \text{ in.}^2$

F.9.1.2 Cracking and Yielding and Ultimate Load Calculations for Slabs

Modulus of rupture, $f_r = 7.5\sqrt{f'_c} = 7.5 \times \sqrt{4500} = 503.11 \text{ psi}$

Moment of inertia of gross area, $I_g = \frac{bh^3}{12} = \frac{14 \times 8^3}{12} = 597.33 \text{ in.}^4$

Distance from the section centroid to the extreme tension fiber, $y_t = \frac{h}{2} = \frac{8}{2} = 4$ in.

Cracking Moment, $M_{cr} = \frac{f_r I_g}{y_t}$

$$M_{cr} = \frac{503.11 \times 597.33}{4} = 75.13 \text{ kip-in.} = 6.26 \text{ kip-ft.}$$

Cracking load, $P_{cr} = \frac{2M_{cr}}{a} = 3.66 \text{ kip}$

After Cracking

Modulus of elasticity of concrete, $E_c = 57000\sqrt{f'_c} = 57000 \times \sqrt{4500} = 3823676.2 \text{ psi}$

Section curvature at cracking, $\phi_{cr} = \frac{M_{cr}}{E_c I_g} = \frac{75.13}{3823.67 \times 597.33} = 0.00003289/\text{in.}$

Strain in Concrete, $\epsilon_{cr} = \frac{f_r}{E_c} = \frac{503.11}{3823676.2} = 0.0001316$

Using $c = \frac{\epsilon_{cr}}{\phi_{cr}} = \frac{0.0001316}{0.00003289} = 4.0012 \text{ in.}$

From strain compatibility, strain in steel, $\epsilon_s = \epsilon_{cr} \times \left(\frac{d-c}{c}\right) = 0.0001316 \times \left(\frac{4.937-4.0012}{8-4.0012}\right)$
 $= 0.0000308$

At Yielding

Strain in steel, $\epsilon_s = \epsilon_y = \frac{f_y}{E_s} = \frac{75}{29000} = 0.002586 \text{ in./in.}$

Using strain compatibility, $\frac{\epsilon_c}{c} = \frac{\epsilon_y}{d-c}$

Rearranging, $c = \frac{d\epsilon_c}{\epsilon_y + \epsilon_c} = \frac{4.937\epsilon_c}{0.002586 + \epsilon_c}$

Assuming a linear stress – strain relationship before yield

Compression Force in Concrete, $C = \frac{1}{2} f_c b c$

Where, $f_c =$ compressive stress in concrete $= \epsilon_c E_c$

Therefore, $C = \frac{1}{2} f_c b c = \frac{1}{2} \epsilon_c E_c b c = 0.5 \times \epsilon_c \times 3283.676 \times 14 \times c = 22985.732 c \epsilon_c$

Tension in Top Steel Reinforcement, $T = A_s f_y = 0.62 \times 75 = 46.5 \text{ kips}$

Assuming equilibrium, Tension force = Compressive force

$$46.5 = 22985.732c\varepsilon_c$$

Determining c and ε_c by solving Eqn. A1 and Eqn. A2 simultaneously, gives

Strain in concrete, $\varepsilon_c = 0.000937$ in./in.

Depth to neutral axis, $c = 2.16$ in.

Moment at Yield, $M_y = A_s f_y \left(d - \frac{c}{3} \right) = 0.62 \times 75 \times \left(4.937 - \frac{2.16}{3} \right) = 196.10$ kip-in.

Load at Yield, $P_y = \frac{2M_y}{a} = \frac{2 \times 196.10}{41} = 9.56$ kip

Ultimate Load

Assuming concrete crushing strain, $\varepsilon = 0.003$

Concrete strain at peak compressive stress, $\varepsilon_0 = 0.002$

Compression in concrete, $C = \alpha f'_c b c$

Using parabolic stress strain curve of concrete

$$\begin{aligned} \text{The stress intensity coefficient, } \alpha &= \frac{\varepsilon_0}{\varepsilon} \left[\ln \left[\left(\frac{\varepsilon}{\varepsilon_0} \right)^2 + 1 \right] \right] = \frac{0.002}{0.003} \left[\ln \left[\left(\frac{0.002}{0.003} \right)^2 + 1 \right] \right] \\ &= 0.7858 \end{aligned}$$

Assumed depth of neutral axis, $c = 0.94$ in. (determined from trial and error using excel program)

Therefore, $C = 0.7858 \times 4.5 \times 14 \times 0.94 = 46.53$ kip

Steel strain, $\varepsilon_s = \varepsilon_c \times \left(\frac{d-c}{c} \right) = 0.003 \times \left(\frac{4.937-0.94}{0.94} \right) = 0.01275$ in./in $> \varepsilon_y = 0.002207$ in./in.

Therefore, use $f_s = f_y = 75$ ksi

Tension in Steel, $T = A_s \times f_s = 0.62 \times 75 = 46.5$ kip

Therefore, equilibrium has been established, $C = T = 46.5$ kip

Location of resultant coefficient, β

$$\beta = 1 - \frac{2 \left[1 - \frac{\varepsilon_0}{\varepsilon} \right] \tan^{-1} \left(\frac{\varepsilon}{\varepsilon_0} \right)}{\ln \left[\left(\frac{\varepsilon}{\varepsilon_0} \right)^2 + 1 \right]} = 1 - \frac{2 \left[1 - \frac{0.002}{0.003} \right] \tan^{-1} \left(\frac{0.003}{0.002} \right)}{\ln \left[\left(\frac{0.003}{0.002} \right)^2 + 1 \right]} = 0.4149$$

Ultimate Moment Capacity, $M_u = T(d - \beta c) = 46.5 \times (4.937 - 0.4149 \times 0.94) = 211.44 \text{ kip-in.}$
 $= 17.62 \text{ kip-ft.}$

Ultimate Load, $P_u = \frac{2M_u}{a} = \frac{2 \times 211.44}{41} = 10.3 \text{ kip}$

F.9.2 Calculation of Deflection for Slabs Using Moment Curvature Relation

Mid-span deflection was calculated from bending moment and radius of curvature relation

$$\frac{1}{R} = \frac{M}{EI}; \quad \frac{1}{R} = \frac{d^2x}{dy^2}; \quad M = EI \frac{d^2x}{dy^2}$$

Where,

M is the bending moment; I is the second moment of area about the centroid; E is the modulus of elasticity; dy/dx is the slope, y represents deflection, R is the radius of curvature, and EI is the flexural stiffness.

Figure A.2 shows the details of the loading of a slab from the bottom

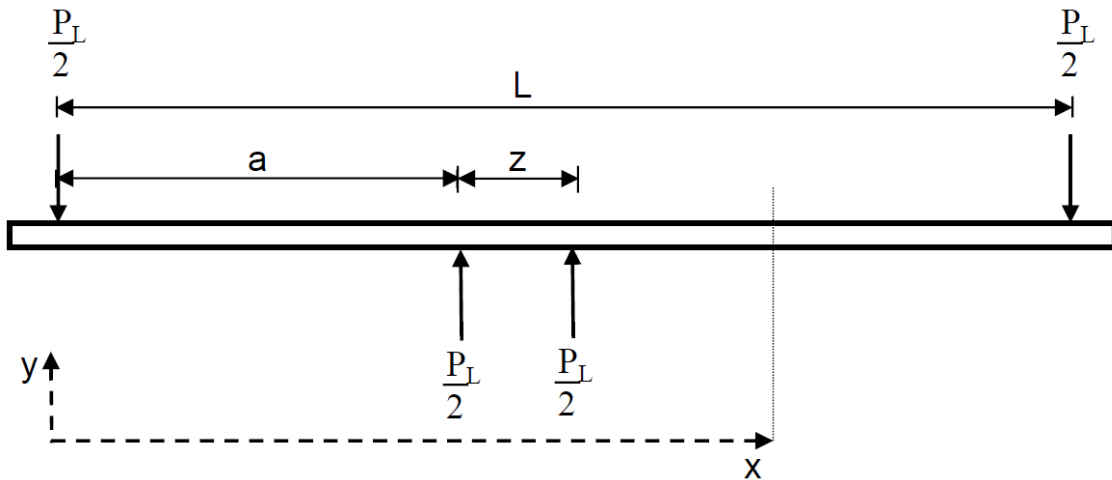


Figure F.68 Loading of Slab from the Bottom

$P_L/2 = 5 \text{ kip}; a = 41 \text{ in.}; Z = 8 \text{ in.}$

The bending moment at position X including the midspan section is given by:

$$EI \frac{d^2y}{dx^2} = 5(x - 41) + 5(x - 45) - 5x = 5x - 430$$

Integrate with respect to x once; $EI \frac{dy}{dx} = \frac{5x^2}{2} - 430x + A$ [B.1]

$$\text{Integrate with respect to } x \text{ again; } EIy = \frac{5x^3}{6} - 215x^2 + Ax + B \quad [\text{B.2}]$$

A and B are constants of integration and must be found from the boundary conditions.

These are at $x = 0, y = 0$ (no deflection at left support point)

at $x = 90, y = 0$ (no deflection at right support point)

putting $x = 0$ and $y = 0$ in Eqn. B.2 results in $B = 0$

Substitute $B = 0, x = 90,$ and $y = 0$ in Eqn. B.2 and we get $A = 6930$

Substitute $A = 12600$ and $B = 0$ into Eqn. B.2 and the complete equation is

$$EIy = 0.833x^3 - 215x^2 + 12600x \quad [\text{B.3}]$$

Substitute $x = 45$ in Eqn. A.3 and solving for y gives the midspan deflection

$$EI = EI_e = 3823.67 \times 104.83 = 400835.326$$

$$\text{Midspan deflection, } y = \frac{0.833(45)^3 - 215(45)^2 + 12600(45)}{400835.326} = 0.52 \text{ inches}$$

F.9.3 Calculation of Deflection for Slabs Using Elastic Equation

The slab deflection was calculated based on elastic principles of mechanics.

Moment capacity of slab, $M_N = 17 \text{ kip-ft.} = 204 \text{ kip-in.}$

Since loading was applied to the bottom of the slabs

$$M_N = M_L - M_D$$

$$M_D = \text{Dead load moment} = 10.46 \text{ kip-in.}$$

$$M_L = \text{Live load moment} = M_N + M_D = 204 - 10.46 = 193.54 \text{ kip-in.}$$

$$M_L = \frac{P_L a}{2}$$

$$\text{Applied load, } P_L = \frac{2M_L}{a} = \frac{2 \times 193.54}{41} = 9.44 \text{ kip}$$

Cracked moment of inertia was determined using the transformed section

$$I_{cr} = bk^2jd^3/2$$

Where

kd = distance from the bottom of the slab to the neutral axis

jd = moment arm for the equivalent compression and tension forces

$$\text{Top reinforcement ratio, } \rho = \frac{A_S}{bd} = \frac{0.62}{14 \times 4.937} = 0.00897$$

Modular ratio, $n = 7.584$

$$k = \sqrt{(\rho n)^2 + 2\rho n} - \rho n = \sqrt{(0.00897)^2 + 2 \times 0.00897 \times 7.584} - (0.00897 \times 7.584)$$

$$k = 0.3009$$

$$j = 1 - k / 3 = 1 - 0.3009/3 = 0.8996$$

$$I_{cr} = 14 \times (0.3009)^2 \times (0.8996) \times \frac{(4.937)^3}{2} = 68.60 \text{ in}^4$$

$$\text{Effective moment of inertia, } I_e = \left\{ \left(\frac{M_{cr}}{M_a} \right)^3 I_g + \left[1 - \left(\frac{M_{cr}}{M_a} \right)^3 \right] I_{cr} \right\} \leq I_g$$

Where

$$\text{Gross moment of inertia, } I_g = 597.33 \text{ in}^4$$

$$\text{Maximum applied moment, } M_a = 193.54 \text{ kip-in.}$$

$$I_e = \left\{ \left(\frac{79.2}{193.54} \right)^3 597.33 + \left[1 - \left(\frac{79.2}{193.54} \right)^3 \right] 68.60 \right\} = 104.83 \text{ in}^4 \leq I_g$$

Deflection at midspan is given by,

$$\Delta = \frac{wa}{24EI_e} (3l^2 - 4a^2)$$

Where $E = 3823.67$ ksi, effective span, $l = 7.5$ ft. = 90 in.

Applied load, $w = P_L/2$

$$\Delta = \frac{\frac{9.44}{2}(41)}{24(3823.67)(104.83)} [3(90)^2 - 4(41)^2] = 0.35 \text{ in.}$$

F.9.4 Direct Tension Crack Width Calculations for Prisms

ACI 224.2R-92 and Rizkalla and Hwang (1993) equations were used to determine cracking load and maximum crack widths of the prisms.

Section and material properties of UB-#5 prism

#3 rebar area $A_s = 0.11 \text{ in}^2$

Gross concrete area of UB-#5 prism, $A_g = 3.41 \times 3.91 = 13.33 \text{ in}^2$

Concrete compressive strength on day of test $f_c' = 4800$ psi

Tensile strength of steel reinforcement, $f_y = 75$ ksi

Modulus of elasticity of concrete, $E_c = 57000\sqrt{f_c'} = 57000 \times \sqrt{4800} = 3949075.84$ psi

Modulus of elasticity of steel, $E_s = 29,000$ ksi

Modular ratio, $n = E_s/E_c = 7.34$

Effective concrete cover, $t_e = 1.7$ in.

Tensile strength of concrete (from Rizkalla & Hwang, 1993),

$$f'_t = (f'_c)^{2/3} = (4800)^{2/3} = 284.55 \text{ psi}$$

$$\text{Reinforcement ratio for prism, } \rho = \frac{A_s}{A_g} = \frac{0.31}{13.33} = 0.0233$$

F.9.4.1 Calculation of Cracking Load for Specimen using ACI-224.2R-92

The cracking load of a prism is given by

$$P_{cr}(1 - \rho + n\rho)A_g f'_t = (1 - 0.0233 + 7.34 \times 0.0233) \times (13.33 \times 284.55) = 4.3 \text{ kip}$$

B2.2: Calculation of Cracking Load for Specimen by Rizkalla and Hwang (1983)

The cracking load of a prism is given by

$$P_{cr} = (1 + n\rho)A_c f_{cr}$$

Where:

$$A_c = A_g = 13.33 \text{ in}^2; f_{cr} = f'_t = 284.55 \text{ psi}$$

$$P_{cr}(1 + n\rho)A_c f_{cr} = (1 + (7.34 \times 0.0233)) \times 13.33 \times 284.55 = 4.43 \text{ kip}$$

Reduction of Bridge Deck Cracking through Alternative Material Usage

APPENDIX G EFFECT OF SLAB-PIER CAP CONNECTION

Prepared by:
Anil Patnaik, Ph.D.
Abdullah Alzlfawi
and
Srikanth Marchetty

Prepared for:
The Ohio Department of Transportation,
Office of Statewide Planning & Research

State Job Number 135260
November 2017
Draft Final Report



TABLE OF CONTENTS

TABLE OF CONTENTS.....	1
LIST OF FIGURES	2
LIST OF TABLES.....	3
APPENDIX G.....	4
EFFECT OF SLAB-PIER CAP CONNECTION.....	4
G.1 INTRODUCTION	4
G.2 BACKGROUND REGARDING THE STRUCTURAL MODELING	4
<i>G.2.1 Spine Model</i>	4
<i>G.2.2 Grillage Models</i>	5
G.3 STRUCTURAL ANALYSIS OF ODOT BRIDGE DAR-118-8.49	5
<i>G.3.1 Modeling of Bridge DAR-118-8.49</i>	6
G.3.1.1 Assignment of Restraints and Materials	6
G.3.1.2 Load Cases	7
G.3.1.3 Dynamic Load Allowance	8
G.3.1.4 HL-93 Load Combinations	9
G.3.1.5 Analysis of Bridge DAR-118-8.49	10
G.4 BRIDGES WITH STANDARD SPANS FROM THE ODOT BRIDGE INVENTORY	11
G.5 EFFECT OF CONNECTION TYPE ON MOMENT VALUES	15
G.6 EXPERIMENTAL TESTING OF SLABS WITH DIFFERENT CONNECTION TYPES.....	17
<i>G.6.1 Preparation of Test Specimens</i>	18
<i>G.6.2 Test Setup</i>	20
<i>G.6.3 Test Results on Connection Type</i>	21
G.7 SUMMARY AND CONCLUSIONS	23
REFERENCES	24

LIST OF FIGURES

Figure G.1: Sectional view of the Box Girder with Truck Load on the Exterior Girder (Vaziri, 2016)	5
Figure G.2 Superstructure model: (a) Real structure scheme, (b) Spine model, (c) Grillage model (Pipinato, 2016).....	6
Figure G.3 Bridge DAR-118-8.49 Frame Model in SAP2000	7
Figure G.4 Load Due to Future Wearing Surface	7
Figure G.5 AASHTO Moving Load Types	8
Figure G.6 Three Load Cases for HL-93 Truck	9
Figure G.7 Moment Envelope Diagram for Dead Load Condition	10
Figure G.8 Moment Envelope Diagram for FWS Load Condition	10
Figure G.9 Moment Envelope Diagram for HL93 Truck Load.....	10
Figure G.10 Moment Envelope Diagram for HL93 Lane Load	11
Figure G.11 Pier Cap and Slab Connection Details Showing Rigid Connection (left) and Pin Connection (Right).....	15
Figure G.12 Scheme A: Pin Connection between Slab and Pier Cap.....	16
Figure G.13 Scheme B: Rigid Connection between Slab and Pier Cap	16
Figure G.14 Sectional Details of Slab with Pin Connection Type	18
Figure G.15 Sectional Details of Slab with Rigid Connection Type	18
Figure G.16 Formwork for Column Showing Connection Type and Curing	19
Figure G.17 Formwork and Casting of Slabs	19
Figure G.18 Curing of Slab Specimens	20
Figure G.19 Typical Testing of Slab with Rigid Connection Type.....	20
Figure G.20 Cracks in Specimen with a Rigid Connection	21
Figure G.21 Cracks in Specimen with a Pin Connection.....	21
Figure G.22 Stress versus Crack Width for Slabs with Two Connection Types.....	22
Figure G.23 Load versus Deflection for Slabs with Two Connection Types.....	22

LIST OF TABLES

Table G.1 Dynamic Load Allowance	8
Table G.2 Unfactored Moments Obtained from SAP2000.....	11
Table G.3 Comparison of Moments Due to Dead Load Only (SAP2000 vs. ODOT)	12
Table G.4 Comparison of Moments for HL-93 Truck (SAP2000 vs. ODOT).....	13
Table G.5 Comparison of Moments for HL-93 Lane Load (SAP2000 vs. ODOT)	13
Table G.6 Bridge Details Considered in SAP2000 Analysis.....	15
Table G.7 Negative Moment at Slab and Pier Region for Schemes A and B	17

APPENDIX G

EFFECT OF SLAB-PIER CAP CONNECTION

G.1 Introduction

This section outlines the results of the structural analysis of bridges with various spans using SAP2000 structural analysis software and the comparison of the moment capacity of bridges with ODOT design values. The effects of a change in the slab and pier cap connection from rigid to pin was studied to investigate the difference in the negative moment values over the pier region. In addition, scaled-down tests were performed to determine the differences in crack patterns and crack widths on the tension side of the slab when using different types of connections.

G.2 Background regarding the Structural Modeling

The main goal for analyzing a structure is to determine the internal forces, stresses and deformations of the structure under numerous load conditions. The structural modeling incorporates three mathematical models, which include the following:

- Structural model, which has three basic components: structural members or components, joints (nodes, connecting edges or surfaces), and boundary conditions (supports and foundations);
- Material model, which defines the actual materials and includes material properties; and
- Load model, which considers the type of load and the load distribution (Caltrans, 2015).

Modeling of bridges can also be achieved through the use of the finite element method (FEM) approach. SAP2000, CT-Bridge and CSI-Bridges are the most common software packages used for modeling bridges. As per Caltrans (2015), the superstructure modeling is classified into the spine model and the grillage model.

G.2.1 Spine Model

The bridge deck is modeled as a 3D frame in which the superstructure consists of a series of straight beam elements, where the elements are located in the longitudinal direction along the centerline of the superstructure at its center of gravity. All superstructure elements are modeled as beam elements. Spine modeling uses shorter computing time in analyzing the structure. However, this model does not capture all responses, since the superstructure is modeled as one beam in the center of the bridge. Moreover, the spine model does not consider the location of the trucks in the transverse direction; thus, it does not provide the full effect of the truck on the bridge. In this case, the designer needs to use other factors to obtain the transverse effect of the truck, as shown in Figure G.1 (Vaziri, 2016).

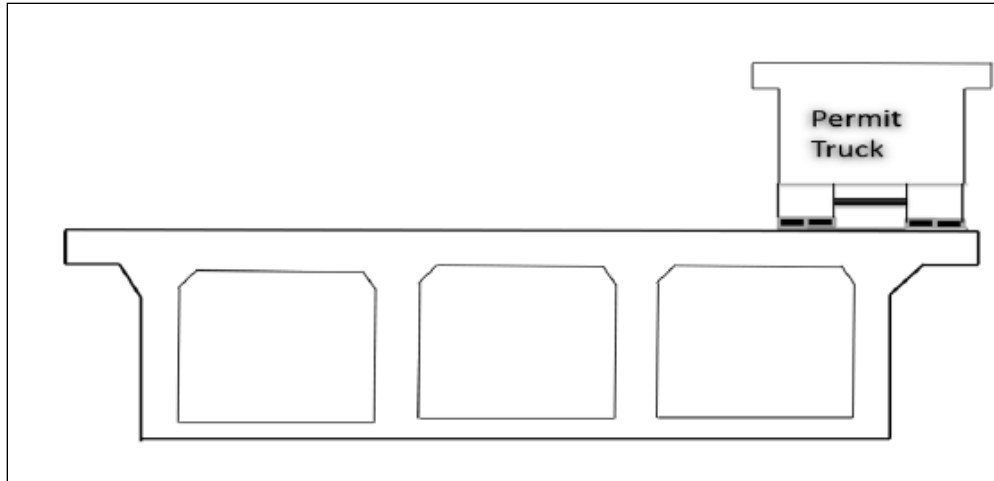


Figure G.1: Sectional view of the Box Girder with Truck Load on the Exterior Girder (Vaziri, 2016)

G.2.2 Grillage Models

The grillage model is a 3D space grid in which the superstructure can be modeled as beam elements in both the longitudinal and the transverse direction of the bridge. The longitudinal members are located at the center of gravity of each girder line (web and slab), whereas the transverse beams are intended to model the bridge deck and diaphragms (Pipinato, 2016). The substructure elements are also modeled as beam elements so that their member properties match with the three-dimensional orientation of the piers or columns. This approach is normally adopted in case of a complicated structure such as a bridge that is very long or very narrow (Caltrans, 2015).

G.3 Structural Analysis of ODOT Bridge DAR-118-8.49

Bridge DAR-118-8.49 in Darke County, Ohio (ODOT District 7), which was constructed in 2014, was selected from the ODOT bridge inventory to facilitate a comparison of the moment values obtained in SAP2000 with those provided in the ODOT design sheets. For the structural analysis, it is important to note the skew angle of the bridge prior to modeling. A skewed bridge is characterized by its skew angle, which can be defined as the angle between the centerline of a support (abutment or pier) and a line normal to the bridge centerline (AASHTO, 2012). AASHTO LRFD recommends that bridges with a skew angle less than or equal to 20° be designed as straight bridges, as shown in Figure G.2. The skew angle of the bridge DAR-188-8.49 is 15° ; therefore, the bridge has been analyzed as a straight bridge by the spine model approach.

Structural Analysis Package 2000 (SAP2000, v.17; created by Computers and Structures, Inc.) was used to perform the structural analysis for all bridges with two-dimensional frame elements. The properties of the section and dimensions of the standard bridges were obtained from the ODOT standard drawings. The procedure for modeling and analysis for Bridge DAR-188-8.49 is described in the following subsections.

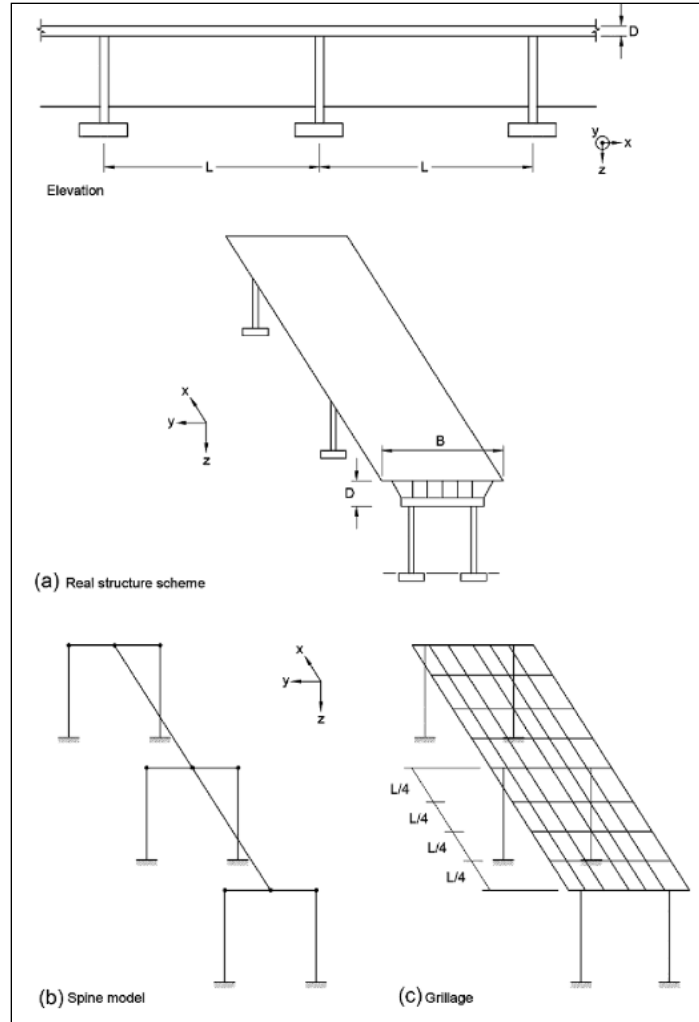


Figure G.2 Superstructure model: (a) Real structure scheme, (b) Spine model, (c) Grillage model (Pipinato, 2016)

G.3.1 Modeling of Bridge DAR-118-8.49

A model of Bridge DAR-118-8.49 with two-dimensional beam elements was created in SAP2000. The model was created in x - z plane; the total length of the bridge is 78 feet, which was divided into three spans as frames of 24 ft., 30 ft., and 24 ft. Each frame was again divided into two segments by meshing equally, as shown in Figure G.3.

G.3.1.1 Assignment of Restraints and Materials

Joint restraints were applied to the model at points A, C, E, and G. Joint A was assigned as a pinned support, which is restricted from moving in both the x and z directions but is allowed to rotate about the y axis. Joints C, E, and G were assigned as roller supports. Roller supports are restricted from moving in the vertical direction (the z direction). However, they have free movement in the horizontal direction and free rotation about the y -axis, as shown in Figure G.3.

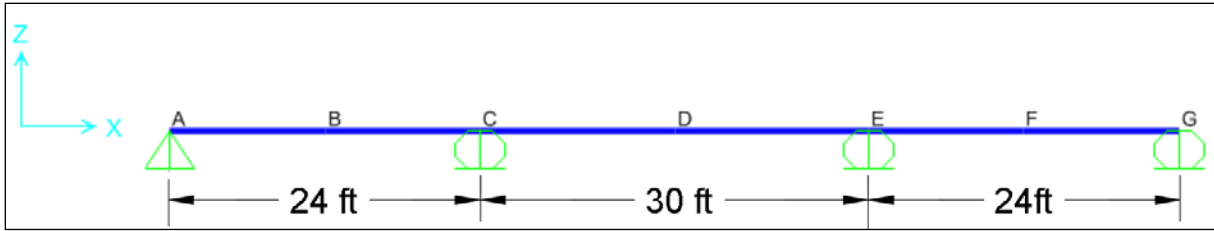


Figure G.3 Bridge DAR-118-8.49 Frame Model in SAP2000

Material properties were defined using the information from ODOT standard drawings for Bridge DAR-188-8.49. The six frames were assigned with a section that was 12 inches wide and 16 inches deep.

G.3.1.2 Load Cases

Bridges are designed to carry both static loads and moving loads. These loads are illustrated in detail as follows:

Static Loads

Static loads could be classified as follows:

- Dead load (DL). The dead load consists of the self-weight of the structure, including the deck weight, sidewalks, utility services, and other structures. The dead load option was selected in SAP2000 so that dead load would automatically be included in the analysis of Bridge DAR-118-8.49.
- Future wearing surface (FWS). The future wearing surface is a top layer of wearing surface that may be placed on the bridge at a future date. The load due to the future wearing surface is distributed uniformly over the entire bridge. According to AASHTO (2012), the future wearing surface of a highway bridge is 60 psf. as shown in Figure G.4.

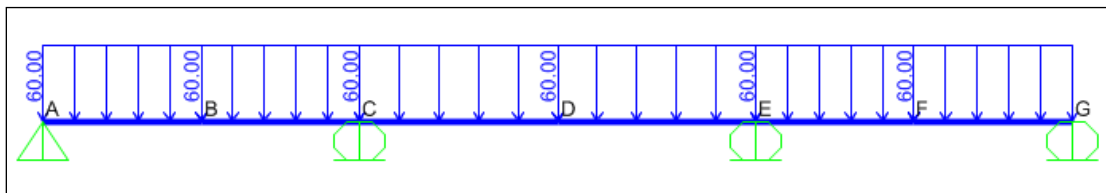


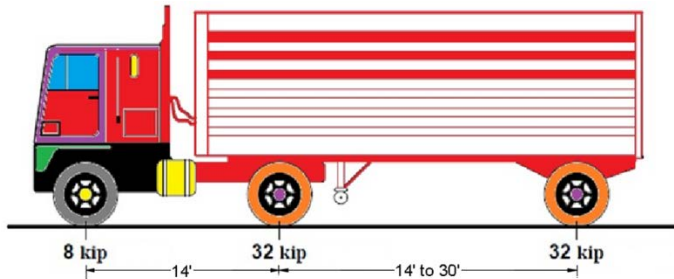
Figure G.4 Load Due to Future Wearing Surface

Moving Loads

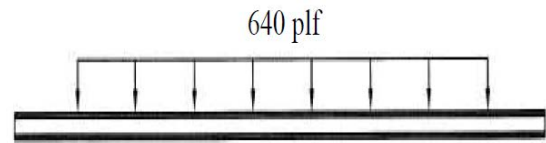
Moving loads include HL-93 loads, as follows:

- HL-93 truck load. HL-93 truck loading has a leading axle load of 8 kips, followed by an axle load of 32 kips at a constant distance of 14 ft., trailed by a third axle load of 32 kips at a distance varying between 14 ft. to 30 ft. from the second axle load, as can be seen in Figure G.5(a).

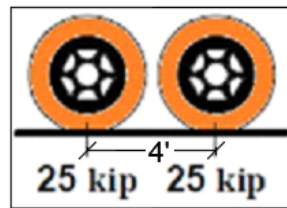
- HL-93 Lane Load. The HL-93 lane load is a uniformly distributed load that has a magnitude of 640 pounds per foot, as shown in Figure G.5(b).
- HL-93 Tandem. The HL-93 tandem is a two-axle load 25 kips each, where the distance between the two axles is 4 feet, as shown in Figure G.5(c).



(a) Standard HL-93 truck load



(b) Standard HL-93 Lane Load



(c) Tandem Wheel Loads

Figure G.5 AASHTO Moving Load Types

G.3.1.3 Dynamic Load Allowance

Since the roadway surfaces on a bridge are typically not perfectly smooth and the suspension systems of the trucks respond to roadway roughness with oscillations, a dynamic load allowance (IM) should also be used in the bridge analysis. The following impact factors were considered in the moment analysis. The IM for fatigue and truck loads are identical to those in AASHTO Section 3.6.21 (AASHTO, 2012), as shown in Table G.1.

- Impact factor for lane load is = IM lane = 1
- Impact factor for fatigue load is = IM truck = $1 + \frac{15}{100}$
- Impact factor for truck load is = IM truck = $1 + \frac{33}{100}$

Table G.1 Dynamic Load Allowance

Component	Dynamic Load Allowance (IM)
Deck Joints – All Limit States	75%
All Other Components	
• Fatigue and Fracture Limit State	15%
• All Other Limit States	33%

G.3.1.4 HL-93 Load Combinations

HL-93 theoretical AASHTO vehicular loading comprises variations and combinations of tandem trucks, truck loading, and lane loading (as illustrated in Figure G.6). In this system, Cases 1 and 2 consider a positive moments, whereas Cases 3 for negative moments. When loading the superstructure with HL-93 loads, only one vehicle per lane is permitted on the bridge at a time, except for Cases 3. In the analysis performed in SAP2000, lane load was not considered with any other load combination i.e. along with tandem and HL-93 truck.

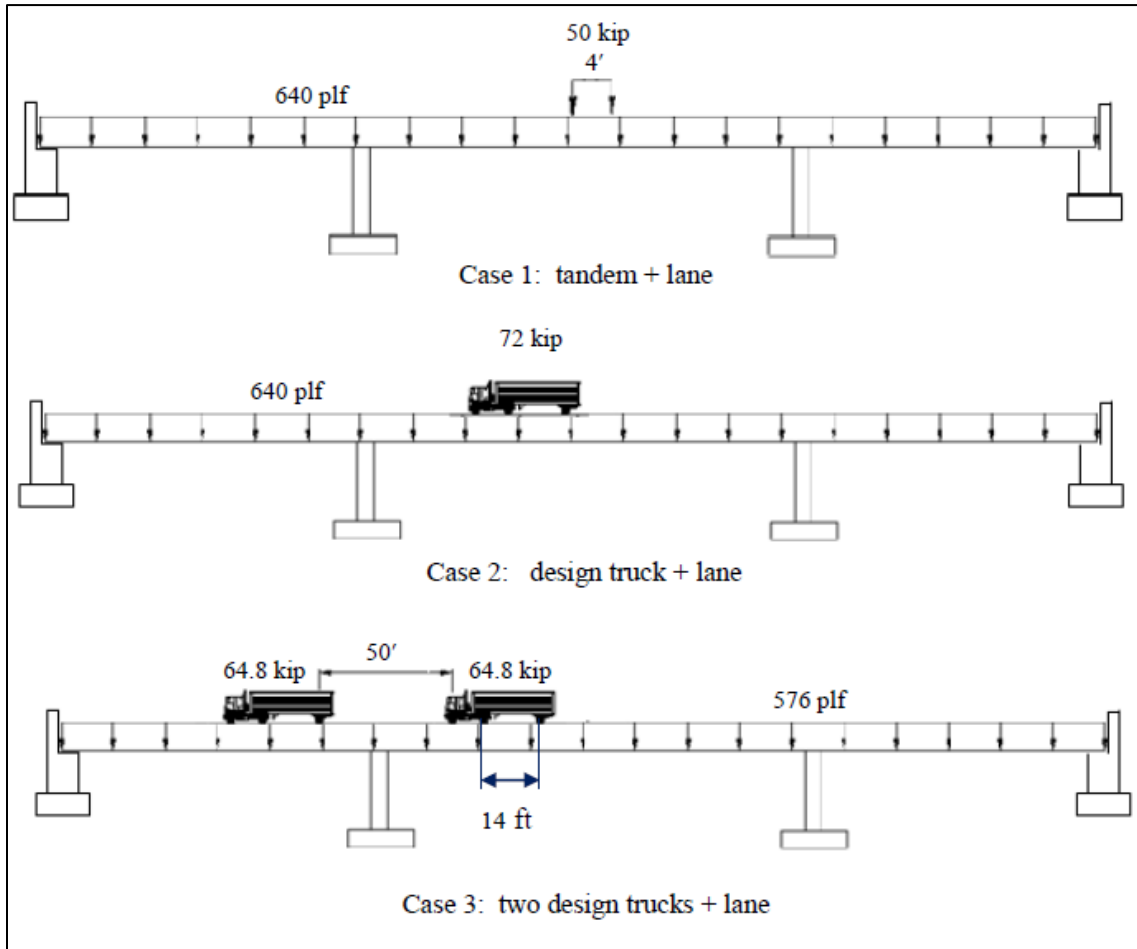


Figure G.6 Three Load Cases for HL-93 Truck

G.3.1.5 Analysis of Bridge DAR-118-8.49

The analysis of Bridge DAR-118-8.49 was performed in SAP2000 for all load cases, and the moment envelopes are shown in Figures G.7 to G.10.

- Static Load Analysis:
 - Dead Load

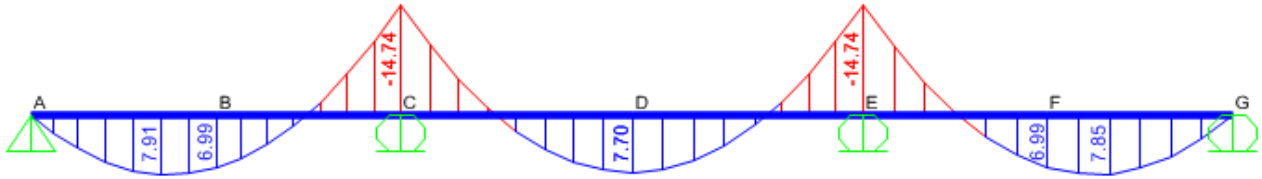


Figure G.7 Moment Envelope Diagram for Dead Load Condition

- Future Wearing Surface (FWS)

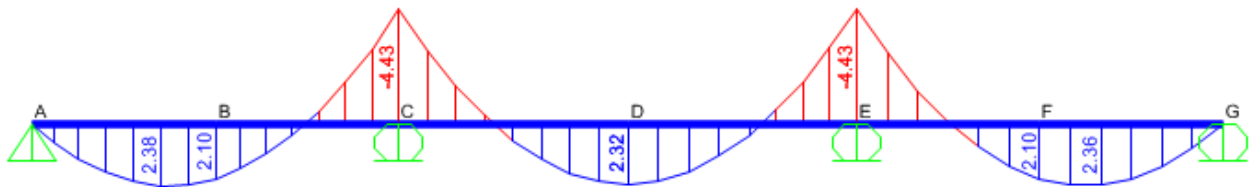
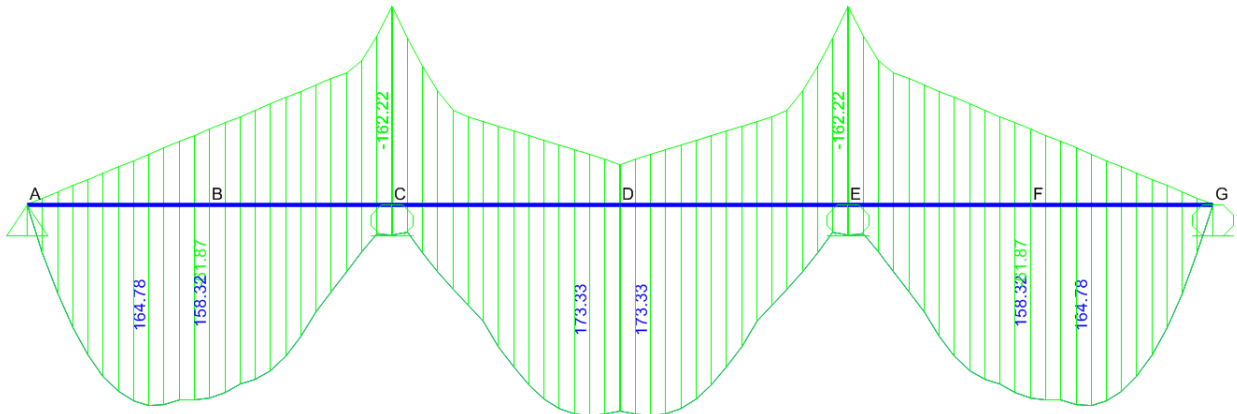


Figure G.8 Moment Envelope Diagram for FWS Load Condition

- Moving Load Analysis:
 - HL-93 Truck Load



Z

Figure G.9 Moment Envelope Diagram for HL-93 Truck Load

- HL-93 Lane Load

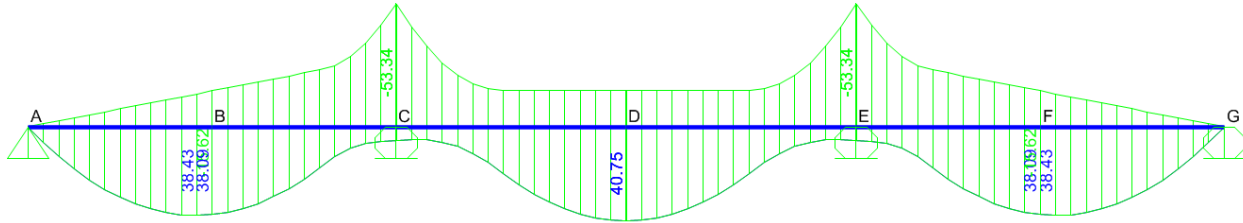


Figure G.10 Moment Envelope Diagram for HL-93 Lane Load

The moments for each load case are presented in Table G.2. As can be noticed from this table, the moment values obtained from SAP2000 are in close agreement with ODOT design values.

Table G.2 Unfactored Moments Obtained from SAP2000 for Bridge DAR-118-8.49

Bridge Name	Spans (ft.)	Load Cases	Unfactored Moments		
			Moments (kips-ft.)		
			Maximum Positive Moment		Maximum Negative Moment
			M_{ac} (Exterior span)	M_{ce} (Interior span)	
DAR -118-8.49	24-30-24	Dead Load	7.9	7.7	14.7
		FWS Load	2.4	2.3	4.4
		HL-93 Truck Load	164	173	162.5
		HL-93 Lane Load	38	41	53

G.4 Bridges with Standard Spans from the ODOT Bridge Inventory

Analysis of selected bridges from the ODOT bridge inventory that have standard spans was performed in SAP2000 to compare the moment values obtained from SAP2000 with the design values provided by ODOT. The bridge was modeled in 2D as a frame model and analyzed for dead load, HL-93 truck load and HL-93 lane load separately and presented in Tables G.3 to G.5.

Table G.3 Comparison of Moments Due to Dead Load Only (SAP2000 vs. ODOT)

No.	Bridge Spans (ft.)	Deck Thickness (ft.)	Dead Load					
			Max. Positive Moment (kip-ft.)				Max. Negative Moment (kip-ft.)	
			M _{ac} (Exterior span)		M _{ce} (Interior span)			
			ODOT	SAP2000	ODOT	SAP2000	ODOT	SAP2000
1	14-17.5-14	11	1.9	1.9	1.8	1.8	3.5	3.5
2	15-18.75-15	11.5	2.2	2.1	2.1	2.1	4.1	4
3	16-20-16	12	2.6	2.6	2.6	2.6	4.9	4.9
4	17-21.25-17	12.5	3.2	3.1	3.1	3	5.9	5.8
5	18-22.5-18	13	3.6	3.6	3.5	3.5	6.7	6.6
6	19-23.75-19	13.5	4.2	4.2	4.1	4.1	7.9	7.8
7	20-25-20	14	4.9	4.8	4.8	4.7	9.2	9
8	21-26.25-21	14.5	5.4	5.4	5.3	5.5	10.2	10.4
9	22-27.5-22	15	6.3	5.8	6.2	5.7	11.8	10.9
10	23-28.75-23	15.5	7.1	7	6.7	6.9	13.2	13.2
11	24-30-24	16	7.9	7.9	7.7	7.7	14.8	14.8
12	25-31.25-25	16.5	9	8.9	8.8	8.6	16.8	16.5
13	26-32.50-26	17	9.7	10.1	9.5	9	18.2	18.4
14	27-33.75-27	17.5	11	11	10.7	10.7	20.6	20.5
15	28-35-28	18	12.4	12.2	12.1	11.8	23.2	22.6
16	29-36.25-29	18.5	13.3	13.4	12.9	13	24.8	24.9
17	30-37.5-30	19	14.8	14.8	14.4	14.3	27.7	27.4
18	31-38.75-31	19.5	16.2	16.2	15.7	15.7	30.1	30.1
19	32-40-32	20	17.6	17.7	17.1	17.2	32.9	32.9
20	33-41.25-33	20.5	19.4	19.2	18.9	18.6	36.3	35.8
21	34-42.5-34	21	21	20.9	20.1	20.2	39	38.9
22	35-43.75-35	21.5	22.7	22.7	22.1	21.9	42.5	42.2
23	36-45-36	22	24.9	24	24.3	23.2	46.6	44.7
24	37-46.25-37	22.5	26.3	26.5	25.6	25.7	49.2	49.4
25	38-47.5-38	23	28.7	28.6	28	27.7	53.8	53.3
26	39-48.75-39	23.5	30.3	30.8	29.5	29.8	56.6	57.3
27	40-50-40	24	32.9	33	32.1	32	61.6	61.6
28	41-51.25-41	24.5	35.8	35.5	34.8	34.5	66.9	66.1
29	42-52.5-42	25	37.5	38	35.6	36.9	70.2	70.7
30	43-53.75-43	25.5	41	40.7	40	39.5	76	75.6
31	44-55-44	26	44	43.4	43	42.2	82	80.7
32	45-56.25-45	26.5	46	46.3	45	44.9	86	86.1
33	46-57.5-46	27	50	49.3	48	47.8	93	91.6

Table G.4 Comparison of Moments for HL-93 Truck (SAP2000 vs. ODOT)

No.	Bridge Spans (ft.)	HL - 93 Truck Load					
		Max. Positive Moment (kip-ft.)				Max. Negative Moment (kip-ft.)	
		M _{ac} (Exterior span)		M _{ce} (Interior span)			
		ODOT	SAP2000	ODOT	SAP2000	ODOT	SAP2000
1	14-17.5-14	104.2	110	105.3	106	89.5	88.4
2	15-18.75-15	114.5	121	115.2	116	97	96
3	16-20-16	124.4	129	125.3	126	103.5	102.4
4	17-21.25-17	134.4	138	135.7	136	109.9	109
5	18-22.5-18	144.9	146	145.3	146.3	116.9	116
6	19-23.75-19	154.6	155	156.1	156.3	124.3	122.2
7	20-25-20	165.4	166	166.1	167	132	129
8	21-26.25-21	174.8	177	176.2	193	139.4	143
9	22-27.5-22	185.2	186	186.9	187	147.9	146.5
10	23-28.75-23	195.4	196.2	196.8	197.5	154.7	154
11	24-30-24	205.7	206.4	207	208	162.5	162
12	25-31.25-25	216.7	217	217.6	218	169.9	169.4
13	26-32.50-26	226.2	227	227.9	228.5	177.6	177.2
14	27-33.75-27	237	237.5	238.3	239	185.3	185
15	28-35-28	246.9	247.4	248.2	248.3	192.9	192
16	29-36.25-29	257.1	258.1	258.9	260	200.5	200.2
17	30-37.5-30	268.2	268.4	269.5	270	208.3	208
18	31-38.75-31	278.3	279	280.2	280.3	215.6	215.5
19	32-40-32	288.6	289.1	290	291	223.4	223
20	33-41.25-33	298.5	299.2	300.7	301.2	231	231
21	34-42.5-34	308.8	310	311.4	312	238.6	238
22	35-43.75-35	319.8	320	326.6	322	246.3	246
23	36-45-36	328.7	331	329	333	253.6	254
24	37-46.25-37	340.3	341	342.6	343	260.5	261
25	38-47.5-38	351	351.2	352	353.3	267.3	268
26	39-48.75-39	362	362	363	364	273.8	275
27	40-50-40	371	372	377	374.1	280	281.2
28	41-51.25-41	381	382.4	387	385	286	287.4
29	42-52.5-42	392	393	406	408	292	293.5
30	43-53.75-43	403	404.1	420	422	297	299.3
31	44-55-44	412	419	435	436	302	305
32	45-56.25-45	423	433	449	450.1	310	310.4
33	46-57.5-46	433	447.3	461	464	318	317.5

Table G.5 Comparison of Moments for HL-93 Lane Load (SAP2000 vs. ODOT)

No.	Bridge Spans (ft.)	HL - 93 Lane Load					
		Max. Positive Moment (kip-ft.)				Max. Negative Moment (kip-ft.)	
		M _{ac} (Exterior span)		M _{ce} (Interior span)			
		ODOT	SAP2000	ODOT	SAP2000	ODOT	SAP2000
1	14-17.5-14	13.1	13.1	13.8	14.5	18.2	17
2	15-18.75-15	14.9	15	15.9	16.7	20.9	19.5
3	16-20-16	17.1	17.1	18.1	18.9	17.1	22.2
4	17-21.25-17	19.1	19.4	20.4	21.4	26.8	25.1
5	18-22.5-18	21.4	21.7	22.9	24	30.1	28.2
6	19-23.75-19	24.1	24.2	25.5	26.7	33.5	31.4
7	20-25-20	26.4	26.8	28.3	29.6	37.1	34.8
8	21-26.25-21	29.1	29.6	31.2	33.2	40.9	38.8
9	22-27.5-22	32.3	32.4	34.2	35.8	44.9	42.1
10	23-28.75-23	35.3	35.4	37.4	39.2	49.1	46
11	24-30-24	38.1	38.6	40.7	42.7	53.5	50.1
12	25-31.25-25	41.3	41.8	44.2	46.3	58.1	54.3
13	26-32.50-26	45.1	45.4	47.7	48.8	62.8	57.8
14	27-33.75-27	48.6	48.8	51.5	57	67.7	63.4
15	28-35-28	52.3	52.5	55.4	58.1	72.8	68.2
16	29-36.25-29	55.6	56.3	59.4	62.3	78.1	73.1
17	30-37.5-30	59.5	60.3	63.6	66.7	83.6	78.3
18	31-38.75-31	64.1	64.3	67.9	71.2	89.2	83.6
19	32-40-32	68.3	68.6	72.3	75.9	95.1	89
20	33-41.25-33	72.6	72.9	76.9	73.9	101.1	96
21	34-42.5-34	77.1	77.4	81.7	78.4	107.4	102
22	35-43.75-35	81.7	82	86.5	83.1	113.8	108.1
23	36-45-36	85.7	84.9	91.6	85.9	120.4	111.8
24	37-46.25-37	90.5	91.7	96.7	92.9	127.1	120.7
25	38-47.5-38	95.4	96.7	102	97.9	134.1	127.3
26	39-48.75-39	101	101.8	100	103.2	142	134.1
27	40-50-40	106	107.1	114	108.6	149	141.1
28	41-51.25-41	112	111.1	119	121.4	157	156.8
29	42-52.5-42	117	116.6	125	127.3	164	158.3
30	43-53.75-43	123	122.3	131	133.5	172	165.9
31	44-55-44	129	128	137	139.8	180	173.7
32	45-56.25-45	135	133.9	143	146.2	188	181.7
33	46-57.5-46	140	139.9	150	152.8	197	189.9

G.5 Effect of Connection Type on Moment Values

ODOT commonly uses a rigid connection between the pier cap and the slab at the pin support locations for structural slab bridges. Bridge DAR-118-8490 was recently built with a modified connection type at the slab and the pier cap connection as shown in Figure G.11. As this analysis was mainly focused on investigating the effect of the connection type on the negative moment values, one bridge with rigid connection and one with pin connection were selected from the ODOT bridge inventory as mentioned in Table G.6.

Table G.6 Bridge Details Considered in SAP2000 Analysis

S.No	District	Name of The Bridge	Spans (ft.)	Deck Thickness (in.)	Year Built	Skew	Loading	Substructure Type
1	5	KNO-62-18820	24-30-24	16	2013	None	HL-93	Capped Pile and Pier
2	7	DAR-118-8490	24-30-24	18	2014	15° LF	HL-93	Cap and Column

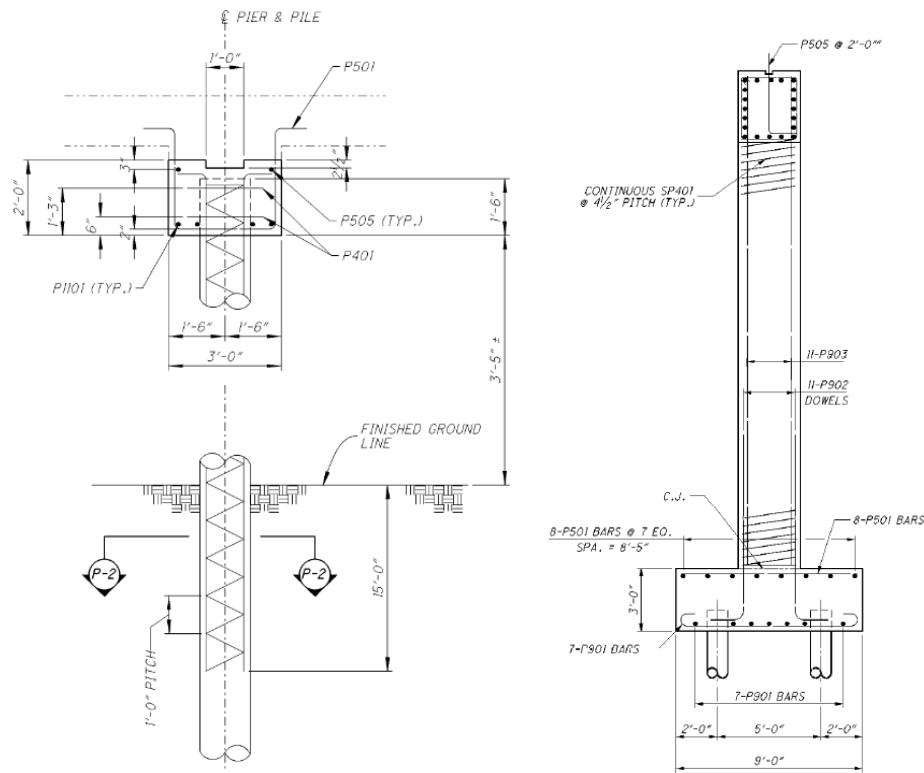


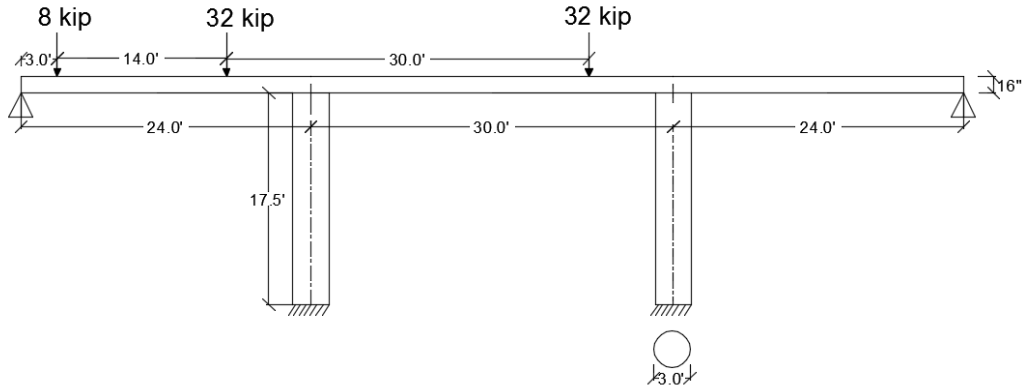
Figure G.11 Pier Cap and Slab Connection Details Showing Rigid Connection (left) and Pin Connection (Right)

To evaluate the effect of pier-slab connection on the moment distribution, two schemes were considered:

- Scheme A: Pin Connection: slab and pier connected with a straight dowel bar . The pier length used was 17.5 ft. as mentioned in standard drawings. To compare between the

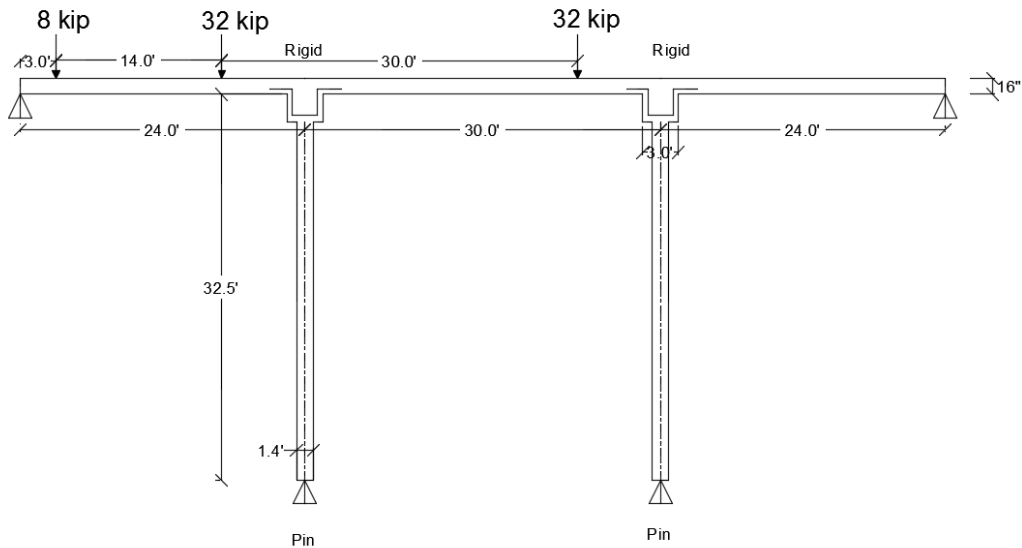
different connection types, the slab thickness of 16 inches was used as shown in Figure G.12. The end conditions for the piles was fixed.

- Scheme B: Rigid Connection: slab and pier connected with a U-Shaped rigid bar. The pier length was modied to 32.5 ft. by adding additional 30% to the actual pier length to consider a pin location along the pier as shown in Figure G.13.



Scheme (A) for HL-93 Truck (Static)

Figure G.12 Scheme A: Pin Connection between Slab and Pier Cap



Scheme (B) for HL-93 Truck (Static)

Figure G.13 Scheme B: Rigid Connection between Slab and Pier Cap

Analysis was performed for static HL-93 truck load positioned as shown in figure G.12 and G13, as well as moving load conditions. The results for both the Schemes A and B are presented in Table G.7. On comparison of negative moments over the pier cap for static loading condition, it was observed that negative moments for scheme A was lower than scheme B.

Whereas in the moving load conditions, the negative moments over the pier cap of scheme B is higher than scheme A as found in table G7.

Table G.7 Negative Moment at Slab and Pier Region for Schemes A and B

Type of Connection between Slab and Pier-Cap	Type of Analysis	Type of Loading	Max. +ve Moment Exterior Span AB (kip-ft.)	Max. -ve Moment Over Pier (kip-ft.) B	Max. +ve Moment Interior Span BC (kip-ft.)
Pin Connection (Scheme A)	Moving Load Analysis	HL-93 Truck	165	162	173
		Tandem	206	128	208
		Two Tandems @26'	206	212	208
	Static Load Analysis	HL-93 Truck	88	109	105
Rigid Connection (Scheme B)	Moving Load Analysis	HL-93 Truck	156	154	155
		Tandem	194	141	186
		Two Tandems@26'	194	205	186
	Static Load Analysis	HL-93 Truck	84	132	95
Design Values Based on ODOT Excel Sheet					
		HL-93	205.7	162.5	207

G.6 Experimental Testing of Slabs with Different Connection Types

In order to test slabs with different connection types, the slab designs presented in Chapter 6 were modified to accommodate a pier at the center similar to an actual bridge. Two connection types (pin and rigid) were adopted to test the effect of the connection type on cracking in bridge decks. The sectional details of the piers were scaled down accordingly to match the scaled-down slab specimen. The details of the slab and pier specimens constructed with a pin connection and a rigid connection are shown in Figure G.14 and Figure G.15, respectively.

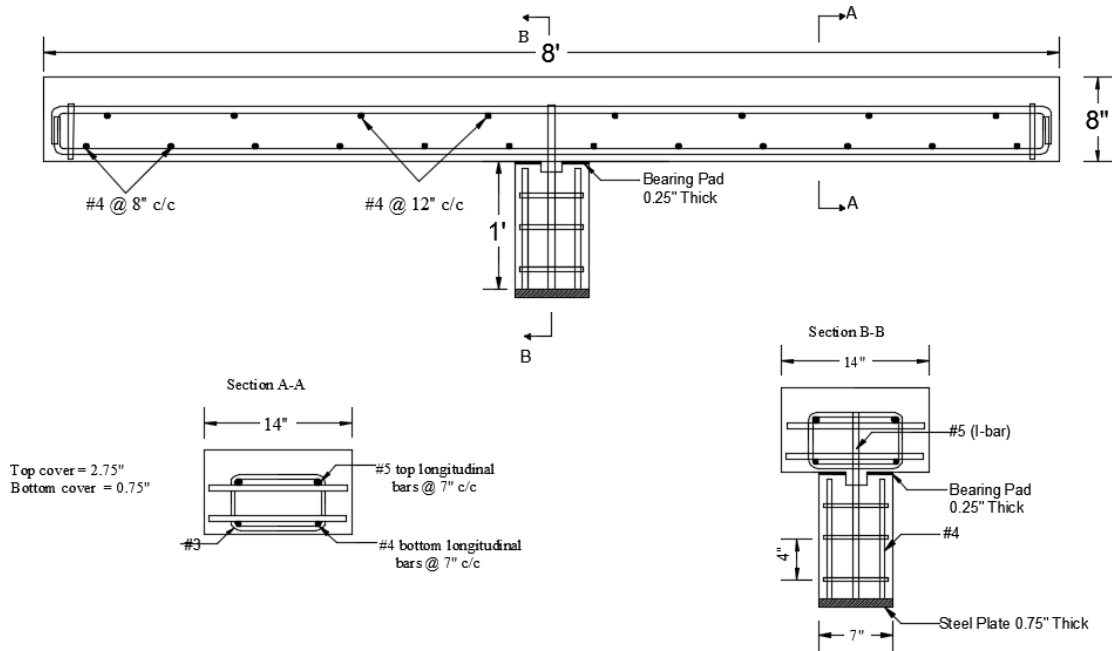


Figure G.14 Sectional Details of Slab with Pin Connection Type

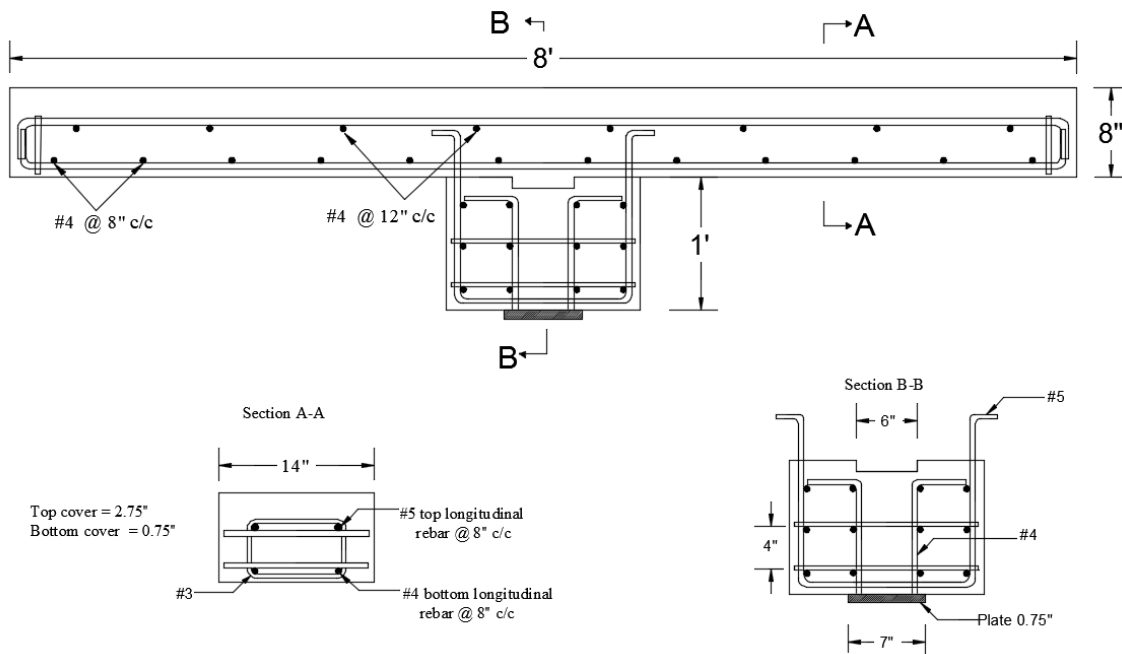


Figure G.15 Sectional Details of Slab with Rigid Connection Type

G.6.1 Preparation of Test Specimens

To prepare specimens for testing, column portion of the specimens was first cast and cured for seven days to achieve a minimum compressive strength of 2,500 psi. The column specimen with a pin connection had a dowel bar protruding from the top of the column as seen in

Figure G.16 (left), and the slab specimens with rigid connections had U-shaped bars protruding from the top as seen in Figure G.16 (Right).



Figure G.16 Formwork for Column Showing Connection Type and Curing

The slab specimens, with the mix design similar to that specified in Table G.3, were prepared in such a way that they would be able to accommodate columns at the center location. As the slabs were raised above the ground level to accommodate columns, small concrete beams were used to support the formwork, as shown in Figure G.17. The specimens were wet cured by water at room temperature; the slabs were then covered with wet burlap to retain moisture for a longer period of time and were covered in plastic sheeting to prevent the evaporation of moisture, as shown in Figure G.18. The slab specimens were cured for 21 days to achieve a minimum compressive strength of 4500 psi.



Figure G.17 Formwork and Casting of Slabs



Figure G.18 Curing of Slab Specimens

G.6.2 Test Setup

The specimens were setup on the testing frame in such a way that load was applied from under the column to create negative moment on the tension face at the top. Two dial gages were used—one at the mid-span location and another at the quarter-span location—to monitor the deflections as shown in Figure G.19. Four strain gages were attached to the tension reinforcement and were connected to a data acquisition system, and StrainSmart data acquisition software (provided by Micro-Measurements) was used to record the strains. In addition, a load cell was connected to continuously record the applied loads during testing. The load from the bottom of the column was applied using a manually-operated hydraulic jack system. The patterns and widths of cracks that formed on the top surface of the slab were recorded manually at every 250 lbs. of loading.

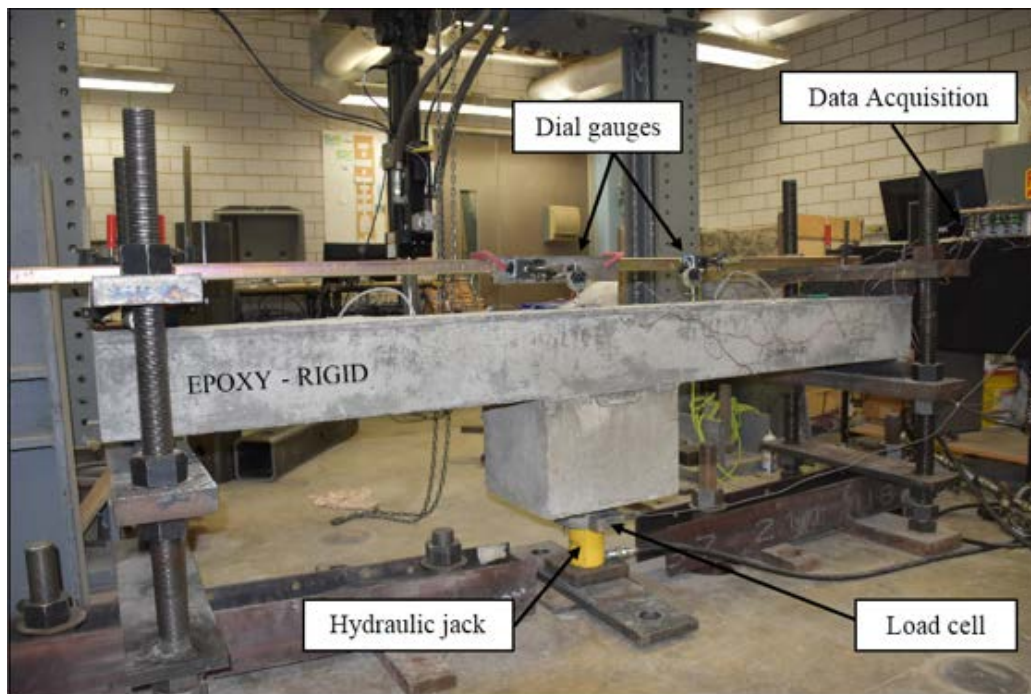


Figure G.19 Typical Testing of Slab with Rigid Connection Type

G.6.3 Test Results on Connection Type

The slabs with the two connection types cracked at nearly the same load level. In the case of slabs with a rigid connection, no cracks were formed over the pier cap region; the five cracks that did form were distributed on the slab, as seen in Figure G.20. In the case of the slab with a pin connection, four cracks formed, and one of these cracks formed right above the column center line. The cracks were relatively evenly spaced as seen in Figure G.21.



Figure G.20 Cracks in Specimen with a Rigid Connection



Figure G.21 Cracks in Specimen with a Pin Connection

Plots showing stress versus crack width and load versus deflection generated from the test data are presented in Figure G.22 and Figure G.23, respectively. From Figure G.22, it can be noticed that there is not much difference in the crack width results for specimens with a pin connection and a rigid connection. In Figure G.23, it can be seen that the deflection in the pin connection was marginally higher than the deflection in the rigid connection.

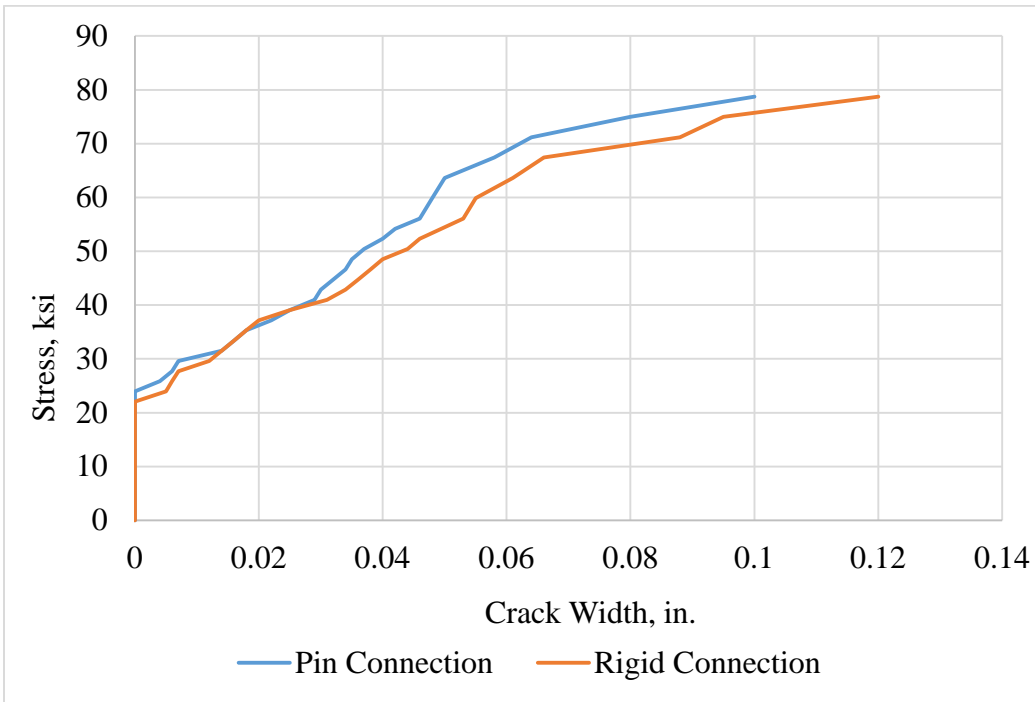


Figure G.22 Stress versus Crack Width for Slabs with Two Connection Types

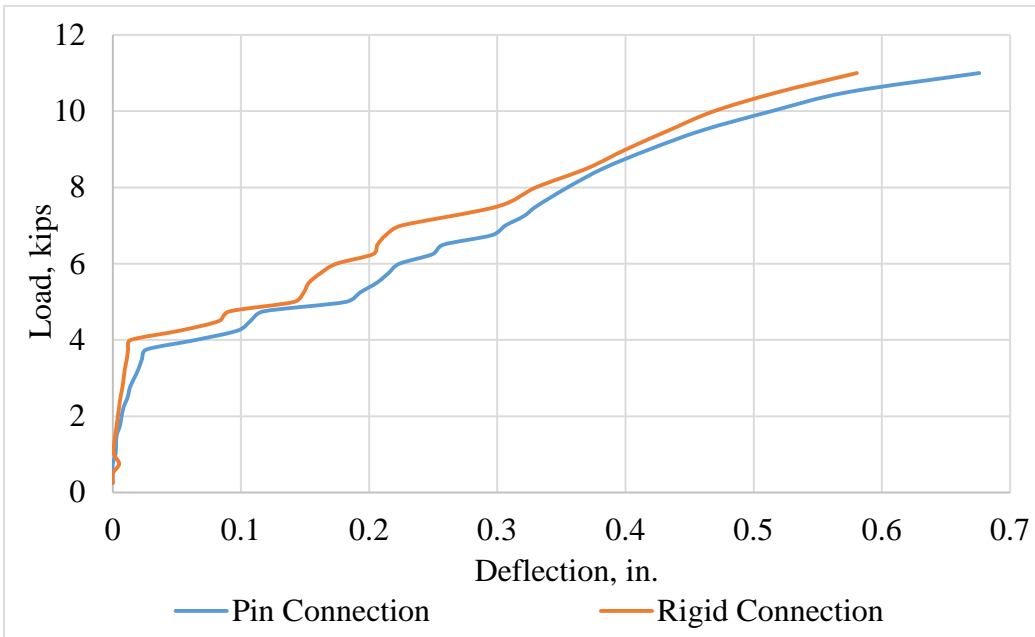


Figure G.23 Load versus Deflection for Slabs with Two Connection Types

G.7 Summary and Conclusions

The effects of a change in the slab and pier-cap connection from rigid connection to pin connection was studied to investigate the difference in the negative moment values over the pier region. In addition, scaled-down tests were performed to determine the differences in crack patterns and crack widths on the tension side of the slab when using these two types of connections. Structural analysis of the two types of connections revealed that the maximum negative live load moment at the pier cap is reduced by about 20% when a pinned connection is used. However, the structural tests did not show much difference in the cracking widths of the two types of connections, maybe because of the symmetric loading applied in the tests.

REFERENCES

- Atorod Azizinamini, P. P., (2013). “Design Guide for Bridges for service Life.” Washington: National Cooperative Highway Research Program.
- Bhagwat, Y., (2014). “Effect on Super Structure of Integral Abutment Bridge under Fixed and Pinned Pile Head Connections.” International Knowledge Shearing Platform, 97-105.
- Connal, J., (2004). “Integral Abutment Bridges” – Australian and US. AUSTRROADS, 1-19.
- Constructor. (2017). “Integral Bridges.” Retrieved from The Constructor: <https://theconstructor.org/structures/integral-bridges/1217/>
- Guangyang Hou, S., & and Suren Chen, P. M., (20-17). “Bent Connection Options for Curved and Skewed SMC Bridges in Low-to-Moderate Seismic Regions”. American Society of Civil Engineers, 1-11.
- IOWA., (2006). “Office of Bridges And Structures”. Retrieved from IOWA.gov: <https://iowadot.gov/bridge/bridge-and-culvert-standards/bridge-standards>
- M Ala Saadeghvaziri, W. R., (August 2004). “Improvement of Continuity Connection over Fixed Piers.” Newark: Department of Civil and Environmental Engineering New Jersey Institute of Technology, NJ 07102.
- Patnaik. A. and P. Baah. (2015). “Cracking Behavior of Structural Slab Bridge Decks,” Report No. FHWA/OH-2015/4. Ohio Department of Transportation, Columbus, OH. January. Available at https://www.dot.state.oh.us/Divisions/Planning/SPR/Research/reportsandplans/Reports/2015/Structures/134708_FR.pdf
- Sami Arsoy, R. M., (1999). “The Behavior of Integral Abutment Bridges.” Virginia: Virginia Department of Transportation.

Reduction of Bridge Deck Cracking through Alternative Material Usage

APPENDIX H BRIDGE IMPLEMENTATION WITH FIBER REINFORCED CONCRETE

Prepared by:
Anil Patnaik, Ph.D.
and
Srikanth Marchetty

Prepared for:
The Ohio Department of Transportation,
Office of Statewide Planning & Research

State Job Number 135260
November 2017
Draft Final Report



TABLE OF CONTENTS

TABLE OF CONTENTS.....	1
LIST OF FIGURES	2
LIST OF TABLES	3
APPENDIX H.....	4
BRIDGE IMPLEMENTATION WITH FIBER REINFORCED CONCRETE.....	4
H.1 INTRODUCTION	4
H.2 TEST PLACEMENT AT OSBORNE, INC.	4
<i>H.2.1 Test Slabs and Beams for Trial Cast</i>	4
<i>H.2.2 Slump and Air Content Test</i>	6
<i>H.2.3 Casting of Trial Slabs and Beams</i>	7
<i>H.2.4 Finished Surface of the Slabs</i>	8
H.3 HINCKLEY BRIDGE SLAB PLACEMENT.....	8
<i>H.3.1 Mix Design Used</i>	9
<i>H.3.2 On-Site Slump and Air Content Tests</i>	9
<i>H.3.3 Placement of Concrete on the Bridge Deck</i>	10
<i>H.3.4 Consolidation of Concrete</i>	11
<i>H.3.5 Surface Finishing</i>	11
<i>H.3.6 Finished Surface of Deck</i>	12
<i>H.3.7 Burlap Placement</i>	12
<i>H.3.8 Curing of the Deck</i>	12
<i>H.3.9 Cylinder Compressive Strength</i>	13
H.4 INSPECTION OF THE BRIDGE DECK WHILE THE BRIDGE IS IN SERVICE	14
H.5 SUMMARY AND CONCLUSIONS	14
REFERENCES	15

LIST OF FIGURES

Figure H.1 Test Placement at Osborne, Inc. Test Site	4
Figure H.2 Euclid TUF-Strand SF 101T94 (left) and Placement of Fibers on Conveyer at the Batching Plant (right).....	5
Figure H.3 Formwork for Trial Slabs	5
Figure H.4 Deep Shoulder Benches Considered for Trial Casting.....	6
Figure H.5 Slump Test (left) and Air Content Test (right).....	6
Figure H.6 Placement of Concrete into the Formwork for Slab 1 and Beams	7
Figure H.7 Placement of Concrete into the Formwork for Slab 2 and Deep Shoulder Benches....	7
Figure H.8 Surface Finish of Slab 1 and Slab 2.....	8
Figure H.9 The Selected Three-Span Bridge in Hinckley, Ohio	8
Figure H.10 Reinforcement Mesh (left); Pier Cap and Slab Connection (right)	9
Figure H.11 Air Content Testing (left) and Slump Testing (right) at the Site.....	10
Figure H.12 Air Content Test (left) and Slump Test (right).....	10
Figure H.13 Placement of Concrete into the Bridge Deck Formwork	11
Figure H.14 Three-way Surface Finish Process Adopted for the Bridge Deck.....	11
Figure H.15 Finished Surface of the Bridge Deck.....	12
Figure H.16 Placement of Wet Burlap over the Bridge Deck	12
Figure H.17 Curing of the Bridge Deck.....	13
Figure H.18 Typical Compressive Strengths of Cylinders Tested at 28 Days	13

LIST OF TABLES

Table H.1 Slump and Air Content Test Results.....	7
Table H.2 Design Mix Proportions (Osborne Medina, Inc.)	9

APPENDIX H

BRIDGE IMPLEMENTATION WITH FIBER REINFORCED CONCRETE

H.1 Introduction

Based on our research in this project, it was recommended to use polypropylene fibers in the concrete mix to arrest these cracks and consequently increase the service life of the bridge decks in Ohio with a high dosage (10 lb/yd³) of polypropylene fiber in concrete. A bridge located in Hinckley, Ohio, was selected as the site of the demonstration project. The selected bridge was a three-span continuous slab bridge with spans of a 24 ft.–30 ft.–24 ft. configuration with a slab thickness of 16 inches. Since this demonstration project was first of its kind in Ohio to use a high dosage of fibers, a trial concrete placement was planned to develop a mix design that is easily workable that would also meet the requirements for slump and air content.

H.2 Test Placement at Osborne, Inc.

A test placement for a concrete mixture containing polypropylene fibers was conducted on June 6, 2017, at Osborne Inc. in Medina, Ohio (Figure H.1). A concrete mix design with 10 lb/yd³ of polypropylene fibers (supplied by Euclid Chemicals, Cleveland, Ohio) was developed by the engineers at Osborne, and the trial placement was performed to gain a better understanding of the mix design, workability, slump, air content and surface finish of the fibrous concrete mixture. The concrete placement was attended by ODOT SMEs, engineers, representatives from Euclid Chemical, and members of the research team from The University of Akron.



Figure H.1 Test Placement at Osborne, Inc. Test Site

H.2.1 Test Slabs and Beams for Trial Cast

Two trial slabs and several deep shoulder benches were placed along with a few cylinders and beams. The slabs considered were unreinforced and had a larger area-to-thickness ratio than standard bridge deck slabs in order to verify proper placement, consolidation and finishing. The mix design used for the concrete was ODOT QC2 along with 10 lb/yd³ of Euclid TUF-Strand SF 101T94 polypropylene fibers. The fibers were added directly into the concrete mixing drum along with other materials as shown in Figure H.2. A batch of six cubic yards of concrete was prepared for the trial placement, with a total fiber quantity of 60 pounds (20 bags of 3 pounds each).



Figure H.2 Euclid TUF-Strand SF 101T94 (left) and Placement of Fibers on Conveyor at the Batching Plant (right)

The concrete was mixed as per ASTM C192, using superplasticizers, air entraining agents, and Eucon WR 91 (Euclid Chemical) as the admixtures to maintain a slump of 4 to 5 inches per ASTM C143 and an air content of 6 to 8% per ASTM C231. This percentage of air content was a crucial factor in the design, considering the durability of bridge decks exposed to freeze/thaw cycles. The mixed concrete was loaded into the truck and the drum of the truck was rotated at 6 rotations/min. for a total of 20 minutes. This was done to simulate the travel time for the concrete to be transported from the concrete plant to the bridge deck under actual conditions. The dimensions of the trial slabs were 4 ft. x 8 ft. x 3 inches thick (Figure H.3) and the deep shoulder benches were 2 ft. x 6 ft. x 24 inches deep (Figure H.4).



Figure H.3 Formwork for Trial Slabs



Figure H.4 Deep Shoulder Benches Considered for Trial Casting

H.2.2 Slump and Air Content Test

Slump and air content of the mix were monitored prior to the casting to ensure compliance for slump and air content. The concrete was placed into the mold for the slump cone and into the air content cylinder. ASTM C143 and ASTM 231 standard test procedures were followed, and the concrete was found to have 2.5 inches of slump and 7% of air content. Figure H.5 shows the slump cone test and the air content test conducted at site. This initial mix was used in one of the two test slabs as well as in a few of the cylinders and beams. The mix was then improved by adding an additional one gallon of super plasticizer in order to increase the slump. The results of slump and air content tests for both test slabs are presented in Table H.1.



Figure H.5 Slump Test (left) and Air Content Test (right)

Table H.1 Slump and Air Content Test Results

Serial No.	Mix Design	Slump (inches)	Air Content (%)
1	JMF Mix	2.5	6
2	JMF Mix + 1 Gallon Super Plasticizer	5	10

H.2.3 Casting of Trial Slabs and Beams

The concrete was placed in the formwork of the slabs and 6" x 6" x20" beams. It was observed that the workability was adequate for concrete with such a high fiber content, and the concrete was free of fiber balls. The initial mix was used for placing Slab 1 and beams, and the improved mix was used for placing Slab 2 and benches. Figures H.6 and H.7 show the placement of concrete into the molds for the slabs, beams and benches.



Figure H.6 Placement of Concrete into the Formwork for Slab 1 and Beams



Figure H.7 Placement of Concrete into the Formwork for Slab 2 and Deep Shoulder Benches

H.2.4 Finished Surface of the Slabs

After casting, the slabs were compacted normally with hand tools, as the thickness of the slabs was relatively small, and the slabs surfaces were finished manually using trowels. The surfaces of Slab 1 and Slab 2 are shown in Figure H.8. It was observed that the mix design with an additional one gallon of super plasticizer finished well and had a smooth surface.



Figure H.8 Surface Finish of Slab 1 and Slab 2

H.3 Hinckley Bridge Slab Placement

The casting of a deck slab of a bridge located in Hinckley Township, Ohio, was scheduled on June 17, 2017, beginning at 2:30 a.m. The selected bridge (shown in Figure H.9) is a three-span continuous slab bridge deck with a span configuration of 24 ft.–30 ft.–24 ft. with a deck thickness of 16 inches. The bridge was designed with a cap and pier connection at the two pier cap locations and semi integral abutments at the ends.



Figure H.9 The Selected Three-Span Bridge in Hinckley, Ohio

The reinforcement details for the deck to be installed at the selected bridge were designed according to CS-01-08 standards using epoxy-coated steel reinforcing bars. The top steel was #8 steel with 6-inch spacing, and the bottom steel was #6 steel with 5.5-inch spacing. The slab and the pier cap were connected by a rigid connection type with a #6 U-shaped bar. Figure H.10 shows the reinforcement mesh of the slab before placement and the reinforcement at the connection of the pier cap and slab.



Figure H.10 Reinforcement Mesh (left); Pier Cap and Slab Connection (right)

H.3.1 Mix Design Used

Class QC2 concrete with 10 lb. /yd³ of polypropylene fibers was recommended for the placement of this bridge. The typical mix design proportions for a minimum compressive strength of 4500 psi are presented in Table H.2.

Table H.2 Design Mix Proportions (Osborne Medina, Inc.)

Material	Design Quantity	Batched Quantity
Portland Cement Type 3	500 lb.	3985 lb.
SLAG	215 lb.	1795 lb.
57 Stone	1200 lb.	9600 lb.
Sand	1100 lb.	9060 lb.
8 Stone	550 lb.	4380 lb.
Water	33.7 gal.	228 gal.
Super	16 /C	912 oz.
Air	0.35 /C	20 oz.

H.3.2 On-Site Slump and Air Content Tests

Slump and air content of the mix are the critical parameters considered for the approval of concrete. ODOT requires a slump of 4 to 5 inches and an air content of 6 to 8% to be maintained in the mix to achieve the desired workability, consolidation and finish. Slump and air content tests were performed at regular intervals (Figure H.11) to ensure the mix design satisfied ODOT requirements before it was placed on the deck.

ASTM C143 and ASTM C231 methods were followed at the site to test for slump and air content, respectively. Additional cylinders for each truckload of concrete were made and retained for future tests. It was observed that the average slump was about 4.5 inches and the average air content was 6% (Figure H.12).



Figure H.11 Air Content Testing (left) and Slump Testing (right) at the Site



Average Air Content ~ 6%

Average Slump: 4.5 inches

Figure H.12 Air Content Test (left) and Slump Test (right)

H.3.3 Placement of Concrete on the Bridge Deck

Once the concrete was approved after the slump and air content tests, the concrete from the trucks was loaded onto a conveyor system. The concrete was then moved on the conveyor over a long boom and dropped from the chute onto the bridge deck formwork. The details of concrete placement in formwork is shown in Figure H.13. The temperature at the site during the placement was about 71°F, and the relative humidity was about 60%.



Figure H.13 Placement of Concrete into the Bridge Deck Formwork

H.3.4 Consolidation of Concrete

The concrete placed in the formwork was vibrated using pin vibrators. The concrete was spread uniformly and then consolidated well. From visual observation, the concrete was seemed to be adequately consolidated to allow for proper finishing.

H.3.5 Surface Finishing

The surfaces at the edges of the slab were finished manually using trowels. A surface finishing process was then adopted to finish the surface of the slab as shown in Figure H.14. In this process, rollers move transversely over the length of the bridge, consolidating the concrete and leveling it. The rollers were followed by a flat plate trowel finishing of the surface. It was important to have a good surface finish on the slab, as the concrete contained a high dosage of fibers. To reduce the extrusion of fibers on the surface, burlap finishing was adopted to further smoothen the surface of the deck as shown in Figure H.14. The process was continuous over the entire length of the deck surface, starting at one end of the bridge and continuing to the other end. The three process finishing was found to provide a much better surface finish than the finish obtained for the slabs in the trial casting at the Osborne concrete plant.



Figure H.14 Three-way Surface Finish Process Adopted for the Bridge Deck

H.3.6 Finished Surface of Deck

The finished surface seemed to be acceptable, as shown in Figure H.15. Very few fibers were observed to be protruding from the deck surface, as can commonly occur for deck slabs containing such a high dosage of fibers. As the fibers used in the mix for the bridge deck were made from polymers, it is expected that they will wear out over time once the bridge is opened to traffic.



Figure H.15 Finished Surface of the Bridge Deck

H.3.7 Burlap Placement

Once the surface of bridge deck was finished, it was left exposed to sunlight for a few minutes. Four feet wide wet burlap sheets were placed transverse to the span of the bridge. The wet burlap, was placed very carefully so as to cover the entire area of wet concrete, as shown in Figure H.16.



Figure H.16 Placement of Wet Burlap over the Bridge Deck

H.3.8 Curing of the Deck

Once the bridge was completely covered with wet burlap, a plastic sheet was placed on top of the burlap to prevent the deck from drying too quickly during the curing process (Figure H.17). Proper curing procedures were followed in the construction of the bridge deck to ensure optimum


results. Wet curing was done by maintaining continuous flow of water under the burlap for seven days.



Figure H.17 Curing of the Bridge Deck

H.3.9 Cylinder Compressive Strength

The cylinders collected from the site on the day of cast, were cured for 28 days and the tested for compressive strength. The typical results of compressive strength is shown in figure H.18.



Soil Testing & Engineering, Ltd.
GEOTECHNICAL ENGINEERING, SUPERVISORY, FIELD, MATERIALS TESTING & INSPECTION SERVICES

REPORT OF CONCRETE COMPRESSIVE STRENGTH

Project Name: ODOT 163003 Project No.: 17-0027
 Client: Rietschlin Bros Date: 6/17/2017

FIELD DATA (Sampling: ASTM C172)

General Location: Deck Lot/Sublot: _____ Set No.: 3 QC2
 General Description: _____ Sample from: Truck
 Date Placed: 6/17/2017 Plant: Osborne Medina
 Time Made/Batched: _____ Truck No.: _____
 Time Unloaded: 7:45 AM Ticket No.: 740869
 Time Cylinder Made: 7:45 AM (ASTM C31) Plasticizer added: _____
 Slump (in): 5 (ASTM C143) Water added: _____
 Air Content (%): 4.9% (ASTM C231) Cement: _____
 Air Temp. (°F): _____ Mix: JMF# 3610Q2BP
 Concrete Temp. (°F): 70 (ASTM C1064) Fine Aggregate: Sand
 Unit Weight (pcf): 142.31 (ASTM C138) Coarse Aggregate: #57, #8

Data Submitted by: J. Crowe

COMPRESSION TEST RESULTS (ASTM C39 & C1231)

Specimens Made by: J. Crowe Specimen Cast Date: 6/17/2017

Required Strength: 4,500 psi @ 28 days

Lab No.	Set No.	Cylinder	Curing Type	Test Date	Age (days)	Daily Avg. Cyl. Diam. (in.)	Daily Avg. C.S.A. (in ²)	Weight (lbs.)	Max. Load (lbs.)	Strength (psi)
	3 QC2	A	Tank	7/15/17	28	4.008	12.62	8.34	67360	5340
	3 QC2	B	Tank	7/15/17	28	4.008	12.62	8.42	67370	5340
	3 QC2	C	Tank	7/15/17	28	4.008	12.62	8.36	65710	5210

Type 1 C Type 2 Type 3 Type 4 JK Type 5 Type 6

Test Performed by: A. Golfarb Reviewed by: Shafi Alam P.E.

Revised 6-13-14

675 SHEERINGS ROAD • SUITE F • DUBLIN, OHIO 43016 • 614.761.4700 • FAX 614.761.8630
 630 ORCHARD LANE #301 • BEAVERCREEK, OHIO 45424 • 937.426.3100 • FAX 937.426.7633

Figure H.18 Typical Compressive Strengths of Cylinders Tested at 28 Days

H.4 Inspection of the Bridge Deck while the Bridge is in Service

The bridge was opened to traffic after a month from the day the deck was cast. The bridge was visually inspected on 08-03-2017, to monitor any formation of cracks over the negative moment region and was found to have developed absolutely no cracks. Also, there were no shrinkage cracks observed during the inspection. The bridge may be monitored every year to see if any cracks develop on the deck over the pier caps.

H.5 Summary and Conclusions

Based on the finding from this project, it was recommended to use polypropylene fibers in the concrete mix for bridge decks with a high dosage of 10 lb/yd³ to arrest cracks and consequently increase the service life of the decks in Ohio. A bridge located in Hinckley, Ohio, was selected as the site for a demonstration project. The selected bridge was a three-span continuous slab bridge with spans of 24 ft.–30 ft.–24 ft. and a slab thickness of 16 inches. Since this demonstration project was first of its kind in Ohio to use a high dosage of fibers, a trial concrete placement was done to develop a mix design that is easily workable to meet the requirements for slump and air content including an acceptable surface finish.

The implementation project that was completed in Hinckley, Ohio with a polypropylene fiber dosage of 10 lb/yd³ demonstrated that placement, consolidation and finishing of the proposed fiber-reinforced concrete were very similar to that of normal concrete. The bridge was opened to traffic after a month from the day the deck was cast. The bridge was visually inspected several times after being open to traffic, to verify if any cracks developed over the negative moment region. It was found that no visible cracks developed on this pilot bridge over the period of inspections of about three months.

REFERENCES

- ASTM C143 / C143M-15a “Standard Test Method for Slump of Hydraulic-Cement Concrete.” ASTM International, West Conshohocken, PA. 2015. Available at <https://www.astm.org/Standards/C143.htm>
- ASTM C192 / C192M-16a “Standard Practice for Making and Curing Concrete Test Specimens in the Laboratory.” ASTM International, West Conshohocken, Pennsylvania. 2016. Available at <https://www.astm.org/Standards/C192.htm>
- ASTM C231 / C231M-17a “Standard Test Method for Air Content of Freshly Mixed Concrete by the Pressure Method.” ASTM International, West Conshohocken, Pennsylvania. 2017. Available at <https://www.astm.org/Standards/C231.htm>